MASARYK UNIVERSITY

FACULTY OF MEDICINE

DEPARTMENT OF PATHOLOGICAL PHYSIOLOGY

INTERPLAY BETWEEN AGGRESSIVE PROSTATE CANCER

METABOLISM AND BIOMECHANICS

Habilitation thesis

Brno 2021   MUDr. Jaromír Gumulec, Ph.D.

Summary

Introduction. The invasion of cancer cells and metastasis formation is energetically highly demanding process. The increase of cancer cell mobility during metastasis formation is accompanied by a reinforcement of the cytoskeletal architecture, cell-cell, and cell-ECM interactions. There is a tempting theory that more deformable cells (of lower Young modulus) are favoured for metastatic spreading. However, data regarding prostate tumors suggest the opposite – a stiffening of cancer cells. The aim here is (a) to analyse prostate cell mechanical properties by a panel of methods, (b) to analyse how cell mechanical properties change through the cancerogenesis, (c) whether quantitative phase imaging correlates with standard approaches used for cell mechanophenotyping, (d) whether advanced image analysis algorithms can be used in the extraction of image features from quantitative phase images specific for aggressive/stiff cells, (e) how metabolic reprogramming is linked with these processes, and (f) how these processes are regulated and potentially targeted.

Methods. By using atomic force microscopy, quantitative phase imaging, confocal microscopy, transcriptomic techniques and migratory and cell invasiveness assays and by analysis of metabolic intermediates the metabolic and biomechanical phenotype of cells was analysed. Deep learning approaches were used for image processing and translation.

Results. We demonstrated potential of quantitative phase imaging for fast label-free and non-contact cell mechanophenotyping. Primary prostate tumor-derived Caveolin-1 (CAV1)-non-expressing-cells are more pliable and predominantly performing OXPHOS, while metastasis-derived, high-CAV1-expressing cells are are mechanically stiffer and predominantly employing glycolysis and rerouting the use of amino acids as energetical sources, specifically aspartate. Upon induction of zinc resistance further increase of stiffness was observed in metastatic cells together with alteration in cancer cell metabolites, amino acids in particular.

Conclusions. Here we demonstrated potential of machine learning in quantitative phase imaging. It was shown to be a powerful tool for image segmentation, classification of aggressive cancer cells and extraction of features from quantitative phase image not visible by the naked eye and thus enabled to connect biophysical and mechanical features of the cells with biological cellular processes.

Contents

1   Papers included in the habilitation thesis

Papers presented in this thesis aim to address how cell mechanical properties change during the pathogenesis of prostate cancer on *in vitro* model and how it relates with other well-described tumor hallmark –tumor metabolic state. Following papers are an integral part of this thesis. Their mutual connection and a broader context are discussed in the following chapters.

1.   STEPKA, P., V. VSIANSKY, M. RAUDENSKA, J. GUMULEC, et al. Metabolic and Amino Acid Alterations of the Tumor Microenvironment. Current Medicinal Chemistry, 2021, 28(7), 1270-1289.

Experimental work (%)	Supervision (%)	Manuscript (%)	Research direction (%)
-	30%	30%	30%

2.   RAUDENSKA, M., J. GUMULEC, J. BALVAN AND M. MASARIK Caveolin-1 in oncogenic metabolic symbiosis. International Journal of Cancer, Oct 2020, 147(7), 1793-1807.

Experimental work (%)	Supervision (%)	Manuscript (%)	Research direction (%)
-	40%	40%	50%

3.   GUMULEC, J., J. SOCHOR, M. HLAVNA, M. SZTALMACHOVA, et al. Caveolin-1 as a potential high-risk prostate cancer biomarker. Oncology Reports, Mar 2012, 27(3), 831-841.

Experimental work (%)	Supervision (%)	Manuscript (%)	Research direction (%)
90%	0%	60%	15%

4.   VICAR, T., J. BALVAN, J. JAROS, F. JUG, et al. Cell segmentation methods for label-free contrast microscopy: review and comprehensive comparison. BMC Bioinformatics, June 28 2019, 20(1), 360.

Experimental work (%)	Supervision (%)	Manuscript (%)	Research direction (%)
70%	90%	60%	90%

5.   VICAR, T., J. GUMULEC, J. BALVAN, M. HRACHO, et al. Label-Free Nuclear Staining Reconstruction in Quantitative Phase Images Using Deep Learning. In L. LHOTSKA, L. SUKUPOVA, I. LACKOVIC AND G.S. IBBOTT. *World Congress on Medical Physics and Biomedical Engineering 2018, Vol 1*. New York: Springer, 2019, vol. 68, p. 239-242.

Experimental work (%)	Supervision (%)	Manuscript (%)	Research direction (%)
50%	40%	40%	70%

6.   RAUDENSKA, M., M. KRATOCHVILOVA, T. VICAR, J. GUMULEC, et al. Cisplatin enhances cell stiffness and decreases invasiveness rate in prostate cancer cells by actin accumulation. Scientific Reports, 2019/02/07 2019, 9(1), 1660.

Experimental work (%)	Supervision (%)	Manuscript (%)	Research direction (%)
50%	30%	70%	30%

7.   ELSAYAD, K., G. URSTOGER, C. CZIBULA, C. TEICHERT, et al. Mechanical Properties of cellulose fibers measured by Brillouin spectroscopy. Cellulose, May 2020, 27(8), 4209-4220.

Experimental work (%)	Supervision (%)	Manuscript (%)	Research direction (%)
25%	5%	20%	5%

8.   KRATOCHVILOVA, M., M. RAUDENSKA, Z. HEGER, L. RICHTERA, et al. Amino Acid Profiling of Zinc Resistant Prostate Cancer Cell Lines: Associations With Cancer Progression. Prostate, May 2017, 77(6), 604-616.

Experimental work (%)	Supervision (%)	Manuscript (%)	Research direction (%)
30%	100%	80%	70%

9.   HEGER, Z., J. GUMULEC, N. CERNEI, H. POLANSKA, et al. Relation of exposure to amino acids involved in sarcosine metabolic pathway on behavior of non-tumor and malignant prostatic cell lines. Prostate, May 2016, 76(7), 679-690.

Experimental work (%)	Supervision (%)	Manuscript (%)	Research direction (%)
25%	20%	40%	20%

10.   RAUDENSKA, M., J. BALVAN, M. FOJTU, J. GUMULEC, et al. Unexpected therapeutic effects of cisplatin. Metallomics, Jul 2019, 11(7), 1182-1199.

Experimental work (%)	Supervision (%)	Manuscript (%)	Research direction (%)
-	30%	40%	30%

2   Introduction

During a multistep oncogenic process, cancer cells need to perform changes in metabolic phenotype to maintain energy for cancer cell invasion, survival in circulation, or homing in a distant site [3]. Accordingly, aberrant tumor cell metabolism is one of the key tumor hallmarks and a possible therapeutic target [4]. Historically, metabolic changes were first linked with glucose metabolism. A phenomenon described in 1924 by Otto Warburg – the "Warburg effect" is characterized by a switch from oxidative phosphorylation (OXPHOS) to glycolysis in a presence of oxygen – the aerobic glycolysis. Despite the inefficiency of this process from the perspective of ATP-per-glucose extraction ratio, its inevitable advantage over oxidative phosphorylation is speed, making glycolysis beneficial for the rapidly dividing cancer cells[3], although it is energetically harmful on the whole-body level.

Cancer cell invasion and metastasis formation is energetically highly demanding process. The cancer cells not only need to increase their migratory capacity, but they also pass through the mechanical barriers during the metastasis formation. The energetic demands of cancer cells to overcome mechanical barriers during the cancer progression are high, consuming up to 50% of cellular ATP [5]. These barriers cause significant physical forces to affect cancer cells during their migration through extracellular matrix (ECM) (stretching, internal tension), crossing the endothelial barrier into circulation, presence in circulation (shear stress), and during migration to a secondary niche (increased motility). To overcome this, cancer cells adapt to these forces by several strategies. The cells undergo epithelial-mesenchymal transition, which enables migratory and invasive properties by changes in cell-cell and cell-ECM adhesions and by cytoskeletal remodelation [3]. These factors trigger mechanotransduction which in turn modulate the cancer cells' signalling by favouring metabolic and mechanic settings enabling successful invasion and cell survival in hostile environments. Rearrangement of cancer cells' actin cytoskeleton associated with cell stiffening is a key process resulting from mechanotransduction. Changes in cell mechanic phenotype and metabolic reprogramming are therefore not separate cancer hallmarks. Instead, these two processes are highly interdependent. For instance, glycolysis responds to architectural features of actomyosin cytoskeleton via TRIM21-mediated regulation of phosphofructokinase [6].

Prostate tumors are the most common type of tumors in men. These tumors share unique metabolic and biomechanical features. Metabolic specificity is attributed to the prostate-specific

effects of zinc ions. Due to the physiological zinc accumulation in benign cells, mitochondrial aconitase is inhibited, which causes a blockage of Krebs cycle and thus a decrease in OXPHOS. On the other hand, malignant cells show a decrease in zinc accumulation and thus increased OXPHOS. Therefore, no Warburg effect is observable in primary tumors of prostate [7]. However, the metabolic phenotype of prostate cancer changes during its progression with an increase of aerobic glycolysis in secondary tumors [8]. Therefore, although metabolic targeting seems to be an attractive therapeutic target, simplistic strategies like glycolysis inhibition fail, because this problem is multidimensional (metabolism changes during cancer progression as well as there are differences between cell populations in tumor microenvironment (TME)).

This thesis aims to characterize how the metabolic phenotype changes through the prostate cancer progression and how it scales with changes of biomechanical features of the cancer cells. Together with routinely used methods to analyse cell biomechanics, a potential way to describe the mechanical phenotype of cells using label-free quantitative phase microscopy is tested. The informative value of the quantitative phase image (QPI) is further expanded utilizing machine learning methods.

In a series of scientific papers, we demonstrated (on an *in vitro* model) that highly aggressive prostate cancer cells are mechanically stiffer and at the same time characteristic by a spectrum of metabolic shifts – cells are more anaerobic and overly metabolize essential amino acids.

2.1   Cell mechanics – important cancer hallmark

From the spectrum of the existing mechanical properties of the materials, the most relevant cellular biomechanical parameters include elasticity, viscosity and adhesiveness [9]. Cells have viscoelastic properties, however, from the perspective of cancer cells, the elastic properties dominate over the viscous properties [10]. The elastic properties – "stiffness" of the material – is defined as the extent to which the material resists the deformation with a defined applied force [11]. Stiffness of the structures is determined by the material properties – its composition and its organisation [12]. Specifically, the determinant of tissue stiffness is the composition and the organisation of extracellular matrix and the main determinants of cellular stiffness are cytoskeleton, focal adhesions and nuclear deformability [12]. Stiffness is expressed as Young modulus in Pascals and in the context of biomedical applications it scales in the orders of 10^1–10^3 Pa in most cells, 10^4 Pa in muscle, 10^7 Pa in tendons and up to 10^9 Pa in bone [9]

Tumor tissues are typically stiffer as a consequence of higher fibrous tissue crosslinking in extracellular matrix – desmoplastic reaction [13]. As extracellular matrix (ECM) stiffness is linked

with tumor aggressiveness and patient prognosis, there has been an extensive effort to characterize how the mechanical properties of the ECM can affect the cancer cells. Physiologically, cells can sense the physical properties of the environment and transduce signals to the cellular level. Integrins and focal adhesion proteins act as transducers that convert the extracellular matrix signals downstream to the cells in a process called mechanotransduction.

The mechanical signals from stiff ECM are transduced to cells through integrins and focal adhesion proteins, which in turn regulate processes favouring cell survival. Such mechanical stimuli can modulate epithelial-to-mesenchymal transition, intravasation and affect metabolic adaptation, cell death and resistance to radiotherapy and chemotherapy [3; 14]. Therefore, tumors with higher desmoplasia were characterized as more aggressive and more resistant to conventional treatments [15; 16]. Accordingly, the cell mechanical properties are altered by this mechanism.

These cytoskeletal rearrangements, together with changes of numbers of focal adhesions and with the deformability of nucleus, are factors that affect cellular mechanical properties. Generally, most tumor cells isolated from tumor tissues are usually softer compared to non-tumor counterparts [17]. The (cancer) cell migration and the cell mechanical properties are tightly connected processes because cytoskeletal rearrangements are associated with both of these. Therefore, migration (metastatic potential) and stiffness are typically inversely proportional [12]. Soft and deformable cells are favoured in multistep oncogenesis – for such cells, it is easier to migrate through small gaps or crowded ECM [10]. However, despite many studies, the association of cellular stiffness with metastatic potential is not as unequivocal as the ECM stiffness. The uncertainness is underlined by several factors, such as a particular type of technique used to determine cellular stiffness and cell culture method [12].

As different physical forces affect cells throughout the process of cancer progression, a spectrum of methods to describe cell mechanical properties is used. In the circulation, cell deformation occurs during intravasation and extravasation. Aggressive cells are usually more deformable, and deformability cytometry might be employed to measure this. During the passage through the endothelial wall, aggressive cells are predominantly softer. This can be measured by atomic force microscopy (AFM). In the secondary site, tensile and contractile forces affect the cells. To measure this, tensile biaxial stretching or traction force microscopy is usually employed [18; 19]. Quantitative phase imaging (QPI) demonstrated to be a new promising technique to study cell mechanic phenotype. As the light passes through physically different structures of the cell, the light phase is changing. The quantitative phase imaging is a non-invasive technique with high intrinsic contrast even for naturally transparent objects such

as live cells [20]. Using this technique it is possible to extract cell dry mass (in pg/μm^2) from the phase (in radians) according to the Barer and Davies [21; 22]. Since the changes of cytoskeletal architecture are associated with the consequent changes in the cell biomechanical characteristics including cell stiffness and cell motility [23], cell dry mass is also expected to be correlated with changes of cell mechanics. Such finding was demonstrated by Eldridge et al: the authors applied QPI to characterize cellular stiffness by using an effective spring constant. The authors also showed that this metric further correlated to cellular mass distribution [24]. However, the association between the phase shift and cell biomechanics is still under research and a direct comparison of this technique with AFM is not straightforward. Nevertheless, the deployment of QPI in cell mechanics might provide significant benefits over AFM as the latter is characteristic by low throughput and cell-cantilever mechanical stress [18].

Taken together, changes in biomechanics are crucial for tumor development. The consequences of mechanotransduction in stiff environments were intensively studied and relatively rigidly show a link between increased ECM stiffness and worse prognosis. However, the crosstalk between cell adhesion molecular machinery and metabolic reprogramming is still far from being understood [3]. Similarly, the determinants of cellular stiffness, underlying mechanisms, consequences, and an impact of cancer cells stiffening or softening on patient prognosis is still not satisfactorily clarified.

2.2   Metabolic changes through tumor progression

As mitochondrial ATP production is dramatically more effective in ATP-per-glucose ratio, most differentiated eukaryotic cells use OXPHOS as a main source of ATP. Glucose is typically metabolised to pyruvate during glycolysis. This results from a generation of small amounts of ATP. Subsequently, pyruvate is transferred to mitochondria and undergoes oxidation to acetyl-CoA, which in turn enters the Krebs cycle. Protons created during Krebs cycle are transferred by NAD+ and FADH to an inner mitochondrial membrane and thereby creating pH gradient. This gradient is in turn discharged in oxidative phosphorylation (OXPHOS) in the presence of oxygen by producing high amounts of ATP. OXPHOS is, therefore, a major strategy to synthesize energy.

On the other hand, cancer cells are characterized by the urgent needs of energy supplies, not concerning the effectivity of ATP production. Although the OXPHOS is highly effective, it is a highly complex process. Glycolysis, on the other hand, is despite low ATP extraction levels per glucose molecule extremely fast process. As a consequence, in the cancer cells, the Warburg

effect reroutes the synthesis of ATP to glycolysis, which results in the accumulation of intermediate metabolites needed for cell proliferation.

Although tumor cells typically shift to aerobic glycolysis, some tumor cells preserve high OXPHOS, a "reverse Warburg effect". One of such examples are primary prostate cancer cells. The resulting metabolic phenotype is however not a constant phenomenon – it changes through the tumor progression according to the actual needs of individual cells. Accordingly, a focus cannot be given only to the metabolism of glucose, but also to other macronutrients. For instance, the supply of amino acids is important for tumor cells to sustain their proliferative drive. Alongside their direct role as substrates for protein synthesis, they can have roles in energy generation and a redox balance [25]. This is of great importance in nutrient-poor situations which often develop in tumor microenvironment. Moreover, it has been shown that cancer cells are specific by auxotrophism, that is inability to synthetize compounds required for growth. From the perspective of amino acids, the perspective of essential and non-essential might not apply in every situation [25]. Author's experimental publications on these topics are discussed in chapters 4.3.1 and 4.3.2.

In the following review [8] we summarize current evidence on how amino acid metabolism changes throughout progression and point out to specific tumor types which differ in auxotrophism for specific amino acids.

STEPKA, P., V. VSIANSKY, M. RAUDENSKA, J. GUMULEC, et al. Metabolic and Amino Acid Alterations of the Tumor Microenvironment. Current Medicinal Chemistry, 2021, 28(7), 1270-1289.

article text hidden due to licensing restrictions

article text hidden due to licensing restrictions

article text hidden due to licensing restrictions

article text hidden due to licensing restrictions

article text hidden due to licensing restrictions

article text hidden due to licensing restrictions

article text hidden due to licensing restrictions

article text hidden due to licensing restrictions

article text hidden due to licensing restrictions

article text hidden due to licensing restrictions

article text hidden due to licensing restrictions

article text hidden due to licensing restrictions

article text hidden due to licensing restrictions

article text hidden due to licensing restrictions

article text hidden due to licensing restrictions

article text hidden due to licensing restrictions

article text hidden due to licensing restrictions

article text hidden due to licensing restrictions

article text hidden due to licensing restrictions

article text hidden due to licensing restrictions

2.3 Caveolin-mediated metabolic symbiosis in tumor stroma

Multiple populations exist within the tumor microenvironment (stromal cells, immune cells, various subpopulations of cancer cells). From the perspective of metabolism, a specific symbiosis between the stromal and tumor cells develops in order to reroute the nutrients to energy-demanding cancer cells. For instance, cancer-associated fibroblasts (CAFs) surrounding malignant cells are characteristic by enhanced aerobic glycolysis and high lactate efflux via MCT4 transporter [26]. This enables the uptake of CAF-produced nutrients by the cancer cells. Similar symbiosis was described also in tumor-associated macrophages or between multiple subpopulations of cancer cells [4; 27].

Interestingly, these populations often vary in caveolin-1 (CAV1) expression (low CAV1 in CAFs and high CAV1 in cancer cells). CAV1 is a 21 kDa protein predominantly localized in caveolar membrane structures, caveolae. It regulates cellular metabolism via providing docking sites for glycolysis enzymes (aldolase, phosphofructokinase), it affects mitochondrial bioenergetics via upregulation of mitochondrial amounts and respiration rate, it regulates glutaminolysis and affects autophagy [28]. Within tumor microenvironment, it is a regulator of cellular metabolic reprogramming. For example, in colorectal cancer, it has been shown that an increase of CAV1 resulted in increased glucose intake and increased ATP production. Nevertheless, CAV1 effect is context dependent. In some cell types, high CAV1 support the glycolytic phenotype while in others CAV1 knockdown is associated with higher levels of glycolysis [29].

However, the effects of CAV1 are far beyond regulation of cellular metabolism and it participates in mechanotransduction [30], cell migration and mechanical stress responses [31; 32], indicating that caveolins are crucial regulators of cell mechanic and cell metabolic phenotype during tumor progression. Physiologically caveolin-rich caveolae are important in cell types under mechanic stress like smooth muscle cells, which are exposed to stretch, and endothelial cells, which face high shear stress [33; 34]. Caveolae flattening may provide a buffer for tensile forces and prevent the cell lysis due to mechanical stress. During mechanical stress surface-to volume ratio may increase as the caveolar membrane is released, resulting in cellular protection [35].

Prostatic tumors are – compared to most epithelial tumors – not characteristic by high glucose intake and high glycolysis (no Warburg effect). This is important diagnostically as primary prostate tumors are usually not detectable by FDG-PET scans. Nevertheless, Warburg effect is detectable in later stages of cancerogenesis. These findings resulted in a formulation of hypotheses for this thesis (chapter 3): That is: the level of CAV1 differs in various prostate tumor cell

populations and throughout the tumor progression is associated with changes in cell mechanics and metabolic reprogramming.

In the review by Raudenska et al. [4], a role of caveolin-1 in the cancer cell metabolic reprogramming is discussed. Moreover, a link between cell mechanics and CAV1 is discussed here.

RAUDENSKA, M., J. GUMULEC, J. BALVAN AND M. MASARIK Caveolin-1 in oncogenic metabolic symbiosis. International Journal of Cancer, Oct 2020, 147(7), 1793-1807.

Caveolin-1 in oncogenic metabolic symbiosis

Martina Raudenska [1], Jaromir Gumulec [1,2,3], Jan Balvan [1,2,3] and Michal Masarik [1,2,4]

[1]Department of Physiology, Faculty of Medicine, Masaryk University, Brno, Czech Republic
[2]Department of Pathological Physiology, Faculty of Medicine, Masaryk University, Brno, Czech Republic
[3]Department of Chemistry and Biochemistry, Mendel University in Brno, Brno, Czech Republic
[4]BIOCEV, First Faculty of Medicine, Charles University, Vestec, Czech Republic

Metabolic phenotypes of cancer cells are heterogeneous and flexible as a tumor mass is a hurriedly evolving system capable of constant adaptation to oxygen and nutrient availability. The exact type of cancer metabolism arises from the combined effects of factors intrinsic to the cancer cells and factors proposed by the tumor microenvironment. As a result, a condition termed oncogenic metabolic symbiosis in which components of the tumor microenvironment (TME) promote tumor growth often occurs. Understanding how oncogenic metabolic symbiosis emerges and evolves is crucial for perceiving tumorigenesis. The process by which tumor cells reprogram their TME involves many mechanisms, including changes in intercellular communication, alterations in metabolic phenotypes of TME cells, and rearrangement of the extracellular matrix. It is possible that one molecule with a pleiotropic effect such as Caveolin-1 may affect many of these pathways. Here, we discuss the significance of Caveolin-1 in establishing metabolic symbiosis in TME.

Background

The rapid proliferation rate of tumor cells needs effective metabolic pathways to fulfill the demanding energy requirements of neoplastic growth while generating a sufficient amount of biosynthetic precursors to maintain cell anabolism and redox homeostasis of cancer cells. Accordingly, severe reprogramming of cellular metabolism is an accepted hallmark of cancer.[1] It is now well established that oncogene activation and aberrant growth factor signaling can mediate a metabolic reprogramming of cancer cells. However, the essential role of the tumor microenvironment (TME) cannot be neglected. The tumor is an evolving system capable of adaptation to oxygen and nutrient availability. To achieve that, proliferating cancer cells successfully alter the metabolic composition of the microenvironment. Cancer cells also use different signal molecules and signaling metabolites to create tumor-supporting TME. Metabolic communication in TME involves symbiotic nutrient sharing to support tumor growth and nutrient competition to impair anticancer immunity. Intercellular metabolic pathways in the TME are analogous to normal physiological processes, only directed to support tumorigenesis.[2] Physiological

metabolic process co-opted by tumors is, for example, the glucose–lactate shuttle in the brain.[3]

The process by which tumor cells reprogram their TME involves many strategies, including changes in intercellular communication, altering TME cells metabolic phenotypes, and rearrangement of the extracellular matrix. It is possible that one molecule with a pleiotropic effect such as Caveolin-1 (CAV1) may affect many of these strategies and can be a driver molecule for oncogenic metabolic symbiosis.

Caveolins

The family of mammalian caveolins has three members, Caveolin-1 (CAV1) encoded by *CAV1* gene with 4 exons (localized on 7q31.2), Caveolin-2 (CAV2) encoded by *CAV2* gene with 3 exons (localized on 7q31.2), and Caveolin-3 (CAV3), also known as M-caveolin, encoded by *CAV3* gene with 2 exons (localized on 3p25.3). CAV1 and CAV2 are co-expressed in many various tissues, whereas CAV3 is expressed predominantly in all muscle cell types and astrocytes.[4,5] Cellular caveolins can be found in several forms, such as cytoplasmatic, secreted and membrane-bound form.[6] Membrane-bound caveolins have both the N-terminal and the C-terminal domains localized at the cytoplasmic side of the membrane. CAV2 requires CAV1 for stabilization and plasma membrane localization.[7] CAV1 and CAV2 can be found in the plasma membrane as CAV1 homo-oligomers (oligomers containing only CAV1), or hetero-oligomers containing both CAV1 and CAV2.[8,9] The tertiary structure of caveolins comprises the intramembrane domain and the scaffolding domain with a cholesterol-binding motif and a β-sheet organized region involved in the oligomerization of caveolin molecules. The hairpin topology of caveolins is further modulated by cholesterol.[10] Therefore, caveolin epitopes can be masked and at the plasma membrane may not be recognizable by specific caveolin antibodies unless cholesterol is depleted.[11]

Two CAV1 isoforms (α and β) have been identified: a slower-migrating 24-kDa α-isoform and a faster-migrating 21-kDa β-isoform. To generate these isoforms, alternative initiation of translation from a single mRNA transcript is used. The resulting isoforms differ in their N-terminal protein sequence (the β isoform is truncated by 31 residues), but both contain a complete C-terminus (Fig. 1). Caveolae are cholesterol-rich plasma membrane invaginations whose formation requires CAV1 and CAVIN1 (also known as Polymerase I and transcript release factor, PTRF). In the absence of CAVIN1, CAV1 forms noncaveolar membrane domains known as scaffolds.[12] Super-resolution microscopy identified three distinct scaffold domains: smaller S1A and S2B scaffolds and larger hemispherical S2 scaffolds.[13] Functions of the CAV1 scaffold may include regulation of focal adhesions, growth factor receptor signaling and raft-dependent endocytosis.[14] The abundance of caveolae is cell-type-dependent. They are extremely important in cells facing to mechanical stress such as smooth muscle cells (highly exposed to stretch) and in endothelial cells (highly exposed to shear stress).[15,16]

As both isoforms of CAV1 were found within caveolae (α and β), the N-terminal sequence is apparently not required for caveolar localization. A CAV1α region between amino acids 66 and 70 seems to be necessary for the exit from the endoplasmic reticulum. The amino acids 71–80 manage the inclusion of CAV1 oligomers into detergent-resistant areas of the Golgi apparatus and amino acids 91–100 and 134–154 regulate oligomerization and the exit from the Golgi apparatus.[17] CAV1 C-terminal domain contains a trans-Golgi localization signal.[18] Taken together, newly synthesized CAV1 transits through the Golgi apparatus before reaching the plasma membrane. The transport from the Golgi apparatus can be regulated by lipids and is accompanied by oligomerization, detergent insolubility and masking of specific caveolin epitopes by cholesterol.

CAV1-interacting molecules

CAV1 was identified as a substrate of proto-oncogenic kinases SRC,[20] ABL1[21] and FYN.[22] In some cellular conditions, CAV1 can be also phosphorylated due to signaling of mammalian target of rapamycin (mTOR) complex 2 (mTORC2),[23]

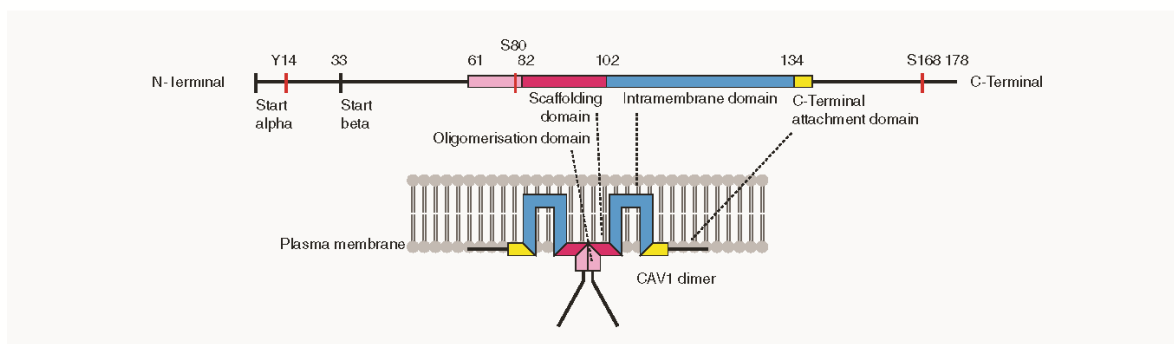**Figure 1.** Caveolin-1. Schematic diagram of CAV1 isoforms α and β and localization of CAV1 dimer in the plasma membrane. Numbers above the lines indicate the order of amino acids. Important phosphorylation sites in CAV1 are marked by red stripes. Adapted from Parton *et al.*, J Cell Sci, 2006, 119, 787.[19] [Color figure can be viewed at wileyonlinelibrary.com]

epithelial growth factor (EGF)[24] or in response to reactive oxygen species (ROS).[25] In all caveolin paralogs examined to date, only S80 and S168 could serve as common phosphorylation sites. The important phosphorylation site Y14 is exclusive for CAV1. The phosphorylation of Y14 results in a conformational change, which causes the exposure of the N-terminus for interactions with the actin cytoskeleton, most probably *via* proteins such as Filamin A or C-terminal SRC kinase (CSK)[10,26,27]. Accordingly, Y14 phosphorylation induces biogenesis of caveolae *via* actin-dependent mechanotransduction and inactivation of the early growth response-1 (Egr1) transcription factor.[28]

A fraction of CAV1 localized in caveolae has been reported to interact with many signaling proteins *via* a direct interaction between caveolin scaffolding domain (CSD; amino acids 81–101) and the conserved caveolin binding motifs (CBMs) of the interacting proteins.[29,30] Nevertheless, a recent study has challenged the validity of this model. The assessment of direct protein–protein interactions in a model system that can discriminate between membrane-bound caveolar CAV1 and a soluble form of CAV1 showed no significant interaction between caveolar CAV1 and several proteins containing CBMs, including eNOS, PPAR-γ, PTEN, RhoA and DSG2. On the other hand, the interaction between caveolar CAV1 and c-SRC, DNM2, FYN, and TRAF2 interaction was confirmed.[31] The result for eNOS is particularly surprising because of the proposed interaction of caveolar CAV1 with eNOS when CAV1 anchors eNOS in caveolae, which limits its translocation and activation and thereby reduces its capacity to generate NO.[32 34] However, as caveolae formation and CAV1 downstream signaling function through independent mechanisms,[35] CSD of soluble CAV1 can be involved in eNOS regulation. For example, CAV1 with F92A mutation within CSD forms caveolae but leads to increases in NO bioavailability *in vivo*.[35]

CAV1 in cells and tissues

CAV1 is expressed at different levels in different tissues. The highest organ-specific CAV1 protein expression is in the lung, proximal digestive tract, female tissues and skin (according to the proteinatlas.org). The highest cell-specific levels of CAV1 were found in adipocytes, endothelial cells, fibroblasts, smooth muscle cells and a variety of epithelial cells.[36]

Caveolins were originally discovered as critical proteins for the formation of caveolae in lipid rafts, which are specialized plasma membrane domains containing high concentrations of cholesterol, and were named based on this fact. Caveolae were originally thought to be involved only in the process of pinocytosis. Later, their role has expanded to include endocytosis, transcytosis, cholesterol homeostasis, signal transduction, mechanotranduction, cell migration and mechanical stress responses.[37 40] In addition to caveolae, caveolins are also expressed in the membrane of several organelles and cellular structures including Golgi apparatus,[41]

endoplasmic reticulum,[42] mitochondria,[6] nucleus,[43] lysosomes,[44] peroxisomes,[45] endocytic vesicles, extracellular vesicles (EVs; e.g., exosomes)[6,46 48] or lipid droplets.[49] There are types of cells that preferentially target CAV1 to either the cytoplasm, mitochondria or to the secretory pathway and had little CAV1 in caveolae.[6] CAV1 entry into the regulated secretory pathway is probably regulated by Serine 80. CAV1 mutant (S80A), which cannot be phosphorylated, targets CAV1 to caveolae. Consequently, it is not secreted even in the presence of dexamethasone, a secretory phenotype-inducing agent.[42] Caveolin-containing EVs may have high impact on intercellular communication inside the tumor stroma and particular on metabolic reprogramming[50] as EVs were shown to transfer functional RNAs and proteins to recipient cells causing manipulation of gene and protein expression in these recipient cells.[47,51] CAV1 was identified as essential for sorting of selected miRNAs into EVs.[48] Indeed, it has been recently shown that CAV1-containing EVs transport adhesion proteins and promote malignancy in breast cancer cells.[47] Moreover, CAV1 is strongly expressed on exosomes secreted by human melanoma cells,[52] prostasomes[53] and EVs released from the plasma membrane of osteoblasts.[54] It was also found that after effective ablation of the *CAV1* gene in adipocytes, CAV1 protein remained abundant due to CAV1-containing extracellular vesicles derived from neighboring endothelial cells.[55]

Taken together, CAV1 can be targeted to a variety of intracellular locations (Fig. 2) and therefore has caveolae-independent roles, such as lipid transport, membrane trafficking, signal transduction, regulation of gene expression and mitochondrial functions.[30] These facts deeply illustrate the pleiotropic and context-dependent role of CAV1.

CAV1 and Oxidative Phosphorylation

Several studies reveal that CAV1 is involved in the modulation of mitochondrial functions as CAV1 deficiency decreases mitochondrial respiration and reduces the activity of respiratory chain complexes.[56,57] CAV1 deficiency does not alter mitochondrial morphology or numbers but results in the proteasome-dependent degradation of Complexes I, III, IV and V upon oxidant stimulation.[58] Furthermore, low CAV1 expression also causes defective lipid metabolism and high dependency on glucose.[59 61] On the other hand, mitochondria with increased caveolin showed a decrease in apoptotic stress and targeted gene transfer of caveolin to mitochondria in C57Bl/6 mice increases cardiac mitochondria tolerance to calcium and also enhances respiratory function. In contrast, mitochondrial function is abnormal in caveolin-knockout mice.[62]

CAV1 may further modulate mitochondrial function by regulating cholesterol flux, as loss of CAV1 expression leads to cholesterol accumulation in the mitochondrial membrane, increased oxidative stress and cell death.[63] CAV1 may also control mitochondrial functions through the regulation of AFG3L2. This ATP-dependent protease is an essential
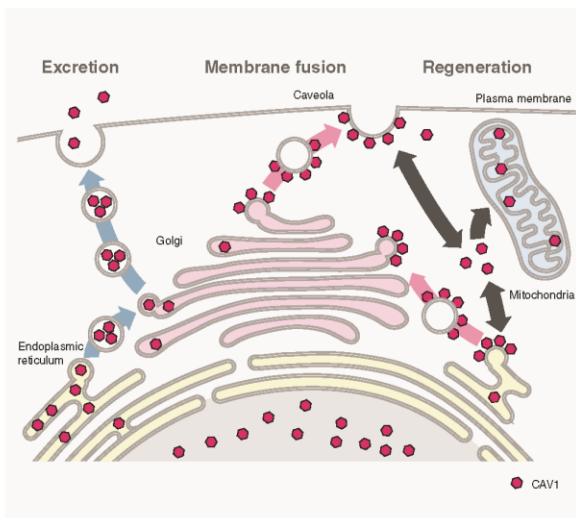
Figure 2. Intracellular localization of CAV1. CAV1 can be inserted cotranslationally into the ER membrane (pink arrow path), then can be incorporated into vesicles that move to the Golgi apparatus. In the Golgi apparatus, CAV1 oligomerizes and becomes detergent-insoluble. Once it reaches the cell membrane, CAV1 incorporates into caveolae that can be internalized and recycled. During the caveolae internalization, CAV1 can probably enter the cytoplasm of the cell as a soluble protein anchored in lipid particles. It may go to the ER and bind newly synthesized cholesterol for transport back to caveolae. Another possibility is that the soluble CAV1 remains in the cytosol. It may be incorporated into lipid droplets or can go to mitochondria (gray arrow pathways) or enter the lumen of the ER. In the lumen of the ER, the soluble CAV1 can be incorporated into HDL-like particles that are secreted from the cell (blue arrow pathways). Adapted from Liu *et al.*, J Biol Chem, 2002, 277, 41295–8.[30] [Color figure can be viewed at wileyonlinelibrary.com]

component of the conserved m-AAA complex involved in mitochondrial protein homeostasis. Upon oxidative stress triggering, the CAV1-dependent localization of AFG3L2 to mitochondria prevents mitochondrial damage and consequently, functional respiratory chain complexes are maintained. In the absence of CAV1, AFG3L2 fails to localize to mitochondria and the AFG3L2-mediated protection is lost. Under these conditions, mitochondrial Complexes I, III, IV and V are degraded by cytoplasmic and proteasome-dependent degradation, oxidative phosphorylation is impaired and CAV1 null cells are forced to rely on enhanced glycolysis for their bioenergetic requirements.[58] While the ATP generation by OXPHOS is dispensable for tumorigenesis, loss of mitochondrial Complex III/IV can have severe consequences for pyrimidine biosynthesis in cancer cells because the activity of dihydroorotate dehydrogenase (DHODH), which is a key enzyme of pyrimidine biosynthesis, is associated with the activity of Complex III. It was found that DHODH-driven pyrimidine biosynthesis is an essential pathway linking respiration to tumorigenesis as cancer cells without functional DHODH-driven pyrimidine biosynthesis in mitochondria do

not form tumors and metastases unless they reconstitute respiratory chain by mitochondria acquired from host stroma.[64,65]

A metabolic symbiosis between cancer cells

Most tumors exhibit quite a large volume of intra-tumor heterogeneity and significant metabolic compartmentalization. Tumor mass contains different subpopulations of cancer cells with different metabolic activity, such as proliferative cancer cells having high mitochondrial metabolism and lactate and ketone body uptake, or other cancer cells with low mitochondrial metabolism and high lactate and ketone body production.[66] These heterogeneous subpopulations exist in close relationship in the environment with limited resources. Consequently, they can engage in complex "ecological" interactions including competition and cooperation. The cooperation can be metabolically demanding but can lead to efficient survival, especially in a changing, harsh environment. An established metabolic symbiosis between multiple independent neoplastic subclones is crucial for tumor progression.[67] Metabolic symbiosis within a tumor is well exemplified by the occurrence of a lactate shuttle between glycolytic and oxidative cancer cells.[68,69] Glycolytic cancer cells produce lactate, creating a lactate gradient in the tumor mass. This gradient often mirrors the availability of oxygen and may significantly affect the expression of caveolins[70] (Fig. 3). Rather than being a waste metabolite, secreted lactate is a signaling molecule and powerful fuel of the Krebs cycle used by oxygenated tumor cells instead of glucose. The spared glucose can be then consumed by glycolytic cancer cells through anaerobic glycolysis. Indeed, targeting lactate-fueled respiration by inhibiting lactate transport into oxygenated tumor cells selectively kills hypoxic tumor cells as a result of disturbed metabolic symbiosis.[69]

The lactate-based metabolic symbiosis between tumor cells has been reported in various cancers.[69,71] As the prominent path for lactate uptake, monocarboxylate transporter 1 (MCT1, *SLC16A1* gene) was identified. Inhibiting MCT1 with α-cyano-4-hydroxycinnamate or siRNA in human cervix squamous carcinoma cells that preferentially utilized lactate for oxidative metabolism induced a switch from lactate-fueled respiration to glycolysis.[69] MCT1 expression can be also modulated by tumor suppressor p53. p53 is known to repress MCT1 expression interacting directly with the MCT1 gene promoter and altering MCT1 mRNA stabilization. On the other hand, p53 deficiency results in elevated MCT1 expression. In hypoxic p53(−/−) tumor cells, the expression of MCT1 is further elevated by NF-κB. Following glucose deprivation, upregulated MCT1 in p53(−/−) cells promotes lactate import and mitochondrial respiration.[72]

Pharmacological targeting of metabolic symbiosis may be a promising way to target cancer progression. MCT1 inhibition shows clinical potential in human cervix squamous carcinoma, diffuse large B-cell lymphoma, and invasive ductal carcinoma[69,73,74] High MCT1 expression was more commonly
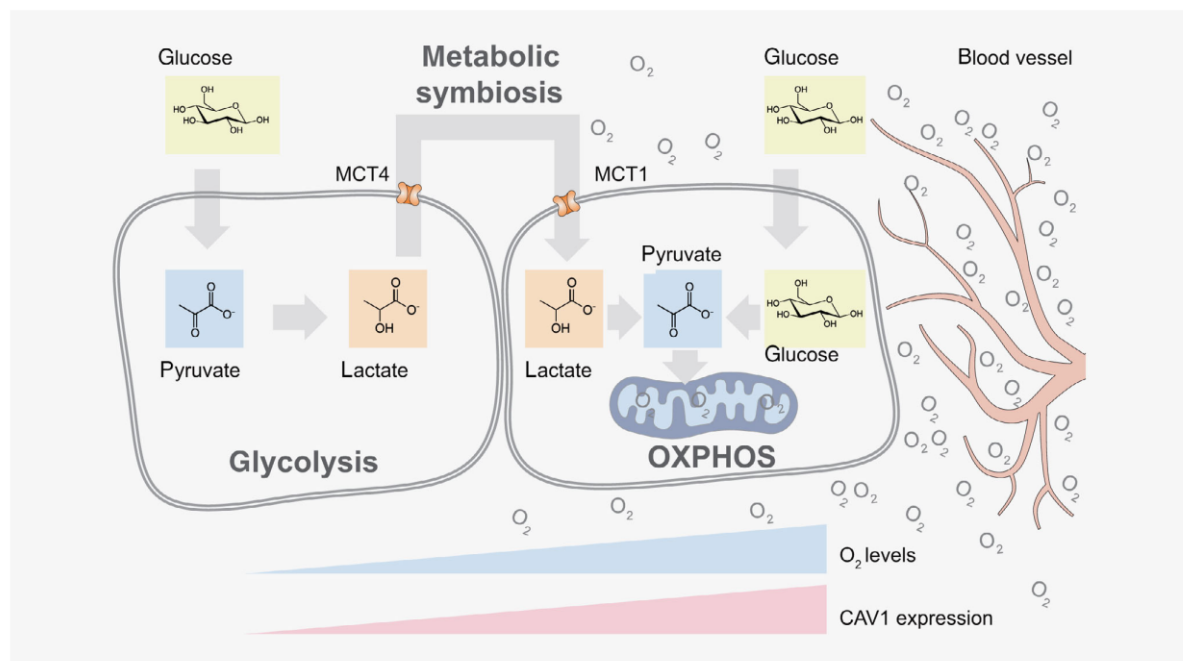
Figure 3. The lactate-based metabolic symbiosis between cancer cells in the TME. The highly glycolytic cancer cells produce lactate, creating a lactate gradient in the tumor microenvironment. This gradient often mirrors the availability of oxygen. Rather than being a waste metabolite, secreted lactate is consumed by well-oxygenated tumor cells instead of glucose. The spared glucose can be then consumed by glycolytic cancer cells through anaerobic glycolysis. Lactate is imported in oxidative cancer cells through monocarboxylate transporter 1 (MCT1, encoded by SLC16A1). Lactate efflux from glycolytic cells is managed mainly by monocarboxylate transporter 4 (MCT4, encoded by SLC16A3). [Color figure can be viewed at wileyonlinelibrary.com]

found in triple-negative breast cancers compared to ER+ and/or PR+ and compared to HER-2+ breast cancers.[74] Accordingly, triple-negative breast cancer cells have been found to use lactate as a primary source of energy, allowing them to survive glucose deprivation for extended periods. This metabolic adaptation is mediated by the estrogen-related receptor alpha (ERRα) nuclear receptor and helps cancer cells to resist anti-PI3K/mTOR targeted therapies. Blockade of lactate oxidation upon genetic or pharmacological inhibition of ERRα activity sensitized breast cancer cells to PI3K/mTOR inhibitors both *in vitro* and *in vivo*.[75] Some antineoplastic effects of statins may be also explained by blocking metabolic symbiosis. Some studies showed that statins impair mitochondrial function and OXPHOS without a compensatory upregulation of glycolysis.[76,77] Some studies also show that statins decrease the expression of CAV1[78–80] which can further contribute to mitochondrial damage.[58] Nevertheless, some statins, such as atorvastatin, increase the number of regulatory T-cells (Treg).[81] Such an increase in Treg numbers may be beneficial in stabilizing atherosclerotic plaque,[82] but on the other hand, it might weaken host antitumor immune responses.[83] Metabolic symbiosis can be disturbed also in other ways. Oxidative, high CAV1 expressing cancer cells seem to be more sensitive to antidiabetic drug metformin.

Metformin is known to inhibit both, Complex I of the respiratory chain and mTOR.[84] mTOR integrates nutrient and mitogen signals to regulate cell growth and cell division. While antagonizing both oxidative and glycolytic groups of cancer cells by inhibiting mTOR, metformin additionally inhibits OXPHOS in oxidative cancer cells relying on mitochondria for energy production. This way may metformin break the metabolic symbiosis between glycolytic and oxidative cancer cells and exert competition for glucose. Accordingly, there is evidence that the anticancer effect of metformin is significantly enhanced when glucose availability is drastically restricted.[85]

Context-dependent expression of CAV1 as a driver of metabolic symbiosis between cancer cells

It has been shown that CAV1 may have both, tumor-suppressive and oncogenic effects. These effects are probably deeply context-dependent (Fig. 4). CAV1 was associated with tumor suppression by inducing G0/G1 arrest *via* a p53/p21-dependent mechanism[86] and by the inhibition of cyclin D1.[87] CAV1 also inhibits the expression of the anti-apoptotic factor Survivin, but only in the presence of E-cadherin.[88] Moreover, targeted downregulation of CAV1 was sufficient to drive cell transformation and hyperactivate the p42/44 MAP kinase cascade.[89] Low CAV1 expression
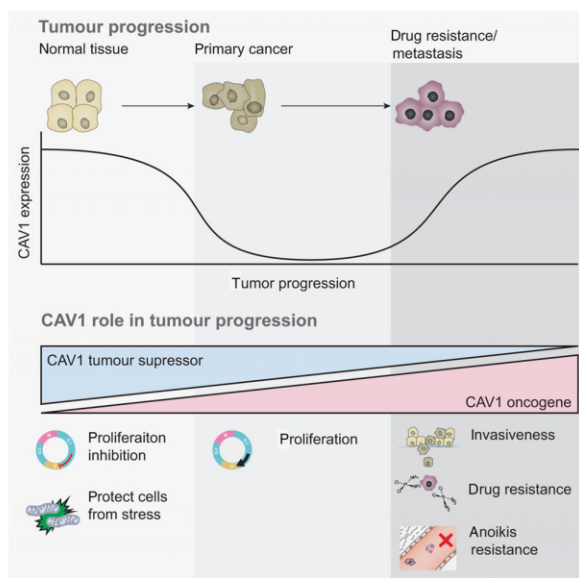
Figure 4. CAV1 during cancer development. CAV1 protects normal cells from damage, helps to maintain normal cell signaling and inhibits excessive proliferation. When CAV1 expression declines below the threshold, cells lose tumor-suppressive effects of CAV1, become sensitive to oncogenic stress and initiate proliferation, anchorage-independent growth and malignant transformation. During cancer progression to the advanced stages or treatment with cytotoxic agents, CAV1 may be re-expressed and help cancer cells escape cell death, induce treatment resistance and metastasis. Adapted from Wang *et al.*, Oncotarget, 2015, 6, 37135–50.[113] [Color figure can be viewed at wileyonlinelibrary.com]

also helps cancer cells to overcome oncogene-induced senescence (OIS). OIS is known as a powerful tumor suppressor mechanism and is dysfunctional in many cancers that have downregulated CAV1 expression.[90,91] Accordingly, many oncogenes, including SRC, RAS, BCR and ABL, have been shown to transcriptionally downregulate CAV1 expression trying to escape OIS.[92,93]

On the other hand, CAV1 was highly expressed on cancer stem cells and affected their chemosensitivity,[94] higher expression of CAV1 induced filopodia and metastases formation in lung adenocarcinoma[95] and promoted anchorage-independent survival by preventing anoikis.[96] CAV1 phosphorylated on Y14 activates RHO-associated protein kinase (ROCK) and SRC signaling with a tumor-promoting effect.[97] In the feedback loop, SRC-dependent tyrosine phosphorylation of CAV1 causes a reversible flattening and aggregation of caveolae at the cell membrane. Consequently, the cells changed from typical morphology to a rounded shape lacking polarity that might directly contribute to the transformed phenotype.[98] Flattening of caveolae may also provide a way to tolerate membrane tension during mechanical stress and prevent damage or cell lysis by changing the volume-to-surface ratio of the cell as the caveolar membrane is released into the bulk plasma membrane.[99] Flattening and dissociation of caveolae are followed

by the disassembly of caveolae and the release of caveolar proteins, including CAV1 and cavins, that may modulate the cellular response to mechanical stimuli at the molecular level.[39,100] For example, due to mechanical stress, the EHD2 ATPase is released from caveolae, SUMOylated and translocated to the nucleus, where it regulates gene transcription.[100]

As shown in Torres *et al.*, it is possible that for exerting the tumor-suppressing effect of CAV1 other interacting molecules, such as E-cadherin, are needed.[88] In cancer cells, where E-cadherin expression or its surface localization is lost,[101,102] CAV1 may not manage its tumor-suppressing role. It was also shown that in the absence of CAVIN1 expression, CAV1 increased anchorage-independent growth of advanced prostate cancer cells. CAVIN1 co-expression reversed this CAV1 effect. These results suggest that CAV1 causing this tumor-promoting effect in advanced prostate cancer is present outside of caveolae.[103] CAV1 was also shown to interact with integrins. Whereas integrin $\alpha1\beta1$ promotes CAV1 dephosphorylation,[104] integrin $\beta1$ activated by acute shear stress or fibronectin-mediated integrin activation induces CAV1 phosphorylation and cytoskeletal rearrangements promoting cell proliferation.[105,106]

It seems clear that alterations in a cellular context and consequent changes in CAV1-interacting molecules can profoundly affect the resulting function of CAV1.[107] It is also obvious that CAV1 expression tightly reflects the actual needs of cancer cells and their obtained resistance (p53 inactivation, resistance to OIS, etc.). For example, the majority of CAV1-positive breast cancers are triple-negative, high proliferative tumors, with aberrant p53 expression.[108] For these reasons, it could be disadvantageous for the evolution of tumor cells to carry permanent deleterious CAV1 mutations, because it may cause greater susceptibility to mitochondrial damage by ROS and other disadvantages.[109] Instead of this, at the cancer onset, CAV1 gene can be repressed by CpG hypermethylation, while re-expression occurs in metastatic foci and lymph nodes.[110,111] Consequently, it is very probable that tumor mass contains cancer cells at a different stage of tumorigenesis with different expression of CAV1. As CAV1-deficient cells are gradually losing their mitochondrial functions,[63] and start to rely on enhanced glycolysis and autophagy for their bioenergetic requirements,[58] reverse Warburg effect in CAV1-expressing cancer cells may appear. These CAV1-expressing tumor cells can, in the presence of CAV1 deficient catabolic cells, reprogram their metabolism toward anabolic metabolism, mitochondrial biogenesis and increased OXPHOS[112] thus establishing the metabolic symbiosis.

CAV1 in the metabolic symbiosis between cancer cells and CAFs

Metabolic symbiosis can also be established between cancer cells and cancer-associated fibroblasts (CAFs). Under physiological conditions, fibroblasts control the turnover of extracellular matrix (ECM), regulate tissue homeostasis and participate in senescence and wound healing. After they exert their functions, they are deactivated or undergo cell death.[114] In solid tumors,

ongoing desmoplasia generates mechanical forces converting normal fibroblasts to permanently active CAFs. CAFs co-evolve with the cancer cells, alter the physical and metabolic structure of the TME and may promote the transformation process by supporting cancer cell growth, angiogenesis, inflammation and metastasis. In some tumor types, CAFs represent up to 80% of the tumor mass.[115] Interestingly, the constitutively activated phenotype of fibroblasts similar to CAFs was also found in fibrotic diseases[116] which are in various tissues directly and/or indirectly regulated by CAV1. CAV1 prevents collagen deposition, fibroblast proliferation and TGF-β signaling through its negative regulation of pathways involving PI3K/AKT, Rho-like GTPase, MAPK (MEK/ERK) or JNK.[117]

It was shown that fibroblasts surrounding malignant cells have low CAV1 expression, high monocarboxylate transporter 4 (MCT4) expression and enhanced aerobic glycolysis[118] with simultaneous increase of mitochondrial activity and high expression of MCT1 transporter in the adjacent epithelial cancer cells. Such a situation enables the uptake of CAF-produced nutrients by these cancer cells. CAV1-deficient stromal fibroblasts also promote angiogenesis by recruiting CAV1-positive microvascular cells.[74,119–121] High MCT4 expression in the stromal tissue has been shown to have an important prognostic role in breast cancer.[122] In prostate cancer, a loss of stromal CAV1 correlated with a high Gleason score and worse prognosis as all metastatic tumors (either from lymph node or bone) were negative for stromal CAV1 staining. Loss of stromal CAV1 also correlated with high CAV1 expression and

activated AKT in prostate cancer cells.[123] This loss of CAV1 expression in CAFs is probably induced by ROS and oxidative stress triggered by adjacent cancer cells and executed by HIF1α activation and autophagic CAV1 degradation.[33] Fibroblasts harboring activated HIF1α showed a dramatic reduction in CAV1 levels, nitric oxide (NO) overproduction, loss of mitochondrial activity and a shift toward aerobic glycolysis resulting in an increase in lactate production. Lactate and other energy-rich metabolites could then be transferred to adjacent cancer cells and may enter their TCA cycle and increase ATP production[124] (Fig. 5). Accordingly, treatment with antioxidants (such as quercetin or N-acetyl-cysteine) or NO inhibitors (L-NAME) was able to reverse many of the CAFs' phenotypes described earlier. It seems that cancer cells may induce oxidative stress in CAFs to support their own survival through the stromal production of nutrients.[125] Moreover, the ROS and NO production in stromal cells themselves could be involved in field cancerization effect. Accordingly, eNOS-expressing fibroblasts downregulate CAV1 and induce mitochondrial dysfunction in adjacent fibroblasts that do not express eNOS. As such, the effects of stromal oxidative stress can be amplified and spread.[125]

Based on the evidence stated earlier, metformin treatment may have a potential to interrupt metabolic symbiosis by forcing oxidative cancer cells to utilize glycolysis through inhibition of Complex I of the respiratory chain, and to disturb metabolic coupling between CAFs and cancer cells.[84,126] Accordingly, highly oxidative cancer cells, such as some
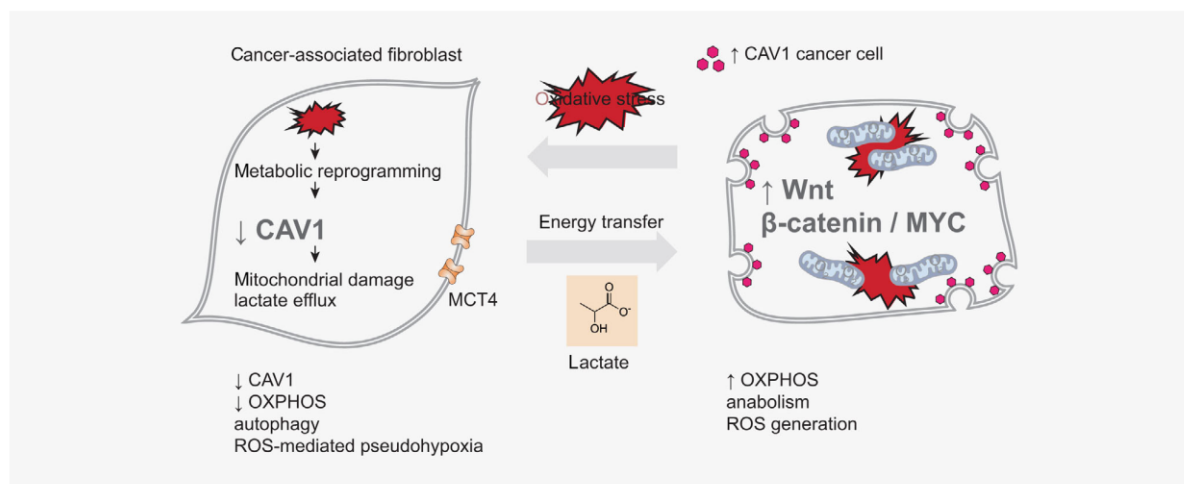
Figure 5. Oncogenic metabolic coupling between CAFs and oxidative cancer. The oncogenic metabolic symbiosis between cancer-associated fibroblasts (CAFs) and tumor cells enables malignant cells to consume metabolic substrates produced by CAFs. Cancer cells mediate metabolic reprogramming of CAFs *via* the secretion of ROS which initiates in CAFs loss of CAV1, mitochondrial damage, aerobic glycolysis, autophagy and catabolic phenotype producing high amounts of metabolites such as lactate, pyruvate or ketone bodies. Loss of CAV1 in CAFs is associated with lactate efflux and high MCT4 expression with concurrent increased mitochondrial mass and mitochondrial activity and high expression of MCT1 transporter in the cancer cells. High mitochondrial mass, associated with upregulated Wnt/β-catenin and MYC signaling, reflects cancer cells' reliance on oxidative metabolism. CAV1, Caveolin-1; MCT4, monocarboxylate transporter 4; OXPHOS, oxidative phosphorylation; ROS, reactive oxygen species. Adapted from Penkert *et al.*, Oncotarget, 2016, 7, 67626–49.[141] [Color figure can be viewed at wileyonlinelibrary.com]

cancer stem cells, have been shown to be very sensitive towards metformin treatment.[127] [130] This effect of metformin is enhanced when glucose availability is markedly restricted.[85] An interesting option may be a combined administration of metformin with 2-deoxyglucose, which is absorbed instead of glucose but is not used for glycolysis.[131] Furthermore, patients with head and neck squamous carcinoma who received metformin were found to have increased stromal CAV1 staining (from 25.7% pretreatment to 62.8% posttreatment).[132] Nevertheless, metformin alone does not seem potent enough to completely inhibit the respiratory chain and other compounds more efficient in respiratory chain inhibition such as MitoTam or cyclic pentamethinium salt may break the metabolic symbiosis more efficiently.[133,134]

The metabolic symbiosis between CAFs and tumor cells develops dynamically depending on the amount of oxygen, extracellular availability of metabolites and the presence of signaling molecules. Therefore, metabolic symbiosis may also occur in the reverse order where the oxidative metabolism of CAFs promotes the growth of glycolytic tumor cells. This can be seen in head and neck cancer (HNSCC). HNSCC CAFs secrete hepatocyte growth factor (HGF) and stimulate a glycolytic phenotype in the HNSCC cells.[135] Furthermore, CAV1 expression in CAFs favors their contractility and consequent directional migration and invasiveness of carcinoma cells.[136] CAV1 binds to intermediate filaments, such as vimentin, which in turn is required for anterior polarization of CAV1 in transmigrating cells and positively modulates the YAP mechanoresponse to substrate stiffness through actin-cytoskeleton-dependent mechanism.[137] [139] CAV1-YAP regulation further modulates pathophysiological processes such as ECM stiffening.[139] Accordingly, we can assume the existence of different CAFs subpopulation in TME.[140] While myofibroblastic types of CAFs with high CAV1 expression may increase the invasiveness of carcinoma cells, secretory CAFs with low CAV1 expression can be useful for oxidative cancer cells through metabolic symbiosis.

CAV1 in the metabolic symbiosis between cancer cells and TAMs

During cancer progression, a heterogeneous population of immune cells is recruited to the primary TME as well as to the premetastatic niche or metastatic sites. Macrophages are the most abundant population among them. The macrophages populating TME and supporting tumor growth are usually termed as tumor-associated macrophages (TAMs). TAMs were shown to promote angiogenesis, invasion, persistent growth and to suppress the cytotoxic response of T-cells.[142] The support of tumor growth can be exerted through various mechanisms such as membrane-cholesterol efflux from macrophages[143] or release of other important nutrients such as pyrimidines or pyruvate.[144,145] Pyrimidine biosynthesis is an essential pathway linking respiration to tumorigenesis.[64] As a result of many anticancer therapies, respiratory chain damage occurs.[146] Without an active respiratory chain cancer cells are dependent on exogenous uridine and pyruvate.[147] Both can be delivered by TAMs.[144,145]

Although TAMs have usually been classified as M2-like macrophages, it has become clear that this classification does not reflect the large variety of TAMs phenotypes.[148] In fact, phenotypic plasticity of TAMs has been shown, wherein macrophages present an inflammatory phenotype in the early phase of tumorigenesis while displaying an immunosuppressive phenotype in the later phases of tumor progression.[149] Accordingly, it was also shown that conditioned media derived from M1 and M2 macrophages support the growth of breast cancer cells differently.[150] Dynamic changes of CAV1 expression in TAMs reflecting different tumor sites and different stages of cancerogenesis were also found. For example, lung metastasis-associated macrophages show a much higher expression of CAV1 than TAMs from primary tumor.[151]

While pro-inflammatory macrophages are known to produce most of their ATP through glycolysis, alternatively activated immunosuppressive and anti-inflammatory macrophages have been shown to utilize rather OXPHOS. Accordingly, treatment of macrophages with IL-4, IL-25 or IL-10 was shown to upregulate OXPHOS.[152] [154] IL-10 also inhibits lipopolysaccharide-induced glucose uptake and glycolysis and suppresses mammalian target of rapamycin (mTOR). Consequently, IL-10 promotes mitophagy that eliminates dysfunctional mitochondria generating ROS.[152] On the other hand, in pro-inflammatory macrophages, MCT4 upregulation represents a positive feedback mechanism to maintain a high glycolytic rate essential to a fully activated inflammatory response.[155]

In TME, TAMs compete with cancer cells for nutrients and consequently undergo changes in their metabolism. Some studies indicate that TAMs exert aerobic glycolysis, which also contributes to their functional reprogramming. Changes in metabolism of TAMs also supported cancer cells invasion and metastasis.[156] [158] Inhibiting glycolysis in TAMs with 2-deoxyglucose disrupted this prometastatic phenotype, reversing the TAM-supported angiogenesis, extravasation and epithelial to mesenchymal transition (EMT).[158]

Importantly, TAMs accumulating in hypoxic areas of tumors express HIF1α and undergo metabolic shift toward aerobic glycolysis.[159] [162] HIF1α activation induces oxidative stress and ROS production by macrophages. Oxidative stress can induce genetic instability and support malignant transformation.[163] Moreover, lactate produced by glycolytic TAMs can serve as metabolic fuel for oxidative cancer cells.[71] Nevertheless, when oxidative cancer cells are not present, lactate is accumulated and can be fished out by TAMs through their MCTs transporters leading to the transcription of the vascular endothelial growth factor (VEGF) and arginase-1 (ARG1) which polarizes TAMs closer to a M2 phenotype[164,165]

as ARG1 expression defines immunosuppressive subsets of TAMs.[166] Arginase hydrolyzes arginine to ornithine and urea and limits arginine availability for NO synthesis. NO production endows macrophages with pro-inflammatory and cytotoxic activity.[167] CAV1 was also shown to inhibit NO synthesis.[168] Moreover, CAV1 confers other anti-inflammatory effects in macrophages *via* the MKK3/p38 MAPK pathway[169] and *via* iron exporter ferroportin stabilization as macrophage ferroportin was mostly detected in detergent-resistant membranes containing CAV1.[170] Accordingly, anti-inflammatory macrophages express high levels and pro-inflammatory macrophages low levels of ferroportin. In line with this profile, pro-inflammatory M1-like macrophages probably favor iron sequestration, whereas anti-inflammatory M2-like macrophages favor iron release which promotes tissue repair and tumor cell proliferation.[171]

Hypoxic tumor areas are characterized by the presence of macrophages expressing high levels of receptors for vascular endothelial growth factor 1 (VEGFR1) that actively secrete matrix metalloproteinase (MMP9) and thus promote angiogenesis and invasion. VEGFR1-MMP9 signaling axis in macrophages is attenuated by high CAV1 expression and low CAV1 expression increased the membrane exposure of VEGFR1 on TAMs resulting in increased activity of MMP9, excessive blood vessel formation and expanded metastatic size.[151]
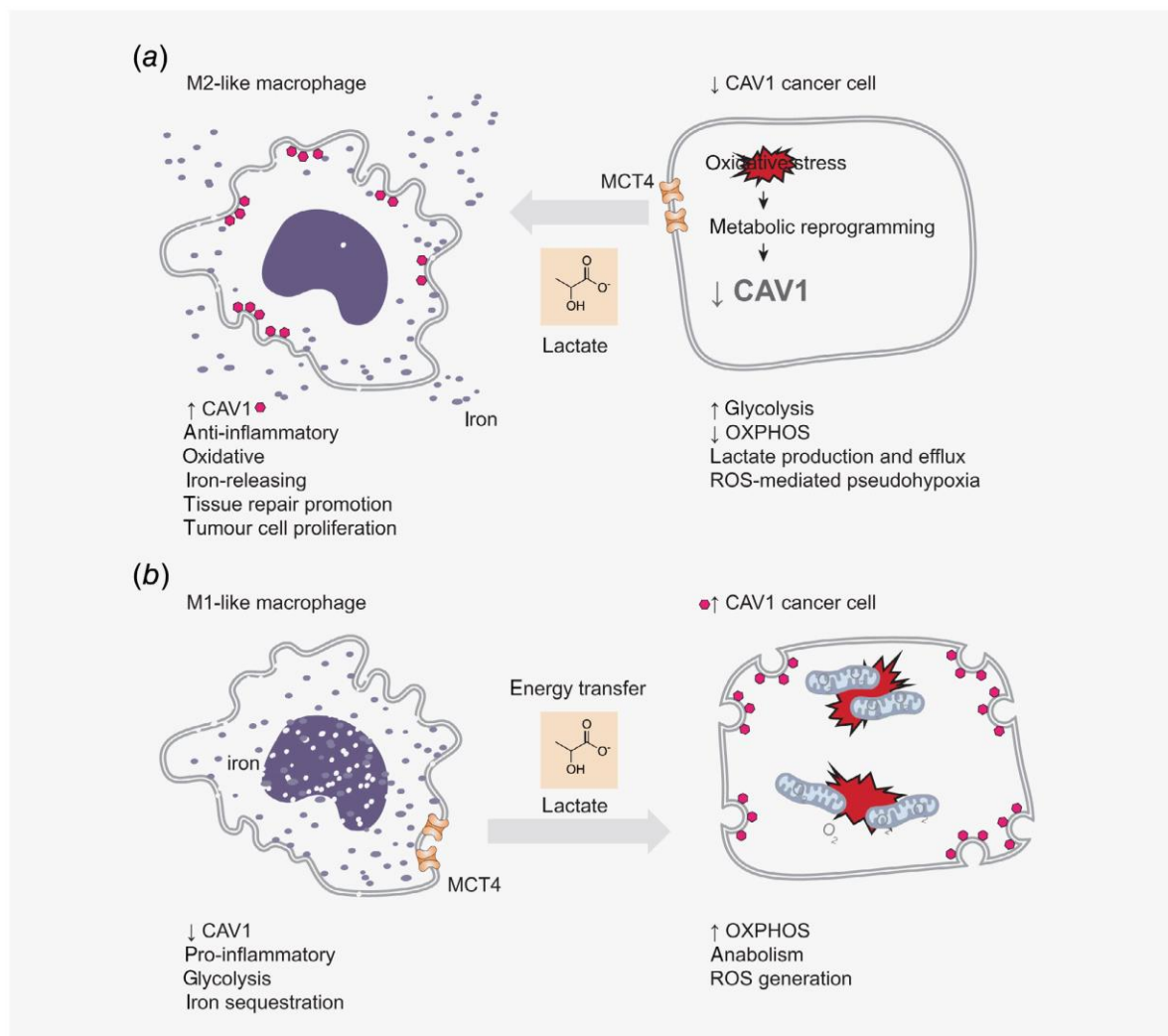
Based on these facts, we can speculate that low CAV1 glycolytic cancer cells producing lactate co-evolve with anti-inflammatory, oxidative, CAV1 expressing, iron releasing M2-like macrophages which promote tissue repair and tumor cell proliferation. On the other hand, glycolytic, low CAV1 expressing, iron-sequestrating, pro-inflammatory M1-like macrophages may form a metabolic symbiosis with CAV1 expressing oxidative cancer cells; (Fig. 6). Evidence supporting the co-evolution of glycolytic cancer cells with anti-inflammatory M2-like macrophages and oxidative cancer cells with pro-inflammatory M1-like macrophages are present in many studies. For example, plasminogen activator inhibitor-1 (PAI-1) promotes the recruitment of monocytes and their polarization to M2-like phenotype[172] and simultaneously drives rearrangement of the actin cytoskeleton, mitochondrial fragmentation and glycolytic metabolism in adjacent cancer cells.[173] Moreover, anti-inflammatory M2-like macrophages produce high amounts of transforming growth factor-beta (TGF-β).[174] TGF-β may induce a switch from oxidative metabolism in hepatocellular carcinoma cells and upregulates the expression of glutamine transporter Solute Carrier Family 7 Member 5 (SLC7A5) and glutaminase 1 (GLS1).[175] As M2 macrophages express high amounts of glutamine synthetase and therefore have high glutamine synthesis, they can supplement cancer cells in TME with glutamine. It is important because glycolytic cancer cells display an addiction to glutamine although glutamine is a nonessential amino acid synthesized from glucose.[176][178] Pharmacological inhibition or

genetic ablation of glutamine synthetase in macrophages promotes an M1-like phenotype, an increase in T cell recruitment and suppression of proangiogenic state and metastasis in a mouse model of Lewis lung carcinoma.[177]

In contrast, studies in many chronic inflammation-induced cancer models indicate the presence of TAMs with an inflammatory (M1-like) phenotype.[179,180] M1 macrophages were shown to activate the Notch signaling in epithelial cells[181] which plays a critical role in the linkages between angiogenesis and cancer stem cells self-renewal.[182] Moreover, M1-like TAMs produce pro-inflammatory cytokines such as IL-6, IL-1β and TNFα.[183] TAM-derived IL-6 induces tyrosine and serine phosphorylation of STAT3 that results in activation of STAT3-responsive genes in cancer cells leading to activation of cell cycle and enhancement of mitochondrial electron transport chain activity. STAT3 has a role in the direct, nontranscriptional regulation of OXPHOS.[184][186] In addition, STAT3 confers a protective role during cellular stress, by the reduction of ROS production and retention of cytochrome C in the mitochondria.[187] Levels of IL-6 in human hepatocellular carcinoma samples correlate with tumor stage and markers of cancer stem cells.[188] Sansone *et al.* have demonstrated that IL-6 induces cancer stem cell renewal *via* Notch3.[189] Furthermore, IL-6 increases glycogen synthesis through PI3kinase-dependent mechanisms and enhances lipid oxidation *via* AMPK-dependent mechanisms.[190] IL-6 also induces survival of prostate cancer cells by inducing Bcl/Stat-mediated signaling, supports resistance to immune checkpoint inhibition in metastatic pancreatic cancer, and enhances human melanoma cell invasiveness.[191][193] Some evidence suggests that this IL-6 signaling needs functional CAV1 in cancer cells.[194] Furthermore, pro-inflammatory macrophages can activate osteoclasts which can then support reactivating of dormant tumor cells in bones.[193,195] IL-6 is also an important mediator for mitochondrial DNA repair.[196]

CAV1 in the crosstalk between adipose tissue and tumors

Obesity has been connected to the enhanced risk and malignancy of many types of cancer. While obesity is linked with cancer development, advanced stages of many cancers are associated with white adipose tissue loss and cachexia.[197] Accordingly, increased consumption of lipids *versus* glucose is a marker of cancer aggressiveness in carcinomas.[198] The primary forms of lipids used by cancer cells as a source of energy through β-oxidation are fatty acids (FA).[199] In highly malignant cancers, endogenous lipogenesis becomes insufficient and cancer cells start to consume FA from other sources. Adipocytes undergoing lipolysis may serve as a source of lipids for cancer cells. This was proved, for example, in ovarian cancer. In providing FA from surrounding adipocytes for ovarian tumors, fatty acid-binding protein 4 (FABP4) has an important role.[200] It was also shown that β-hydroxybutyrate secreted by mammary gland-derived adipocytes enhanced malignancy of MCT2-expressing breast cancer cells.[201]

Figure 6. Oncogenic metabolic coupling between CAFs and TAMs. The oncogenic metabolic symbiosis between tumor-associated macrophages (TAMs) and tumor cells enables cancer cells to manipulate TAMs closer to a M2 phenotype by lactate production (*a*) or to consume metabolic substrates produced by TAMs (*b*). Low CAV1 glycolytic cancer cells producing lactate co-evolve with anti-inflammatory, oxidative, CAV1 expressing, iron releasing M2-like macrophages which promote tissue repair and tumor cell proliferation. On the other hand, glycolytic, low CAV1 expressing, iron-sequestrating, pro-inflammatory M1-like macrophages may form a metabolic symbiosis with CAV1 expressing oxidative cancer cells. In pro-inflammatory macrophages, MCT4 upregulation represents a positive feedback mechanism to maintain a high glycolytic rate essential to a fully activated inflammatory response. [Color figure can be viewed at wileyonlinelibrary.com]

The role of CAV1 in lipid metabolism became obvious with the creation of CAV1 knockout mice. These mice were lean with small adipocytes, had insulin resistance and exhibited defects in insulin signaling.[60] Lipoatrophy caused by CAV1 gene knockout is probably not linked to defective adipocyte differentiation. Some studies indicate that CAV1 deficiency induces excessive autophagy in adipocytes, which is not a physiological response to fasting in normal fat cells.[202,203] Moreover, CAV1-containing extracellular vesicles were shown to be essential for crosstalk between cells in adipose tissue, and loss of this communication may reduce crucial intercellular signaling and disturb homeostasis in adipose tissue.[55]

Recent studies point out that a switch from white to beige/brown fat is involved in energy wasting in cancer-associated cachexia.[204] Two drivers of white to beige/brown transdifferentiation were identified: IL-6[205] and tumor-derived parathyroid-hormone-related peptide.[206] Accordingly, adipocytes in TME exhibit upregulated beige/brown fat characteristics, such

as UCP1 expression and increased catabolism accompanied by the release of metabolites including FA, lactate, pyruvate, and ketone bodies. Tumor cells co-cultivated with mature adipocytes exhibit metabolic adaptation and an aggressive phenotype *in vitro* and *in vivo* and at the same time, these tumor-educated adipocytes showed an increase in beige/brown fat characteristics, such as high UCP1 and MCT4 levels and induced CAV1 loss compared to adipocytes cultivated alone.[207] UCP1 uncouples oxidative phosphorylation from ATP synthesis in the inner mitochondrial membrane to dissipate energy in the form of heat.[208] Nevertheless, CAV1-null mice were unable to liberate triglyceride stores for heat production.[209] In other words, lipolysis in these adipocytes may be connected rather with the release of metabolites than with ATP production or thermogenesis. It was also observed that CAV1-KO adipose tissue contained an increased proportion of infiltrated macrophages compared to control mice.[203] These macrophages can further facilitate the modulation of adipocytes toward tumor-supporting phenotype.[210]

The metabolic symbiosis between cancer cells and adipocytes has not been deeply studied yet and therefore our conclusions are a bit speculative. Nevertheless, they represent an interesting new direction for future research.

Conclusion and Future Perspective

The metabolic symbiosis between stromal cells and cancer cells evolves dynamically depending on the amount of oxygen, extracellular availability of metabolites and the presence of signaling and CAV1-interacting molecules. It is apparent that the different stages of the tumorigenesis present different metabolic challenges to cancer cells and metabolic symbiosis with cells in TME can pronouncedly support cancer progression. The difference in CAV1 expression between cancer cells and cells in TME may contribute to the establishment of oncogenic metabolic symbiosis because CAV1 expression seems to be tightly connected with the type of cell metabolism and with intercellular communication. Nevertheless, the answer is probably more complex than just CAV1 expression levels. To understand the role of CAV1 in cancer metabolism, attention should be paid to CAV1 cellular localization and CAV1-interacting molecules as they can completely twist the resulting effect of CAV1 signals. It will be also important to investigate the role of CAV1 in mechanotransduction pathways involved in tumor progression. How is CAV1 linked to the long-term cellular response to mechanical and metabolic signals is an open question and it seems to be an exciting area of research.

Conflict of interest

The authors declare that they have no competing interests.

References

1. Pavlova NN, Thompson CB. The emerging hallmarks of cancer metabolism. *Cell Metab* 2016;23: 27–47.
2. Lyssiotis CA, Kimmelman AC. Metabolic interactions in the tumor microenvironment. *Trends Cell Biol* 2017;27:863–75.
3. Mangia S, Simpson IA, Vannucci SJ, et al. The in vivo neuron-to-astrocyte lactate shuttle in human brain: evidence from modeling of measured lactate levels during visual stimulation. *J Neurochem* 2009;109:55–62.
4. Nishiyama K, Trapp BD, Ikezu T, et al. Caveolin-3 upregulation activates beta-secretase-mediated cleavage of the amyloid precursor protein in Alzheimer's disease. *J Neurosci* 1999;19: 6538–48.
5. Song KS, Scherer PE, Tang Z, et al. Expression of caveolin-3 in skeletal, cardiac, and smooth muscle cells. Caveolin-3 is a component of the sarcolemma and co-fractionates with dystrophin and dystrophin-associated glycoproteins. *J Biol Chem* 1996;271:15160–5.
6. Li WP, Liu P, Pilcher BK, et al. Cell-specific targeting of caveolin-1 to caveolae, secretory vesicles, cytoplasm or mitochondria. *J Cell Sci* 2001; 114(Pt 7):1397–408.
7. Parolini I, Sargiacomo M, Galbiati F, et al. Expression of caveolin-1 is required for the transport of caveolin-2 to the plasma membrane.

Retention of caveolin-2 at the level of the golgi complex. *J Biol Chem* 1999;274:25718–25.
8. Sargiacomo M, Scherer PE, Tang Z, et al. Oligomeric structure of caveolin: implications for caveolae membrane organization. *Proc Natl Acad Sci USA* 1995;92:9407–11.
9. Das K, Lewis RY, Scherer PE, et al. The membrane-spanning domains of caveolins-1 and -2 mediate the formation of caveolin hetero-oligomers. Implications for the assembly of caveolae membranes in vivo. *J Biol Chem* 1999;274: 18721–8.
10. Fiala GJ, Minguet S. Chapter 3—Caveolin-1: the unnoticed player in TCR and BCR signaling. In: Alt F, ed. *Advances in immunology*. Cambridge, MA: Academic Press, 2018. 83–133.
11. Pol A, Martin S, Fernandez MA, et al. Cholesterol and fatty acids regulate dynamic caveolin trafficking through the Golgi complex and between the cell surface and lipid bodies. *Mol Biol Cell* 2005;16:2091–105.
12. Khater IM, Aroca-Ouellette ST, Meng F, et al. Caveolae and scaffold detection from single molecule localization microscopy data using deep learning. *PLoS One* 2019;14:e0211659.
13. Khater IM, Liu Q, Chou KC, et al. Super-resolution modularity analysis shows polyhedral caveolin-1 oligomers combine to form scaffolds and caveolae. *Sci Rep* 2019;9:9888.

14. Lajoie P, Goetz JG, Dennis JW, et al. Lattices, rafts, and scaffolds: domain regulation of receptor signaling at the plasma membrane. *J Cell Biol* 2009;185:381–5.
15. Cheng JPX, Mendoza-Topaz C, Howard G, et al. Caveolae protect endothelial cells from membrane rupture during increased cardiac output. *J Cell Biol* 2015;211:53–61.
16. Lo HP, Nixon SJ, Hall TE, et al. The caveolin-cavin system plays a conserved and critical role in mechanoprotection of skeletal muscle. *J Cell Biol* 2015;210:833–49.
17. Machleidt T, Li W-P, Liu P, et al. Multiple domains in caveolin-1 control its intracellular traffic. *J Cell Biol* 2000;148:17–28.
18. Schlegel A, Lisanti MP. A molecular dissection of caveolin-1 membrane attachment and oligomerization. Two separate regions of the caveolin-1 C-terminal domain mediate membrane binding and oligomer/oligomer interactions in vivo. *J Biol Chem* 2000;275:21605–17.
19. Parton RG, Hanzal-Bayer M, Hancock JF. Biogenesis of caveolae: a structural model for caveolin-induced domain formation. *J Cell Sci* 2006;119:787.
20. Nomura R, Fujimoto T. Tyrosine-phosphorylated caveolin-1: immunolocalization and molecular characterization. *Mol Biol Cell* 1999;10:975–86.

1804 Caveolin-1 in oncogenic metabolic symbiosis

21. Sanguinetti AR, Mastick CC. c-Abl is required for oxidative stress-induced phosphorylation of caveolin-1 on tyrosine 14. *Cell Signal* 2003;15:289–98.
22. Sanguinetti A, Cao H, Mastick C. Fyn is required for oxidative- and hyperosmotic-stress-induced tyrosine phosphorylation of caveolin-1. *Biochem J* 2003;376:159–68.
23. Hau AM, Gupta S, Leivo MZ, et al. Dynamic regulation of caveolin-1 phosphorylation and caveolae formation by mammalian target of rapamycin complex 2 in bladder cancer cells. *Am J Pathol* 2019;189:1846–62.
24. Orlichenko L, Huang B, Krueger E, et al. Epithelial growth factor-induced phosphorylation of caveolin 1 at tyrosine 14 stimulates caveolae formation in epithelial cells. *J Biol Chem* 2006;281:4570–9.
25. Wehinger S, Ortiz R, Díaz MI, et al. Phosphorylation of caveolin-1 on tyrosine-14 induced by ROS enhances palmitate-induced death of beta-pancreatic cells. *Biochim Biophys Acta* 2015;1852:693–708.
26. Zimnicka AM, Husain YS, Shajahan AN, et al. Src-dependent phosphorylation of caveolin-1 Tyr-14 promotes swelling and release of caveolae. *Mol Biol Cell* 2016;27:2090–106.
27. Sverdlov M, Shinin V, Place AT, et al. Filamin a regulates caveolae internalization and trafficking in endothelial cells. *Mol Biol Cell* 2009;20:4531–40.
28. Joshi B, Bastiani M, Strugnell SS, et al. Phosphocaveolin-1 is a mechanotransducer that induces caveola biogenesis via Egr1 transcriptional regulation. *J Cell Biol* 2012;199:425–35.
29. Patel HH, Murray F, Insel PA. Caveolae as organizers of pharmacologically relevant signal transduction molecules. *Annu Rev Pharmacol Toxicol* 2008;48:359–91.
30. Liu P, Rudick M, Anderson RG. Multiple functions of caveolin-1. *J Biol Chem* 2002;277:41295–8.
31. Jung W, Sierecki E, Bastiani M, et al. Cell-free formation and interactome analysis of caveolae. *J Cell Biol* 2018;217:2141–65.
32. Bernatchez PN, Bauer PM, Yu J, et al. Dissecting the molecular control of endothelial NO synthase by caveolin-1 using cell-permeable peptides. *Proc Natl Acad Sci USA* 2005;102:761–6.
33. Martinez-Outschoorn UE, Sotgia F, Lisanti MP. Caveolae and signalling in cancer. *Nat Rev Cancer* 2015;15:225.
34. Garcia-Cardena G, Fan R, Stern DF, et al. Endothelial nitric oxide synthase is regulated by tyrosine phosphorylation and interacts with caveolin-1. *J Biol Chem* 1996;271:27237–40.
35. Kraehling JR, Hao Z, Lee MY, et al. Uncoupling caveolae from intracellular signaling in vivo. *Circ Res* 2016;118:48–55.
36. Williams TM, Lisanti MP. The caveolin proteins. *Genome Biol* 2004;5:214.
37. Cohen AW, Hnasko R, Schubert W, et al. Role of caveolae and caveolins in health and disease. *Physiol Rev* 2004;84:1341–79.
38. Gilbert G, Ducret T, Savineau JP, et al. Caveolae are involved in mechanotransduction during pulmonary hypertension. *Am J Physiol Lung Cell Mol Physiol* 2016;310:L1078–87.
39. Sinha B, Köster D, Ruez R, et al. Cells respond to mechanical stress by rapid disassembly of caveolae. *Cell* 2011;144:402–13.

40. Navarro A, Anand-Apte B, Parat MO. A role for caveolae in cell migration. *FASEB J* 2004;18:1801–11.
41. Conrad PA, Smart EJ, Ying YS, et al. Caveolin cycles between plasma membrane caveolae and the Golgi complex by microtubule-dependent and microtubule-independent steps. *J Cell Biol* 1995;131(6 Pt 1):1421–33.
42. Schlegel A, Arvan P, Lisanti MP. Caveolin-1 binding to endoplasmic reticulum membranes and entry into the regulated secretory pathway are regulated by serine phosphorylation. Protein sorting at the level of the endoplasmic reticulum. *J Biol Chem* 2001;276:4398–408.
43. Chretien A, Piront N, Delaive E, et al. Increased abundance of cytoplasmic and nuclear caveolin 1 in human diploid fibroblasts in H_2O_2-induced premature senescence and interplay with p38alpha(MAPK). *FEBS Lett* 2008;582:1685–92.
44. Shi Y, Tan S-H, Ng S, et al. Critical role of CAV1/caveolin-1 in cell stress responses in human breast cancer cells via modulation of lysosomal function and autophagy. *Autophagy* 2015;11:769–84.
45. Woudenberg J, Rembacz KP, van den Heuvel FA, et al. Caveolin-1 is enriched in the peroxisomal membrane of rat hepatocytes. *Hepatology* 2010;51:1744–53.
46. Tagawa A, Mezzacasa A, Hayer A, et al. Assembly and trafficking of caveolar domains in the cell: caveolae as stable, cargo-triggered, vesicular transporters. *J Cell Biol* 2005;170:769–79.
47. Campos A, Salomon C, Bustos R, et al. Caveolin-1-containing extracellular vesicles transport adhesion proteins and promote malignancy in breast cancer cell lines. *Nanomedicine (Lond)* 2018;13:2597–609.
48. Lee H, Li C, Zhang Y, et al. Caveolin-1 selectively regulates microRNA sorting into microvesicles after noxious stimuli. *J Exp Med* 2019;216:2202–20.
49. Ostermeyer AG, Paci JM, Zeng Y, et al. Accumulation of caveolin in the endoplasmic reticulum redirects the protein to lipid storage droplets. *J Cell Biol* 2001;152:1071–8.
50. Shu SL, Yang Y, Allen CL, et al. Metabolic reprogramming of stromal fibroblasts by melanoma exosome microRNA favours a pre-metastatic microenvironment. *Sci Rep* 2018;8:12905.
51. Zhang L, Zhang S, Yao J, et al. Microenvironment-induced PTEN loss by exosomal microRNA primes brain metastasis outgrowth. *Nature* 2015;527:100–4.
52. Logozzi M, Milito A, Lugini L, et al. High levels of exosomes expressing CD63 and Caveolin-1 in plasma of melanoma patients. *PLoS One* 2009;4:e5219.
53. Llorente A, de Marco MC, Alonso MA. Caveolin-1 and MAL are located on prostasomes secreted by the prostate cancer PC-3 cell line. *J Cell Sci* 2004;117:5343–51.
54. Sawada N, Taketani Y, Amizuka N, et al. Caveolin-1 in extracellular matrix vesicles secreted from osteoblasts. *Bone* 2007;41:52–8.
55. Crewe C, Joffin N, Rutkowski JM, et al. An endothelial-to-adipocyte extracellular vesicle axis governed by metabolic state. *Cell* 2018;175:695–708.e13.
56. Yu D-M, Jung SH, An H-T, et al. Caveolin-1 deficiency induces premature senescence with

mitochondrial dysfunction. *Aging Cell* 2017;16:773–84.
57. Schilling JM, Dhanani M, Haushalter KJ, et al. Loss of caveolin-1 alters cardiac mitochondrial function and increases susceptibility to stress. *J Mol Cell Cardiol* 2017;112:165.
58. Volonte D, Liu Z, Shiva S, et al. Caveolin-1 controls mitochondrial function through regulation of m-AAA mitochondrial protease. *Aging* 2016;8:2355–69.
59. Fernandez-Rojo MA, Restall C, Ferguson C, et al. Caveolin-1 orchestrates the balance between glucose and lipid-dependent energy metabolism: implications for liver regeneration. *Hepatology* 2012;55:1574–84.
60. Cohen AW, Razani B, Schubert W, et al. Role of caveolin-1 in the modulation of lipolysis and lipid droplet formation. *Diabetes* 2004;53:1261–70.
61. Kuo A, Lee MY, Yang K, et al. Caveolin-1 regulates lipid droplet metabolism in endothelial cells via autocrine prostacyclin-stimulated, cAMP-mediated lipolysis. *J Biol Chem* 2018;293:973–83.
62. Fridolfsson H, Kawaraguchi Y, Ali S, et al. Mitochondria-localized caveolin in adaptation to cellular stress and injury. *FASEB J* 2012;26:4637–49.
63. Bosch M, Mari M, Herms A, et al. Caveolin-1 deficiency causes cholesterol-dependent mitochondrial dysfunction and apoptotic susceptibility. *Curr Biol* 2011;21:681–6.
64. Bajzikova M, Kovarova J, Coelho AR, et al. Reactivation of dihydroorotate dehydrogenase-driven pyrimidine biosynthesis restores tumor growth of respiration-deficient Cancer cells. *Cell Metab* 2019;29:399–416.e10.
65. Berridge MV, Tan AS. Effects of mitochondrial gene deletion on tumorigenicity of metastatic melanoma: reassessing the Warburg effect. *Rejuvenation Res* 2010;13:139–41.
66. Curry JM, Tuluc M, Whitaker-Menezes D, et al. Cancer metabolism, stemness and tumor recurrence: MCT1 and MCT4 are functional biomarkers of metabolic symbiosis in head and neck cancer. *Cell Cycle* 2013;12:1371–84.
67. Tabassum DP, Polyak K. Tumorigenesis: it takes a village. *Nat Rev Cancer* 2015;15:473.
68. Feron O. Pyruvate into lactate and back: from the Warburg effect to symbiotic energy fuel exchange in cancer cells. *Radiother Oncol* 2009;92:329–33.
69. Sonveaux P, Végran F, Schroeder T, et al. Targeting lactate-fueled respiration selectively kills hypoxic tumor cells in mice. *J Clin Invest* 2008;118:3930–42.
70. Varela-Guruceaga M, Milagro FI, Martínez JA, et al. Effect of hypoxia on caveolae-related protein expression and insulin signaling in adipocytes. *Mol Cell Endocrinol* 2018;473:257–67.
71. Hui S, Ghergurovich JM, Morscher RJ, et al. Glucose feeds the TCA cycle via circulating lactate. *Nature* 2017;551:115–8.
72. Boidot R, Vegran F, Meulle A, et al. Regulation of monocarboxylate transporter MCT1 expression by p53 mediates inward and outward lactate fluxes in tumors. *Cancer Res* 2012;72:939–48.
73. Quanz M, Bender E, Kopitz C, et al. Preclinical efficacy of the novel monocarboxylate transporter 1 inhibitor BAY-8002 and associated markers of resistance. *Mol Cancer Ther* 2018;17:2285.

74. Johnson JM, Cotzia P, Fratamico R, et al. MCT1 in invasive ductal carcinoma: monocarboxylate metabolism and aggressive breast cancer. *Front Cell Dev Biol* 2017;5:27.

75. Park S, Chang CY, Safi R, et al. ERRalpha-regulated lactate metabolism contributes to resistance to targeted therapies in breast cancer. *Cell Rep* 2016;15:323–35.

76. Christie CF, Fang D, Hunt EG, et al. Statin-dependent modulation of mitochondrial metabolism in cancer cells is independent of cholesterol content. *FASEB J* 2019;33:8186–201.

77. Urbano F, Bugliani M, Filippello A, et al. Atorvastatin but not pravastatin impairs mitochondrial function in human pancreatic islets and rat beta-cells. Direct Effect of Oxidative Stress. *Sci Rep* 2017;7:11863.

78. Pelat M, Dessy C, Massion P, et al. Rosuvastatin decreases caveolin-1 and improves nitric oxide-dependent heart rate and blood pressure variability in apolipoprotein E−/− mice in vivo. *Circulation* 2003;107:2480–6.

79. Brouet A, Sonveaux P, Dessy C, et al. Hsp90 and caveolin are key targets for the proangiogenic nitric oxide-mediated effects of statins. *Circ Res* 2001;89:866–73.

80. Longster AL, MacDougall DA, Porter KE, et al. In vivo simvastatin treatment differentially affects Caveolin-1 and Caveolin-3 expression in the adult rat myocardium. *Biophys J* 2012; 102:138.

81. Mausner-Fainberg K, Luboshits G, Mor A, et al. The effect of HMG-CoA reductase inhibitors on naturally occurring CD4+CD25+ T cells. *Atherosclerosis* 2008;197:829–39.

82. Ait-Oufella H, Salomon BL, Potteaux S, et al. Natural regulatory T cells control the development of atherosclerosis in mice. *Nat Med* 2006; 12:178–80.

83. Shimizu J, Yamazaki S, Sakaguchi S. Induction of tumor immunity by removing CD25+CD4+ T cells: a common basis between tumor immunity and autoimmunity. *J Immunol* 1999;163:5211–8.

84. Owen MR, Doran E, Halestrap AP. Evidence that metformin exerts its anti-diabetic effects through inhibition of complex 1 of the mitochondrial respiratory chain. *Biochem J* 2000;348 (Pt 3):607–14.

85. Zhuang Y, Chan DK, Haugrud AB, et al. Mechanisms by which low glucose enhances the cytotoxicity of metformin to cancer cells both in vitro and in vivo. *PLoS One* 2014;9:e108444.

86. Galbiati F, Volonte D, Liu J, et al. Caveolin-1 expression negatively regulates cell cycle progression by inducing G(0)/G(1) arrest via a p53/p21 (WAF1/Cip1)-dependent mechanism. *Mol Biol Cell* 2001;12:2229–44.

87. Hulit J, Bash T, Fu M, et al. The cyclin D1 gene is transcriptionally repressed by caveolin-1. *J Biol Chem* 2000;275:21203–9.

88. Torres VA, Tapia JC, Rodriguez DA, et al. E-cadherin is required for caveolin-1-mediated down-regulation of the inhibitor of apoptosis protein surviving via reduced beta-catenin-Tcf/Lef-dependent transcription. *Mol Cell Biol* 2007;27:7703–17.

89. Galbiati F, Volonte D, Engelman JA, et al. Targeted downregulation of caveolin-1 is sufficient to drive cell transformation and hyperactivate the p42/44 MAP kinase cascade. *EMBO J* 1998;17:6633–48.

90. Volonte D, Vyas AR, Chen C, et al. Caveolin-1 promotes the tumor suppressor properties of oncogene-induced cellular senescence. *J Biol Chem* 2018;293:1794–809.

91. Bartholomew JN, Volonte D, Galbiati F. Caveolin-1 regulates the antagonistic pleiotropic properties of cellular senescence through a novel Mdm2/p53-mediated pathway. *Cancer Res* 2009; 69:2878–86.

92. Koleske AJ, Baltimore D, Lisanti MP. Reduction of caveolin and caveolae in oncogenically transformed cells. *Proc Natl Acad Sci USA* 1995;92: 1381–5.

93. Cerezo A, Guadamillas MC, Goetz JG, et al. The absence of caveolin-1 increases proliferation and anchorage-independent growth by a Rac-dependent, Erk-independent mechanism. *Mol Cell Biol* 2009;29:5046–59.

94. Wang Z, Wang N, Li W, et al. Caveolin-1 mediates chemoresistance in breast cancer stem cells via beta-catenin/ABCG2 signaling pathway. *Carcinogenesis* 2014;35:2346–56.

95. Ho CC, Huang PH, Huang HY, et al. Up-regulated caveolin-1 accentuates the metastasis capability of lung adenocarcinoma by inducing filopodia formation. *Am J Pathol* 2002;161: 1647–56.

96. Ravid D, Maor S, Werner H, et al. Caveolin-1 inhibits cell detachment-induced p53 activation and anoikis by upregulation of insulin-like growth factor-I receptors and signaling. *Oncogene* 2005;24:1338–47.

97. Joshi B, Strugnell SS, Goetz JG, et al. Phosphorylated caveolin-1 regulates rho/ROCK-dependent focal adhesion dynamics and tumor cell migration and invasion. *Cancer Res* 2008;68:8210–20.

98. Ko YG, Liu P, Pathak RK, et al. Early effects of pp60(v-src) kinase activation on caveolae. *J Cell Biochem* 1998;71:524–35.

99. Parton RG, del Pozo MA. Caveolae as plasma membrane sensors, protectors and organizers. *Nat Rev Mol Cell Biol* 2013;14:98–112.

100. Torrino S, Shen W-W, Blouin CM, et al. EHD2 is a mechanotransducer connecting caveolae dynamics with gene transcription. *J Cell Biol* 2018;217:4092–105.

101. Onder TT, Gupta PB, Mani SA, et al. Loss of E-cadherin promotes metastasis via multiple downstream transcriptional pathways. *Cancer Res* 2008;68:3645–54.

102. Petrova YI, Schecterson L, Gumbiner BM. Roles for E-cadherin cell surface regulation in cancer. *Mol Biol Cell* 2016;27:3233–44.

103. Moon H, Lee CS, Inder KL, et al. PTRF/cavin-1 neutralizes non-caveolar caveolin-1 microdomains in prostate cancer. *Oncogene* 2014;33: 3561–70.

104. Borza CM, Chen X, Mathew S, et al. Integrin {alpha}1{beta}1 promotes caveolin-1 dephosphorylation by activating T cell protein-tyrosine phosphatase. *J Biol Chem* 2010;285:40114–24.

105. Radel C, Rizzo V. Integrin mechanotransduction stimulates caveolin-1 phosphorylation and recruitment of Csk to mediate actin reorganization. *Am J Physiol Heart Circ Physiol* 2005;288: H936–45.

106. Park JH, Ryu JM, Han HJ. Involvement of caveolin-1 in fibronectin-induced mouse embryonic stem cell proliferation: role of FAK, RhoA, PI3K/Akt, and ERK 1/2 pathways. *J Cell Physiol* 2011;226:267–75.

107. Quest AFG, Gutierrez-Pajares JL, Torres VA. Caveolin-1: an ambiguous partner in cell signalling and cancer. *J Cell Mol Med* 2008;12: 1130–50.

108. Feldman R, Gatalica Z, Reddy SK, et al. Caveolin-1: oncogenic role in breast cancer? Clues from molecular profiling. *J Clin Oncol* 2015;33(28_suppl):134.

109. Wang S, Wang N, Zheng Y, et al. Caveolin-1: an oxidative stress-related target for cancer prevention. *Oxid Med Cell Longev* 2017;2017:7454031.

110. Deb M, Sengupta D, Kar S, et al. Elucidation of caveolin 1 both as a tumor suppressor and metastasis promoter in light of epigenetic modulators. *Tumor Biol* 2014;35:12031–47.

111. Shatz M, Liscovitch M. Caveolin-1: a tumor-promoting role in human cancer. *Int J Radiat Biol* 2008;84:177–89.

112. Wang X, Peralta S, Moraes CT. Chapter 4—Mitochondrial alterations during carcinogenesis: a review of metabolic transformation and targets for anticancer treatments. In: Tew KD, Fisher PB, eds *Advances in Cancer Research*. Cambridge, MA: Academic Press, 2013. 127–60.

113. Wang Z, Wang N, Liu P, et al. Caveolin-1, a stress-related oncotarget, in drug resistance. *Oncotarget* 2015;6:37135–50.

114. Bainbridge P. Wound healing and the role of fibroblasts. *J Wound Care* 2013;22:407–8. 10–12.

115. Madar S, Goldstein I, Rotter V. 'Cancer associated fibroblasts'—more than meets the eye. *Trends Mol Med* 2013;19:447–53.

116. Arcucci A, Ruocco MR, Amatruda N, et al. Analysis of extracellular superoxide dismutase in fibroblasts from patients with systemic sclerosis. *J Biol Regul Homeost Agents* 2011;25: 647–54.

117. Shihata WA, Putra MRA, Chin-Dusting JPF. Is there a potential therapeutic role for Caveolin-1 in fibrosis? *Front Pharmacol* 2017;8:567.

118. Dimmer KS, Friedrich B, Lang F, et al. The low-affinity monocarboxylate transporter MCT4 is adapted to the export of lactate in highly glycolytic cells. *Biochem J* 2000;350(Pt 1):219–27.

119. Bonuccelli G, Whitaker-Menezes D, Castello-Cros R, et al. The reverse Warburg effect: glycolysis inhibitors prevent the tumor promoting effects of caveolin-1 deficient cancer associated fibroblasts. *Cell Cycle* 2010;9:1960–71.

120. Wu KN, Queenan M, Brody JR, et al. Loss of stromal caveolin-1 expression in malignant melanoma metastases predicts poor survival. *Cell Cycle* 2011;10:4250–5.

121. Zhao Z, Han F-H, Yang S-B, et al. Loss of stromal caveolin-1 expression in colorectal cancer predicts poor survival. *World J Gastroenterol* 2015;21:1140–7.

122. Witkiewicz AK, Whitaker-Menezes D, Dasgupta A, et al. Using the "reverse Warburg effect" to identify high-risk breast cancer patients: stromal MCT4 predicts poor clinical outcome in triple-negative breast cancers. *Cell Cycle* 2012;11:1108–17.

123. Di Vizio D, Morello M, Sotgia F, et al. An absence of stromal caveolin-1 is associated with advanced prostate cancer, metastatic disease and epithelial Akt activation. *Cell Cycle* 2009;8: 2420–4.

124. Chiavarina B, Whitaker-Menezes D, Migneco G, et al. HIF1-alpha functions as a tumor promoter in cancer-associated fibroblasts, and as a tumor

suppressor in breast cancer cells. *Cell Cycle* 2010;
9:3534–51.
125. Martinez-Outschoorn UE, Balliet RM, Rivadeneira DB, et al. Oxidative stress in cancer associated fibroblasts drives tumor-stroma co-evolution: a new paradigm for understanding tumor metabolism, the field effect and genomic instability in cancer cells. *Cell Cycle* 2010;9:3256–76.
126. Tassone P, Domingo-Vidal M, Whitaker-Menezes D, et al. Metformin effects on metabolic coupling and tumor growth in oral cavity squamous cell carcinoma coinjection xenografts. *Otolaryngol Head Neck Surg* 2017;158:867–77.
127. Ning X, Du Y, Ben Q, et al. Bulk pancreatic cancer cells can convert into cancer stem cells (CSCs) in vitro and 2 compounds can target these CSCs. *Cell Cycle* 2016;15:403–12.
128. Hirsch HA, Iliopoulos D, Tsichlis PN, et al. Metformin selectively targets cancer stem cells, and acts together with chemotherapy to block tumor growth and prolong remission. *Cancer Res* 2009; 69:7507–11.
129. Farnie G, Sotgia F, Lisanti MP. High mitochondrial mass identifies a sub-population of stem-like cancer cells that are chemo-resistant. *Oncotarget* 2015;6:30472–86.
130. Janiszewska M, Suva ML, Riggi N, et al. Imp2 controls oxidative phosphorylation and is crucial for preserving glioblastoma cancer stem cells. *Genes Dev* 2012;26:1926–44.
131. Lea MA, Chacko J, Bolikal S, et al. Addition of 2-deoxyglucose enhances growth inhibition but reverses acidification in colon cancer cells treated with phenformin. *Anticancer Res* 2011;31:421–6.
132. Curry J, Johnson J, Tassone P, et al. Metformin effects on head and neck squamous carcinoma microenvironment: window of opportunity trial. *Laryngoscope* 2017;127:1808–15.
133. Rohlenova K, Sachaphibulkij K, Stursa J, et al. Selective disruption of respiratory super-complexes as a New strategy to suppress Her2 (high) breast cancer. *Antioxid Redox Signal* 2017; 26:84–103.
134. Krejcir R, Krcova L, Zatloukalova P, et al. A cyclic pentamethinium salt induces cancer cell cytotoxicity through mitochondrial disintegration and metabolic collapse. *Int J Mol Sci* 2019; 20:4208.
135. Kumar D, New J, Vishwakarma V, et al. Cancer-associated fibroblasts drive glycolysis in a targetable signaling loop implicated in head and neck squamous cell carcinoma progression. *Cancer Res* 2018;78:3769–82.
136. Goetz JG, Minguet S, Navarro-Lérida I, et al. Biomechanical remodeling of the microenvironment by stromal caveolin-1 favors tumor invasion and metastasis. *Cell* 2011;146:148–63.
137. Santilman V, Baran J, Parat M-O. Binding to intermediate filaments is required for caveolin-1 polarization in transmigrating cells. *Cancer Res* 2007;67:2994.
138. Jiu Y. Vimentin intermediate filaments function as a physical barrier during intracellular trafficking of caveolin-1. *Biochem Biophys Res Commun* 2018;507:161–7.
139. Moreno-Vicente R, Pavon DM, Martin-Padura I, et al. Caveolin-1 modulates mechanotransduction responses to substrate stiffness through actin-dependent control of YAP. *Cell Rep* 2018;25:1622–35.e6.
140. Nurmik M, Ullmann P, Rodriguez F, et al. In search of definitions: cancer-associated fibroblasts and their markers. *Int J Cancer* 2020;146: 895–905.
141. Penkert J, Ripperger T, Schieck M, et al. On metabolic reprogramming and tumor biology: a comprehensive survey of metabolism in breast cancer. *Oncotarget* 2016;7:67626–49.
142. Cassetta L, Pollard JW. Targeting macrophages: therapeutic approaches in cancer. *Nat Rev Drug Discov* 2018;17:887–904.
143. Goossens P, Rodriguez-Vita J, Etzerodt A, et al. Membrane cholesterol efflux drives tumor-associated macrophage reprogramming and tumor progression. *Cell Metab* 2019;29: 1376–89.e4.
144. Halbrook CJ, Pontious C, Kovalenko I, et al. Macrophage-released pyrimidines inhibit gemcitabine therapy in pancreatic cancer. *Cell Metab* 2019;29:1390–9.e6.
145. Miwa H, Fujii J, Kanno H, et al. Pyruvate secreted by human lymphoid cell lines protects cells from hydrogen peroxide mediated cell death. *Free Radic Res* 2000;33:45–56.
146. Khiati S, Dalla Rosa I, Sourbier C, et al. Mitochondrial topoisomerase I (top1mt) is a novel limiting factor of doxorubicin cardiotoxicity. *Clin Cancer Res* 2014;20:4873–81.
147. Heller S, Schubert S, Krehan M, et al. Efficient repopulation of genetically derived rho zero cells with exogenous mitochondria. *PLoS One* 2013;8: e73207.
148. Xue J, Schmidt SV, Sander J, et al. Transcriptome-based network analysis reveals a spectrum model of human macrophage activation. *Immunity* 2014;40:274–88.
149. Biswas SK, Allavena P, Mantovani A. Tumor-associated macrophages: functional diversity, clinical significance, and open questions. *Semin Immunopathol* 2013;35:585–600.
150. Lindsten T, Hedbrant A, Ramberg A, et al. Effect of macrophages on breast cancer cell proliferation, and on expression of hormone receptors, uPAR and HER-2. *Int J Oncol* 2017;51:104–14.
151. Celus W, Di Conza G, Oliveira AI, et al. Loss of Caveolin-1 in metastasis-associated macrophages drives lung metastatic growth through increased angiogenesis. *Cell Rep* 2017;21:2842–54.
152. Ip WKE, Hoshi N, Shouval DS, et al. Anti-inflammatory effect of IL-10 mediated by metabolic reprogramming of macrophages. *Science (New York, NY)* 2017;356:513–9.
153. Feng J, Li L, Ou Z, et al. IL-25 stimulates M2 macrophage polarization and thereby promotes mitochondrial respiratory capacity and lipolysis in adipose tissues against obesity. *Cell Mol Immunol* 2018;15:493–505.
154. Vats D, Mukundan L, Odegaard JI, et al. Oxidative metabolism and PGC-1beta attenuate macrophage-mediated inflammation. *Cell Metab* 2006;4:13–24.
155. Tan Z, Xie N, Banerjee S, et al. The monocarboxylate transporter 4 is required for glycolytic reprogramming and inflammatory response in macrophages. *J Biol Chem* 2015;290: 46–55.
156. Liu D, Chang C, Lu N, et al. Comprehensive proteomics analysis reveals metabolic reprogramming of tumor-associated macrophages stimulated by the tumor microenvironment. *J Proteome Res* 2017;16:288–97.
157. Arts RJ, Plantinga TS, Tuit S, et al. Transcriptional and metabolic reprogramming induce an inflammatory phenotype in non-medullary thyroid carcinoma-induced macrophages. *Onco Targets Ther* 2016;5:e1229725.
158. Penny HL, Sieow JL, Adriani G, et al. Warburg metabolism in tumor-conditioned macrophages promotes metastasis in human pancreatic ductal adenocarcinoma. *Onco Targets Ther* 2016;5: e1191731.
159. Corzo CA, Condamine T, Lu L, et al. HIF-1alpha regulates function and differentiation of myeloid-derived suppressor cells in the tumor microenvironment. *J Exp Med* 2010;207:2439–53.
160. Burke B, Giannoudis A, Corke KP, et al. Hypoxia-induced gene expression in human macrophages: implications for ischemic tissues and hypoxia-regulated gene therapy. *Am J Pathol* 2003;163:1233–43.
161. Cramer T, Yamanishi Y, Clausen BE, et al. HIF-1alpha is essential for myeloid cell-mediated inflammation. *Cell* 2003;112:645–57.
162. Kelly B, O'Neill LAJ. Metabolic reprogramming in macrophages and dendritic cells in innate immunity. *Cell Res* 2015;25:771–84.
163. Peyssonnaux C, Datta V, Cramer T, et al. HIF-1alpha expression regulates the bactericidal capacity of phagocytes. *J Clin Invest* 2005;115: 1806–15.
164. Ohashi T, Akazawa T, Aoki M, et al. Dichloroacetate improves immune dysfunction caused by tumor-secreted lactic acid and increases antitumor immunoreactivity. *Int J Cancer* 2013;133:1107–18.
165. Colegio OR, Chu NQ, Szabo AL, et al. Functional polarization of tumour-associated macrophages by tumour-derived lactic acid. *Nature* 2014;513:559–63.
166. Arlauckas SP, Garren SB, Garris CS, et al. Arg1 expression defines immunosuppressive subsets of tumor-associated macrophages. *Theranostics* 2018;8:5842–54.
167. MacMicking J, Xie QW, Nathan C. Nitric oxide and macrophage function. *Annu Rev Immunol* 1997;15:323–50.
168. Brouet A, DeWever J, Martinive P, et al. Antitumor effects of in vivo caveolin gene delivery are associated with the inhibition of the proangiogenic and vasodilatory effects of nitric oxide. *FASEB J* 2005;19:602–4.
169. Wang XM, Kim HP, Song R, et al. Caveolin-1 confers antiinflammatory effects in murine macrophages via the MKK3/p38 MAPK pathway. *Am J Respir Cell Mol Biol* 2006;34: 434–42.
170. Auriac A, Willemetz A, Canonne-Hergaux F. Lipid raft-dependent endocytosis: a new route for hepcidin-mediated regulation of ferroportin in macrophages. *Haematologica* 2010;95: 1269–77.
171. Cairo G, Recalcati S, Mantovani A, et al. Iron trafficking and metabolism in macrophages: contribution to the polarized phenotype. *Trends Immunol* 2011;32:241–7.
172. Kubala MH, Punj V, Placencio-Hickok VR, et al. Plasminogen activator inhibitor-1 promotes the recruitment and polarization of macrophages in cancer. *Cell Rep* 2018;25:2177–91.e7.
173. Humphries BA, Buschhaus JM, Chen YC, et al. Plasminogen activator inhibitor 1 (PAI1) promotes actin cytoskeleton reorganization and

glycolytic metabolism in triple-negative breast cancer. *Mol Cancer Res* 2019;17:1142–54.

174. Viola A, Munari F, Sánchez-Rodríguez R, et al. The metabolic signature of macrophage responses. *Front Immunol* 2019;10:1462.

175. Soukupova J, Malfettone A, Hyroššová P, et al. Role of the transforming growth factor-β in regulating hepatocellular carcinoma oxidative metabolism. *Sci Rep* 2017;7:12486.

176. DeBerardinis RJ, Mancuso A, Daikhin E, et al. Beyond aerobic glycolysis: transformed cells can engage in glutamine metabolism that exceeds the requirement for protein and nucleotide synthesis. *Proc Natl Acad Sci USA* 2007;104:19345–50.

177. Palmieri EM, Menga A, Martin-Perez R, et al. Pharmacologic or genetic targeting of glutamine synthetase skews macrophages toward an M1-like phenotype and inhibits tumor metastasis. *Cell Rep* 2017;20:1654–66.

178. Wise DR, Thompson CB. Glutamine addiction: a new therapeutic target in cancer. *Trends Biochem Sci* 2010;35:427–33.

179. Greten FR, Eckmann L, Greten TF, et al. IKKbeta links inflammation and tumorigenesis in a mouse model of colitis-associated cancer. *Cell* 2004;118:285–96.

180. Maeda S, Kamata H, Luo JL, et al. IKKbeta couples hepatocyte death to cytokine-driven compensatory proliferation that promotes chemical hepatocarcinogenesis. *Cell* 2005;121:977–90.

181. Ortiz-Masiá D, Cosín-Roger J, Calatayud S, et al. M1 macrophages activate the notch signalling in epithelial cells: relevance in Crohn's disease. *J Crohns Colitis* 2016;10:582–92.

182. Venkatesh V, Nataraj R, Thangaraj GS, et al. Targeting notch signalling pathway of cancer stem cells. *Stem Cell Investig* 2018;5:5.

183. Mantovani A, Allavena P, Sica A, et al. Cancer-related inflammation. *Nature* 2008;454:436–44.

184. Wegrzyn J, Potla R, Chwae YJ, et al. Function of mitochondrial Stat3 in cellular respiration. *Science (New York, NY)* 2009;323:793–7.

185. Gough DJ, Corlett A, Schlessinger K, et al. Mitochondrial STAT3 supports Ras-dependent oncogenic transformation. *Science (New York, NY)* 2009;324:1713–6.

186. Lee M, Hirpara JL, Eu J-Q, et al. Targeting STAT3 and oxidative phosphorylation in oncogene-addicted tumors. *Redox Biol* 2018;25:101073.

187. Szczepanek K, Lesnefsky EJ, Larner AC. Multitasking: nuclear transcription factors with novel roles in the mitochondria. *Trends Cell Biol* 2012; 22:429–37.

188. Wan S, Zhao E, Kryczek I, et al. Tumor-associated macrophages produce interleukin 6 and signal via STAT3 to promote expansion of human hepatocellular carcinoma stem cells. *Gastroenterology* 2014;147:1393–404.

189. Sansone P, Storci G, Tavolari S, et al. IL-6 triggers malignant features in mammospheres from human ductal breast carcinoma and normal mammary gland. *J Clin Invest* 2007;117: 3988–4002.

190. Al-Khalili L, Bouzakri K, Glund S, et al. Signaling specificity of interleukin-6 action on glucose and lipid metabolism in skeletal muscle. *Mol Endocrinol* 2006;20:3364–75.

191. Mahon KL, Lin HM, Castillo L, et al. Cytokine profiling of docetaxel-resistant castration-resistant prostate cancer. *Br J Cancer* 2015;112: 1340–8.

192. Quaranta V, Rainer C, Nielsen SR, et al. Macrophage-derived Granulin drives resistance to immune checkpoint inhibition in metastatic pancreatic cancer. *Cancer Res* 2018;78:4253–69.

193. Jobe NP, Rosel D, Dvorankova B, et al. Simultaneous blocking of IL-6 and IL-8 is sufficient to fully inhibit CAF-induced human melanoma cell invasiveness. *Histochem Cell Biol* 2016;146: 205–17.

194. Podar K, Tai YT, Cole CE, et al. Essential role of caveolae in interleukin-6- and insulin-like growth factor I-triggered Akt-1-mediated survival of multiple myeloma cells. *J Biol Chem* 2003;278:5794–801.

195. Croucher PI, McDonald MM, Martin TJ. Bone metastasis: the importance of the neighbourhood. *Nat Rev Cancer* 2016;16:373.

196. Zhang X, Tachibana S, Wang H, et al. Interleukin-6 is an important mediator for mitochondrial DNA repair after alcoholic liver injury in mice. *Hepatology (Baltimore, MD)* 2010;52: 2137–47.

197. Lengyel E, Makowski L, DiGiovanni J, et al. Cancer as a matter of fat: the crosstalk between adipose tissue and tumors. *Trends Cancer* 2018;4:374–84.

198. Palm W, Thompson CB. Nutrient acquisition strategies of mammalian cells. *Nature* 2017;546:234–42.

199. Beloribi-Djefaflia S, Vasseur S, Guillaumond F. Lipid metabolic reprogramming in cancer cells. *Oncogene* 2016;5:e189.

200. Nieman KM, Kenny HA, Penicka CV, et al. Adipocytes promote ovarian cancer metastasis and provide energy for rapid tumor growth. *Nat Med* 2011;17:1498–503.

201. Huang CK, Chang PH, Kuo WH, et al. Adipocytes promote malignant growth of breast tumours with monocarboxylate transporter 2 expression via beta-hydroxybutyrate. *Nat Commun* 2017;8:14706.

202. Le Lay S, Briand N, Blouin CM, et al. The lipoatrophic caveolin-1 deficient mouse model reveals autophagy in mature adipocytes. *Autophagy* 2010;6:754–63.

203. Briand N, Le Lay S, Sessa WC, et al. Distinct roles of endothelial and adipocyte Caveolin-1 in macrophage infiltration and adipose tissue metabolic activity. *Diabetes* 2011;60:448–53.

204. Kir S, Spiegelman BM. Cachexia & brown fat: a burning issue in cancer. *Trends Cancer* 2016;2: 461–3.

205. Petruzzelli M, Schweiger M, Schreiber R, et al. A switch from white to brown fat increases energy expenditure in cancer-associated cachexia. *Cell Metab* 2014;20:433–47.

206. Kir S, White JP, Kleiner S, et al. Tumour-derived PTH-related protein triggers adipose tissue browning and cancer cachexia. *Nature* 2014;513: 100–4.

207. Wu Q, Li J, Li Z, et al. Exosomes from the tumour-adipocyte interplay stimulate beige/brown differentiation and reprogram metabolism in stromal adipocytes to promote tumour progression. *J Exp Clin Cancer Res* 2019;38:223.

208. Klingenberg M, Huang S-G. Structure and function of the uncoupling protein from brown adipose tissue. *Biochim Biophys Acta Biomembr* 1999;1415:271–96.

209. Cohen AW, Schubert W, Brasaemle DL, et al. Caveolin-1 expression is essential for proper nonshivering thermogenesis in brown adipose tissue. *Diabetes* 2005;54:679–86.

210. Mayi TH, Daoudi M, Derudas B, et al. Human adipose tissue macrophages display activation of cancer-related pathways. *J Biol Chem* 2012;287: 21904–13.

2.4 Prostate cancer – the unique mechanic and metabolic model

Non-tumor prostate tissue and prostate cancer cells are metabolically highly specific. In primary tumors, no Warburg effect was described. The non-tumor prostatic cells accumulate zinc ions. Due to the inhibitory effect of zinc to mitochondrial aconitase, the non-tumor prostatic cells accumulate citrate. Therefore, citrate metabolization to alpha-ketoglutarate is inhibited and citrate cannot be used as a source of protons in Krebs cycle by non-tumor cells.

On the other hand, malignant cells show a decrease in zinc accumulation and thus increased OXPHOS and no Warburg effect in primary tumors [7]. In addition, the "metabolic phenotype" of prostate cancer differs during its progression. Cells from metastatic sites are characteristic by decreased OXPHOS [8]. The causes and consequences of altered zinc balance are further discussed in detail in a Gumulec et al review [36].

The prostate cancer is not just unique metabolically, but also from the view of cell mechanics. Generally, most tumor cells isolated from tumor tissues are usually softer compared to their non-tumor counterparts, which facilitates migration through confined spaces [17]. In prostate cancer, however, a controversy with this exist: Bastatas and colleagues described increased stiffness (Elastic modulus) *in vitro* as a result of intensified tensile stress generated by the actin cytoskeleton [37]. Kim et al described stiffening together with epithelial-mesenchymal transition in more aggressive paclitaxel-resistant prostate cells DU-145TxR as a result of vimentin, ZEB1 and Snail upregulation [38]. Our results indicate an accordance with this finding [2]. As higher cellular pliability is needed during metastatic cell migration, this may be perceived as an evolutionary disadvantage of prostate tumors. However, hypothetically, such increased pliability is needed just in a short period of metastasis development – once cells reach the secondary niche (typically in a bone metastasis), no such phenotype is needed.

Additionally, we also indicated that zinc ions might be involved in this mechanism. As shown in our Gumulec et al *in vitro* study, more aggressive bone metastasis-derived PC-3 cells were highly sensitive to zinc ions while keeping a high level of resistance to cisplatin, as compared to less aggressive cells from primary tumor [39].

Interestingly, a linkage with prostate tumor aggressiveness and CAV1 gene expression was also shown in our study on patients with prostate adenocarcinoma. The membrane structures caveolae, or specifically the integral caveolae protein CAV1 is an important regulator of cell mechanical properties, oncogenic metabolic symbiosis and metabolic phenotype [28] (see chapter 2.3). Following study performed on a cohort of patients with prostate cancer confirms the importance of caveolin: Patients with high grade and high stage tumors were characteristic by

higher serum CAV1 levels compared to low stage/low grade tumor-bearing patients [40]. Importantly, complexity of CAV1 regulation is underlined by a fact that its association with grade is measurable not just on a cellular level or in the tumor *in situ:* it is also reflected in the patient serum.

GUMULEC, J., J. SOCHOR, M. HLAVNA, M. SZTALMACHOVA, et al. Caveolin-1 as a potential high-risk prostate cancer biomarker. Oncology Reports, Mar 2012, 27(3), 831-841.

Caveolin-1 as a potential high-risk prostate cancer biomarker

JAROMIR GUMULEC[1,2], JIRI SOCHOR[2,3], MARIAN HLAVNA[1], MARKETA SZTALMACHOVA[1,2], SONA KRIZKOVA[2,3], PETR BABULA[2,3], ROMAN HRABEC[4], ARNE ROVNY[4], VOJTECH ADAM[2,3], TOMAS ECKSCHLAGER[5], RENE KIZEK[2,3] and MICHAL MASARIK[1]

[1]Department of Pathological Physiology, Faculty of Medicine, Masaryk University, CZ-625 00 Brno; [2]Department of Chemistry and Biochemistry, Mendel University in Brno, CZ-613 00 Brno; [3]Central European Institute of Technology, Brno University of Technology, CZ-616 00 Brno; [4]Department of Urology, St. Anne's University Hospital Brno, CZ-656 91 Brno; [5]Department of Paediatric Haematology and Oncology, 2nd Faculty of Medicine Charles University, CZ-150 06 Prague 5, Czech Republic

Abstract. Current diagnostic techniques of prostate cancer cannot efficiently distinguish the latent and low-risk forms from the high-risk significant forms of prostate cancer. Caveolin-1 (Cav-1), except other functions, plays an important role in cell transformation and the process of tumorigenesis. Furthermore, Cav-1 is involved in metastatic processes. It has also been shown that Cav-1 expression is induced under stress conditions, such as oxidative stress. The present study focused on the determination of prognostic markers of aggressive (high-grade) forms of prostate cancer. We determined serum Cav-1 and serum markers of antioxidant activity-glutathione (GSH), 2,2-diphenyl-1-picrylhydrazyl (DPPH), Trolox equivalent antioxidant capacity (TEAC), ferric-reducing antioxidant power (FRAP), N,N-dimethyl-1,4-diaminobenzene (DMPD), free radicals method (FRK) and blue chromium peroxide (Cro) in 97 serum samples (82 prostate cancer patients and 15 controls). We found insignificant differences in Cav-1 between the sera of patients and controls (5.69 in the cancer group vs. 5.42 ng/ml in the control group). However, we found a significant (p<0.004) 2.8-fold elevation of Cav-1 in high tumour stages (TNM T4) compared to lower stages and a significant positive association with histological grading (r=0.29, p=0.028). We also found that in patients with high serum Cav-1 the antioxidant capacity of the body is reduced. These findings indicate that Cav-1 may be an interesting tool for the prediction of disease burden.

Correspondence to: Dr Michal Masarik, Department of Pathological Physiology, Faculty of Medicine, Masaryk University, Kamenice 5, CZ-625 00 Brno, Czech Republic
E-mail: masarik@med.muni.cz

Introduction

Discovering and definition of new biochemical markers, which are specifically connected with grave pathological states including tumour diseases, are among the most important objectives of biomedical research. Identification of highly specific and sensitive biomarkers represents the main aim of modern research, because only such biomarkers may be applied towards the early diagnosis of malignant disease, prediction of prognosis and eventually development of an appropriate treatment strategy in clinical practice (1). Malignant tumours occupy the first position among diagnosed diseases due to the improvement of health care. The process of genesis of a tumour cell includes accumulation of alterations in a cell genome, which may develop for decades. Mechanisms of the cell cycle and apoptosis regulation play a crucial role in the protection against these changes.

Prostate carcinoma is the most frequent malignant disease among men in the Czech Republic. Global data about the incidence of prostate carcinoma are not too exact, especially due to fact that a lot of men die due to this disease without its clinical manifestations (2). Substantial progress in the diagnosis of tumour diseases has been observed along with the development of proteomics due to the identification of new tumour markers (3-8). These markers, usually proteins, are closely connected with the development and eventually the progression of the disease and are present in tumour cells in altered concentrations.

Due to the introduction of prostate-specific antigen (PSA) screening in prostate cancer diagnosis, the incidence of this disease has increased by >50% in the recent years. At present, its incidence is higher in comparison with bronchogenic carcinoma with almost half of the men at the age of 80 suffering from prostate carcinoma. PSA represents the routinely used diagnostic marker of prostate carcinoma (9-11). Measurements of PSA blood serum levels began in the early 1980s. There are plenty of methods used for determination of PSA blood serum levels (10,12). However, determination of PSA is not specific and sensitive in the blood serum and its positive predictive value is only about 35%. PSA may also be elevated in various

non-tumour conditions in healthy men. Its level is increased in other prostate diseases (benign prostatic hyperplasia, prostatitis and prostate infections) or with physical activity including cycling. Almost two thirds of men with increased PSA are healthy. Contrariwise, 20% of men suffering from prostate carcinoma have normal PSA levels.

Therefore, it is not surprising that searching for new markers for this type of tumour disease is still a focus of research. Caveolin is a protein, which is often associated with tumour disease as a potential tumour marker. It is an integral membrane protein and important integral part of caveolae membranes. Its presence was already discovered in caveolae membranes in 1953 (13). These membranes are involved in receptor-independent endocytosis. Caveolae are microdomains of lipid rafts, which are rich in sphingolipids and cholesterol and play an essential role in the degradation of cholesterol (14). However, they also participate in transmembrane signalling. There are three known types of caveolin, which differ in their molecular structure and tissue distribution. Caveolin-1 is profusely present in adipocytes, epithelial cells, pneumocytes and fibroblasts. Caveolin-2 is expressed in the cells of mesenchyma, epithelial cells and neuroglia. Caveolin-3 occurs predominantly in muscle cells (15,16). All types of caveolins are investigated in view of the pathogenesis of some diseases (17-20). The connection between caveolin-1 and tumorigenesis has been investigated in many studies (21-24). Caveolin-1 has been demonstrated to regulate cell proliferation, so, it can play an important role in cell transformation and the process of tumorigenesis (23,25,26). Caveolin-1 is also involved in metastatic processes (25). The reason for the participation of caveolin-1 in these processes is the fact that normal epithelial cells are characterized by cell adhesion and the cell is closely connected through the membrane with its surroundings and is able to respond to changes in cell surroundings. Caveolin-1 directly participates in these cell processes, especially due to its connection with integrins. Changes in protein function lead to the lapse of cell functions (adhesion) and cell mobility and the development of metastatic processes (22). Furthermore, it has been demonstrated that caveolin-1 expression is induced under stress conditions, such as oxidative stress (27,28).

Metallothioneins (MT) as a metal-binding proteins represent other promising tumour markers, which are intensely studied in connection with prostate carcinoma among other diseases (29-31). It has been recently demonstrated that metallothioneins play an important role in the development and progression of some tumour diseases (32-42). Enhanced levels of MT in tumour cells are probably closely connected with cell proliferation (43,44). Recent studies point at the overexpression of MT in relation to the metal-based cytostatic agents (45,46). Other potential tumour markers include α-methylacyl-CoA-racemase (AMACR). This substance is a peroxisomal and mitochondrial enzyme involved in β-oxidation of branched fatty acids and in catabolism of bile acids metabolites (47). Increased levels of these proteins have been described in adenocarcinomas and high grade prostatic intraepithelial neoplasia (48). On the other hand, only low levels of this marker are described in benign hyperplasia and in atypical adenomatous hyperplasia (47,49,50).

It is well evidenced that the total antioxidant capacity of the human body is reduced, when patients suffer from a serious disease such as cancer, particularly when the disease is long-term and the patients are of higher age (51-53). Thus, we aimed to determine most of the common markers of antioxidant capacity and to put them into the context with caveolin-1. The originality of this study consists in the analysis and mutual correlation between the above-mentioned tumour markers and the markers of oxidative stress in blood sera of patients suffering from prostate carcinoma. Our results show the necessity for the determination of more tumour markers to aid in the knowledge of the disease stage of the patient and for the identification of optimal treatments.

Materials and methods

Chemical and biochemical reagents. All chemicals of ACS purity were purchased from Sigma-Aldrich (St. Louis, Mo, USA) unless otherwise noted. The primary mouse metallothionein antibody and the secondary anti-mouse horseradish peroxidase (HRP)-conjugated antibody were purchased from Abcam (Cambridge, MA, USA). The primary rabbit PSA and caveolin-1 antibody and the secondary anti-rabbit HRP-conjugated antibody were purchased from Santa Cruz Biotechnology, Inc. (Santa Cruz, CA, USA). The primary rabbit AMACR antibody was purchased from Clonestar (Czech Republic). For chemiluminiscent detection of Western blot membranes the ECL Western blot detection reagents system from Bio-Rad Laboratories (USA) was used.

Sample preparation for electrochemical analysis. The samples of blood serum were denatured at 99°C in a thermomixer (Eppendorf 5430, Germany) for 15 min with shaking and centrifuged at 15,000 x g at 4°C for 30 min (Eppendorf 5402). Heat treatment effectively denatures and removes thermolabile and high-molecular-weight proteins from samples. The prepared samples were used for MT and glutathione (GSH) analyses.

Differential pulse voltammetry-Brdicka reaction. Differential pulse voltammetric measurements were performed with the 747 VA Stand instrument connected to the 746 VA Trace Analyzer and the 695 Autosampler (Metrohm, Switzerland), using a standard cell with three electrodes and cooled sample holder (4°C). A hanging mercury drop electrode (HMDE) with a drop area of 0.4 mm^2 was the working electrode. An Ag/AgCl/3M KCl electrode was the reference and glassy carbon electrode was auxiliary. For data processing GPES 4.9 supplied by EcoChemie was employed. The analysed samples were deoxygenated prior to measurements by purging with argon (99.999%) and saturated with water for 120 sec. Brdicka supporting electrolyte containing 1 mM Co(NH$_3$)$_6$Cl$_3$ and 1 M ammonia buffer [NH$_3$(aq) + NH$_4$Cl, pH 9.6] was used. The supporting electrolyte was exchanged after each analysis. The parameters of the measurement were as follows: initial potential of -0.7 V, end potential of -1.75 V, modulation time 0.057 sec, time interval 0.2 sec, step potential 2 mV, modulation amplitude -250 mV, E$_{ads}$ = 0 V, volume of injected sample: 20 μl (x100 diluted sample with 0.1 M phosphate-buffer pH 7.0). All experiments were carried out at a temperature of 4°C employing the thermostat Julabo F25 (Labortechnik GmbH, Germany).

Determination of low-molecular-mass thiols. High performance liquid chromatography with an electrochemical detection (HPLC-ED) system consisted of two solvent delivery pumps operating in the range of 0.001-9.999 ml/min (Model 582 ESA Inc., Chelmsford, MA), Zorbax Eclipse AAA Column (4.6 x 150 mm 3.5-μm particle size; Varian Inc., CA, USA), and a CoulArray electrochemical detector (Model 5600A, ESA, USA). The sample (30 μl) was injected using an autosampler (Model 540 Microtiter HPLC; ESA, USA). HPLC-ED experimental conditions were as follows. The compositions of the mobile phases were: A, 80 mM trifluoroacetic acid and B, methanol. They were mixed in gradient from 3% B in the first minute, 10 % B in the second to the sixth minute and 98% B from the seventh minute of the separation; flow of the mobile phase was 0.8 ml/min, temperature of the separation was 40°C; working electrodes potential was 900 mV; detector temperature was 30°C; each measurement was done in triplicates. Retention time of the reduced GSH was 5 min. GSH concentration was calculated from a calibration curve (0.5-100 μM). The signal was quantified as a sum of current responses from all working electrodes (54,55). In the case of real sample measurements, the shift of the retention time was of about ±2%.

Determination of antioxidant activity. For determination of antioxidant activity a BS-400 automated spectrophotometer (Mindray, China) was used. It is composed of cuvette space tempered to 37±1°C, reagent space with a carousel for reagents (tempered to 4±1°C), sample space with a carousel for preparation of samples and an optical detector. Transfer of samples and reagents is provided by robotic arm equipped with a dosing needle (error of dosage up to 5% of volume). Cuvette contents are mixed by an automatic mixer including a stirrer immediately after addition of reagents or samples. Contamination is reduced due to its rinsing system, including rinsing of the dosing needle as well as the stirrer by MilliQ water. For detection itself, the following range of wave lengths can be used - 340, 380, 412, 450, 505, 546, 570, 605, 660, 700, 740 and 800 nm. Experimental details on all used spectrometric assays have been previously described (56).

Sodium dodecyl sulphate polyacrylamide gel electrophoresis (SDS-PAGE). The electrophoresis was performed according to Laemmli using a Mini Protean Tetra apparatus with a gel dimension of 8.3 x 7.3 cm (Bio-Rad Laboratories) (57). Firstly we poured 10% (m/V) running gel and then 5% (m/V) stacking gel. The gels were prepared from 30% (m/V) acrylamide stock solution with 1% (m/V) bisacrylamide (SERVA, Germany). The polymerization of the running or stacking gels was carried out at room temperature for 45 min. Prior to analysis the samples were mixed with reducing (DTT, final concentration 400 mM) sample buffer in 4:1 ratio. The samples were boiled for 5 min and then the sample was loaded onto the gel. For determination of molecular mass, the protein ladder, broad or lower range (Bio-Rad Laboratories) was used. The electrophoresis ran at 80 V for 20 min subsequently increased to 120 V for 1 h (Power Basic, Bio-Rad Laboratories) in Tris-glycine buffer (0.025 M Trizma-base, 0.19 M glycine and 0.0035 M SDS, pH 8.3). Silver staining of the gels was performed using the Bio-Rad Silver stain kit according to Merril *et al* (58).

Western blot analysis. After the electrophoretic separation, the proteins were transferred onto a nitrocellulose membrane (Bio-Rad Laboratories) in a Bio-Rad apparatus. The blotting was carried out for 1 h at a constant current of 0.9 mA for 1 cm^2 of the membrane. After the transfer, the membrane was blocked in 5% non-fat milk in PBS (137 mM NaCl, 2.7 mM KCl, 1.4 mM NaH$_2$PO$_4$, and 4.3 mM Na$_2$HPO$_4$; pH 7.4) for 2 h. The incubation with mouse primary antibody in dilution of 1:750 in PBS with 5% non-fat milk was carried out for 12 h at 4°C. After three washing with PBS containing 0.05 % (v/v) Tween-20 (PBS-T) for 5 min the membrane was incubated with secondary antibody (anti-mouse labelled with HRP, Sigma-Aldrich, diluted 1:5,000) for 1 h at room temperature. Then, the membrane was washed three times with PBS-T for 5 min and incubated with the ECL WB detection reagents (Santa Cruz Biotechnology Inc.).

Dot-immunobinding assay. For immunobinding assays PVDF membranes (Bio-Rad Laboratories) were used. The sample (1 μl) was applied and dried. Further the membrane was blocked in 2% bovine serum albumin (BSA) in PBS for 0.5 h with constant shaking. The incubation with the primary antibody (1:500 diluted) was carried out for 1 h at 37°C. After three times repeated washing in PBS containing 0.05% (v/v) Tween-20 (0.05% PBS-T) for 5 min, the membrane was incubated in the presence of secondary antibody at a dilution 1:5,000 for 1 h at 37 C. Then the membrane was washed three times in 0.05% PBS-T for 5 min and incubated in chromogenic substrate [0.4 mg/ml AEC (3-aminoethyl-9-carbazole) in 0.5 M acetate buffer with 0.1% H$_2$O$_2$, pH 5.5]. After sufficient colouring the reaction was stopped by rinsing in water.

tPSA and fPSA determination. Total PSA (tPSA) and free PSA (fPSA) contents were determined by the immunochemistry analyser AIA 600 II (Tosoh, Japan). AIA 600 II is specifically designed for measurement of immunochemistry parameters in biological fluids using reagents of AIA-PACK series. Analyses were carried out according to the manufacturer's instructions. The instrument was calibrated using the AIA-PACK Calibrator set using a 6-point calibration (Tosoh). All reactions were performed in the special disposable test cups containing dried and lyophilized reagents. The immunochemical antigen-antibody reaction employed magnetic particles (1.5 mm). Samples were incubated at 37°C. 4-Methylumbelliferyl phosphate was used as a substrate and fluorescence corresponding to enzymatic activity on magnetic particles was measured.

Determination of serum caveolin-1 protein. For determination of the serum levels of caveolin-1 protein the Human caveolin-1 ELISA Kit (Uscn Life Science, Inc., Wuhan, China; detection range 0.24-15 ng/ml) was used according to the manufacturer's manual. To detect the concentration of serum caveolin-1 level using the ELISA kit, the 60 ng/ml caveolin-1 standard was diluted to the concentration range 0.24-16 ng/ml in duplicates and absorption was measured.

Densitometric and statistical analysis. The signal intensity of bands after immunochemistry analysis was determined using the ImageJ 1.45 software (NIH, USA) as an area under the curve and concentration was calculated according to the protein
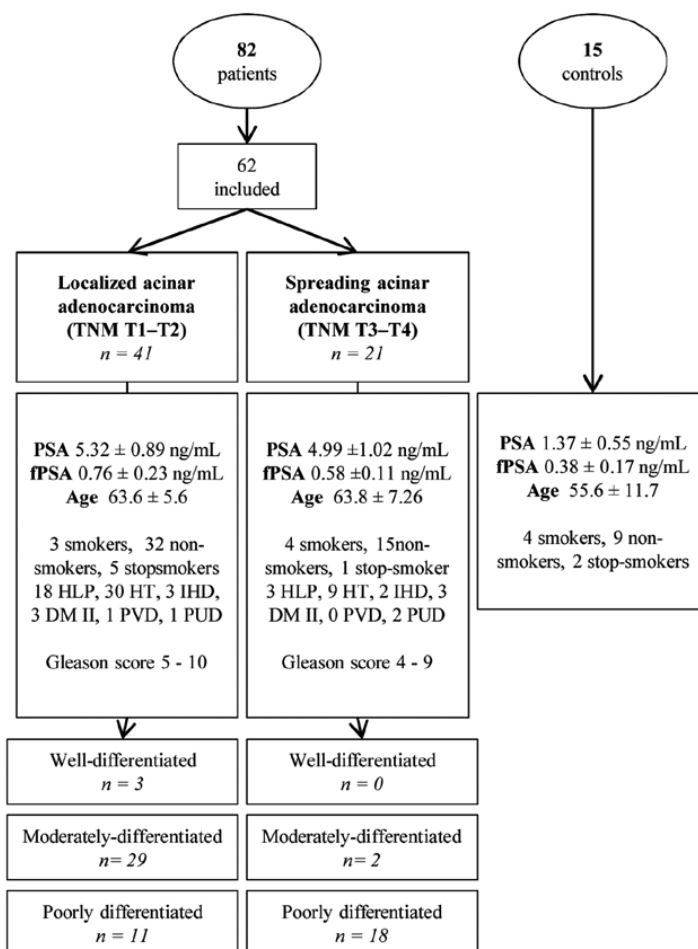
Figure 1. Characterisation of patients and controls. Categorization by tumour localization and differentiation. HLP, hyperlipoproteinaemia; HT, hypertension; IHD, ischaemic heart disease; DMII, diabetes mellitus type II; PVD, peripheral vascular diseas; PUD, peptic ulcer disease.

standard. Software Statistica 9.1 (StatSoft, USA) was used for statistical analysis. To test the normal distribution of data and thus usability of parametric tests, the Kolmogorov-Smirnov test was used. The Student's t-test for independent values was used to evaluate differences between the two groups. Simple linear correlations were performed to reveal the relationships between variables. To characterize data, associations were visualized using tree clustering with Euclidean distances measurement and single linkage. Subsequently, patients divided into clusters using K-means clustering analysis. Unless noted otherwise, a level of statistical significance was designated to p=0.05.

Results

Blood serum caveolin-1 levels were statistically evaluated in groups of controls and histologically verified tumours. Consequently, caveolin-1 level was related to data in the patient's history, such as age, smoking habits, associated diseases, clinical tumour stage and histological grade (Fig. 1). Subsequently, caveolin-1 was related to the level of serum PSA in order to evaluate the use of caveolin-1 as an auxiliary marker along with a PSA. Cluster analysis of PSA and caveolin-1 levels was performed to divide the patients into the groups characterised with high or low caveolin-1 or PSA. In these groups tumour stage and grade was evaluated.

Because tumour pathogenesis and growth are tightly associated with oxidative stress, we also determined serum markers of antioxidant activity, GSH, 2,2-diphenyl-1-picrylhydrazyl (DPPH), Trolox® equivalent antioxidant capacity (TEAC), ferric reducing antioxidant power (FRAP), N,N-dimethyl-1,4-diaminobenzene (DMPD), free radicals method (FRK) and blue chromium peroxide (Cro). We have previously described these methods in detail in study by Sochor *et al* (56). In addition, it has been shown that caveolin-1 is associated with oxidative stress in cancer progression. Thus, we correlated caveolin-1 levels with markers of oxidation and performed cluster analysis to elucidate possible associations. We also associated caveolin-1 with other previously determined potential prostate cancer serum tumour markers, namely α-methylacyl-CoA racemase (AMACR) and metallothionein (MT) which we have previously demonstrated as a high specificity and sensitivity diagnostic tool for prostate cancer diagnosis (59).
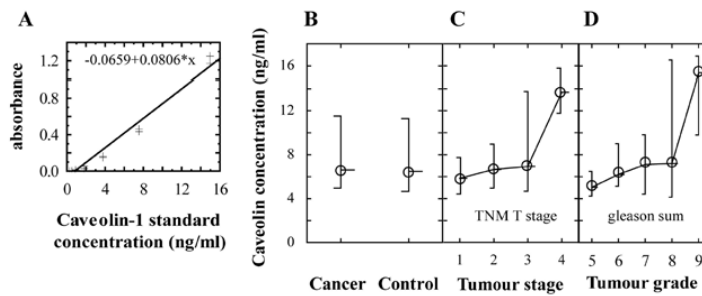
Figure 2. Caveolin-1 in patients. (A) Calibration curve. Absorbance of caveolin-1 standard in concentrations 0.24-16 ng/ml, obtained calibration curve at correlation r=0.98. (B) Serum caveolin-1 in patients and controls. No significant difference between groups was observed. (C) Caveolin-1 in relation to TNM tumour stage. Significantly higher (p<0.004) caveolin-1 level was determined in tumour exceeding seminal vesicles (T4) compared to lower stages of tumour. (D) Caveolin-1 grouped by histological tumour grade (Gleason sum). Higher caveolin-1 level was in high grade tumours (correlation r=0.29 at p=0.028).

Table I. Caveolin-1 and PSA levels in relation to tumour stage (TNM T stage), histological differentiation and tumour grade (Gleason sum score).

	n	PSA (ng/ml)	Free PSA (ng/ml)	Caveolin-1 (ng/ml)
Tumour stage				
T1	1	3.12	0.54	4.19
T2	40	5.41±3.44	0.77±0.44	5.25±2.62
T3	18	5.18±3.96	0.58±0.38	6.60±3.69
T4	3	5.58±4.01	0.57±0.33	14.25±2.19[a]
Tumour differentiation				
Well	3	4.15±1.40	0.63±0.42	4.13±1.27
Moderately	23	4.83±3.50	0.66±0.40	5.64±3.02
Poorly	28	5.95±4.66	0.72± 0.48	6.28±3.32
Tumour grade (Gleason sum score)				
5	5	3.69±1.43	0.46±0.02	3.86±1.11
6	20	5.03±2.56	0.82±0.39	5.11±2.42
7	32	4.85±3.22	0.58±0.37	5.75±2.98
8	3	10.12±8.17	1.02±0.82	6.96±4.83
9	4	6.87±5.03	0.64±0.42	9.99±4.04
10	1	3.90	_[b]	_[b]
Total	62	4.83±3.56	0.66±0.39	5.65±3.02

[a]Significant at p<0.004; [b]insufficient data for Gleason sum score 10 patients.

Tested cohort characteristics. We have analysed sera of 82 patients with histologically verified acinar adenocarcinoma of the prostate and 15 controls (Fig. 1). Out of these patients only 62 patients were selected for further analysis due to the lack of complete history data or insufficient quality of samples (haemolysis and/or extreme values detected). The average age of the patients was 63.7 years and ranged from 48 to 78 years. Of the 62 patients, 49 were non-smokers, 9 were smokers and the rest were former smokers. Forty-two patients (68%) had localized tumours (T1-2) and 20 patients had spreading tumours of higher stage. The tumour differentiation ranged from well differentiated (3 tumours) to poorly differentiated (27 tumours) (Table I). The Gleason sum score ranged within 5-10. Patients had the following associated illnesses:

hypertension (39 patients) hyperlipoproteinaemia (21 patients), ischaemic heart disease (5 patients), diabetes mellitus type II (6 patients), peripheral vascular disease (1 patient), peptic ulcer disease (3 patients), and tumour in history (1 patient). Of 62 patients, 15% did not suffer from any associated disease.

Caveolin-1 in patients and controls. Caveolin-1 standard in the concentration range from 0.24 to 16 ng/ml was used for determining the calibration dependence shown in Fig. 2A. Using linear regression we obtained strictly linear dependence with $R^2>0.99$. The serum caveolin-1 concentration ranged within 1.12-14.15 ng/ml and 1.74-14.97 ng/ml in the patients group and controls, respectively. The mean serum concentrations were 5.69 ng/ml in the cancer group and 5.42 ng/ml

Figure 3. Caveolin-1 and prostate specific antigen (PSA). (A) Caveolin-1-PSA relation weak insignificant correlation was observed (see inset). Three clusters were apparent: patients with low PSA and high caveolin-1 (grey cluster 1), patients with high PSA and high caveolin-1 (dashed cluster 2) and patients with low PSA and low caveolin-1 (dotted grey cluster 3). (B) Tumour stage (TNM T) in three determined PSA/caveolin-1 clusters. Patients with low caveolin-1 and low PSA (cluster 3) had mostly lower grade tumours compared to clusters 1 and 2. (C) Tumour grade (Gleason sum) in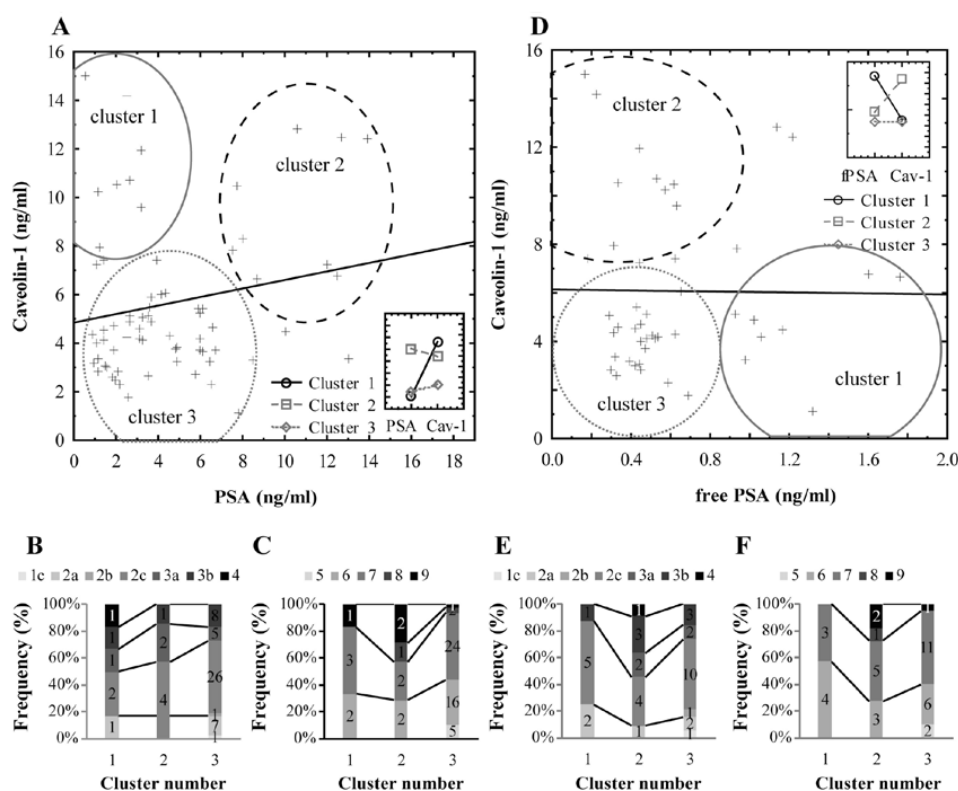 PSA/caveolin-1 clusters of patients. Larger proportion of patients with higher PSA and higher caveolin-1 had higher grade (GS 8,9) tumours compared to patients with high caveolin-1 only (cluster 1) and low PSA and low caveolin-1 (cluster 3). (D) Caveolin-1 and free PSA no significant dependence revealed. Three clusters were apparent: patients with high free PSA and low caveolin-1 (grey cluster 1), patients with high caveolin-1 and low free PSA (dashed cluster 2) and patients with low caveolin-1 and low free PSA (dotted grey cluster 3). (E) Tumour stage (TNM T) in fPSA/caveolin-1 clusters. Patients with low fPSA and high caveolin-1 (cluster 2) had distinctly higher stage tumours compared to other clusters. (F) Tumour grade (Gleason sum) in fPSA/caveolin-1 clusters of patients. Patients with high caveolin-1 and low free PSA (cluster 2) had distinctly higher grade tumours.

in the control group. To verify the normality and thus suitability of parametric methods, the Kolmogorov-Smirnov test was performed. We found caveolin-1 levels were distributed normally ($p<0.1$), thus, independent t-test was used. No significant change between group of controls and patients was determined (Fig. 2B). Cluster analysis revealed statistically significant variance of values in a group of cancer sera and led to classification of patients into two groups: high caveolin-1 and low caveolin-1 (data are not shown). Serum caveolin-1 was subsequently related to tumour stage (TNM T stage) and tumour grade (Gleason score sum) to clarify the differences in values. A similar trend was observed in both relations: caveolin-1 levels remained low in low stage and low grade tumours and distinctly increased in the highest stage and grade tumours (Fig. 2C and D). Patients with tumour spreading beyond the seminal vesicle (TNM T4 stage) had significantly ($p<0.004$) 2.8-fold increased serum caveolin-1 levels compared to T1-3 stages (Table I). However, no statistically significant differences between localised (T1-2) tumours and those that extend through the prostate capsule (T3-4) were detected. In terms of tumour grade and its relation to caveolin-1, patients with

Gleason sum 9 had distinctly higher caveolin-1 levels. This trend was significant ($r=0.29$ at $p=0.028$); however, the difference between Gleason sum 9 patients and others was below the threshold of statistical significance.

In addition, other correlations with data obtained from history were carried out. No statistically important correlations between age of patients and caveolin-1 were found. Level of caveolin-1 was not significantly changed in connection with associated disease-hypertension, ischemic heart disease and hyperlipidaemia, ischemic disease of lower extremities and duodenal ulcer. Similarly, no differences in monitored markers between group of smokers and non-smokers were evident (data not shown).

Caveolin-1 and PSA correlation. Correlation analysis of serum caveolin-1 levels to PSA levels, found that no correlation exists between these proteins ($p=0.13$). When cluster analysis was performed, three groups were found: patients with low caveolin-1 and low PSA (grey dotted ellipse, cluster 3 in Fig. 3A), patients with low PSA and high caveolin-1 (grey cluster 1) and patients with high caveolin-1 and PSA (black dashed cluster 2).
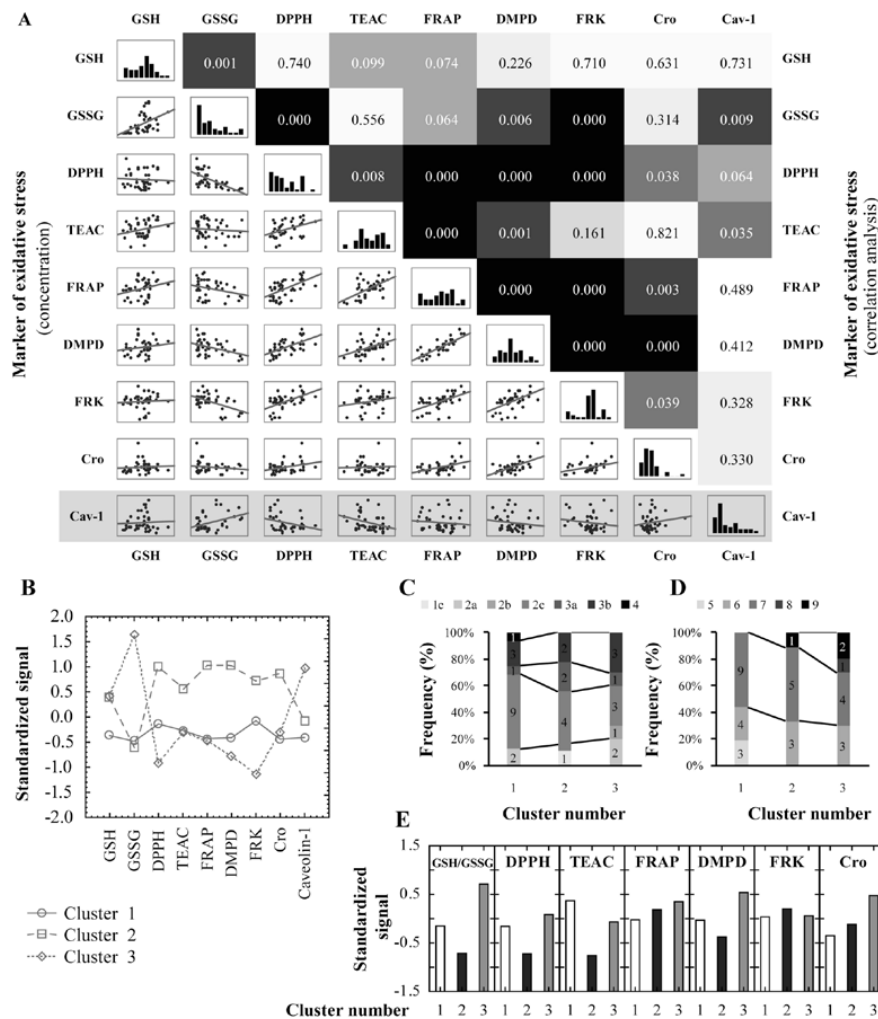
Figure 4. Caveolin-1 and markers of oxidation. (A) Correlations of markers of oxidation and caveolin-1 with each other with distribution histograms (diagonally). Bottom left part displays relations of markers/proteins, the top right part displays statistical significance of correlation (black, more significant trend; white, less significant). Evident significant correlations of caveolin-1 with reduced glutathione (GSH), 2,2-diphenyl-1-picrylhydrazyl (DPPH) and Trolox® equivalent antioxidant capacity (TEAC). (B) Cluster analysis of markers of oxidation together with caveolin-1. Inverse association of caveolin-1 and markers is obvious: the first cluster is characterized by no relations in caveolin-1 and markers of oxidation. The second cluster represents patients with high antioxidative potential (low GSSG and high antioxidative markers) and high caveolin-1. The third cluster represents patients with lower oxidative/antioxidant markers and low caveolin-1. (C) Tumour stage in subsequent clusters. No distinct differences in tumour staging within clusters of high or low caveolin-1/markers of oxidation were evident. (D) Tumour grade (represented as Gleason sum) in subsequent clusters. In the 'low antioxidative potential' cluster 3 are patients of distinctly higher content of high grade tumours compared to other patients. (E) Markers of antioxidant capacity in clusters by PSA/caveolin-1 characterized in Fig. 3A. We found significantly lower levels of the GSH/GSSG ratio, DPPH, TEAC and DMPD in the 'high PSA-high caveolin-1' cluster compared to the other clusters.

To characterize patients within those clusters, stage and grade was plotted in Fig. 3B and C. It is well evident that patients with high caveolin-1 and PSA (cluster 2) had lower proportions of localized tumours T1 and T2 compared to patients where only caveolin-1 is high and the PSA remains low (cluster 1), or where both proteins were low (cluster 3). A similar trend was evident in tumour grading (Fig. 3C), whereas in cluster 3 there was only a minimal proportion of high grade Gleason sum 8 and 9 tumours. In the 'both markers high cluster 2' the proportion of these high grades was about 40%.

A similar association was also observed with caveolin-1 and the free PSA fraction (Fig. 3D). Similarly to the total PSA,

in a group of low free PSA and low caveolin-1 (cluster 3) the proportion of low stage and low grade tumours was higher (Fig. 3E and F). Patients characterised with high serum free PSA and low caveolin-1 were of marginally higher stage and grade compared to the 'low free PSA-low caveolin-1' cluster 3 group, whereas, patients with high serum caveolin-1 and low free PSA were of significant proportion of T3-4 and grade Gleason sum 8 and 9 tumours.

Association of caveolin-1 and oxidative stress. Markers of antioxidant activity were determined in the sera of patients and correlated with serum caveolin-1 level to elucidate
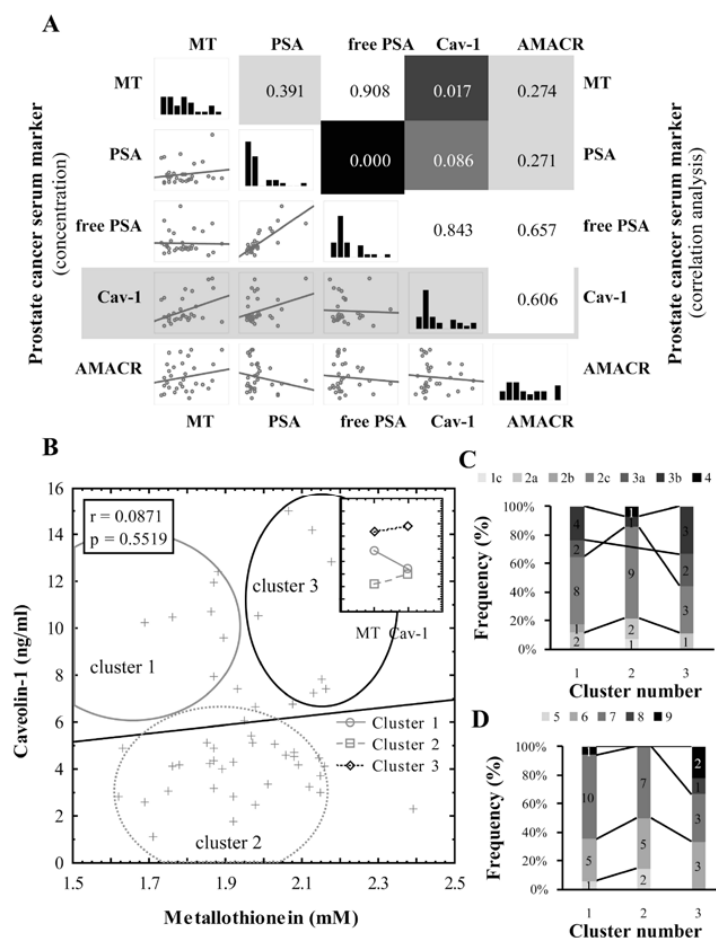
Figure 5. Relation of caveolin-1 to other potential prostate cancer markers. (A) Correlation matrix. A weak significant trend was observed between caveolin-1 and metallothionein (MT), no significant relation between caveolin-1 and PSA and α-methylacyl CoA-racemase (AMACR). (B) Caveolin-1 and MT clustering analysis of clinical data. Three clusters were apparent: patients with higher MT and lower caveolin-1 (grey cluster 1), patients with low MT and low caveolin-1 (grey dotted cluster 2) and patients with high caveolin-1 and high MT (black cluster 3). (C) Tumour stage (TNM T) in MT/caveolin-1 clusters. Higher proportion of high-stage tumours are apparent in cluster 3 compared to cluster 2. (D) Tumour grade (Gleason sum) in clusters of patients. In the cluster with higher MT and higher caveolin-1 (cluster 3) a higher proportion of patients with high-grade tumours is apparent compared to the other clusters.

potential connections. Association between those markers is displayed in Fig. 4A. We observed significant trends between caveolin-1 and reduced GSH, TEAC and borderline significance with DPPH. Among others, our results show that most of the markers of antioxidant capacity correlate more with each other compared to with caveolin-1. Strongest correlations were observed between ferric reducing antioxidant power and N,N-dimethyl-1,4-diaminobenzene and free radical method. In order to elucidate the connections between markers of (anti)oxidation, cluster analysis was performed. Using this procedure, patients were divided into three distinct clusters (Fig. 4B) as follows. Cluster 2 which consists of patients with high antioxidant capacity, low caveolin-1 and low reduced GSH (Fig. 4B); cluster 3 which consists of patients with low antioxidative capacity, high caveolin-1 and high reduced glutathione and cluster 1 which shows no apparent dependencies compared to the previous clusters, and in which the markers of (anti)oxidation are of rather lower levels. In Fig. 4C and D we identified the tumour grade and tumour stage within these

clusters. It is clear from these results that patients with lower antioxidative potential and higher caveolin-1 level (cluster 3) had a higher proportion of high grade (Gleason sum 8,9) tumours compared to others (compare clusters 2 and 3 in Fig. 4D). No similar trend was however observed, if we highlighted tumour stage within these clusters (Fig. 4C).

Then, we aimed our attention at the markers of antioxidative capacity from a different perspective. We related markers of antioxidation to caveolin-1 and PSA together. Three clusters of PSA have been described: high PSA and caveolin-1, high caveolin-1, and low PSA and caveolin-1. In these clusters, the levels of individual antioxidative markers were visualized. We found a significantly lower (p<0.05) level GSH/GSSG ratio, DPPH, TEAC and DMPD in the group of patients with high caveolin-1 and high PSA compared to the group of patients with low serum caveolin-1 and low PSA.

Association of caveolin-1 with other potential tumour markers. We subsequently performed correlation analyses

between caveolin-1 and other potential serum markers of prostate cancer, which we have determined in our previous studies on the same sample set of patients (59). Thus, regarding PSA, which is mentioned in this table for overall complexity, here we show associations of caveolin-1 with MT and AMACR (Fig. 5A). In our previous study we have shown that metallothionein may be utilized as a marker of prostate cancer with high level of sensitivity and specifity (59). We found no major relationships between serum caveolin-1 level and serum MT levels (r=0.08, Fig. 5B). No trend was also observed when associated with AMACR. When cluster analysis on MT and caveolin-1 was carried out in the same way as with PSA or markers of oxidation (Fig. 5A), we found that when both of these serum markers are of high level, worse prognosis is expected, because greater proportion high grade (30 vs. 0% of GS 8-9 tumours in cluster 3 vs. cluster 2) and high stage (30 vs. 14% of T3b and T4 tumours in cluster 3 vs. cluster 2) tumours are present in these patients (Fig. 5C and D).

Discussion

In this study, we may clearly conclude that caveolin-1 is associated with worse prognosis. This we may evidence by three findings: first, higher serum caveolin-1 levels are associated with higher stage and grade tumours (which are of worse prognosis); second, caveolin-1 positively correlates with PSA levels, and third, patients with high serum caveolin-1 have a lower antioxidant capacity of the body. It is highly desirable to differentiate high-risk 'significant' forms of prostate cancer from latent, 'non-significant' forms. We expect that the prediction of high-risk tumours may be estimated when more cancer markers are determined concurrently. Utilization of caveolin-1 together with free and total PSA and possibly also with metallothionein may provide more accurate results in the estimation of prostate cancer risk when determined together. Based on our results we may conclude that patients with low free PSA, high caveolin-1 and high total PSA have worse prognosis compared to patients with lower serum caveolin-1 levels. Similarly, patients, who have high caveolin-1 and low PSA have better prognosis (lower stage and lower grade tumours) compared to patients with high PSA and caveolin-1 together. The similar benefit is also provided by the combined utilization of metallothionein and caveolin-1 as tumour markers, where patients with high metallothionein and low caveolin-1 are of better prognosis compared to patients with high levels of both markers. The merit of the use of fPSA, tPSA, caveolin-1 together as a marker of worse prognosis tumour may be underplayed by this finding. In cancers, the antioxidant capacity is reduced (51-53). Furthermore, patients with reduced antioxidant capacity are of worse prognosis when compared to patients with higher antioxidant potential. We may clearly confirm that the antioxidant capacity is associated with the severity of disease in this experiment by findings shown in Fig. 4D, from which it is apparent that patients with low antioxidative markers are of higher tumour grade.

An important finding of our study is the fact that high caveolin-1 levels are associated with patients of low antioxidative potential. Cluster analysis shown in Fig. 4B clearly points to the relationship between caveolin-1 and the antioxidative capacity of the patient's body. Patients with low caveolin-1

are of better prognosis because their antioxidative capacity is apparently higher (cluster 2 in Fig. 4B), whereas patients with high serum caveolin-1 have apparently lower antioxidative capacity. Due to the fact that caveolin-1 positively correlates with reduced glutathione and negatively correlates with markers of antioxidant capacity (even below the level of significance), we may speculate that caveolin-1 reflects the burden of the disease. This relation has not been published yet. The relationship of caveolin-1 with oxidative stress can also be viewed from another point of view. Recent studies have demonstrated that caveolin-1 is a target molecule in p38 MAPK mediated response to stress conditions such as oxidative stress (27,28). After such stimuli, caveolin-1 is phosphorylated and thus contributes to various signalling pathways (60) resulting most likely in processes, such as premature cellular senescence (27). Thus, the connection of low antioxidant capacity and high caveolin-1 found in our study may be explained as consequence of caveolin-1 mediated response to high oxidative burden. In such long-term high oxidative stress conditions the resulting antioxidant capacity may be reduced, nevertheless, caveolin-1 remains higher. Utilization of multiple protocols for the determination of antioxidative capacity or free radical quenching activity, as performed in this study, may be useful because of discrepancies between the activity measured *in vitro*, and the antioxidative effects observed *in vivo* (61). Each technique is based on different principles and enables determination of the antioxidant activity of specific groups of compounds (56,62,63).

In the recent decade, caveolin-1 was linked with various types of cancers, of which it was most extensively studied in the cancers of the breast and prostate. It was found that tumour tissue and/or serum caveolin-1 levels vary in a cancer-dependent manner and these changes in caveolin-1 levels may be associated with tumour protection or progression (25). When focused on prostate cancer, elevated caveolin-1 expression was observed in tumour tissue and in mice when compared to non-tumour tissue (64-66). According to Thompson *et al*, caveolin-1 is also elevated in the serum of patients with localized tumours compared to healthy controls and patients with benign prostatic hyperplasia (67,68). These findings are inconsistent with ours; we found no significant difference between controls and cancers. However, it has also been revealed that caveolin-1 is connected with tumour progression and metastatic dissemination and is distinctly elevated in androgen resistant tumours. Thus this molecule was suggested as a tissue marker of an aggressive form of cancer (68-74). It has also been shown that suppression of caveolin-1 expression can restore the sensitivity to androgens in androgen-insensitive tumours (65). Higher expression of caveolin-1 was also identified in tissue samples of patients of higher grade tumours and of higher PSA (75). This is in good agreement with our results, where we also identified associations with high stage and high grade tumours with high PSA. Also, according to a study by Karam *et al* on patients before and after radical prostatectomy, patients of higher caveolin-1 are in risk of higher postoperative PSA and thus of worse postoperative prognosis (75). Although we did not compare patients before and after treatment procedures, we similarly observed correlation of caveolin-1 with PSA. Furthermore, worse prognosis could be expected from higher oxidative stress in high caveolin-1 patients.

Our findings together with data from recent studies suggest that caveolin-1 is involved in disease pathogenesis and progression. Clarification can contribute to the understanding of this disease with potential novel targeted therapeutic approaches. Although associations between caveolin-1 and high-risk tumours were identified in this study, we still cannot infer that caveolin-1 may serve as a high-risk aggressive tumour marker even in a phase when tumours are localized in the prostate and thus are still curable. To confirm this, it is necessary to monitor caveolin-1 levels in a follow-up study during the course of prostate cancer progression from its initial stages. It is necessary to verify these facts in the extensive group of patients including those with disseminated disease.

Acknowledgements

References

1. Gannot G, Tangrea MA, Richardson AM, *et al*: Layered expression scanning: multiplex molecular analysis of diverse life science platforms. Clin Chim Acta 376: 9-16, 2007.
2. Bensalah K, Montorsi F and Shariat SF: Challenges of cancer biomarker profiling. Eur Urol 52: 1601-1609, 2007.
3. Duffy MJ: PSA as a marker for prostate cancer: a critical review. Ann Clin Biochem 33: 511-519, 1996.
4. Matsumoto K, Irie A, Satoh T, Kuruma H, Arakawa T and Baba S: Occupational bladder cancer: from cohort study to biologic molecular marker. Med Sci Monitor 11: RA311-RA315, 2005.
5. Sargent DJ, Conley BA, Allegro C and Collette L: Clinical trial designs for predictive marker validation in cancer treatment trials. J Clin Oncol 23: 2020-2027, 2005.
6. Sarrazin S, Adam E, Lyon M, *et al*: Endocan or endothelial cell specific molecule-1 (ESM-1): a potential novel endothelial cell marker and a new target for cancer therapy. Biochim Biophys Acta 1765: 25-37, 2006.
7. Tuxen MK: Tumor marker CA125 in ovarian cancer. J Tumor Marker Oncol 16: 49-68, 2001.
8. Zehentner BK and Carter D: Mammaglobin: a candidate diagnostic marker for breast cancer. Clin Biochem 37: 249-257, 2004.
9. Barry MJ: Prostate-specificy-antigen testing for early diagnosis of prostate cancer. N Engl J Med 344: 1373-1377, 2001.
10. Catalona WJ, Smith DS, Ratliff TL, *et al*: Measurement of prostate-specific antigen in serum as a screening test for prostate cancer. N Engl J Med 324: 1156-1161, 1991.
11. Thompson IM, Pauler DK, Goodman PJ, *et al*: Prevalence of prostate cancer among men with a prostate-specific antigen level ≤4.0 ng per milliliter. N Engl J Med 350: 2239-2246, 2004.
12. Schmid HP, McNeal JE and Stamey TA: Observations on the doubling time of prostate-cancer: the use of serial prostate-specific antigen in patients with untreated disease as a measure of increasing cancer volume. Cancer 71: 2031-2040, 1993.
13. Palade GE: Fine structure of blood capillaries. J Appl Phys 24: 1424-1424, 1953.
14. Patra SK and Bettuzzi S: Epigenetic DNA-methylation regulation of genes coding for lipid raft-associated components: A role for raft proteins in cell transformation and cancer progression (Review). Oncol Rep 17: 1279-1290, 2007.
15. Gould ML, Williams G and Nicholson HD: Changes in caveolae, caveolin, and polymerase 1 and transcript release factor (PTRF) expression in prostate cancer progression. Prostate 70: 1609-1621, 2010.
16. Couet J, Belanger MM, Roussel E and Drolet MC: Cell biology of caveolae and caveolin. Adv Drug Deliv Rev 49: 223-235, 2001.
17. Frank PG, Pavlides S and Lisanti MP: Caveolae and transcytosis in endothelial cells: role in atherosclerosis. Cell Tissue Res 335: 41-47, 2009.
18. Zheng YZ and Foster LJ: Biochemical and proteomic approaches for the study of membrane microdomains. J Proteomics 72: 12-22, 2009.
19. Volonte D, Galbiati F and Lisanti MP: Visualization of caveolin-1, a caveolar marker protein, in living cells using green fluorescent protein (GFP) chimeras. The subcellular distribution of caveolin-1 is modulated by cell-cell contact. FEBS Lett 445: 431-439, 1999.
20. UniProt knowledgebase for Q03135 (Cav1_Human). http://www.uniprot.org/uniprot/Q03135.
21. Shatz M and Liscovitch M: Caveolin-1: a tumor-promoting role in human cancer. Int J Radiat Biol 84: 177-189, 2008.
22. Burgermeister E, Liscovitch M, Rocken C, Schmid RM and Ebert MPA: Caveats of caveolin-1 in cancer progression. Cancer Lett 268: 187-201, 2008.
23. Ando T, Ishiguro H, Kimura M, *et al*: The overexpression of caveolin-1 and caveolin-2 correlates with a poor prognosis and tumor progression in esophageal squamous cell carcinoma. Oncol Rep 18: 601-609, 2007.
24. Zhang Q, Furukawa K, Chew HH, *et al*: Down-regulation of caveolin-1 in mouse Lewis lung cancer P29 is a causal factor for the malignant properties in a high-metastatic subline. Oncol Rep 16: 289-294, 2006.
25. Williams TM and Lisanti MP: Caveolin-1 in oncogenic transformation, cancer, and metastasis. Am J Physiol Cell Physiol 288: C494-C506, 2005.
26. Conde MC, Ramirez-Lorca R, Lopez-Jamar JME, *et al*: Genetic analysis of caveolin-1 and eNOS genes in colorectal cancer. Oncol Rep 16: 353-359, 2006.
27. Dasari A, Bartholomew JN, Volonte D and Galbiati F: Oxidative stress induces premature senescence by stimulating caveolin-1 gene transcription through p38 mitogen-activated protein kinase/ Sp1-mediated activation of two GC-rich promoter elements. Cancer Res 66: 10805-10814, 2006.
28. Chen DB, Li SM, Qian XX, Moon CS and Zheng J: Tyrosine phosphorylation of caveolin 1 by oxidative stress is reversible and dependent on the c-src tyrosine kinase but not mitogen-activated protein kinase pathways in placental artery endothelial cells. Biol Reprod 73: 761-772, 2005.
29. Krizkova S, Adam V, Petrlova J, *et al*: A suggestion of electrochemical biosensor for study of platinum(II)-DNA interactions. Electroanalysis 19: 331-338, 2007.
30. Popiela TJ, Rudnicka-Sosin L, Dutsch-Wicherek M, *et al*: The metallothionein and RCAS1 expression analysis in breast cancer and adjacent tissue regarding the immune cells presence and their activity. Neuro Endocrinol Lett 27: 786-794, 2006.
31. Zelena J, Potesil D, Vacek J, *et al*: Metallothionein as a prognostic marker of tumor disease. Klin Onkol 17: 190-195, 2004.
32. Ebert MPA, Günther T, Hoffmann J, *et al*: Expression of metallothionein II in intestinal metaplasia, dysplasia, and gastric cancer. Cancer Res 60: 1995-2001, 2000.
33. Kasahara K, Fujiwara Y, Nishio K, *et al*: Metallothionein content correlates with the sensitivity of human small cell lung cancer lines to cisplatin. Cancer Res 51: 3237-3242, 1991.
34. Theocharis SE, Margeli AP, Klijanienko JT and Kouraklis GP: Metallothionein expression in human neoplasia. Histopathology 45: 103-118, 2004.
35. Adam V, Baloun J, Fabrik I, Trnkova L and Kizek R: An electrochemical detection of metallothioneins at the zeptomole level in nanolitre volumes. Sensors 8: 2293-2305, 2008.
36. Adam V, Blastik O, Krizkova S, *et al*: Application of the Brdicka reaction in determination of metallothionein in patients with tumours. Chem Listy 102: 51-58, 2008.
37. Fabrik I, Krizkova S, Huska D, *et al*: Employment of electrochemical techniques for metallothionein determination in tumour cell lines and patients with a tumor disease. Electroanalysis 20: 1521-1532, 2008.
38. Eckschlager T, Adam V, Hrabeta J, Figova K and Kizek R: Metallothioneins and cancer. Curr Protein Pept Sci 10: 360-375, 2009.
39. Adam V, Fabrik I, Eckschlager T, Stiborova M, Trnkova L and Kizek R: Vertebrate metallothioneins as target molecules for analytical techniques. TrAC-Trends Anal Chem 29: 409-418, 2010.
40. Adam V, Petrlova J, Wang J, Eckschlager T, Trnkova L and Kizek R: Zeptomole electrochemical detection of metallothioneins. PLoS One 5: e11441, 2010.
41. Ryvolova M, Krizkova S, Adam V, *et al*: Analytical methods for metallothionein detection. Curr Anal Chem 7: 243-261, 2011.
42. Kizek R, Trnkova L and Palecek E: Determination of metallothionein at the femtomole level by constant current stripping chronopotentiometry. Anal Chem 73: 4801-4807, 2001.

43. Cherian MG, Jayasurya A and Bay BH: Metallothioneins in human tumors and potential roles in carcinogenesis. Mutat Res 533: 201-209, 2003.
44. Jin R, Huang J, Tan PH and Bay BH: Clinicopathological significance of metallothioneins in breast cancer. Pathol Oncol Res 10: 74-79, 2004.
45. Kelly SL, Basu A, Teicher BA, Hacker MP, Hamer DH and Lazo JS: Overexpression of metallothionein confers resistance to anticancer drugs. Science 241: 1813-1815, 1988.
46. Theocharis S, Karkantaris C, Philipides T, et al: Expression of metallothionein in lung carcinoma: correlation with histological type and grade. Histopathology 40: 143-151, 2002.
47. Kuefer R, Varambally S, Zhou M, et al: α-methylacyl-CoA racemase: expression levels of this novel cancer biomarker depend on tumor differentiation. Am J Pathol 161: 841-848, 2002.
48. Luo J, Zha S, Gage WR, et al: α-methylacyl-CoA racemase: a new molecular marker for prostate cancer. Cancer Res 62: 2220-2226, 2002.
49. Xu J, Stolk JA, Zhang X, et al: Identification of differentially expressed genes in human prostate cancer using subtraction and microarray. Cancer Res 60: 1677-1682, 2000.
50. Evans AJ: α-methylacyl CoA racemase (P504S): overview and potential uses in diagnostic pathology as applied to prostate needle biopsies. J Clin Pathol 56: 892, 2003.
51. Buttke TM and Sandstrom PA: Oxidative stress as a mediator of apoptosis. Immunol Today 15: 7-10, 1994.
52. Droge W: Free radicals in the physiological control of cell function. Physiol Rev 82: 47-95, 2002.
53. Valko M, Rhodes CJ, Moncol J, Izakovic M and Mazur M: Free radicals, metals and antioxidants in oxidative stress-induced cancer. Chem Biol Interact 160: 1-40, 2006.
54. Potesil D, Petrlova J, Adam V, et al: Simultaneous femtomole determination of cysteine, reduced and oxidized glutathione, and phytochelatin in maize (Zea mays L.) kernels using high-performance liquid chromatography with electrochemical detection. J Chromatogr A 1084: 134-144, 2005.
55. Petrlova J, Mikelova R, Stejskal K, et al: Simultaneous determination of eight biologically active thiol compounds using gradient elution-liquid chromatography with Coul-Array detection. J Sep Sci 29: 1166-1173, 2006.
56. Sochor J, Ryvolova M, Krystofova O, et al: Fully automated spectrometric protocols for determination of antioxidant activity: advantages and disadvantages. Molecules 15: 8618-8640, 2010.
57. Laemmli UK: Cleavage of structural proteins during assembly of head of bacteriophage-T4. Nature 227: 680-685, 1970.
58. Merril CR, Dunau ML and Goldman D: A rapid sensitive silver stain for polypeptides in polyacrylamide gels. Anal Biochem 110: 201-207, 1981.
59. Krizkova S, Ryvolova M, Gumulec J, et al: Electrophoretic fingerprint metallothionein analysis as a potential prostate cancer biomarker. Electrophoresis 32: 1952-1961, 2011.
60. Volonte D, Galbiati F, Pestell RG and Lisanti MP: Cellular stress induces the tyrosine phosphorylation of caveolin-1 (Tyr(14)) via activation of p38 mitogen-activated protein kinase and c-Src kinase - Evidence for caveolae, the actin cytoskeleton, and focal adhesions as mechanical sensors of osmotic stress. J Biol Chem 276: 8094-8103, 2001.
61. Duplancic D, Kukoc-Modun L, Modun D and Radic N: Simple and rapid method for the determination of uric acid-independent antioxidant capacity. Molecules 16: 7058-7067, 2011.
62. Bartosz G: Non-enzymatic antioxidant capacity assays: limitations of use in biomedicine. Free Radic Res 44: 711-720, 2010.
63. Prior RL and Cao GH: In vivo total antioxidant capacity: comparison of different analytical methods. Free Radic Biol Med 27: 1173-1181, 1999.
64. Tahir SA, Ren CZ, Timme TL, et al: Development of an immunoassay for serum caveolin-1: a novel biomarker for prostate cancer. Clin Cancer Res 9: 3653-3659, 2003.
65. Nasu Y, Timme TL, Yang G, et al: Suppression of caveolin expression induces androgen sensitivity in metastatic androgen-insensitive mouse prostate cancer cells. Nat Med 4: 1062-1064, 1998.
66. Yang G, Truong LD, Wheeler TM and Thompson TC: Caveolin-1 expression in clinically confined human prostate cancer: a novel prognostic marker. Cancer Res 59: 5719-5723, 1999.
67. Tahir SA, Frolov A, Hayes TG, et al: Preoperative serum caveolin-1 as a prognostic marker for recurrence in a radical prostatectomy cohort. Clin Cancer Res 12: 4872-4875, 2006.
68. Thompson TC, Tahir SA, Li L, et al: The role of caveolin-1 in prostate cancer: clinical implications. Prostate Cancer Prostatic Dis 13: 6-11, 2010.
69. Watanabe M, Yang G, Cao GW, et al: Functional analysis of secreted caveolin-1 in mouse models of prostate cancer progression. Mol Cancer Res 7: 1446-1455, 2009.
70. Tahir SA, Yang G, Ebara S, et al: Secreted caveolin-1 stimulates cell survival/clonal growth and contributes to metastasis in androgen-insensitive prostate cancer. Cancer Res 61: 3882-3885, 2001.
71. Yang G, Truong LD, Timme TL, et al: Elevated expression of caveolin is associated with prostate and breast cancer. Clin Cancer Res 4: 1873-1880, 1998.
72. Thompson TC, Timme TL, Li L and Goltsov A: Caveolin-1, a metastasis-related gene that promotes cell survival in prostate cancer. Apoptosis 4: 233-237, 1999.
73. Li LK, Yang G, Ebara S, et al: Caveolin-1 mediates testosterone-stimulated survival/clonal growth and promotes metastatic activities in prostate cancer cells. Cancer Res 61: 4386-4392, 2001.
74. Mouraviev V, Li LK, Tahir SA, et al: The role of caveolin-1 in androgen insensitive prostate cancer. J Urol 168: 1589-1596, 2002.
75. Karam JA, Lotan Y, Roehrborn CG, Ashfaq R, Karakiewicz PI and Shariat SF: Caveolin-1 overexpression is associated with aggressive prostate cancer recurrence. Prostate 67: 614-622, 2007.

2.5   Cell mechanics assessment in the era of imaging

Taken together, our *in vivo* and patient-based [40] experiments indicate accordingly with literature that both prostate cells' mechanic phenotype, CAV1 signalling and zinc(II) regulation differ through prostate cancer progression. As metabolism and biomechanical hallmarks of prostatic tumors are unique, the specific interplay between these processes and specific regulatory mechanisms are expected. However, there are no clear conclusions regarding the necessity of these processes for cancerogenesis in the prostate as the evolutionary advantages and constraints of these metabolic and mechanical changes are not known. However, novel high-throughput high-resolution imaging techniques like QPI might be promising in the understanding of prostatic biomechanical phenotype. Moreover, because this technique enables direct visualisation of mitochondrial network and simultaneous multimodal fluorescence imaging, this approach might be suitable in the understanding of metabolic and mechanical interplay in prostate cancer cells.

Different methods to study cell mechanics are used nowadays with dramatically differing force profiles (AFM, real-time deformability, tensile biaxial stretching, traction-force microscopy, etc.) [18; 19]. For the most commonly used technique – AFM, the cell-cantilever contact is needed, causing distinct mechanical stress to cells [18] and making correlative imaging problematic and time-lapse experiments near-impossible. Thus, there is a growing interest in using non-invasive label-free optical methods to probe mechanical properties such as Brillouin microscopy [41-43] and quantitative phase imaging [2; 44; 45]. With this in mind, the combination of techniques or ideally correlative acquisition could provide new meta-information on cell mechanical properties.

However, these techniques differ in frequency scale of measurement and need different models to determine Young modulus. Absolute Young modulus values are therefore typically technique-dependent making the biological significance of the measured parameters still not fully understood [18]. Brillouin shift depends only on mechanical properties (i.e., the longitudinal modulus and the mass density) and is itself a mechanical property [43]. For modulus reconstruction, however, a correlative image of refractive index (n) is needed, further enabling to study how modulus scales with n in various cells/subcellular regions under various conditions.

2.5.1   Quantitative imaging provides physical specificity

Cells are optically thin objects. Therefore, it is challenging to generate intrinsic contrast in such objects [46] and contrast enhancement based on phase information is needed [47]. The downside

of contrast enhancement is an introduction of artefacts; phase contrast images contain halo and shade-off, differential image contrast introduces non-uniform shadow-cast artefacts [47]. In addition, the phase contrast image is an intensity distribution, in which the phase information is coupled nonlinearly and cannot be retrieved quantitatively [46].

Quantitative phase image, on the other hand, does not provide molecular specificity. Nevertheless, the label-free quantitative phase image is specific physically. Moreover, compared to the fluorescence image, the acquired data do not correspond to relative intensity range, but instead are quantitative by nature – data reconstructed from the holograms is represented in physical units – radians [48]. It therefore provides quantitative information about local thickness of the sample as well as about its refractive index. Nevertheless, molecular specificity is needed in biological experiments. With this regard, multimodal imaging was developed.

2.5.2   Multimodal correlative microscopy

Fluorescence microscopy is the most commonly used microscopic technique in the current biology. It provides molecular specificity in sample [49]. Quantitative phase imaging, although physically specific, lacks this specificity and this restricts broader use of this technique. To overcome this, multimodal approaches were developed, combining phase imaging with Raman spectroscopy [50], Brillouin spectroscopy [51], multispectral light sources [52], structural illumination microscopy [53], or with fluorescent imaging.

Such imaging of the sample with more complementary modalities combined creates new composite which is not just a combination of the two modalities, it provides additional meta-information about the sample. Specifically, the combination of quantitative phase imaging with fluorescent microscopy was demonstrated to benefit from a high spatial resolution of QPI together with molecular specificity of fluorescent staining [49]. Such benefit was shown in cell death classification and prediction [44; 45], analysis of cytoskeleton or cell movement [54; 55]. As the acquisition of QPI is fast, the generation of large datasets makes it possible to extract complex information from these datasets using advanced image analysis methods. For instance, machine learning has enabled the translation of qualitative and quantitative phase images into fluorescence images [48]. The possibilities of such approaches are discussed in the next chapter.

2.5.3   Artificial intelligence in biomedical image

During 2015-2020, deep learning algorithms have become methods of choice for biomedical image analysis [56]. Nowadays, these techniques are used for image classification (pathology

vs physiology), detection of objects (lesions, cells, organelles, or others), segmentation of regions of images (tissues, cells, subcellular regions), registration or other tasks. Most applications are observed in neurology, retinal images, chest X-ray imaging, and in digital pathology. The broadness of deep learning (DL) is evident for analysis of MRI brain images, where DL was deployed for disorder classification (Alzheimer disease, mild cognitive impairment, schizophrenia), segmentation of anatomical sites, detection of lesions (tumors, micro bleedings, lacunes), survival prediction, image enhancement [56].

Deep learning has been widely adopted also on retinal fundus images to classify diabetic retinopathy and retinopathy of prematurity, the glaucoma-like disc, macular oedema and age-related macular degeneration[57], showing performance similar to a panel of experts [56]. The tremendous potential of deep learning in the medical images can be evidenced by Poplin et al study also on retinal fundus images: The authors demonstrated it is possible to extract even gender, age or systolic blood pressure with remarkable accuracy just from retinal images – the parameters which are beyond the possibilities of human experts in the field [58]. While experts would annotate the gender based on fundus images with accuracy close to 50:50, the custom-designed DL network did so with area under curve (AUC) 0.97. Such results were made possible because of enormous dataset size – it was trained on data from 284,335 patients and validated on two independent datasets [58]. This example demonstrates that images contain patterns indiscernible by the human eye which can be advantageously extracted using machine-learning strategies.

The most commonly used network designs deployed on medical images are convolutional neural networks and recurrent neural networks. In medical images, the networks are used as "supervised", meaning that an expert manually annotates a portion of dataset used for training, which is then used for the network in the learning process (expert annotates tumor vs non-tumor zone, cell vs background, neutrophils vs macrophages, etc.). Of the convolutional neural network architectures, U-Net [59] is the most commonly used one for microscopic image cell detection, morphometry, or counting. Regardless of the architecture used, it still holds that the dataset size is a bottleneck for the network performance. If either image acquisition is slow or manual annotation by expert is time-consuming and introduces some level of subjectivity, the capabilities of the machine learning are untapped. Seen from cellular mechanobiology perspective, atomic force microscopy or Brillouin spectroscopy provide valuable data, but the acquisition speed of these methods is slow, roughly one field of view per tens of minutes. Due to the low throughput of these techniques, the deployment of contemporary machine learning techniques on such datasets is highly challenging.

New deep learning approaches – Variational autoencoder or Generative adversarial networks provide a great advantage – user annotation is not necessary. These architectures can mainly be deployed in data augmentation or in specific scenarios like shown in our study by Vicar et al. [60] discussed in a results section 4.2.2.

The deep learning neural networks are typically criticized to be uninterpretable black boxes, where researchers cannot deduce biological explanations that drive the machine decisions. This might not be an issue as approaches to overcoming this exist, as shown in Zaritsky et al study on classification of highly aggressive melanoma cells [61]. The authors "reverse-engineered" the neural network and *in silico* generated cell images based on machine-made classification decisions. In the other words, this approach was used to amplify cellular features of metastatic efficiency. These images unveiled pseudopodial extensions and increased light scattering as functional hallmarks of metastatic cells compared to non-metastatic ones [61]. In our Majercik et al. study [62] we performed a classification of highly aggressive prostate cancer cells based on quantitative phase imaging. In a similar way as performed by Zaritsky et al study, we generated "attention maps" of the cells to highlight the areas based on which the network decisions were made in order to avoid the "black box bias".

Machine learning is also suitable in the microscopic analysis of quantitative phase imaging. Specifically, it has been employed in quantitative phase imaging to overcome low molecular specificity of this technique [49]. Recently, deep learning has enabled the translation of qualitative and quantitative phase images into fluorescence images [48]. Such combination – when powered by AI – can enable diagnosis of diseases based on molecular specificity and morphology at single-cell level [49]. Machine learning was employed in image classification based on QPI data for cancer cells [63], red[64] and white blood cells[65], bacteria[66],[67] and others [68]. Such approaches open new avenues for biomedical research and diagnosis [49].

In this thesis, artificial intelligence was demonstrated to solve several tasks. It was shown to be powerful for image segmentation [47; 69-71] (chapter 4.1), cancer cells classification [62], extraction of features from quantitative phase image not visible by naked eye [60; 72] and thus enabled to explain the molecular specificity of a technique primarily showing biophysical and mechanical features of the cells. The aspects of deep learning in medical imaging are further discussed in Gumulec and Vicar book chapter [69].

3 Key points of the habilitation thesis

Papers presented in this thesis aim to address how cell mechanical properties change during the pathogenesis of prostate cancer on *in vitro* model and how it relates with other well-described tumor hallmarks – such as tumor metabolic state. As the existing mechanophenotyping methods are low-throughput, low-resolution and invasive, with atomic force microscopy as a typical example, the potential of label-free optical techniques was evaluated. It was furthermore investigated whether quantitative phase image contains data not evident by the naked eye, which can be deployed in aggressive cell classification. Finally, mechanisms underlying the altered mechanical and metabolic phenotype were studied. Specifically, the following hypotheses were addressed:

- Mechanics of the prostate cancer cells changes during cancer progression
- Quantitative phase imaging is suitable to describe biomechanical properties of cells
- There are patterns in quantitative phase maps of cancer cells which are not evident by the naked eye but underline the change of mechanical phenotype (that is, label-free quantitative phase image contains specific "meta-information").
- Caveolin-1 is involved in the mechanical and metabolic reprogramming of prostate cancer cells.

3.1 Key methods

Key methodological approaches are mentioned in this chapter. Details of these methods specific for particular experiments and more routine methods are in the Methods section of respective papers. The thesis lies on a combination of cellular and molecular biology techniques to describe cell features like migration rate, cell death or division, metabolomic techniques to describe cell metabolic states, microscopic techniques to acquire data, bioinformatic techniques for image analysis.

3.1.1 Imaging techniques

Multiple microscopic techniques were employed in this study to describe the physical and molecular properties of cells. These include contrast-enhancing live-cell label-free methods (phase

contrast, differential image contrast), quantitative phase imaging, atomic force microscopy, confocal and epifluorescence microscopy, and Brillouin spectroscopy. The details of these methods are explained in the Methods sections of the respective articles, while here, the principle and methodological details of crucial microscopic methods are described.

Quantitative phase imaging was performed on two designs of microscopes: coherence-controlled holographic microscope capturing 2D images of cell dry mass and optical diffraction tomography, acquiring 3D images of refractive index. For coherence-controlled holographic microscopy Q-PHASE (Telight, Brno) was used. Objectives Nikon Plan 10/0.30 were chosen. Holograms were captured by CCD camera (XIMEA MR4021 MC-VELETA). The entire image reconstruction and image processing were performed in Q-PHASE control software.

Refractive index tomograms were acquired on an optical diffraction tomography microscope with rotational scanning 3D Cell Explorer (Nanolive SA, Lausanne, Switzerland) with Nikon BE Plan 60x NA 0.8. The size of the acquired tomogram was 93.1×93.1×35.7 μm (xyz). Samples were measured in cell medium which refractive index was measured on digital refractometer DR201-95 (Krüss, Germany) and used as a reference. Software Steve 1.6.3496 (Nanolive SA) was used for image acquisition. Image processing and statistic techniques

Atomic force microscopy was performed on bioAFM microscope JPK NanoWizard 3 (JPK, Berlin, Germany) placed on the inverted optical microscope Olympus IX-81 (Olympus, Tokyo, Japan). The typical approach/retract settings were identical with a 15 μm extend/retract length, Setpoint value of 1 nN, a pixel rate of 2048 Hz and a speed of 30 μm/s. The system operated under closed-loop control. After reaching the selected contact force, the cantilever was retracted. The retraction length of 15 μm was sufficient to overcome any adhesion between the tip and the sample and to make sure that the cantilever had been completely retracted from the sample surface. Force-distance (FD) curve was recorded at each point of the cantilever approach/retract movement. The Young's modulus (E) was calculated by fitting the Hertzian-Sneddon model on the FD curves measured as force maps (64×64 points) of the region containing either a single cell or multiple cells. Soft uncoated AFM probes HYDRA-2R-100N (Applied NanoStructures, Mountain View, CA, USA), i.e., silicon nitride cantilevers with silicon tips are used for stiffness studies because they are maximally gentle to living cells (not causing mechanical stimulation).

3.1.2   Methods to study cell migration and invasiveness

To study aggressiveness, invasiveness and migration, a panel of assays was used. MTT was used to analyse the toxicity of selected inductors/inhibitors. Wound healing assay was performed to analyse migration speed. For this approach, cells were incubated for 24h after a formation of the wound in a fully confluent well. A ratio between the wound area in a time point 0 and 24 was used as an approach metric of migration. Migration was also measured in open area with low-density seeded cells and the individual cell migration was tracked using QPI. Cell growth and invasiveness were analysed in real-time on an impedance-based device (xCELLigence (Acea Biosystems, CA, USA). Colony-forming assays were performed mostly to determine cell reproductive death after cytotoxic treatment. In 6-well plates cells were seeded in a density ranging 100-2000 cells and after 1-3 weeks the number of colonies was calculated using an in-house software script.

4   Commentary to the articles

The key aim of this thesis is to link the prostate cancer cell mechanical properties with cancer cell metabolic reprograming and cancer cell aggressiveness - well-described tumor hallmarks. As discussed in the chapter 2.5.1, quantitative phase imaging has potential to describe the biomechanical properties of prostate cancer cells of varying aggressiveness and their connection to these cells' metabolism is investigated in this thesis. Therefore, first, bioinformatic strategies employing artificial intelligence in computer vision are designed to meaningfully extract features from the quantitative phase image suitable for mechanobiology. As these techniques were optimized and the potential of QPI was established in this field, its biological function was explained using traditional cell biological and molecular biological approaches. Finally, its linkage with changes in metabolic phenotype was described.

4.1   Image segmentation: an important step of image data processing

Computer vision in biomedical images is applicable for various tasks – detection of pathologic lesions, classification of tissue/cell types, and many others. Nevertheless, prior these tasks area of interest needs to be segmented from an unwanted background (e.g., tumor region and non-tumor region in hematoxylin-eosin slides, brain tissue from other tissues in MRI, cells from the surface in microscopy). Such task is a process which divides the image into several logical and meaningful areas.

Quantitative phase image is a new imaging modality. Therefore, no standardized image processing pipelines exist either for classification of such data, but also for its segmentation. Therefore, the following study by Vicar et al. [47] was designed, aiming to define optimal image segmentation pipeline. In addition, its "segmentability" was compared to routinely used label-free microscopy techniques – phase contrast microscopy, differential interference contrast microscopy, and Hoffman modulation contrast microscopy.

A three-step strategy was proposed in this study: First, areas of interest (cells) were separated from a background in a semantic segmentation step. In this first step, however, individual cells are not separated from each other. This separation is initiated in the following step – object detection. Based on semantic segmentation and object detection, individual cells can be successfully identified (instance segmentation).

This study provided us valuable conclusions important for further research: first, it confirmed the advantage of quantitative phase image over other contrast-enhancing label-free microscopy methods: QPI is artefact-free and is quantitative – meaning that similar structures (nucleoli, nuclei, mitochondria) have identical values (radians, or cell dry mass density) between experiments. In the other words, nuclei, nucleoli, and other structures are physically specific [41]. Due to these properties, the "segmentability" of QPI image is more accurate, facilitating further QPI data processing. Second, it was clearly demonstrated that machine-learning strategies dominate over traditional model-based approaches. Of note, no deep-learning strategies were employed, instead, networks with simpler architecture, random-forest based like Ilastik [73], Trainable Weka Segmentation [74] were tested in pipelines. For deep-learning strategies even higher levels of segmentation accuracy are expected and possible deep-learning based segmentation approaches are discussed in Gumulec et al. [69] book chapter.

For QPI, relatively simple strategies like thresholding followed by watershed were sufficient. However, a combination of Weka probability map segmented with Graph-cut [75], followed by object detection with generalized radial symmetry transform [76] and finally segmented by marker-controlled watershed [77] gives superior results. Segmentation pipelines proposed in this study were subsequently deployed on the following quantitative phase imaging workflows so data extraction from this technique can be standardized.

Despite Vicar et al [47] 2019 study demonstrated higher "segmentability" of objects (adherent cells) acquired by QPI over other microscopic techniques, it did not show the highest-possible segmentation scores for cells. That is because model-based techniques were used Therefore, in a following 2021 study [70] we aimed to increase the segmentation score for objects – cells – in a QPI microscopy image by use of deep-learning techniques. In order to remove inevitable features of deep learning, that is limited transferability to microscopic images (of cells) not used in the learning process, unique pipeline was designed. Non-deep learning transfer with adjustable parameters is used in the post-processing step. Additionally, we proposed a self-supervised pretraining technique using nonlabelled data of images of multiple cell types, which is trained to reconstruct multiple image distortions and improved the segmentation performance [70]. Because no manual annotation was necessary for this pre-training stage, large amounts of microscopic images (~ 2000) might be used in the network, that is an amount hardly feasible in a supervised, that is annotated, type of network. The proposed self-supervised pretraining method improved both segmentation performance and transferability to different cell types [70]. Nevertheless, despite these two approaches for QPI cell segmentation, the model-based one, as well as the deep-learning-based one were intended to segment whole cells. Therefore, an effort

was also given to segment subcellular elements, specifically nuclei and nucleoli. Another quantitative phase method, the optical diffraction tomography with 60x magnification was used in this aim. We have managed to distinguish between objects and background with average dice coefficients of 0.83, 0.78 and 0.63 for whole cells, nuclei and nucleoli respectively. Also in this step the pretraining further improved the segmentation performance especially for nuclei and nucleoli, 21% and 16% respectively [71].

VICAR, T., J. BALVAN, J. JAROS, F. JUG, et al. Cell segmentation methods for label-free contrast microscopy: review and comprehensive comparison. BMC Bioinformatics, June 28 2019, 20(1), 360.

BMC Bioinformatics

METHODOLOGY ARTICLE   **Open Access**

Cell segmentation methods for label-free contrast microscopy: review and comprehensive comparison

Tomas Vicar[1,2], Jan Balvan[3,4], Josef Jaros[6,7], Florian Jug[5], Radim Kolar[1], Michal Masarik[3,4] and Jaromir Gumulec[2,3,4*]

Abstract

Background: Because of its non-destructive nature, label-free imaging is an important strategy for studying biological processes. However, routine microscopic techniques like phase contrast or DIC suffer from shadow-cast artifacts making automatic segmentation challenging. The aim of this study was to compare the segmentation efficacy of published steps of segmentation work-flow (image reconstruction, foreground segmentation, cell detection (seed-point extraction) and cell (instance) segmentation) on a dataset of the same cells from multiple contrast microscopic modalities.

Results: We built a collection of routines aimed at image segmentation of viable adherent cells grown on the culture dish acquired by phase contrast, differential interference contrast, Hoffman modulation contrast and quantitative phase imaging, and we performed a comprehensive comparison of available segmentation methods applicable for label-free data. We demonstrated that it is crucial to perform the image reconstruction step, enabling the use of segmentation methods originally not applicable on label-free images. Further we compared foreground segmentation methods (thresholding, feature-extraction, level-set, graph-cut, learning-based), seed-point extraction methods (Laplacian of Gaussians, radial symmetry and distance transform, iterative radial voting, maximally stable extremal region and learning-based) and single cell segmentation methods. We validated suitable set of methods for each microscopy modality and published them online.

Conclusions: We demonstrate that image reconstruction step allows the use of segmentation methods not originally intended for label-free imaging. In addition to the comprehensive comparison of methods, raw and reconstructed annotated data and Matlab codes are provided.

Keywords: Microscopy, Cell segmentation, Image reconstruction, Methods comparison, Differential contrast image, Quantitative phase imaging, Laplacian of Gaussians

Background

Microscopy has been an important technique for studying biology for decades. Accordingly, fluorescence microscopy has an irreplaceable role in analyzing cellular processes because of the possibility to study the functional processes and morphological aspects of living cells. However, fluorescence labeling also brings a number

of disadvantages. These include photo-bleaching, difficult signal reproducibility, and inevitable photo-toxicity (which results not only from staining techniques but also from transfection) [1]. Label-free microscopy techniques are the most common techniques for live cell imaging thanks to its non-destructive nature, however, due to the transparent nature of cells, methods of contrast enhancement based on phase information are required.

The downside of contrast enhancement is an introduction of artifacts; Phase contrast (PC) images contain halo and shade-off, differential image contrast (DIC) and Hoffman Modulation Contrast (HMC) introduce non-uniform

*Correspondence: j.gumulec@med.muni.cz
[2]Department of Physiology, Faculty of Medicine, Masaryk University, Kamenice 5, CZ-62500 Brno, Czech Republic
[3]Department of Pathological Physiology, Faculty of Medicine, Masaryk University, Kamenice 5, CZ-62500 Brno, Czech Republic
Full list of author information is available at the end of the article

shadow-cast artifacts (3D-like topographical appearance). Although various segmentation procedures have been developed to suppress these artifacts, a segmentation is still challenging.

On the other hand, quantitative phase imaging (QPI), provides artifact-free images of sufficient contrast. Although there are no standardized methods for the segmentation of QPI-based images, fundamental methods for segmentation of artifact-free images (e.g. from fluorescence microscopy) will be utilized.

In this review, we describe and compare relevant methods of the image processing pipeline in order to find the most appropriate combination of particular methods for most common label-free microscopic techniques (PC, DIC, HMC and QPI). Our aim is to evaluate and discuss the influence of the commonly used methods for microscopic image reconstruction, foreground-background segmentation, seed-point extraction and cell segmentation. We used real samples - viable, non-stained adherent prostatic cell lines and captured identical fields of view and cells manually segmented by a biologist. Compared to microscopic organisms like yeast or bacteria, adherent cells are morphologically distinctly heterogeneous and in label-free microscopy, the segmentation is therefore still a challenge. We will use the most common imaging modalities used by biologist and we will provide a recommendation of image processing pipeline steps for particular microscopic technique.

The segmentation strategies tested herein are selected to provide the most heterogeneous overview of recent state of the art excluding the simplest and outdated methods (e.g. simple connected component detection, ultimate erosion, distance transform without h-maxima etc.). Deep-learning strategies are intentionally not included due to their distinct differences, high demands on training data and the range of possible settings (training hyperparameters, network architecture, etc.).

Results

In the paragraphs below we provide a detailed summary of each image processing step from the pipeline (see Fig. 1), followed by short description of achieved results. We start with description of "all-in-one" tools and continue with image reconstruction, foreground-background segmentation, cell detection and final single cell segmentation (i.e. instance segmentation).

Due to the large number of tested methods and approaches, we have decided to introduce a specific designation of the methods. We used prefix in order to refer to image reconstruction ('r'), foreground-background segmentation ('s') and cell detection ('d') and finally to all-in-one tools ('aio'). The list of these designations, number of parameters to be adjusted in these methods and computational demands are provided in Table 1.

"All-in-one" tools

First, we performed an analysis with the available commercial and freeware "all-in-one" tools including FARSIGHT [2], CellX [3], Fogbank [4], FastER [5], CellTracer [6], SuperSegger [7], CellSerpent [8], CellStar [9], CellProfiler [10] and Q-PHASE' Dry mass guided watershed (DMGW) [11]. As shown in Table 2 the only algorithm providing usable segmentation results for raw images is Fogbank, which is designed to be an universal and easy to set segmentation tool. Very similar results were provided by CellProfiler, which is easy to use tool allowing to crate complete cell analysis pipelines, however, it works sufficiently only for reconstructed images. The QPI' dedicated DMGW provided exceptional results, but for this microscopic technique only. The remaining methods did not provide satisfactory results on label free data; FastER, although user-friendly, failed because of the nature of its maximally stable extremal region (MSER) detector. FARSIGHT failed with the automatic threshold during foreground segmentation. CellX failed in both the cell detection with gradient-based Hough transform and in the membrane pattern detection because of indistinct cell borders. The remaining segmentation algorithms - CellStar, SuperSegger, CellSerpent - were completely unsuitable for label-free non-round adherent cells with Dice coefficient < 0.1 and thus are not listed in Table 2 and Fig. 4.

Because of the low segmentation performance of the examined "all-in-one" methods, we decided to divide the segmentation procedure into four steps - (1) image reconstruction (2) background segmentation, (3) cell detection (seed expansion) and (4) segmentation tailored to the specific properties of individual microscopic techniques (see Fig. 1).

Image reconstruction

As shown, the performance of most "all-in-one" methods is limited for label-free data, in particular due to the presence of contrast-enhancing artifacts in microscopic images. Image reconstruction was therefore employed to reduce such artifacts. Methods by Koos [12] and Yin [13] (further abbreviated rDIC-Koos and rDIC-Yin, respectively) were used for DIC and HMC images. Images of PC microscopy were reconstructed by Top-Hat filter involving algorithm by the Dewan [16] (rPC-TopHat), or Yin method (rPC-Yin) [14].

Generally, following conclusions apply for image reconstructions:

- No distinctive differences in image reconstruction efficacy were observed between the microscopic methods apart from QPI, as shown in Fig. 2 (described by area under curve, AUC, see Methods for details).
- The AUC of QPI was distinctly higher with values near 0.99

Fig. 1 Block diagram showing segmentation approach. For details of individual steps, see Results and Materials and Methods.EGT, empirical gradient treshold; LoG, Laplacian of Gaussians, DT, distance transform, MSER maximally stable extremal region
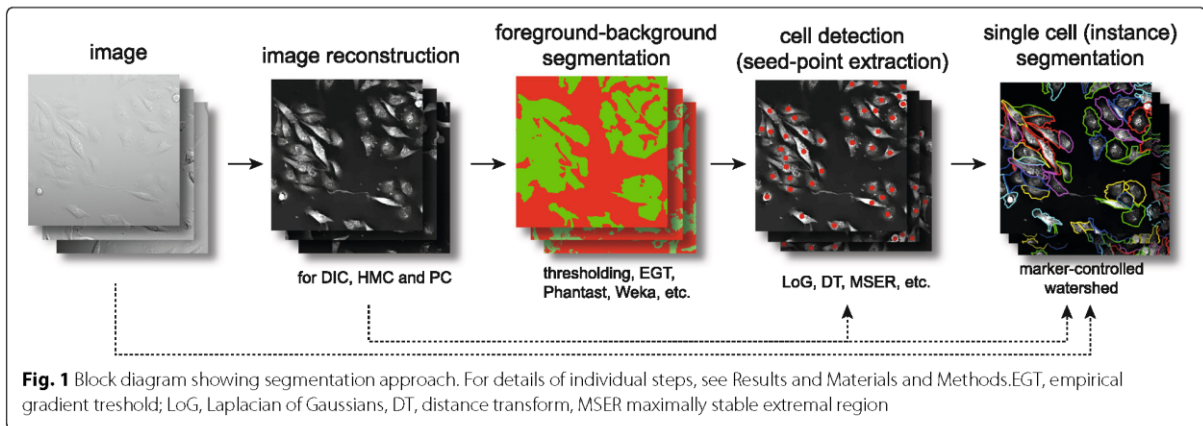
- Computationally more-demanding methods (rDIC-Koos and rPC-Yin) perform better except for relatively simple rPC-Top-Hat, which provides similar results
- Probability maps generated by sWeka or sIllastik can be used like reconstructions in later segmentation steps. The advantage of this approach is the absence of the need to optimize parameters.

DIC and HMC reconstructions
With regard to the morphology of reconstructed images, rDIC-Koos provides a detailed structure of the cells with distinctive borders from the background. For rDIC-Yin [13], details of the reconstructed cells are more blurred and uneven background with the dark halos around the cells (see Fig. 2) complicating the following segmentation. As a result, AUC of rDIC-Yin was distinctly lower as compared with the others.

Both rDIC-Koos [12] and rDIC-Yin [13] methods work on the principle of minimizing their defined energy function. The main difference is that better-performing Koos [12] uses l1-norm (instead of l2) for sparse regularization term. Yin's l2-norm, on the other hand, enables derivation of closed form solution, which is much simpler and thus faster to compute. Time needed for the reconstruction is dramatically different - 2.1 s, 36.6 min, 13.1 min and 0.17 s for rDIC-Koos, rDIC-Yin, rPC-Koos and rPC-TopHat, respectively. rDIC-Koos also introduces a parameter for the number of iterations, which is however insensitive within the tested range.

Although these methods were not designed for use on HMC images, the same conclusions also apply for the reconstruction of those images, which showed only slightly worse results. The results of reconstruction accuracy can be seen in Fig. 2. Combinations of the best-performing parameters are listed in the Additional file 1.

Phase contrast reconstruction
From the perspective of cellular morphology of reconstructed images, rPC-TopHat creates artifacts between closely located cells with the borders precisely distinguishable. Reconstruction based on rPC-Yin [14] causes an even background without observable artifacts around the cells, however cell borders are missing and mitotic cells are not properly reconstructed (see Fig. 2).

The optimization of the PSF parameters of rPC-Yin reconstruction is problematic. The PSF parameters of a particular microscope are not always listed or known. Searching for these parameters with optimization proved to be complicated. Because the optimizing function is not smooth and contains many local local extrema, the result changes significantly and chaotically even with a small change of parameters or, at the same time, combinations of parameter settings give very similar (near optimal) results.

Regarding the computational times, the rPC-Yin reconstruction works very similarly as the rDIC-Koos approach for DIC, with similar computational difficulties. The result of a simple top-hat filter unexpectedly turned out to be comparable to the complex and computationally difficult rPC-Yin method. For the reconstruction performance see Fig. 2, for optimal parameter setting see the Additional file 1.

Foreground-background segmentation
In the next step of the workflow, the image foreground (cells) was segmented from the image background. Both unprocessed and reconstructed images were used. Following strategies were used for the foreground-background segmentation: (a) Thresholding-based methods: simple threshold (sST), automatic threshold based on Otsu et al. [17] (sOtsu), and Poisson distribution-based treshhold (sPT) [2], (b) feature-extracting strategies: empirical gradient threshold (sEGT) [18] and approaches specific for PC microscopy by Juneau et al. (sPC-Juneau) [19], Jaccard et al. (sPC-Phantast) [21], and Topman (sPC-Topman) [20]), (c) Level-Set-based methods: Castelles et al. [22] (sLSCaselles), and Chan-Vese et al. [23] (sLS-

Table 1 List of tested segmentation methods and all-in-one segmentation tools and definition of abbreviations

Segmentation step	Abbreviation	Description	Setable parameters	Computational time	Ref.
All in one tools					
	aioFasright	Nucleus editor of Farsight toolkit	N/A	4.96 s	[2]
	aioCellX	segmentation, fluorescence quantification, and tracking tool CellX	N/A	10.30 s	[3]
	aioFogbank	single cell segmentation tool FogBank according Chalfoun	N/A	12.00 s	[4]
	aioFastER	fastER - user-friendly tool for ultrafast and robust cell segmentation	N/A	0.42 s	[5]
	aioCellProfiler	tool for cell analysis pipelines including single cell segmentation	N/A	11.8 s	[10]
	aioDMGW	Dry mass-guided watershed method, (Q-PHASE, Tescan)		1.00 s	
Reconstruction					
	rDIC-Koos	DIC/HMC image reconstruction according Koos	2	36.60 min	[12]
	rDIC-Yin	DIC/HMC image reconstruction according Yin	2	2.10 s	[13]
	rPC-Yin	PC image reconstruction according Yin	4	13.10 min	[14]
	rPC-Tophat	PC image reconstruction according Thirusittampalam and Dewan	1	0.17 s	[15, 16]
Foreground-background segmentation					
	sST	simple thresholding	1	< 0.01 s	
	sOtsu	thresholding using Gaussian distribution	0	<0.01 s	[17]
	sPT	thresholding using Poisson distribution	0	<0.01 s	[2]
	sEGT	empirical gradient threshold	3	0.24 s	[18]
	sPC-Juneau	Feature extraction approach according Juneau	3	0.26 s	[19]
	sPC-Topman	Feature extraction approach according Topman	4	0.35 s	[20]
	sPC-Phantast	Phantast toolbox developed by Jaccard	5	0.35 s	[21]
	sLS-Caselles	Level-set with edge-based method	2	31.40 s	[22]
	sLS-ChanVese	Level-set with region-based method	2	11.10 s	[23]
	sGraphCut	Graph-Cut applied on recosntructed and raw data	2	15.80 s	[24]
	sWekaGraphCut	Graph-Cut applied on probability maps generated by Weka	2	31.80 min**	[24]
	sIlastikGraphCut	Graph-Cut applied on probability maps generated by Ilastik	2	31.52 min**	[24]
	sIlastik	machine learning tool by Sommer	N/A	31.20 min+21 s*	[25].
	sWeka	machine learning tool by Arganda-Carreras	N/A	27.60 min+2.20 min*	[26]
Cell detection (seed-point extraction)					
	dLoGm-Peng	multiscale LoG by Peng	4	3.60 s	[27]
	dLoGm-Kong	multiscale LoG by Kong	5	4.20 s	[28]
	dLoGg-Kong	generalized LoG filter by Kong	2	46.40 s	[28]
	dLoGg-Xu	generalized LoG filter by Xu	3	5.10 s	[29]

Table 1 List of tested segmentation methods and all-in-one segmentation tools and definition of abbreviations (*Continued*)

Segmentation step	Abbreviation	Description	Setable parameters	Computational time	Ref.
	dLoGh-Zhang	Hessian analysis of LoG images by Zhang	1	8.90 s	[30]
	dFRST	fast radial-symmetry transform	5	153.10 s	[31]
	dGRST	generalized radial-symmetry transform	5	572.30 s	[32]
	dRV-Qi	radial voting methods by Qi et al.	5	95.00 s	[33]
	dDT-Threshold	distance transform by Thirusittampalam, threshold-generated foreground	4	0.11 s	[15]
	dDT-Weka	distance transform by Thirusittampalam, sWeka-generated foreground	3	0.11 s‡	[15]
	dMSER	maximally stable extremal region method (MSER)	3	2.10 s	[34]
	dCellDetect	machine learning method based on MSER	1	141.70 s/60.20 s*	[35]
Single cell (instance) segmentation					
	MCWS†	Marker-conttrolled watershed	0	1.40 s	
	MCWS-dDT†	Marker-conttrolled watershed on DT image	0	1.41 s	

For detailed list of optimized parameters see Additional file 1. * computational time for learning based approaches indicated as two values for learning and classification. ** computational time for Weka+Graph cut combination shown as sum time of these methods. ‡ not includes time for Weka probability map creation, † indicate final segmentation step following foreground-background segmentation and seed-point extraction. Number of parameters in "all-in-one" approaches not shown because of the GUI-based nature, similarly, not shown for learning-based approaches, see Methods section for details. Computational time shown for one 1360×1024 DIC field of view

ChanVese), (d) Graph-cut [24], and (e) Learning-based Ilastik [25], and Trainable Weka Segmentation [26].

Based on the obtained results, this step can be considered the least problematic in segmentation, with the following general findings:

- Well-performing methods (e.g. sWeka, sIllastik, sLS-Caselles,sEGT, sPC-Juneau) are robust enough to work even on unreconstructed data.
- Image reconstruction improves foreground-background segmentation efficacy and once reconstructed, there are no distinct differences in segmentation efficacy between microscopic techniques
- QPI performs dramatically better even unreconstructed
- Learning-based methods (sWeka and sIlastik) perform better by a few units of percents. Its performance can further be improved with GraphCut.
- More time-consuming methods (sLS-Caselles, sLS-ChanVese, sGraphCut, sWeka, sIlastik) does not necesarily provide better results. For detailed results, see chapters below and Fig. 3.

Threshold-based approaches

The Simple threshold (sST) provides better results than automatic thresholding techniques assuming Poisson distribution (sPT) or Otsu method (sOtsu). The potential of these automatic techniques lies in the segmentation of images, where optimal threshold value varies between the images. However, this is not necessary for QPI images (constant background value increases success of sST) and for reconstructed images with background removal (background values are close to zero, so the histogram cannot be properly fitted with Gaussian or Poison distribution, see Table 2). There are not any parameters to optimize for sOtsu and sPT methods, which is the main advantage. The results of thresholding could be potentially improved by morphological adjustments. Regarding the computational times, these are the simplest and thus the fastest possible methods, which are listed mainly to provide basic idea about the segmentability of our data.

Feature-extraction-based approaches

The feature-based approaches - sEGT, sPC-Topman, sPC-Phantast and sPC-Juneau are all mainly based on the extraction of some feature image, which is then thresholded and morphologically modified. Because of feature thresholding strategies, the segmentation is possible without the image reconstruction. Thus these methods are among the most straightforward approaches to extract and threshold some local features (e.g. absolute value of gradient or local standard deviation).

All these methods can be easily adjusted, have the same number of parameters and the segmentation performance is very similar (see Table 1) with slightly better-performing sEGT. Compared to the other feature-extraction-based methods, sEGT includes elimination of small holes.
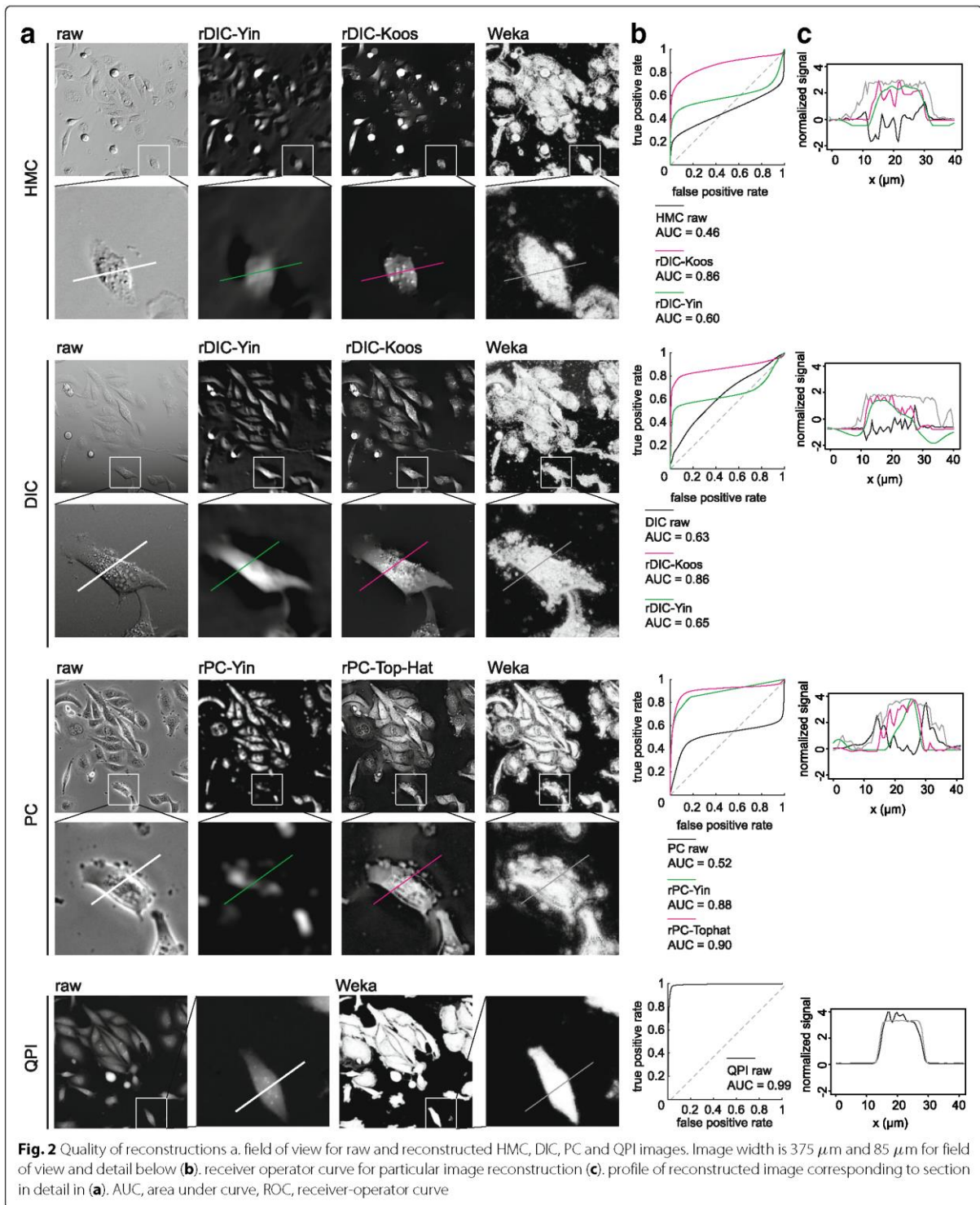
Table 2 The segmentation efficacy (shown as Dice coefficient) of individual segmentation steps on raw and reconstructed image data

Method	Segmentation efficacy (Dice coefficient)									
	QPI	DIC			HMC			PC		
	raw	raw	rDIC Koos [12]	rDIC Yin [13]	raw	rDIC Koos [12]	rDIC Yin [13]	raw	rPC Yin [14]	rPC TopHat [15]
Foreground-background segmentation										
sWekaGraphCut	0.96	0.86	0.89	0.84	0.86	0.84	0.84	0.86	0.80	0.84
sIllastikGraphCut	0.94	0.87	0.89	0.84	0.87	0.84	0.84	0.80	0.80	0.84
sWeka	0.94	0.85	0.87	0.80	0.85	0.82	0.79	0.81	0.72	0.81
sIlastik	0.94	0.85	0.86	0.80	0.82	0.82	0.79	0.84	0.72	0.82
sLS-Caselles	0.88	0.83	0.82	0.79	0.84	0.79	0.79	0.77	0.75	0.79
sEGT	0.89	0.88	0.85	0.64	0.86	0.79	0.70	0.74	0.68	0.79
sPC-Phantast	N/A	N/A	N/A	N/A	N/A	N/A	N/A	0.77	N/A	N/A
sPC-Juneau	0.85	0.85	0.84	0.59	0.82	0.77	0.69	0.73	0.72	0.76
sPC-Topman	N/A	N/A	N/A	N/A	N/A	N/A	N/A	0.72	N/A	N/A
sLS-ChanVese	0.61	0.48	0.74	0.55	0.68	0.67	0.36	0.64	0.65	0.76
sGraphCut	0.92	0.38	0.78	0.64	0.32	0.59	0.58	0.40	0.70	0.74
sST	0.92	0.339	0.76	0.61	0.31	0.72	0.53	0.40	0.69	0.73
sPT	0.83	0.34	0.60	0.34	0.30	0.46	0.08	0.29	0.67	0.73
sOtsu	0.62	0.34	0.36	0.31	0.28	0.16	0.18	0.24	0.51	0.66
Cell detection (seed point extraction)										
dGRST	0.94	0.65	0.79	0.85	0.75	0.81	0.85	0.81	0.77	0.88
dLoGm-Kong	0.90	0.83	0.90	0.86	0.72	0.84	0.85	0.52	0.69	0.78
dFRST	0.94	0.58	0.78	0.82	0.70	0.78	0.82	0.82	0.74	0.88
dLoGm-Peng	0.89	0.71	0.86	0.78	0.69	0.83	0.86	0.51	0.73	0.84
dLoGg-Kong	0.85	0.83	0.80	0.84	0.74	0.82	0.83	0.43	0.72	0.79
dDT-Weka	0.81	0.68	0.81	0.74	0.73	0.72	0.75	0.80	0.76	0.78
dLoGg-Xu	0.84	0.77	0.80	0.80	0.65	0.81	0.78	0.52	0.71	0.78
dDT-Threshold	0.94	0.26	0.91	0.86	0.54	0.86	0.84	0.49	0.76	0.81
dRV-Qi	0.77	0.61	0.57	0.58	0.70	0.48	0.48	0.82	0.59	0.65
dMSER	0.93	0.06	0.55	0.58	0.29	0.82	0.69	0.65	0.79	0.68
dCellDetect	0.92	0.00	0.88	0.89	0.00	0.83	0.84	0.00	0.71	0.81
dLoGh-Zhang	0.82	0.13	0.52	0.64	0.25	0.63	0.65	0.49	0.70	0.61
Single cell (instance) segmentation										
MCWS-dDT†	0.77	0.58	0.66	0.61	0.47	0.54	0.55	0.52	0.37	0.62
MCWS†	0.82	0.55	0.69	0.63	0.26	0.54	0.53	0.41	0.39	0.60
aioFogbank	0.71	0.54	0.55	0.42	0.44	0.38	0.39	0.46	0.34	0.19
aioCellProfiler	0.69	0.37	0.55	0.38	0.19	0.45	0.27	0.09	0.41	0.54
aioDMGW	0.82	0.08	0.62	0.38	0.00	0.48	0.29	0.10	0.39	0.65
aioFasright	0.21	0.15	0.43	0.00	0.00	0.26	0.14	0.03	0.37	0.57
aioCellX	0.34	0.03	0.08	0.21	0.02	0.18	0.05	0.07	0.03	0.16
aioFastER	0.09	0.03	0.07	0.00	0.02	0.17	0.01	0.25	0.08	0.06

Sorted by Dice coefficient (high to low). N/A, not applicable, for foreground background segmentation, methods designated for PC image were not deployed on other microscopic modalities

The performance of feature-extraction methods is technique-dependent with the highest scores for DIC and QPI and the lowest (but still high) for PC. This is mostly due to halos in PC; although sPC-Topman and sPC-Phantast are extended by the elimination of PC artifact regions, sPC-Topman have even worse results

Fig. 2 Quality of reconstructions a. field of view for raw and reconstructed HMC, DIC, PC and QPI images. Image width is 375 μm and 85 μm for field of view and detail below (**b**). receiver operator curve for particular image reconstruction (**c**). profile of reconstructed image corresponding to section in detail in (**a**). AUC, area under curve, ROC, receiver-operator curve

than sEGT or sPC-Juneau and sPC-Phantast leads to a slight improvement only for a cost of more parameters to be set.

From feature thresholding methods, sEGT was shown to be the best with only a small number of parameters and great versatility. Because of its percentile based threshold,

Fig. 3 Foreground-background segmentation step. **a** representative images showing tested foreground-background segmentation methods of rDIC-Koos-reconstructed DIC image. Dependency between area used for training and Dice coefficient for learning-based approach Ilastik (**b**) and Weka (**c**). scalebar indicates 50 μm
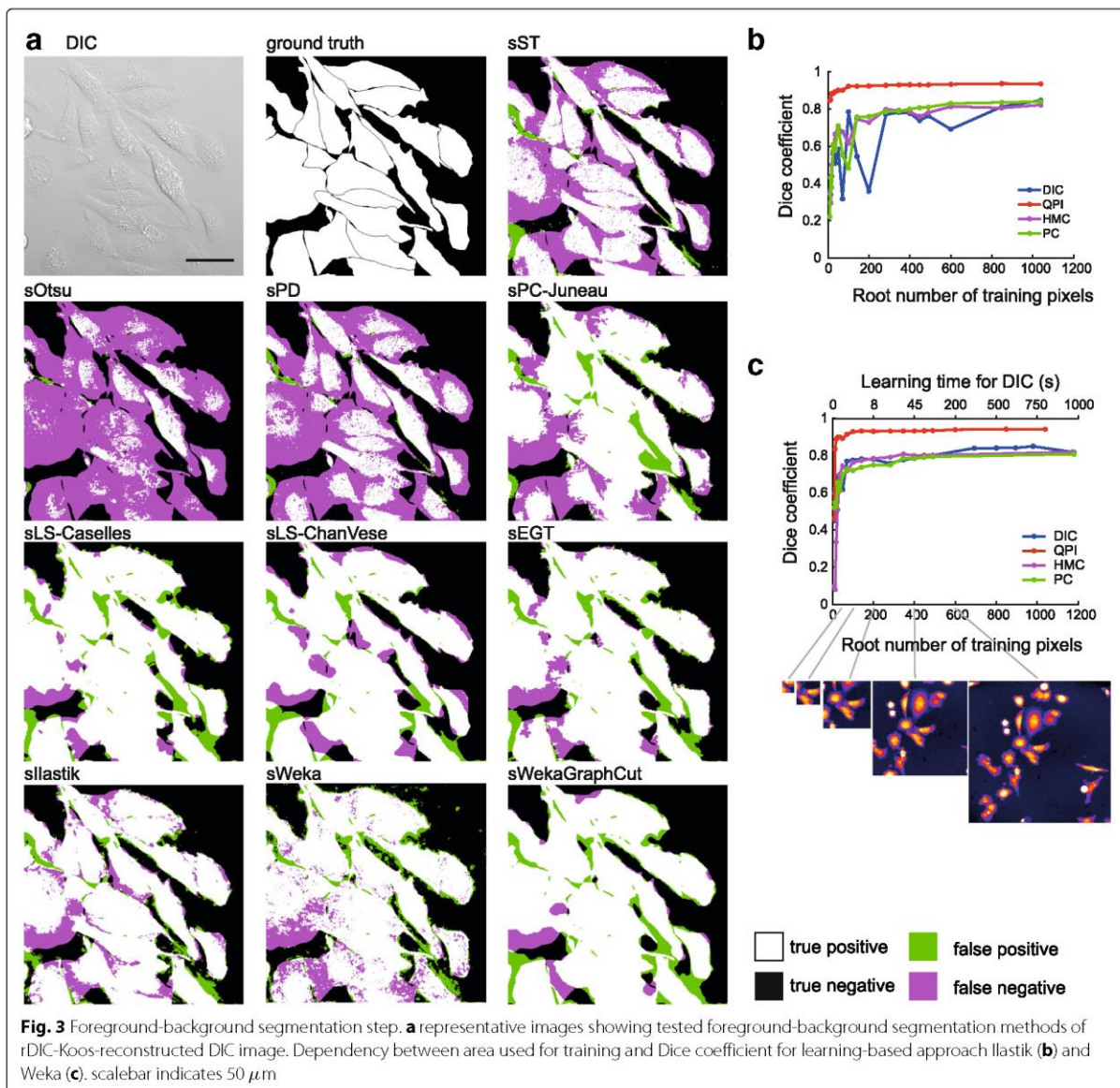
it can be used even with a default setting, which achieves e.g. 0.84 Dice coefficient value for QPI. Compared to threshold-based methods, feature-extraction strategies perform approximately 10% better. Considering the computational demands, these methods are very simple and fast - comparable to simple thresholding.

Level-set-based approaches
Both sLS-Caselles [22] and sLS-ChanVese [23] active contours tended to shrink too much, which was compensated by setting additional force to negative sign, which leads to a tendency of the contour to grow. The increase of the

additional force leads to a better Dice coefficient value until a breaking point, after which it leads to the total divergence of the contour. Still, the value of additional force had a much greater influence than the smoothness parameter.

Compared to the above-mentioned foreground-background segmentation strategies, the level-set based methods are relatively complicated and computationally difficult (tens of seconds vs. less than 1 s per FOV, Table 1). In their basic forms, two parameters are needed to be set. Another great disadvantage is that proper initialization is required, mainly the sLS-Caselles method

is very sensitive to initialization. Based on segmentation results, sLS-ChanVese is applicable on reconstructed images only, and does not even reach the segmentation efficacy of simple threshold results. On the other hand, sLS-Caselles is applicable on raw images, but only for PC images it surpasses the otherwise much faster sEGT.

Graph-cut
There is a large number of methods and modifications based on Graph-Cut. Herein, we tested the basic model only. When Graph-cut was employed on the reconstructed images (sGraphCut), the highest Dice coefficient was obtained among non-trainable approaches except for rPC-Tophat, being surpassed by sLS-ChanVese. Nevertheless, Graph-Cut does not outperform simple threshold dramatically, providing roughly 2% increase in Dice coefficient and is only suitable for reconstructed data.

Regarding differences between microscopic methods, the Graph-cut approach was most suitable for reconstructed DIC images, followed by PC and HMC. Regarding the computational times, this method performs similarly as the level-set-based strategies (tens of seconds per FOV - Tables 1 and 2). Optimized values are shown in Additional file 1.

Trainable approaches
Trainable Weka segmentation (sWeka) and Ilastik (sIlastik) were employed in this step. Similarly to the feature-extracting approaches, these are applicable on raw, unreconstructed data. Both sIlastik and sWeka outperformed all tested foreground-background segmentation methods with Dice coefficient up to 0.94 for QPI and up to 0.85 for DIC, HMC and PC.

Regardless of the imaging modality used, there was an identifiable "breakpoint" in the dependency between the area size used for learning and the segmentation efficacy after which no dramatic increase in Dice coefficient was observed, see Fig. 3. For DIC, PC, and HMC it was approx. at the size 70×70 px., for QPI, distinctly smaller area was necessary, approx. 25×25 px. These areas roughly correspond to the cell size. However, to demonstrate the theoretical maximum of this method and to compare it with Ilastik, learning from one whole FOV for DIC, HMC, and PC and from 3 FOVs for QPI was deployed (see Table 2.

Next, an effect of learning from one continuous area in one FOV, or smaller patches of same sizes from multiple FOVs was tested. On DIC data it was demonstrated that learning from multiple areas causes significant, but slight 2% increase increase in Dice coefficients.

No increase of Dice coefficient was observed when different filters were enabled apart from the set of default ones ("default" vs "all") as well as changing of minimum/maximum sigma. This was tested with a random search approach and with the Dice coefficient varying ±0.01. Both Weka and Ilastik provide almost the same segmentation results and are identically time-demanding.

There are two parameters to be optimized: terminal weights and edge weight. Edge weight (designated as "smoothness" in the GUI, range 0-10) reflects a penalty for label changes in the segmentation (higher values cause smoother result).

Furthermore, probability maps generated by sWeka and Ilastik under optimal settings were exported and these maps were further segmented by Graph-Cut (sWekaGraphCut/sIlastikGraphCut) and optimized in a same manner as sGraphCut on reconstructed data. A slight increase of the segmentation efficacy caused the sWekaCraphCut/sIlastikCraphCut combination to be the most efficient foreground-background segmentation method for QPI, HMC, and PC, only being surpassed by EGT on raw DIC image data. More importantly, this was achieved without the need of the image reconstruction.

Cell detection (seed-point extraction)
Once the foreground (cells) is separated from the background, the next step is to identify individual cells (seed points). The following strategies were used: (a) Cell shape-based, Laplacian of Gaussian (LoG) variants Peng et al. [27] (dLoGm-Peng), Kong et al.[28] (dLoGm-Kong), Hessian Zhang et al.[30] (dLoGh-Zhang), generalized Kong et al. [28] (dLoGg-Kong), generalized Xu et al. [29] (dLoGg-Xu), (b) Cell shape-based, generalized radial symmetry transform [32] (dGRST), fast radial symmetry transform [31] (dFRST), (c) Qi et al.[33] radial voting (dRV-Qi), (d) distance transform [15] (dDT-Threshold, dDT-Weka), (e) Maximally Stable Extremal Region [34] (dMSER), and (f) dCellDetect [35]. Following general conclusions are applicable for this segmentation step:

- Seed-point extraction is crucial step of cell segmentation
- The requirement of reconstructed images is a significant bottleneck of the seed-point extraction
- multiscale and generalized LoG are among the most robust and to some extent work also on unreconstructed data
- Radial symmetry transform-based strategies perform well
- Seed-point extraction is exceptional on QPI data
- Learning-based approach dCellDetect provide exceptional results on reconstructed data.

Laplacian of Gaussian-based strategies
Multiscale LoG filters (dLoGm-Peng and dLoGm-Kong) perform similarly as generalized versions (dLoGg-Kong

and dLoGg-Xu), but Hessian-based LoG (dLoGh-Zhang) were significantly worse in some cases. As for the traditional microscopic methods, LoG approaches enables the highest achievable segmentation efficacy. It was found out that particular combinations of reconstruction-LoG filter perform better than others; an optimal reconstruction-seed-point extraction combination is rDIC-Koos followed by dLoGm-Peng for DIC, rDIC-Koos plus dLoGm-Kong for HMC, and rPC-Tophat plus dLoGm-Peng for PC. Moreover, there were dramatic differences in cell detection between QPI and the remaining contrast-enhancing microscopic methods. On the other hand, there were no differences with Dice coefficient 0.9 for both QPI and DIC with dLOGm-Kong (Fig. 4).

Hessian variant dLoGh-Zhang achieved low segmentation efficacy on our samples of adherent cells (of various sizes) due to the use of one estimated optimal kernel size only (see Table 2). dLoGg-Kong originally completely fails for some modalities due to the wrong cell size estimation caused by sub-cellular structures, which produce higher signal then cells. This was eliminated by introducing a new σ_{min} parameter, limiting the lower scale.

Regarding the computational times, LoG-based are among faster techniques, being surpassed only by the distance transform.

Radial symmetry transform-based strategies

Compared to the computationally-simple LoG-based techniques, the dFRST [31] and generalized dGRST [32] provide better results for unreconstructed QPI images and, notably, for unreconstructed HMC and PC images. On reconstructed data, a possible application is for PC data with results very close to QPI segmentation. Nevertheless, computational times in the orders of hundreds of seconds need to be taken into account.

Radial voting

Radial voting (dRV-Qi) approach [33] does not achieve the results of fast LoG-based strategies for all microscopic modalities, either raw or reconstructed, while being computationally comparable to radial symmetry transform-based approaches. Thus, it is considered not suitable for such data.

Distance transform

The strong advantage of the distance transform [15] is its speed, which is the highest among other seed-point extraction strategies. Segmentation efficacy of the tested version with optimal thresholding (dDT-Threshold) is the highest among all microscopies except for PC, but image reconstruction is needed. An alternative approach is to use WEKA for binary image generation (dDT-Weka), where cells are less separated than in a case of optimal threshold.

Maximally stable extremal region

Compared to the relatively consistent performance of LoG between microscopic techniques, the dMSER approach [34] is distinctly more suitable for HMC reconstructed by rDIC-Koos and PC reconstructed by rPC-Yin, where the segmentation performance as well as computational requirements are identical or similar to LoG.
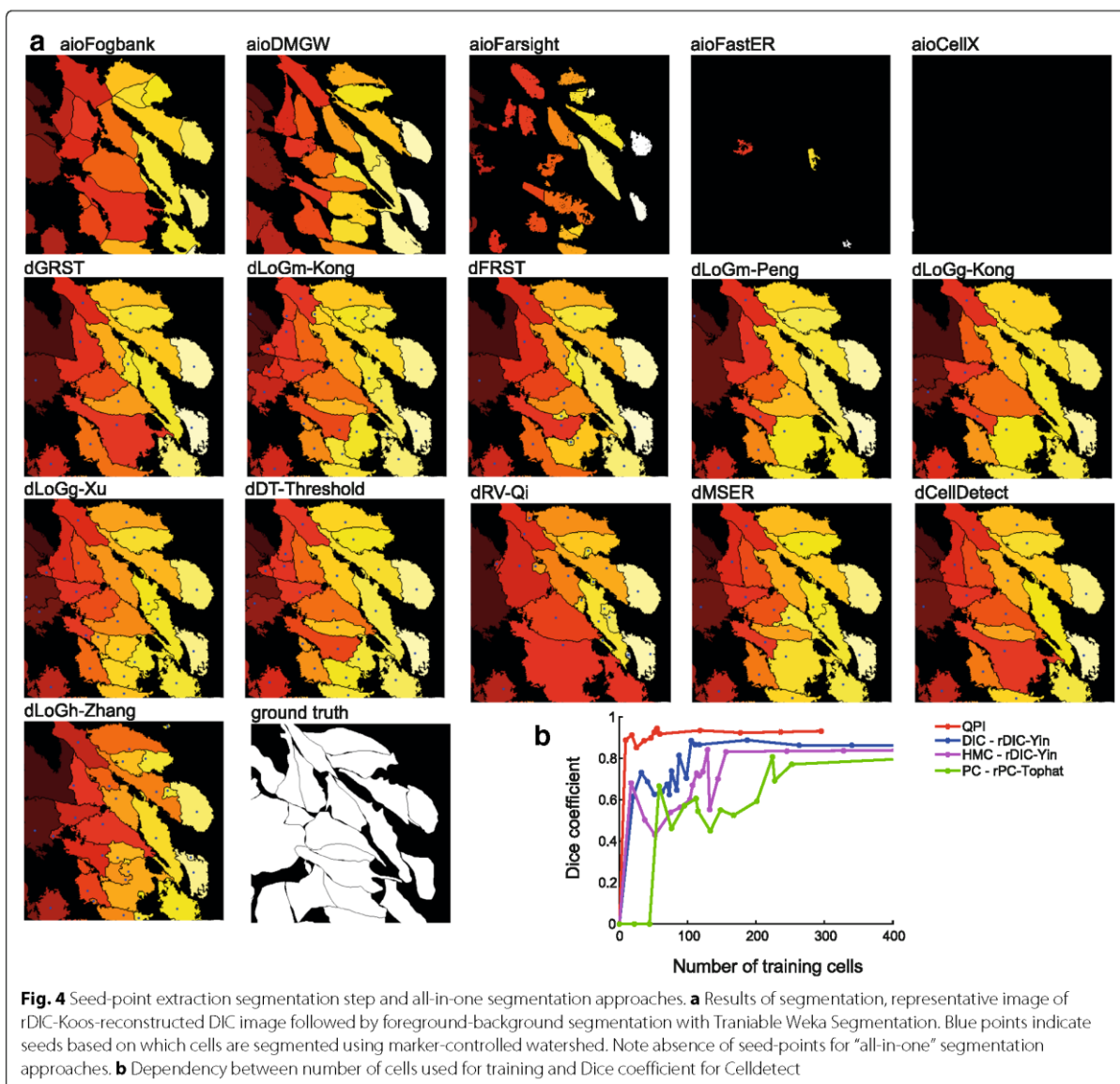
CellDetect

The CellDetect approach uses [35] maximally stable extremal region for segmentation. Adherent cells in unreconstructed DIC/HMC/PC images are, however, dramatically heterogeneous structures. Thus, there are no elements registered for learning and thus the performance of CellDetect was similar to aioFastER methods. On the reconstructed data, it performs similarly as LoG- or distance transform-based methods. Nevertheless, because the trainable nature of this technique, enormous computational time demands must be taken into account (up to 100-fold higher than DT). Segmentation of microscopic elements of low shape heterogeneity (e.g. yeast) would profit from CellDetect significantly.

Single cell (instance) segmentation

The data which underwent reconstruction, foreground segmentation and seed-point extraction were finally segmented by Marker-controlled watershed (MCWS) applied on distance transform or on images directly. Compared to previous steps, errors generated by this step have only minimal impact on overall segmentation quality, providing few-pixel-shifts to one or other adjacent cells. The distance transform approach is more universal but, in case the cells are well-separated, MCWS-only approach can provide better results. When compared to "all-in-one" segmentation strategies, the approach proposed by us provides dramatically better results except of proprietary software for quantitative phase imaging (see Table 2). With this in regard, the development of a new method which is strictly based on the nature of mass-distribution-QPI images could provide even better results.

Finally, it was assessed how the segmentation accuracy's individual steps are affected by morphological aspects of cells. Following aspects were studied (Fig. 5): cellular circularity and level of contact of cells with other cells (isolated cells vs cells growing together in densely populated areas, expressed as a percentage of cellular perimeter in contact with other cells). The circularity ranged 38.2 to 63.5%, median 51.2%, (percentage of cells with a circularity 100%: 2.1%), the percentage of perimeter ranged 4.1–41.9%, median 22.0% (percentage of cells with no contact with others 21.7%). Cells with circularity ranges 0–40% and 70–100% were considered low- and high-circularity cells. Regarding the

Fig. 4 Seed-point extraction segmentation step and all-in-one segmentation approaches. **a** Results of segmentation, representative image of rDIC-Koos-reconstructed DIC image followed by foreground-background segmentation with Traniable Weka Segmentation. Blue points indicate seeds based on which cells are segmented using marker-controlled watershed. Note absence of seed-points for "all-in-one" segmentation approaches. **b** Dependency between number of cells used for training and Dice coefficient for Celldetect

degree of contact with other cells, cells whose 0–15% and 50–100% of perimeter was in contact with other cells were designated "isolated" and "growing together", respectively.
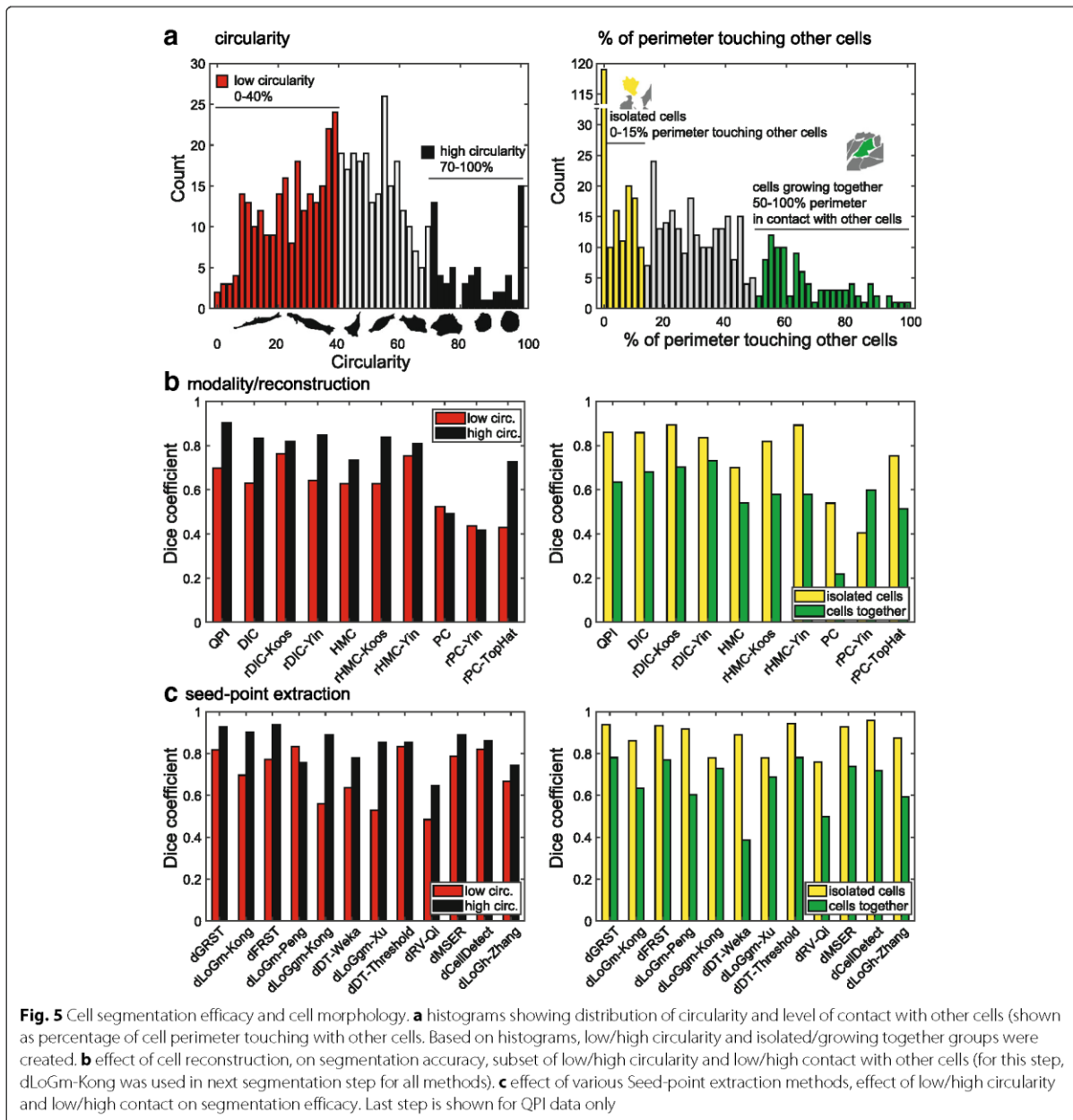
It was found out that the reconstruction method does not affect a difference in segmentation accuracy between highly- and low-circular cells (the segmentation accuracy in highly circular cells is in average 15% better for all reconstruction methods) without significant variations for individual methods. Seed-point extraction, however, is much more cell-shape-dependent (Fig. 5c). Because these methods are blob detectors by nature, the result is better for more circular cells with most methods. However, the dDT-Treshold and dCellDetect are not affected by

circularity and are among the most efficient segmenting tools at the same time.

Regarding the effect of a degree of contact with other cells, method of image reconstruction does not affect a difference in segmentation between densely and sparsely populated areas (20% better segmentation results for isolated cells). Seed-point extraction accuracy is however even more profoundly affected by a level of contacts with other cells (in average 25% better segmentation for isolated cells).

Discussion
During the last two decades, the amount of approaches to segment microscopic images increased dramatically. The

83

Fig. 5 Cell segmentation efficacy and cell morphology. **a** histograms showing distribution of circularity and level of contact with other cells (shown as percentage of cell perimeter touching with other cells. Based on histograms, low/high circularity and isolated/growing together groups were created. **b** effect of cell reconstruction, on segmentation accuracy, subset of low/high circularity and low/high contact with other cells (for this step, dLoGm-Kong was used in next segmentation step for all methods). **c** effect of various Seed-point extraction methods, effect of low/high circularity and low/high contact on segmentation efficacy. Last step is shown for QPI data only

precise segmentation of label-free live-cell microscopic images remains challenging and not completely solved task. Furthermore, different microscopic techniques make this task more difficult due to different image properties provided.

Accordingly, the aim of this study was to compare the most heterogeneous spectrum of segmentation methods to real data of the same cells from multiple contrast microscopic modalities. The properties of each processing step has been evaluated and segmentation accuracy has been compared.

We used human adherent cells, which are much more heterogeneous in shape and thus much bigger challenge for segmentation than the segmentation of spherical bacteria or yeast. Based on the described results, we can now summarize, discuss and suggest several findings directed to both biologists and bioinformaticians from different points of view.

84

Segmentability of microscopic techniques

When considering a microscopy technique for label-free segmentation, there were no dramatic differences in the segmentation efficacy between DIC, HMC or PC. However, the highest segmentation efficacy was obtained when QPI microscopy was used due to the higher image quality (without significant artefacts and high image contrast). In principle, approaches originally intended for fluorescence segmentation are applicable for these images. QPI technique should be also the choice, when a fast, high throughput segmentation is desirable, because no image reconstruction is needed and simple thresholding with MSER - Seeded watershed provides satisfactory results.

Performance of segmentation steps

Regarding individual processing steps, the most crucial are image reconstruction and seed-point extraction methods. Foreground-background segmentation, on the other hand, can be considered the least problematic part, where no dramatic differences between methods were observed, except that learning-based approaches scored better. Regarding the seed-point extraction, however, a reconstructed image is needed for almost all approaches (except dDT-Weka), making seed-point extraction dependent on precise reconstruction. Not all foreground-background segmentation methods need reconstructed images, because some are compatible with raw DIC or PC images (e.g. sWeka, sLS-Caselles, sEGT) and generally perform well. Omitting the reconstruction step will need the seed point extraction methods applicable to raw data (eg. dDT-Weka or DT with different foreground-background segmentation), which can slightly reduce the quality of cell segmentation. It was also evident, that not all reconstruction algorithms are suitable for the seed-point extraction (high Dice coefficient in the foreground segmentation step does not guarantee suitability for the seed-point extraction). It also cannot be stated that the time-consuming methods are dramatically better-performing in the seed-point extraction. Here, the learning-based approach provided better results, too. Below we provide short workflow summary for each microscopic technique:

- QPI – this technique usually provides images with the best image properties with respect to automated image processing. We observed that Weka probability map segmented with Graph-cut, followed by seed-point extraction with dGRST and finally segmented by Marker-controlled watershed gives superior results. In general, any segmentation approach used, QPI gained the highest segmentation efficacy.
- PC – for this modality we suggest simple and fast reconstruction with Top-Hat filter, and dGRST or

dFRST for seed-point extraction. Graph-cut applied to probability Weka probability maps produce best foreground-background segmentation. Final segmentation is slightly improved if Marker-controlled watershed is applied to distance transform image (instead of intensity image).
- DIC/HMC – the images from these modalities are similar, which leads us to suggestion that the same pipeline can be applied to both. We suggest to use rDIC-Koos method for reconstruction and Graph-cut applied to probability Weka probability maps for foreground-background segmentation. Thresholding with distance transform (dDT-Threshold) is best for seed-point extraction, finally segmented by Marker-controlled watershed. Although DIC and HMC have a lot of similar features, DIC produce generally better results.

All-in-one packages are extremely popular in biologist community and more or less provide the complex solution for single cell segmentation task. However, these packages implement common image processing methods (some of them described here) and together with graphical user interface and interactions, provide rich possibilities for segmenting the images. We can conclude that FogBank and CellProfiler tools achieve the highest segmentation efficacy among these approaches (without need of programming skills) and it is also universal for various imaging modalities. Both FogBank and CellProfiler use a similar generalizable approach based on the combination of watershed and distance transform, however, CellProfiler also includes a possibility to build complete cell analysis pipelines and as such should be default choice without programming.

Deep-learning remarks

Intentionally, our focus was set on a spectrum of traditional strategies while the rapidly-developing spectrum of deep-learning-based segmentation was omitted. The main practical limitation of application of deployment of pre-trained U-net or other deep learning method (transfer learning) is the need for sufficiently large training dataset (covering different modalities and cell types/shapes). However, the image databases for segmentation tasks are not as large and complex as ImageNet [36], which became a standard for pre-training of classification-based networks. For this reason, available models use only pre-trained encoder [37], which is pre-trained for classification on ImageNet. As such, we leave this investigation for future work, where deeper-comparison is highly needed, especially for different amounts of training data and from view of computational requirements.

Despite the tremendous success of deep learning approaches applied in many computer vision tasks

including live cell imaging, there is no straightforward way how to use these methods for cell segmentation of touching dense populated cells. One of the approaches to achieve separated mask for each cell is to predict simple binary foreground mask, but giving higher weight to correct prediction on the boundary as in [38]. Another simple solution is to predict three pixel classes – background, foreground and cell boundary as in [39], which provides better separation of cells. On the other hand, deep learning can be also used for cell detection by regression of 2D Gaussians on the position of centroids as in [40]. In [41], authors combined detection and segmentation into simultaneous prediction with one U-Net network, where one prediction map predicts distance to cell boundary (after thresholding we obtain foreground-background segmentation) and second map predicts distance to cell centroid (detections are obtained with local maxima detection). These techniques are very promising, however, their testing is out of scope of this paper because our dataset is not sufficiently large for training of these algorithms and there is no standard way how to use deep learning for cell segmentation, leading to enormous number of possible setups to test in order to achieve fair comparison to classical methods.

Remarks and limitations

Because of Matlab platform was used, the information regarding computational time is approximate with a large software-dependent space for its reduction. All segmentation steps were performed in a sequential way. Thus parallel processing may provide a distinct improvement for most of the methods, but this was beyond the scope of this study. Based on a distinctive difference in a segmentation accuracy between "all-in-one" methods and individual methods reviewed herein, well-performing methods usually have more than three parameters to be set (usually not even corresponding with morphological features of the cells). Thus it is still difficult, if not impossible, to automatize the whole segmentation process. In a spite of this, deep-learning approaches provide some alternative – instead of setting optimized parameters, user needs just to provide a training dataset.

Although there are several excellent reviews on such segmentation, a study practically comparing the to-date best-performing approaches on real data from various microscopic techniques is still missing. In [42] the authors review a broad spectrum of segmentation methods to segment histological images. In [43] the authors focus on available tools with GUI. The author of [44] summarizes historical progress of cell segmentation methods. There are also works on comparing QPI, DIC and PC, but in [45], the authors compare modalities without segmentation and in [46] authors test algorithms only on QPI data, without considering image reconstructions. In Ulman et al.

[47] the authors compared segmentation and tracking on various microscopic methods, including 2D fluorescent, DIC and PC. Many detection errors can be eliminated with tracking. Thus the comparisons with our review might be rather relative. Similarly to our results, one of the best-performing algorithms "KTH-SE" used a relatively simple thresholding together with a precise seed-point extraction (tracking in their case). This underlines the fact that a precise seed-point extraction is the most crucial segmentation aspect. Also a segmentation performance was significantly lower in the "Fluo-C2DL-MSC" dataset characteristic by low circularity of cells.

Our study has several limitations. These include the focus on the segmentation of adherent cells, not those cultivated in the 3D matrix or suspension-cultured counterparts. Also the ground truth manual segmentation was performed by a human, although experienced biologist. The problem of overlapping cells was present, although relatively rare. Using the learning-based approaches it was demonstrated that those surpass the transitional strategies. This predicts a future success for deep-learning methods and probably also their future superiority. Also, in accordance with cell time-lapse trend in microscopy, cell segmentation is just the first part of the story with cell tracking being another one.

Conclusion

In this study, we performed a comprehensive testing of image processing steps for single cell segmentation applicable for label-free images. We searched for published methods, which are used by biologists and bioinformaticians, we assessed the suitability of used data and we carefully tested particular segmentation steps (image reconstruction, foreground-background segmentation, seed-point extraction and cell segmentation) and compared them with available "all-in-one" approaches. As expected, learning-based methods score among the best-performing methods, but well-optimized traditional methods can even surpass these approaches in a fraction of the time. We demonstrated that the image reconstruction step makes it possible to use segmentation methods not directly applicable on the raw microscopic image.

Herein we collected a unique set of similar field-of-view image of the same cells acquired by multiple microscopic techniques and annotated by experienced biologist. The raw and reconstructed data is provided, together with the annotated ground truth and Matlab codes of all approaches.

Methods
Dataset
Cell culture and culture condition
PNT1A human cell line was used in the experiment. This cell line was derived from normal adult prostatic epithelial

cells immortalized by transfection with a plasmid containing SV40 genome with defective replication origin. The cell line was purchased from HPA Culture Collections (Salisbury, UK). PNT1A cells were cultured in RPMI-1640 medium supplemented with antibiotics (penicillin 100 U/ml and streptomycin 0.1 mg/ml) with 10% fetal bovine serum (FBS). Prior microscopy acquisition, cells were maintained at 37°C in a humidified (60%) incubator with 5% CO_2 (Sanyo, Japan). Intentionally, high passage number of cells was used ($>$ 30) in order to describe distinct morphological heterogeneity of cells (rounded and spindle-shaped, relatively small to large polyploid cells). For acquisition purposes, cells were cultivated in Flow chambers μ-Slide I Luer Family (Ibidi, Martinsried, Germany).

Microscopic image acquisition and dataset characteristics

QPI microscopy was performed on Tescan Q-PHASE (Tescan, Brno, Czech Republic), with objective Nikon CFI Plan Fluor 10 $\times$ /0.30 captured by Ximea MR4021MC (Ximea, Münster, Germany). Imaging is based on the original concept of coherence-controlled holographic microscope [48, 49], images are shown as a 32bit file with values corresponding to pg/μm^2 recalculated from radians according to Barer and Davies [50, 51].

DIC microscopy was performed on Nikon A1R microscope (Nikon, Tokyo, Japan) with a Nikon CFI Plan Apo VC 20 $\times$ /0.75 objective captured by a Jenoptik ProgRes MF CCD camera (Jenoptik, Jena, Germany).

HMC microscopy was performed on Olympus IX71 microscope (Olympus, Tokyo, Japan) with Olympus CplanFL N 10 $\times$ /0.3 RC1 objective captured by Hamamatsu Photonics ORCA-R2 CCD camera (Hamamatsu Photonics K.K., Hamamatsu, Japan).

PC microscopy was performed on a Nikon Eclipse TS100-F microscope, with a Nikon CFI Achro ADL 10 $\times$ /0.25 objective captured by Jenoptik ProgRes MF CCD camera.

The captured dataset characteristics are summarized in Table 3. All data were manually segmented by an expert in cell biology as ground truth for segmentation and detection. Same areas of sample were captured using these microscopes, but due to the cell movement and different FOV size the overlap is not absolute.

All-in-one segmentation tools

Here are described "all-in-one" approaches (designated with "aio" prefix).

aioFARSIGHT

FARSIGHT toolkit 0.4.5 module Nucleus editor [2] consists of an automatic Poisson threshold binarization refined with graph-cut (applied on a binary foreground image) and produces initial segmentation containing cell clusters. Next, Multiscale Laplacian-of-Gaussian is used to produce feature map (image where blobs are enhanced - see "LoG filters" section for more details), which is segmented by local clustering algorithm. This clustering algorithm then produces rough cell cluster separation. Finally α-Expansions (multilabel graph cut) is used to refine segmentation, with novel method of Graph colouring for more efficient computation (see [2] for more details).

The first set of parameters was cell-shape-derived: "min scale" and "max scale" (the minimum and maximum scale of the multiscale Laplacian of Gaussian filter) were set based on a measured radius of equivalent circle of cells, "xy clustering res" (resolution of the local maximum clustering) was set similarly as "min scale", and "min object size" was set as the area of the smallest cell. The second set of parameters was optimized: "high sensitivity" (enable/disable high sensitivity binarization), "finalize segmentation" (enable/disable the segmentation refinement step), "use distance map" (enable/disable the use of the distance constraint to select the LoG scales), and "refinement range" (parameter sets the maximum distance that an initial contour can be shifted).

aioCellX

Dimopoulos et al. [3] approach consists of seed generation with gradient-based Hough transform, construction of membrane patterns images for each seeed (cross-correlation with estimated membrane profile) and segmentation of each such image with graph-cut. After that, statistical morphological outliers are removed and individual regions are combined (almost identical regions are merged and overlaps are resolved).

CellX includes a GUI, where user can interactively set cell size range, maximal cell length and estimated membrane profiles.

aioFogbank

In Chalfoun et al. [4] Fogbank, foreground is segmented with EGT. Seeds are detected as connected regions after percentile thresholding (with some distance and size constraints). Pixels above a defined percentile level are then connected to the nearest seed-point. Either intensity or gradient image and either Euclidean or geodesic distance are used for computation.

Table 3 Data-set summary

Modality	FOV size	Image size	Num. of FOVs	Num. of cells
QPI	376×376 μm	600×600 px	18	637
PC	1253×944 μm	1360×1024 px	10	2387
DIC	627×472 μm	1360×1024 px	11	862
HMC	867×660 μm	1344×1024 px	11	1297

aioFastER

Hilsenbeck et al. [5] FastER applies MSER to construct component tree and SVM for classification of regions into groups of cells or false detections. Finally non-overlapping regions with the highest score are selected. It shares CellDetect similarities (see "CellDetect" section), but this algorithm uses 9 features for SVM classification only and does not compute globally optimal solution, thus being computationally faster. To achieve complete segmentation (not only detection as CellDetect), authors modified their approach on the algorithmic level. Size constraints of cells (measured min/max cell size) were set and "de-noise" parameter setting were optimized (off/on/strong). Larger number of FOVs used for training were tested without improvement.

Dry mass-guided watershed

The dry mass-guided watershed method (designated as aioDMGW) is a thresholding-based approach, implemented as a part of Analyzer module of Q-PHASE software 6.803 (Tescan, Brno, Czech Republic). First the phase image is slightly smoothed and foreground is separated from background using thresholding. Then watershed starting from the local maxima is performed. The decision of merging of touching segments, or leaving them separated, is based upon the sums of pixel values (i.e. dry mass) in each touching segment. The optimized parameters are: threshold; min segment sum (the minimum accepted sum of pixel values in each segment used to filter out noise and cell debris); max merge sum (the threshold of sum of pixel values of touching segments used to decide if the segments should be merged or left separated).

aioCellProfiler

The CellProfiler [10] is a strong segmentation tool, however, we perceive it more as a platform where a substantial part of the segmentation strategies used here can be reproduced. Nevertheless, we evaluated output of "IndetifyPrimaryObject" module, which combines thresholding and watershed. Watershed is used twice, for seed-point extraction and final single cell segmentation, and it is applied to either intensity or DT image. Additionally, module uses some smoothing and it remove seed-points bellow some allowed distance. Measured range of cell radiuses and optimal threshold (see Additional file 1) were used and we optimized betwen application to intensity or DT image for both steps.

Other all-in-one tools

Following algorithms were reviewed but not used in comparison with reasons stated below:

CellTracer [6] consists of 3 steps – foreground segmentation, border segmentation and cell segmentation by model fitting. This approach is more suitable for yeast-or bacteria-shaped objects (coccus- or bacillus-shaped with distinctive borders). Similar issues were observed in SuperSegger [7], CellSerpent [8] or CellStar [9].

Image reconstruction techniques

DIC, HMC and PC image formation process can be described as convolution between the original image of the scene and 2D PSF. For PC images *PSF* is [13]

$$PSF_{PC}(x,y) = \delta(x,y) - airy\left(\sqrt{x^2+y^2}\right) \tag{1}$$

where $\delta(\cdot)$ is Dirac delta function and *airy*$(\cdot)$ is Airy pattern. This leads to halo and shade-off artifacts (see Fig. 2). For DIC image *PSF* is difference of two Gaussians [52]:

$$PSF_{DIC}(x,y) = -xu\exp\left(-\frac{x^2+y2}{\sigma}\right) - yv\exp\left(-\frac{x^2+y2}{\sigma}\right) \tag{2}$$

where σ is Gaussian standard deviation and $\mathbf{u} = [u\ v]^T$ is unit vector specifying shear direction. It means that DIC image is derivation under shear direction visible as 3D-like topographical appearance (see Fig. 2). The inverse PSF then can be used for image reconstruction. The goal of these reconstruction algorithms is to produce image of blob-like cells qualitatively corresponding to cell mass (similar to QPI). The methods described bellow are designated with prefix "r" (reconstruction), original modality and author, where possible.

DIC reconstruction methods were well reviewed in [12]. Based on the results of this study, two methods were chosen: (a) fast, computationally-efficient Yin et al. approach [13] (in following parts designated as "rDIC-Yin") and (b) more computationally-demanding Koos et al. [12] (designated as "rDIC-Koos"). HMC images have the similar properties as DIC and therefore the same reconstruction algorithms were tested.

For PC reconstruction [14], two methods were chosen (a) more complex computationally-demanding method based on PSF model (designed as "rPC-Yin") (b) simple Top-hat filtering (designated as "rPC-Tophat").

rDIC-Koos

Method proposed by Koos [12] (rDIC-Koos) uses an energy minimization with data term and total variation regularization term

$$E = \frac{1}{2}\iint_{\Omega}(\mathbf{u}\cdot\triangledown(K*\hat{f}) - \mathbf{g})^2 + w_s|\triangledown\hat{f}|d\Omega \tag{3}$$

where $\cdot$ denotes dot product, $\triangledown$ denotes gradient, $\mathbf{u} = [u\ v]^T$ is unit vector specifying shear direction, Ω is image domain and K is kernel which approximate PSF without derivative (Gaussian function), where $\triangledown K = PSF_{DIC}(x,y)$.

Euler-Lagrange equation of data term for symmetric kernel K leads to

$$u\partial_x g + v\partial_y g - \iint_W K\left(u^2\partial_x^2\hat{f} + 2uv\partial_x\partial_y + v^2\partial_y^2\hat{f}\right) = 0 \tag{4}$$

where ∂_x and ∂_y denotes partial derivatives and W is a local window (with size of kernel). Finally, this can be solved with gradient descent iterative method as

$$\hat{f}^{(t+1)} = \hat{f}^{(t)} - w_a\left(u^2\partial_x^2\hat{f}^{(t)} + 2uv\partial_x\hat{f}^{(t)} + v^2\partial_y^2\hat{f}^{(t)}\right) * K$$
$$+ u\partial_x G + v\partial_y G - div\left(\frac{\nabla\hat{f}^{(t)}}{||\nabla\hat{f}^{(t)}||}\right) \tag{5}$$

where $\hat{f}^{(t+1)}$ is reconstructed image in next iteration, *div* denotes divergence. Last term is proposed by total variation regularization.

Besides of shear angle, which is assumed to be known (or recognizable from image - typically multiple of 45), rDIC-Koos method has three parameters - weight of smoothness (total variation) regularization w_s, step size of gradient descent w_a and number of iteration *it*. Smooth regularization sets compromise between noise elimination and details preservation. Too large step size leads to method divergence and too small step size leads to slow convergence. Number of iterations has a small influence on the result; default value 20000 was used. For setting of other parameters see Additional file 1.

rDIC-Yin

Yin et al. [13] presented a reconstruction method for DIC images (rDIC-Yin) working with multiple shear directions, but with some simplification in equations it also works on images with one shear angle direction. Authors assumed that distortion of the microscope can be modeled by convolution with PSF

$$\mathbf{g} = \mathbf{d} * \mathbf{f} \tag{6}$$

where $\mathbf{d}$ is PSF (in general a directional first-derivative-of-Gaussian kernel, but simple difference without Gaussian is used for simplification), $\mathbf{g}$ is acquired image and $\mathbf{f}$ is original image. Simple inverse filtering leads to highly noisy images, which can be reduced by regularization. This can be achieved with optimization of energy function which must be minimized over whole image domain

$$\mathbf{E}(\hat{\mathbf{f}}) = (\mathbf{d} * \hat{\mathbf{f}} - \mathbf{g})^2 + w_s(\mathbf{a} * \hat{\mathbf{f}})^2 + w_r\hat{\mathbf{f}}^2 \tag{7}$$

This equation is composed of data term, smooth term and sparse term (all with l_2 penalization, where w_s and w_r are weights for the smooth and sparse regularizations, respectively). $\hat{\mathbf{f}}$ is reconstructed image (approximation of $\mathbf{f}$). Smoothness is achieved by setting a restored

pixel value to be close to the average of its neighbors (where $\mathbf{a} = [1, 1, 1; 1, -8, 1; 1, 1, 1]/8$). Sparse regularization causes the value of background pixels to be close to zero. Optimization of function has close-form solution in Fourier space ($\hat{\mathbf{F}} = \mathcal{F}\{\hat{\mathbf{f}}\}$ etc.)

$$\hat{\mathbf{F}} = -(\mathbf{D} \odot \mathbf{G}) \oslash (w_s\mathbf{A} \odot \mathbf{A} + w_r - \mathbf{D} \odot \mathbf{D}) \tag{8}$$

where "$\oslash$" and "$\odot$" denotes element-wise division and multiplication, respectively.

Besides shear angle, rDIC-Yin has two parameters only, w_s and w_r, which set smoothness and sparse regularizations, respectively.

rPC-Yin

In [14] Yin et al. used a deconvolution with sparse constraint regularization to reconstruct PC images. This method was further expanded with dictionary of diffraction patterns [53], which deals with problematic mitotic cells. This method is in fact a segmentation method as presented in the Su at al. paper [53] and it therefore cannot be used as preprocessing (i.e. reconstruction) step. rPC-Yin [14] is very similar to rDIC-Yin [13] with modified equation 7 to linear equation system with l_1 penalization for the sparse term.

$$\mathbf{E}(\bar{\hat{\mathbf{f}}}) = (\mathbf{H}\bar{\hat{\mathbf{f}}} - \bar{\mathbf{g}})^2 + w_s\bar{\hat{\mathbf{f}}}^T\mathbf{L}\bar{\hat{\mathbf{f}}} + w_r|\Lambda\bar{\hat{\mathbf{f}}}| \tag{9}$$

where $\bar{\hat{\mathbf{f}}}$ and $\bar{\mathbf{g}}$ are vectorized restored and acquired images, $\mathbf{H}$ is the transfer matrix of the image formation model and $\mathbf{L}$ is Laplacian matrix (corresponding to different expression of operators $\mathbf{d}$ and $\mathbf{a}$ in the equation 7). Λ is positive diagonal matrix defining sparseness, w_s and w_r are weights for the smooth and sparse regularizations. Because of l_1 penalization of sparseness (known to be better than l_2) there in no closed-form solution. It can be solved with an iterative algorithm which is based on non-negative multiplicative updating (for more implementation details see [14]). PSF (which leads to $\mathbf{H}$) is then modeled by the equation 1, where airy pattern is

$$airy(r) = R\frac{J_1(2\pi Rr)}{r} - (R - W)\frac{J_1(2\pi(R - W)r)}{r} \tag{10}$$

where R and W are PSF-dependent parameters - outer radius (R) and ring width (W) of phase ring and $J_1(\cdot)$ is the first order Bessel function of the first kind. rPC-Yin has also optimization parameters w_s and w_r which define weights of components of optimized energy function. Other parameters not discussed in [14] were set to default value (*radius* $= 2, epsilon = 100, gamma = 3, scale = 1, maxiter = 100, tol = 10^{-16}$). Because of large computational time, optimization of PSF and optimization parameters was done separately - first proper PSF was found (other parameters set to default value $w_s = 1$ and $w_r = 0.5$) and then optimal W and R values were used in optimization of w_s and w_r.

rPC-Tophat

Top-hat filtering (referred here as rPC-Tophat) was used by Thirusittampalam et al. [15] and Dewan et al. [16] for halo artifacts elimination. This simple heuristic approach shows very promising results and it is considered as the next PC reconstruction technique in this paper.

Reconstruction based on top-hat filtering with disk-shaped structuring element has only one adjustable parameter - radius of structuring element, which is roughly equal to the radius of the cell, with optimal value $r = 16$.

Foreground-background segmentation

Thirteen methods has been tested and to make it more clear, the methods are designated with prefix "s" (segmentation), original modality and the author, where possible.

Thresholding

Three threshold-based techniques were used for the foreground-background segmentation. Simple threshold (named as sST) and two automatic threshold algorithms, Otsu [17] (sOtsu) and Poisson distribution [2] (sPT).

Automatically determined thresholds varies between FOVs, so a better result can be expected. sOtsu assumes that gray-scale values are mixture of two Gaussian distributions. Nevertheless, for the adherent cell images the mixture of two Poisson distributions is sometimes more suitable [2], thus sPT was tested. For ST, threshold value was optimized with 100 steps between minimal and maximal value.

Empirical gradient threshold

Chalfoun et al. [18] described an empirical gradient threshold method (referred here as sEGT), which uses empirically derived model for threshold estimation. sEGT was described to work with different microscopic modalities (PC, DIC, brightfield and fluorescence) and is applicable also on the others, including raw (unreconstructed) images. sEGT utilizes a Sobel operator to compute absolute value of gradient, then the percentile-based threshold is found, followed by the binary morphological operations. Three parameters must be set beforehand: minimal cell size (removing small objects), minimal hole (removing small holes) and manual fine-tune (decreasing or increasing the estimated threshold). For all these methods minimal object size was determined from a ground true mask of the training images.

sPC-Juneau

Juneau et al. [19] described simple segmentation method (referred here as sPC-Juneau) designed for PC images. It computes a range map (difference between minimum and maximum in local window), which is then thresholded. Consequently, all holes and small objects in the binary image are removed. Thus these parameters are optimized: window size, threshold and minimal object size. Although originally designed for PC images, it is applicable for other modalities as well.

sPC-Phantast

Jaccard et al. [21] developed a software toolbox PHANTAST consisting of foreground segmentation techniques specialized for PC microscopy images. It computes local contrast

$$C = \frac{\sqrt{G * I^2 - (G * I)^2}}{G * I} \tag{11}$$

where G is a Gaussian kernel with standard deviation σ. The resulting local-contrast image is then globally thresholded and halos are corrected. For halos correction, the gradient direction is computed by eight Kirsch filters (8 directions). Halo pixels are initialized with boundary pixels of binary image, then iteratively each halo pixel points to its gradient direction and two adjacent directions, where each of these three pixels is marked as halo if it is considered foreground (for bright halos gradient points in and for dark cells gradient points out). Maximum cell area fraction removed as halo is restricted and after elimination of halos, small objects and holes are removed. This leads to 5 parameters - Gaussian σ, threshold, halo area fraction, minimal hole size and minimal object size.

sPC-Topman

Topman et al. [20] described another method for foreground segmentation originally intended for PC images. This approach applies two filters, one with a small and one with a large local window computing the standard deviation, where both are thresholded. The result is an intersection of these two binary images, where binary image from large window is morphologically eroded (with morphological element of half the size of the large window) and final image is morphologically opened and closed. This leads to 4 parameters - two window sizes, threshold, and morphological element size.

LevelSets

Matlab implementation of level-set method with function *activecontour* was used. This implementation includes an edge-based method [22] (referred as sLS-Caselles) and region-based method [23] (referred as sLS-ChanVese). Both methods use a Sparse-Field implementation [54] for contour evolution and both have two adjustable parameters - smoothness of the result contour and additional force, which leads to a tendency of the contour to grow or shrink. While sLS-ChanVese segments the image into

two regions based on the mean region intensities, sLS-Caselles segments the image based on the edges. The level-set methods were initialized with morphologically-dilated binary results of Weka segmentation, because it provides similar initial contours for all modalities. Number of iterations of the evolution was set to 1000, which was shown to be enough for all types of images and all parameter settings.

Trainable Weka Segmentation

Next, a machine learning tool for microscopy pixel classification Trainable Weka Segmentation v.3.2.13 was used [26] (designated as sWeka). Compared to previous foreground-background segmentation strategies, this approach was primarily used directly on the raw data. Weka was trained using the following default training features (Gaussian blur, Sobel filter, Hessian eigenvalues, difference of Gaussians filter, membrane projections) as well all remaining available filters (variance filter, minimum filter, maximum filter, median filter, anisotropic diffusion, bilateral filter, lipschitz filter, kuwahara filter, gabor filters, Sobel filter, laplacian filter, structure, entropy filter). For these filters it is also possible to set a σ range, which specifies the filter size. Other parameters were set to default values, random forest classifier was set to 200 trees (WEKA FastRandomForest). Because of learning nature of this approach, the effect of following factors on segmentation efficacy was optimized: (a) number of fields of view used for learning (b) training features used for learning ("all" and "default" training features), (c) effect of various fields of view used for training (one continuous area in one FOV, or smaller patches of same sizes from multiple FOVs), (d) size of FOV used for learning (increasing the area from 6×6 px to 1360×1024 px). Moreover, probability maps were exported and used for further analyses.

Ilastik

Another tested machine learning tool for pixel classification was Ilastik v.1.3.0 [25]. Ilastik uses a random forest classifier [55] with 100 trees and is very similar to WEKA. Ilastik was launched using the following settings: enabled all training features: raw intensity, gradient magnitude, difference of Gaussians, Laplacian of Gaussian, structure tensor eigenvalues and the Hessian matrix eigenvalues - all with 7 Gaussian smoothings with $\sigma = 0.3 - 10px$.

Ilastik was optimized accordingly as Weka. It allows a computationally expensive automatic selection of suitable features. Based on a first optimization step, there was no significant difference between "optimal" and "all" features. Thus, in a spite of this and a fact that Ilastik has less available features then WEKA, "all" features were used in further steps.

Graph-cut approach

An ImageJ plugin for Graph-Cut (v. 1.0.2) based on the reimplementation of Kolmogorov's maxflow v3.01 library [24] was used. The following data were used as an input for Graph-Cut: (a) Probability maps generated by Weka (referred as sWekaGraphCut), (b) images reconstructed with approaches described in "Image reconstruction approaches" and (c) raw image data (both referred as sGraphCut). There are two parameters to be optimized: terminal weight and edge weight. Edge weight (designated as "smoothness" in the GUI, range 0-10) reflects a penalty for label changes in the segmentation (higher values cause smoother result). Terminal weights (designated as "foreground bias", range 0-1) correspond to a cost of assigning background pixels to the foreground.

Terminal weights (foreground bias in GUI) affect the segmentation efficacy distinctly, thus its optimization is crucial. On the other hand, edge weight (smoothness) corresponds to the size of individual cells and has been roughly estimated from 0.4 to 0.8 for used cell sizes (between 1000 and 4000 pixels, respectively).

Cell detection (seed-point extraction)

The cell detection (seed-point extraction) plays a key role in the segmentation of the overlapping objects. For densely clustered and touching cells a precise cell detection has the most significant influence to the final segmentation accuracy. The primary goal in the cell detection is to recognize the presence of the individual objects in the image. Finally, combination of successful foreground-background separation followed by identification of individual cells enable to segment individual cells. There is a considerable amount of methods for cell detection and the mostly used and cited methods are described and evaluated in this paper. Because most of the described methods require blob-like cells, image reconstruction is necessary in most cases (except LoG and generalized LoG filters by Kong et al. [28]).

The tested seed-point extraction methods usually include parameters related to the cell radius (minimal and maximal). For this reason we estimated these values from the ground truth masks. Background segmentation from the previous step was used to eliminate falsely detected seeds in the background. Some of the tested methods already include this step (e.g. dLoGg-Xu [29]). The binary background masks produced by trainable Weka segmentation were used for this purpose. For clarity, the methods described bellow are designated with prefix "d" (detection), image processing approach and author, where possible.

LoG filters

Because of distinctive popularity of the LoG filter for the blob object detection, many modifications of this detector

exist, e.g. multi-scale LoG, Hessian LoG, generalized LoG. LoG filter at a scale σ is defined by equation

$$LoG(\mathbf{x}, \sigma) = \nabla^2 G(\mathbf{x}, \sigma) = \frac{\sigma^2 - ||\mathbf{x}||^2}{2\pi\sigma^6} e^{\frac{-||\mathbf{x}||^2}{2\sigma^2}}, \qquad (12)$$

where G is 2D Gaussian function, $\mathbf{x} = (x, y)$ and $||\cdot||$ is Euclidean norm [27]. In principle, this filter works as a matched filter for blobs.

Multi-scale LoG filtering uses a bag of LoG filters with m different sigma values, which leads to $m - D$ feature space. As proved by Lindeberg [56], LoG responses must be normalized $LoG(\mathbf{x}, \sigma)_{norm} = \sigma^\gamma LoG(\mathbf{x}, \sigma)$ for scale invariance, where $\gamma = 2$ for scale invariance, but it can be refined for a preference of larger or smaller objects.

Peng et al. [27] used Maximum Intensity Projection (MIP) of the series of LoG-filtered images $MIP(\mathbf{x}) = \max_\sigma(LoG_{norm}(\mathbf{x}, \sigma))$, with threshold applied to resulting 2D image, where binary objects correspond to the detected cells. This method (further designated as dLoGm-Peng) has the following parameters: minimal sigma σ_{min}, maximal sigma σ_{max}, sigma step $\Delta\sigma$, γ and threshold.

Kong et al. [28] searched for local maxima higher than defined threshold in whole $m - D$ LoG scale space with elimination of overlapping regions by a pruning process. In the pruning process, the overlapping blobs are eliminated, where only blob with larger value in $m - D$ scale space is preserved. This method has these parameters: σ_{max}, sigma step $\Delta\sigma$, γ, threshold and maximal overlap ratio. Here for σ the logarithmic step is used. This method is referred as dLoGm-Kong.

Hessian analysis of LoG (referred as dLoGh-Zhang) described by Zhang et al. [30] uses the same bag of LoG-filtered images, but optimal scale identification and cell center detection is different. It is known, that local Hessian matrix is positive definite for blob-like structures. The Hessian H (computed from LoG-filtered image) at position (x, y) can be approximated with differences in 2×2 neighborhood. Each connected region with a positive definite Hessian is considered as cell, where H is a positive definite matrix when H_{11} is positive and $det(H)$ is positive.

$$H(x, y, \sigma) = \begin{pmatrix} \frac{\partial LoG(x,y;\sigma)}{\partial x^2} & \frac{\partial LoG(x,y;\sigma)}{\partial x \partial y} \\ \frac{\partial LoG(x,y;\sigma)}{\partial y \partial x} & \frac{\partial LoG(x,y;\sigma)}{\partial y^2} \end{pmatrix}. \qquad (13)$$

Optimal is considered a such scale where the mean intensity of the LoG-filtered image is maximal on the positive definite locations, and these positive definite regions are the detected cells. Method is insensitive to choice of range and steps of σ, which leaves only γ parameter to be optimized. Zhang [30] also uses unsupervised classification to

identified true cells only, but in our case this leads to deterioration of the results only and thus was not included in the testing.

Intuitively rotationally-symmetric LoG kernels are very sensitive to irregular cell shape. For this reason Kong et al. [28] proposed a generalized LoG filter (referred as dLoGg-Kong) for the detection of the elliptical shapes. They derived an equation for elliptical kernel with two standard deviations σ_x, σ_y and orientation Θ. Method also includes a specific scale normalization with a parameter α and automatic choice of sigma range based on the initial analysis with circular LoG filters. For every pixel position, a feature image is created as a sum of all filter responses and detected cells are local maxima in this image (see [28] for more details). Thanks to the automatic σ estimation, there is one parameter only - α. Method uses integer kernel sizes smaller than estimated σ_{max}. Small kernels produce false peaks on a sub-cellular structures in our data. These artefacts are eliminated by adding a σ_{min} parameter, which corresponds to a minimal cell radius.

Xu et al. (referred as dLoGg-Xu) [29] sped up this technique by summation of the filters with the same kernel orientation Θ, which is possible thanks to the distributive property of convolution. Instead of automatic estimation of σ range, they estimate it from cell radii. Moreover this technique includes a different normalization (without parameter) and mean-shift clustering for elimination of multiple-time detected seeds. Parameters of this method are: σ range and mean shift window size.

A similar approach was described also in Peng et al. [27] method. Parameter range of σ is estimated based on cell radius as $\sigma = r/\sqrt{2}$. For dLoGm-Peng we used estimated σ_{max} and σ_{min}. Step of σ ($\Delta\sigma$) is insensitive parameter, therefore we set it to 1. For setting of other parameters see Additional file 1. Authors [27] used $\gamma = 2$, which is proven to lead to the theoretical scale invariance. When $\gamma < 2$ the smaller objects are preferred, for $\gamma > 2$ the larger objects are preferred. Appropriate setting of γ leads to mean Dice coefficient improvement +0.089 for dLoGm-Peng method and for this reason we add γ to optimized parameters for both dLoGm-Peng and dLoGm-Kong methods. Similarly for dLoGm-Kong we used estimated σ_{max} and σ_{min} with 13 logarithmic steps like the authors[28] (for other parameter settings see Additional file 1). Extension by γ parameter leads to 3 parameters (besides of cell radii), which are sensitive and must be properly set. Both generalized LoG methods try to avoid parameters setting, where dLoGg-Xu has cell size-related parameters only (we set it based on estimated radius) and dLoGg-Kong has one adjustable parameter - scale normalization factor, but cell size estimation is automatic. Both generalized LoG methods are computationally expensive (see Table 1), but dLoGg-Xu reduces the computational time by a reduction of number of convolutions.

Distance transform

Distance transform (DT) of foreground image is defined as a distance to the nearest background pixel (Euclidean distance is chosen as metric). Local maxima of the generated distance map are considered as cells. This method often detects many false cells. For this purpose h-maxima transform is used [15], which uses a grayscale morphology for elimination of small local maxima, where parameter h sets the depth of local maxima to be eliminated. We used two modifications of this method; dDT-Threshold, where binary foreground is computed with optimized threshold and dDT-Weka, where foreground from Weka segmentation is used. Other parameter of this method is maximal size of objects and holes, which are eliminated before applying of the DT.

Fast radial-symmetry transform

Fast radial-symmetry transform [31] (referred as dFRST) is a general method for the detection of circular points of interest applicable to approximately circular objects. Pixels with absolute value of gradient greater than threshold β vote in its gradient direction at the distance of radius $r \in R$, where R is set of radii, determined based on object/cell size. If bright blobs are only considered detection, positions of affected pixel is given by an equation

$$P(\mathbf{x}) = \mathbf{x} + round\left(\frac{g(\mathbf{x})}{\|g(\mathbf{x})\|}r\right) \tag{14}$$

where $g(\mathbf{x})$ represents the gradient and *round* operator rounds each vector element to its nearest integer. On position $P(x)$, an orientation projection image O_r is increased by 1 and magnitude projection image M_r by $\|g(\mathbf{x})\|$. Transformation is defined as mean over all radii

$$S = \frac{1}{N}\sum_{r \in R} F_r * G_r \tag{15}$$

where

$$F_r(\mathbf{x}) = \frac{M_r(\mathbf{x})}{k}\left(\frac{|\hat{O}_r(\mathbf{x})|}{k}\right)^{\alpha} \tag{16}$$

$$\hat{O}_r(\mathbf{x}) = \begin{cases} O_r(\mathbf{x}) & \text{if } |O_r(\mathbf{x})| < k \\ k & otherwise \end{cases} \tag{17}$$

where G_r is a Gaussian kernel, α is the radial strictness parameter and k is a scaling factor normalizing different radii (where typically $k \approx 10$). Inspired by Ram et al. [57], we use a gray-scale dilatation to small local maxima suppression in S. Local maxima are then considered as cells. As R we use all integer values between estimated minimal and maximal cell radius. The parameters for this method include: radial strictness α, scaling factor k, size of morphology structuring element δ, and gradient threshold β.

Generalized Radial-symmetry transform

The generalized radial-symmetry transform as described by Bahlman et al. [32] (referred as dGRST) is able to deal with elliptical shapes because affine transform is employed.. Similarly to generalized LoG filters, we can compute response for different axis scalings and rotations. The dGRST principle is similar to dFRST method, but the gradient $g(x)$ is transformed to

$$\hat{g}(\mathbf{x}) = GMG^{-1}M^{-1}g(\mathbf{x}) \tag{18}$$

where

$$M = \begin{bmatrix} 0 & 1 \\ -1 & 0 \end{bmatrix} \tag{19}$$

and G is affine transformation matrix - for ellipse it is rotation and scaling with parameters θ, a and b. We can set $r = 1$ and used a and b to adjust the size of the desired ellipse axis. All integer values between estimated minimal and maximal cell radius with $a > b$ and 6 steps for θ were used for a and b. Bahlmann at al. [32] mentioned also a Gaussian kernel specified by affine transformation parameters θ, a and b. For consistency with dFRST, we use Gaussian kernel with $\sigma = 0.5$ distorted with G transformation. Remaining parameters are identical to dFRST.

Radial voting

Qi et al. [33] presented a modification of radial voting for cells in histopathology specimens (reffered here as dRV-Qi). It is based on an iterative radial voting described previously [58], but works as a single-path voting followed by a mean-shift clustering. Every pixel with position $\mathbf{x} = [x, y]$ vote in Gaussian smoothed gradient direction $\alpha(\mathbf{x})$, with cone shaped-kernel function (voting area).

$$A(x, y, r_{min}, r_{max}, \Delta) = \{x + rcos\phi, y + rsin\phi | r_{min} < r < r_{max}, \theta - \Delta < \phi < \theta + \Delta\} \tag{20}$$

where θ is an angle of vector $\alpha(\mathbf{x})$, $\{r_{min}, r_{max}\}$ is kernel radial range and Δ is the kernel angular range. In addition, voting sector is weighted by Gaussian function with center located at kernel center. Every pixel (with gradient above certain threshold) update voting image V by adding voting pixel gradient magnitude $|g(\mathbf{x})|$ to all pixels under kernel. Voting image is then thresholded with several thresholds and results are summed and clustered with mean-shift algorithm. For more details see [33]. We used estimated r_{min} and r_{max} from the ground truth images, thresholds were set to 0.2, 0.3,...0.9-times the maximum of image, and we optimized sigma of gradient Gaussian smoothing, sigma of Gaussian for kernel and mean shift bandwidth. We also vote with all pixels, not only with pixels with high gradient magnitude, because computational time of our implementation is not dependent on number of voting pixels. Besides [33] we also tested original [58]

and newer [59] methods, but both were less suitable for adherent cells.

Maximally stable extremal region

Extremal regions of gray-value image are defined as connected components of thresholded image $I_t = I > t$ for some t in this method (designated as dMSER). As described in [34], dMSER produces stable extremal regions of image which are stable in sense of area variation w.r.t. changing threshold t. Minimal stability of extracted region can be set with two parameters - threshold step δ defining the percentage of intensity range and maximal relative area change with this step. This method generates many regions which can overlap. Finally, the smallest regions generated with the highest threshold are picked. This is achieved by finding of the local maxima in the sum of binary images of all regions. Another option is the usage of most stable region from the overlapped ones, but this was shown to be noneffective in our case.

CellDetect

Arteta et al. [35] implementation of CellDetect uses MSER to identify the candidate regions, followed by a classification of true regions. Method extracts 92-dimensional feature vector with object histograms and shape descriptors. Training proceeds in two phases. In the first phase, training of binary SVM and its evaluation is done, which produces score for each region. Region with one seed-point and highest score (one for each seed-point) is used as ground truth for the next phase. In the second phase, structured SVM is used for classification of the regions within each tree created from the overlapping regions, but non-overlap constrains are included. For more details see [35]. Method requires few training images with simple dot annotation and proper setting of MSER detector to achieve high recall.

Single cell (instance) segmentation

After image reconstruction, foreground-background segmentation and seed-point extraction, individual cells were segmented using Marker-controlled (or seeded) watershed [60]. This step showed to be less crucial, because inaccuracy in placing border between cells has a small influence to segmentation efficacy only. Thus, for combining of foreground and seeds into the final segmentation, we test only this simple but very robust technique. Note that more advanced methods exist - e.g. graph-cut [61], or level-set [62] based.

Maker-controlled watershed is similar to classic watershed approach, with restriction of local minima positions into detected seeds location, which can be simply done with mathematical morphology operations. Besides of straightforward application on our images, we proposed a second approach applied on DT image,

which does not require an intensity valley between separated cells. For DT image we use geodesic distance transform [63] with distances from seeds (the distance within the foreground pixels only, ignoring the background).

General parameter optimization strategy

Grid search with 10 steps was used for the optimization of parameters of all methods, where suitable range was selected experimentally by a few manual tests. Parameters with large searched range (relatively large difference between lower and upper bound) were searched with logarithmic scale. The same parameters ranges were used for all modalities. All parameters were properly set for training images and then these values were used for all testing images. For background segmentation and detection methods Dice coefficient was used as an objective function (used e.g. in [18]). For image reconstruction techniques the area under ROC curve (AUC) generated by thresholding was used (as well as in [14] or [12]). Because of large computational difficulty of some methods, we attempted to eliminate such parameters from optimization, which does not influence the objective function. If threshold is optimized parameter, its value was optimized between a minimal and maximal intensity of image pixels, with 100 steps for simplicity. Before application of each method, images were normalized into interval [0,1], where minimal and maximal values of the first image of each sequence were used as a reference for the normalization.

Evaluation of results

The F_1 score (Dice coefficient) was used as a measure of segmentation accuracy for (1) foreground-background segmentation, (2) seed-point extraction, and (3) single cell segmentation, with following modifications:

Foreground-background segmentation evaluation

For the evaluation of cell segmentation, Dice coefficient was used as follows:

$$Dice = \frac{2|X \cap Y|}{|X| + |Y|} \tag{21}$$

where $|\cdot|$ is number of pixels of region, X and Y are ground truth and result segmentation, respectively. Dice coefficient is equal to F_1-score, but this term is used for pixel-wise evaluation. Another metric used for segmentation evaluation is Jaccard index, which is related to Dice coefficient as:

$$Jaccard = \frac{Dice}{2 - Dice} \tag{22}$$

which is monotonically increasing function on interval $< 0, 1 >$ (the range of Dice values). This means that order

of quality of segmentation algorithms w.r.t. Jaccard is same as w.r.t. Dice coefficient and for this reason we evaluated only Dice coefficient.

Dice coefficient was computed for evaluation of the foreground segmentation results using all pixels in the image.

Seed-point extraction evaluation

Single dot labels (seeds) are considered as cell detection results. If some method produces pre-segmented regions, then centroids are used as labels. Because our ground truth corresponds to the binary segmented cells, we consider as TP (true positive) such cells having one seed only. As FP (false positive) are considered cells with additional seeds in one cell and with seeds outside cells. FN (false negative) are cells without any seed. To evaluate the performance of the cell detection, Dice coefficient (F_1 score) was used

$$Dice = \frac{2TP}{2TP + FP + FN}. \tag{23}$$

In some papers the accuracy of the centroid positions is also evaluated. Nevertheless, these positions are not very significant for cell segmentation. Therefore, we didn't evaluate this accuracy.

Single cell segmentation evaluation

For single cell segmentation evaluation the F_1 score (Dice coefficient) is used in a similar manner as for foreground-background segmentation evaluation with following modifications: We dealt with correspondence of objects. We used same evaluation of correspondence as [64] in their SEG evaluation algorithm – cell are considered as matching if:

$$|X \cap Y| > 0.5|X| \tag{24}$$

which ensures unambiguous pairing. The final measure of Dice was calculated as the mean of the Dice coefficient of all the reference objects. The cells which are on the image boundary were labeled and they are not included in the evaluation.

A computer with following specifications was used to estimate computational times: Intel Core i5-6500 CPU, 8 GB RAM.

Additional file

Additional file 1: Optimal values for parameters of individual reconstruction methods (xlsx table). * highest value not reducing sensitivity, ** not learned because of identification of small number of regions. nan, not a number. (XLSX 17 kb)

Abbreviations
AUC: Area under curve; DIC: Differential image contrast; DMGW: Dry mass-guided watershed; DT: Distance transform; EGT: Empirical gradient treshold; FOV: Field of view; FRST: First radial symmetry transform; GRST: Generalized Radial symmetry transform; HMC: Hoffman modulation contrast

LoG: Laplacian of Gaussian; MCWS: Marker-controlled watershed; MIP: Maximum intensity projection MSER: maximally stable extremal region; PC: Phase contrast; PD: Poisson distribution; PSF: Point spread function; PT: Poisson treshold; ROC: Receiver-operator curve; RV: Radial voting; ST: Simple treshold

Availability of data and materials
Annotated image dataset and image reconstructions used in our study are available for download in the Zenodo repository (https://zenodo.org, Digital Object Identifier: https://doi.org/10.5281/zenodo.1250729). Matlab code is available at GitHub https://github.com/tomasvicar/Cell-segmentation-methods-comparison.

Authors' contributions
TV designed the workflow, selected segmentation methods, performed analysis in Matlab and Python and wrote manuscript. JB performed in vitro experiments, designed experiment, JJ performed HMC and helped with in vitro experiments, FJ designed foreground-background segmentation and seed-point extraction structure, helped with trainable approaches and graph cut, RK helped with selection of segmentation strategies and corrected the manuscript, MM provided ideas for segmentation, supported in vitro experiment, JG designed experiment, wrote manuscript and coordinated work. All the authors have read and approved the final manuscript.

Ethics approval and consent to participate
not applicable.

Consent for publication
not applicable.

Competing interests
The authors declare that they have no competing interests.

Publisher's Note
Springer Nature remains neutral with regard to jurisdictional claims in published maps and institutional affiliations.

Author details
[1]Department of Biomedical Engineering, Faculty of Electrical Engineering and Communication, Brno University of Technology, Technicka 3058/10, CZ-61600 Brno, Czech Republic. [2]Department of Physiology, Faculty of Medicine, Masaryk University, Kamenice 5, CZ-62500 Brno, Czech Republic. [3]Department of Pathological Physiology, Faculty of Medicine, Masaryk University, Kamenice 5, CZ-62500 Brno, Czech Republic. [4]Central European Institute of Technology, Brno University of Technology, Purkynova 656/123, CZ-612 00 Brno, Czech Republic. [5]Max Planck Institute of Molecular Cell Biology and Genetics, Pfotenhauerstr. 108, DE-01307 Dresden, Germany. [6]Department of Histology and Embryology, Faculty of Medicine, Masaryk University, Kamenice 5, CZ-62500 Brno, Czech Republic. [7]International Clinical Research Center, St. Anne's University Hospital, Pekarska 664/53, CZ-65691 Brno, Czech Republic.

References
1. Wang Z, Millet L, Chan V, Ding H, Gillette MU, Bashir R, Popescu G. Label-free intracellular transport measured by spatial light interference microscopy. J Biomed Opt. 2011;16(2):026019–0260199. https://doi.org/10.1117/1.3549204.

2. Al-Kofahi Y, Lassoued W, Lee W, Roysam B. Improved automatic detection and segmentation of cell nuclei in histopathology images. IEEE Trans Biomed Eng. 2010;57(4):841–52. https://doi.org/10.1109/TBME.2009.2035102.
3. Dimopoulos S, Mayer CE, Rudolf F, Stelling J. Accurate cell segmentation in microscopy images using membrane patterns,. Bioinformatics (Oxford, England). 2014;30(18):2644–51. https://doi.org/10.1093/bioinformatics/btu302.
4. Chalfoun J, Majurski M, Dima A, Stuelten C, Peskin A, Brady M. FogBank: a single cell segmentation across multiple cell lines and image modalities,. BMC Bioinformatics. 2014;15(1):6598. https://doi.org/10.1186/s12859-014-0431-x.
5. Hilsenbeck O, Schwarzfischer M, Loeffler D, Dimopoulos S, Hastreiter S, Marr C, Theis FJ, Schroeder T. Faster: a user-friendly tool for ultrafast and robust cell segmentation in large-scale microscopy. Bioinformatics. 2017;33(13):2020-28. https://doi.org/10.1093/bioinformatics/btx107.
6. Wang Q, You L, West M. Celltracer: Software for automated image segmentation and line-age mapping for single-cell studies. Duke University; 2018. http://www.stat.duke.edu/~mw/MWextrapubs/Wang2008.pdf.
7. Stylianidou S, Brennan C, Nissen SB, Kuwada NJ, Wiggins PA. Supersegger: robust image segmentation, analysis and lineage tracking of bacterial cells. Mol Microbiol. 2016;102(4):690–700.
8. Bredies K, Wolinski H. An active-contour based algorithm for the automated segmentation of dense yeast populations on transmission microscopy images. Comput Vis Sci. 2011;14(7):341–52.
9. Versari C, Stoma S, Batmanov K, Llamosi A, Mroz F, Kaczmarek A, Deyell M, Lhoussaine C, Hersen P, Batt G. Long-term tracking of budding yeast cells in brightfield microscopy: Cellstar and the evaluation platform. J R Soc Interface. 2017;14(127):20160705.
10. Carpenter AE, Jones TR, Lamprecht MR, Clarke C, Kang IH, Friman O, Guertin D. a., Chang JH, Lindquist R. a., Moffat J, Golland P, Sabatini DM. CellProfiler: image analysis software for identifying and quantifying cell phenotypes,. Genome Biol. 2006;7(10):100. https://doi.org/10.1186/gb-2006-7-10-r100. http://arxiv.org/abs/arXiv:1201.3109v1.
11. Tescan AS. Q-PHASE: Quantitative, Label-free Imaging Cytometry. https://www.tescan.com/en-us/technology/light-microscopy/q-phase. Accessed 30 Apr 2018.
12. Koos K, Molnár J, Kelemen L, Tamás G, Horvath P. DIC image reconstruction using an energy minimization framework to visualize optical path length distribution. Sci Rep. 2016;6:30420. https://doi.org/10.1038/srep30420.
13. Yin Z, Ker DFE, Kanade T. Restoring DIC microscopy images from multiple shear directions. In: Lecture Notes in Computer Science (including Subseries Lecture Notes in Artificial Intelligence and Lecture Notes in Bioinformatics). vol. 6801 LNCS; 2011. p. 384–97. https://doi.org/10.1007/978-3-642-22092-0.
14. Yin Z, Kanade T, Chen M. Understanding the phase contrast optics to restore artifact-free microscopy images for segmentation. Med Image Anal. 2012;16(5):1047–62. https://doi.org/10.1016/j.media.2011.12.006. http://arxiv.org/abs/NIHMS150003.
15. Thirusittampalam K, Hossain MJ, Ghita O, Whelan PF. A novel framework for cellular tracking and mitosis detection in dense phase contrast microscopy images. IEEE J Biomed Health Inf. 2013;17(3):642–53. https://doi.org/10.1109/TITB.2012.2228663.
16. Dewan MAA, Ahmad MO, Swamy MNS. A method for automatic segmentation of nuclei in phase-contrast images based on intensity, convexity and texture. IEEE Trans Biomed Circ Syst. 2014;8(5):716–28. https://doi.org/10.1109/TBCAS.2013.2294184.
17. Otsu N. A threshold selection method from gray-level histograms. IEEE Trans Syst Man Cybern. 1979;9(1):62–6. https://doi.org/10.1109/TSMC.1979.4310076.
18. Chalfoun J, Majurski M, Peskin A, Breen C, Bajcsy P, Brady M. Empirical gradient threshold technique for automated segmentation across image modalities and cell lines. J Microsc. 2015;260(1):86–99. https://doi.org/10.1111/jmi.12269.
19. Juneau P-M, Garnier A, Duchesne C. Selection and tuning of a fast and simple phase-contrast microscopy image segmentation algorithm for measuring myoblast growth kinetics in an automated manner. Microsc Microanal. 2013;19(4):855–66.
20. Topman G, Sharabani-Yosef O, Gefen A. A method for quick, low-cost automated confluency measurements. Microsc Microanal. 2011;17(6):915–22.
21. Jaccard N, Griffin LD, Keser A, Macown RJ, Super A, Veraitch FS, Szita N. Automated method for the rapid and precise estimation of adherent cell culture characteristics from phase contrast microscopy images. Biotech Bioeng. 2014;111(3):504–17.
22. Caselles V, Kimmel R, Sapiro G. Geodesic active contours. Int J Comput Vis. 1997;22(1):61–79.
23. Chan TF, Vese LA. Active contours without edges. IEEE Trans Image Process. 2001;10(2):266–77. https://doi.org/10.1109/83.902291.
24. Boykov Y, Kolmogorov V. An experimental comparison of min-cut/max-flow algorithms for energy minimization in vision. IEEE Trans Pattern Anal Mach Intell. 2004;26(9):1124–37. https://doi.org/10.1109/TPAMI.2004.60.
25. Sommer C, Straehle C, Köthe U, Hamprecht FA. Ilastik: Interactive learning and segmentation toolkit. In: 2011 IEEE International Symposium on Biomedical Imaging: From Nano to Macro; 2011. p. 230–3. https://doi.org/10.1109/ISBI.2011.5872394.
26. Arganda-Carreras I, Kaynig V, Rueden C, Eliceiri KW, Schindelin J, Cardona A, Seung HS. Trainable weka segmentation: a machine learning tool for microscopy pixel classification. Bioinformatics. 2017. https://doi.org/10.1093/bioinformatics/btx180.
27. Peng H, Zhou X, Li F, Xia X, Wong STC. Integrating multi-scale blob/curvilinear detector techniques and multi-level sets for automated segmentation of stem cell images. In: 2009 IEEE International Symposium on Biomedical Imaging: From Nano to Macro. IEEE; 2009. p. 1362–5. https://doi.org/10.1109/ISBI.2009.5193318. http://ieeexplore.ieee.org/document/5193318/.
28. Kong H, Akakin HC, Sarma SE. A generalized laplacian of gaussian filter for blob detection and its applications. IEEE Trans Cybern. 2013;43(6):1719–33. https://doi.org/10.1109/TSMCB.2012.2228639.
29. Xu H, Lu C, Berendt R, Jha N, Mandal M. Automatic nuclei detection based on generalized laplacian of gaussian filters. IEEE J Biomed Health Inform. 2017;21(3):826–37.
30. Zhang M, Wu T, Bennett KM. Small blob identification in medical images using regional features from optimum scale. IEEE Transactions on Biomedical Engineering. 2015;62(4):1051–62. https://doi.org/10.1109/TBME.2014.2360154.
31. Loy G, Zelinsky A. Fast radial symmetry for detecting points of interest. IEEE Trans Pattern Anal Mach Intell. 2003;25(8):959–73. https://doi.org/10.1109/TPAMI.2003.1217601.
32. Bahlmann C. Fast radial symmetry detection under affine transformations. In: Proceedings of the 2012 IEEE Conference on Computer Vision and Pattern Recognition (CVPR). CVPR '12. Washington, DC: IEEE Computer Society; 2012. p. 932–9. http://dl.acm.org/citation.cfm?id=2354409.2354741.
33. Qi X, Xing F, Foran DJ, Yang L. Robust segmentation of overlapping cells in histopathology specimens using parallel seed detection and repulsive level set. IEEE Trans Biomed Eng. 2012;59(3):754–65.
34. Matas J, Chum O, Urban M, Pajdla T. Robust wide-baseline stereo from maximally stable extremal regions. Image Vis Comput. 2004;22(10):761–7. https://doi.org/10.1016/j.imavis.2004.02.006.
35. Arteta C, Lempitsky V, Noble JA, Zisserman A. Learning to Detect Cells Using Non-overlapping Extremal Regions. Miccai. 2012;Figure 1:1–8. https://doi.org/10.1007/978-3-642-33415-3.
36. Russakovsky O, Deng J, Su H, Krause J, Satheesh S, Ma S, Huang Z, Karpathy A, Khosla A, Bernstein M, et al. Imagenet large scale visual recognition challenge. Int J Comput Vis. 2015;115(3):211–52.
37. Iglovikov V, Shvets A. Ternausnet: U-net with vgg11 encoder pre-trained on imagenet for image segmentation. 2018. arXiv preprint arXiv:1801.05746.
38. Ronneberger O, Fischer P, Brox T. U-Net: Convolutional Networks for Biomedical Image Segmentation. Medical Image Computing and Computer-Assisted Intervention. 2015. https://doi.org/10.1007/978-3-319-24574-4_28.
39. Sadanandan SK, Ranefall P, Wählby C. Feature Augmented Deep Neural Networks for Segmentation of Cells. Computer Vision – ECCV 2016 Workshops. In: Computer Vision – ECCV 2016 Workshops. Amsterdam: Springer International Publishing; 2016. https://doi.org/10.1007/978-3-319-46604-0_17.
40. Van Valen DA, Kudo T, Lane KM, Macklin DN, Quach NT, DeFelice MM, Maayan I, Tanouchi Y, Ashley EA, Covert MW. Deep learning automates the quantitative analysis of individual cells in live-cell imaging experiments. PLoS Comput Biol. 2016;12(11):1005177.

Image segmentation: an important step of image data processing 4.1

Vicar *et al. BMC Bioinformatics*   (2019) 20:360   Page 25 of 25

41. Schmidt U, Weigert M, Broaddus C, Myers G. Cell detection with star-convex polygons. In: Medical Image Computing and Computer Assisted Intervention - MICCAI 2018 - 21st International Conference, Granada, Spain, September 16-20, 2018, Proceedings, Part II; 2018. p. 265–73. https://doi.org/10.1007/978-3-030-00934-2_30.

42. Xing F, Yang L. Robust nucleus/cell detection and segmentation in digital pathology and microscopy images. IEEE Rev Biomed Eng. 2016;9: 234–63. https://doi.org/10.1109/RBME.2016.2515127.

43. Wiesmann V, Franz D, Held C, Münzenmayer C, Palmisano R, Wittenberg T. Review of free software tools for image analysis of fluorescence cell micrographs. J Microsc. 2015;257(1):39–53.

44. Meijering E. Cell segmentation: 50 years down the road [life sciences]. IEEE Signal Process Mag. 2012;29(5):140–5.

45. Kasprowicz R, Suman R, O'Toole P. Characterising live cell behaviour: Traditional label-free and quantitative phase imaging approaches. Int J Biochem Cell Biol. 2017;84:89–95.

46. Loewke NO, Pai S, Cordeiro C, Black D, King BL, Contag CH, Chen B, Baer TM, Solgaard O. Automated cell segmentation for quantitative phase microscopy. IEEE Trans Med Imaging. 2017.

47. Ulman V, Maška M, Magnusson KEG, Ronneberger O, Haubold C, Harder N, Matula P, Matula P, Svoboda D, Radojevic M, Smal I, Rohr K, Jaldén J, Blau HM, Dzyubachyk O, Lelieveldt B, Xiao P, Li Y, Cho S-Y, Dufour A, Olivo-Marin JC, Reyes-Aldasoro CC, Solis-Lemus JA, Bensch R, Brox T, Stegmaier J, Mikut R, Wolf S, Hamprecht FA, Esteves T, Quelhas P, Demirel Ö, Malström L, Jug F, Tomančák P, Meijering E, Muñoz-Barrutia A, Kozubek M, Ortiz-de-Solorzano C. An objective comparison of cell tracking algorithms. Nat Methods. 2017. https://doi.org/10.1038/NMETH.447.

48. Kolman P, Chmelík R. Coherence-controlled holographic microscope. Opt Express. 2010;18(21):21990–2004. https://doi.org/10.1364/OE.18.021990.

49. Slabý T, Kolman P, Dostál Z., Antoš M., Lošťák M, Chmelík R. Off-axis setup taking full advantage of incoherent illumination in coherence-controlled holographic microscope. Opt Express. 2013;21(12): 14747–62. https://doi.org/10.1364/OE.21.014747.

50. Davies H, Wilkins M. Interference microscopy and mass determination. Nature. 1952;169(4300):541. https://doi.org/10.1038/169541a.

51. Barer R. Refractometry and interferometry of living cells. J Opt Soc Am. 1957;47(6):545–56. https://doi.org/10.1364/JOSA.47.00054.

52. Koos K, Molnar J, Horvath P. DIC Microscopy Image Reconstruction Using a Novel Variational Framework. 2015. International Conference on Digital Image Computing: Techniques and Applications (DICTA). 2015. https://doi.org/10.1109/DICTA.2015.7371252.

53. Su H, Yin Z, Kanade T, Huh S. Phase contrast image restoration via dictionary representation of diffraction patterns. Med Image Comput Comput Assist Interv. 2012;15(3):615–22.

54. Whitaker RT. A level-set approach to 3d reconstruction from range data. Int J Comput Vis. 1998;29(3):203–31.

55. Breiman L. Random forests. Mach Learn. 2001;45(1):5–32. https://doi.org/10.1023/A:1010933404324.

56. Lindeberg T. Feature detection with automatic scale selection. Int J Comput Vis. 1998;30(2):79–116.

57. Ram S, Rodríguez JJ. Symmetry-based detection of nuclei in microscopy images. In: 2013 IEEE International Conference on Acoustics, Speech and Signal Processing; 2013. p. 1128–32. https://doi.org/10.1109/ICASSP.2013.6637826.

58. Parvin B, Yang Q, Han J, Chang H, Rydberg B, Barcellos-Hoff MH. Iterative voting for inference of structural saliency and characterization of subcellular events. IEEE Trans Image Process. 2007;16(3):615–23. https://doi.org/10.1109/TIP.2007.891154.

59. Lu C, Xu H, Xu J, Gilmore H, Mandal M, Madabhushi A. Multi-pass adaptive voting for nuclei detection in histopathological images. Sci Rep. 2016;6:33985. https://doi.org/10.1038/srep33985.

60. Parvati K, Rao P, Mariya Das M. Image segmentation using gray-scale morphology and marker-controlled watershed transformation. Discret Dyn Nat Soc. 2008;2008:384346. https://doi.org/10.1155/2008/384346.

61. Daněk O, Matula P, Ortiz-de-Solórzano C, Muñoz-Barrutia A, Maška M, Kozubek M. Segmentation of touching cell nuclei using a two-stage graph cut model. In: SCIA: 2009. Oslo: Springer. p. 410–19. https://doi.org/10.1007/978-3-642-02230-2_42.

62. Zhou Y, Kuijper A, Heise B, He L. Cell Segmentation Using Level Set Method. Linz: Johannes Kepler University; 2007. https://pdfs.semanticscholar.org/33b2/7d8696026b5f4f7eac7095ff30e9c920621a.pdf.

63. Ikonen L, Toivanen P. Shortest routes on varying height surfaces using gray-level distance transforms. Image Vis Comput. 2005;23(2):133–41.

64. Maška M., Ulman V, Svoboda D, Matula P, Matula P, Ederra C, Urbiola A, España T, Venkatesan S, Balak DMW, Karas P, Bolcková T., Štreitová M, Carthel C, Coraluppi S, Harder N, Rohr K, Magnusson KEG, Jaldén J, Blau HM, Dzyubachyk O, Křížek P, Hagen GM, Pastor-Escuredo D, Jimenez-Carretero D, Ledesma-Carbayo MJ, Muñoz-Barrutia A, Meijering E, Kozubek M, Ortiz-de-Solorzano C. A benchmark for comparison of cell tracking algorithms. Bioinformatics. 2014;30(11):1609–17. https://doi.org/10.1093/bioinformatics/btu080.

4.2 Artificial intelligence in quantitative microscopy

Quantitative phase enables high-throughput imaging of subtle changes of the cell mass distribution. Cell dry mass is calculated from phase according to Barer and Davies [21; 22]. Due to the inherent low phototoxicity of this technique, long time-lapse acquisitions are feasible. Cell dry mass is a dynamically changing during degradative or biosynthetic cell processes and therefore the technique enables to extract detailed quantitative information on cell morphology and cell topography during various processes including cell division, cell growth, cell communication, or cell death [44]. This technique, therefore, has a promising role in the cancer studies.

Quantitative nature of this microscopic technique and possibility to acquire large dataset (hundreds to thousands of fields of view per time-lapse) open a possibility of machine learning deployment in image analysis instead of mere visual assessment of the images or simple morphometry (measuring areas or intensities).

In the following subchapters, the potential of QPI to include information not evident by naked eye will be tested to reconstruct specific subcellular structures originally labelled fluorescently. Specifically, synthetic imaging of nuclear staining from a quantitative phase image without the presence actual fluorescence information (DAPI, Hoechst, or another nuclear staining) was performed in a paper by Vicar et al [47]. Furthermore, deep learning-based classification of two types of prostatic cells characteristic by varying degrees of aggressiveness was performed (conference proceedings by Majercik et al. [62])

4.2.1 Synthetic nuclei reconstruction from the label-free quantitative phase

Compared to fluorescent dyes routinely used in fluorescence microscopy, label-free quantitative phase imaging does not provide biological specificity but provides a physical specificity to underlying structures of samples (DNA, proteins, lipids...). Although some cellular structures can be well recognized by the naked eye in a quantitative phase (nucleus, nucleoli, mitochondria, and some others), most others are not.

 "Synthetic" staining using deep learning is however possible in this case: such approach is applicable to highlight fluorescently labelled structures from a label-free image without actual fluorescent labelling [78].

Such approach is of great biological interest for live-cell imaging as in many cases fluorescent staining is not possible (due to technical obstacles), requires fixation or causes phototoxicity and is thus not suitable for time-lapse experiments. First, we employed a U-Net and SegNet

convolutional neural networks (CNN) to generate the synthetic staining in the following paper [72] and used a segmentation overlap with nuclei masks (segmented based on the nuclear channel) as a metric. We determined a dice coefficient 0.78 for PNT1A and DU-145 cell line synthetic nuclei staining (this metric is explained in our Vicar et al study [47], chapter 4.1).

VICAR, T., J. GUMULEC, J. BALVAN, M. HRACHO, et al. Label-Free Nuclear Staining Reconstruction in Quantitative Phase Images Using Deep Learning. In L. LHOTSKA, L. SUKUPOVA, I. LACKOVIC AND G.S. IBBOTT. *World Congress on Medical Physics and Biomedical Engineering 2018, Vol 1.* New York: Springer, 2019, vol. 68, p. 239-242.

Label-Free Nuclear Staining Reconstruction in Quantitative Phase Images Using Deep Learning

Tomas Vicar, Jaromir Gumulec, Jan Balvan, Michal Hracho, and Radim Kolar

Abstract

Fluorescence microscopy is a golden standard for contemporary biological studies. However, since fluorescent dyes cross-react with biological processes, a label-free approach is more desirable. The aim of this study is to create artificial, fluorescence-like nuclei labeling from label-free images using Convolution Neural Network (CNN), where training data are easy to obtain if simultaneous label-free and fluorescence acquisition is available. This approach was tested on holographic microscopic image set of prostate non-tumor tissue (PNT1A) and metastatic tumor tissue (DU145) cells. SegNet and U-Net were tested and provide "synthetic" fluorescence staining, which are qualitatively sufficient for further analysis. Improvement was achieved with addition of bright-field image (by-product of holographic quantitative phase imaging) into analysis and two step learning approach, without and with augmentation, were introduced. Reconstructed staining was used for nucleus segmentation where 0.784 and 0.781 dice coefficient (for DU145 and PNT1A) were achieved.

Keywords

Deep learning • Quantitative phase imaging
Cell analysis • Cell nuclei segmentation

T. Vicar (✉) · M. Hracho · R. Kolar
Department of Biomedical Engineering, Brno University of Technology, Brno, Czech Republic
e-mail: vicar@feec.vutbr.cz

T. Vicar · J. Gumulec
Department of Pathological Physiology, Masaryk University, Brno, Czech Republic

J. Gumulec · J. Balvan
Department of Physiology, Masaryk University, Brno, Czech Republic

J. Gumulec
Central European Institute of Technology, Masaryk University, Brno, Czech Republic

1 Introduction

Fluorescence microscopy is a golden standard for contemporary biological studies. Regardless of the staining probe used, the purpose of such approach is to (1) identify individual cells, (2) localize processes to cytoplasm/nucleus or to (3) facilitate cell tracking in image analysis. Nevertheless, the usage of any fluorescent probes, e.g. transfection-based ones (see [1]) affect the cellular physiology due to unavoidable photo-toxicity. This include changes in cellular morphology, migration, division and various others. With this in regard, a label-free approach is an promising alternative. While most of the other label-free microscopic techniques (DIC, PC, etc.) suffer from artifacts like a halo in phase contrast, a quantitative phase imaging lacks those. Thus the image processing is dramatically easier.

Convolution neural networks (CNNs) has proved to be efficient tool for both classification and segmentation tasks, including applications on biological data like microscopic cell images [2]. Major disadvantage of such process is high demands for training data, where creation of labeled database is highly time consuming and biological tasks often require an expert. Our approach to deal with this task for cell nuclei segmentation, is to use fluorescence staining from simultaneous acquisition of fluorescence and label-free modality. If we train a model on such data, this model then can be used for nuclei segmentation on data without fluorescence. This approach therefore enables a creation of a training set with tens of thousands of cells without the need of manual annotations.

2 Materials and Methods

2.1 Experimental Data

Adherent cell lines from prostate non-tumor tissue (PNT1A) and metastatic tumor tissues (DU145) were used in the experiment. All cell lines were cultured in RPMI-1640

medium supplemented with antibiotics (penicillin 100 U/ml and streptomycin 0.1 mg/ml) with 10% fetal bovine serum (FBS). Prior microscopy acquisition, the cells were maintained at 37 °C in a humidified (60%) incubator with 5% CO_2 (Sanyo, Japan). For acquisition purposes, the cells were cultivated in Flow chambers μ-Slide I Lauer Family (Ibidi, Martinsried, Germany).

Objective Nikon Plan 10/0.3 was used for hologram acquisition with a CCD camera (XIMEA MR4021MC). For the fluorescence mode a solid state light source (Lumencor Aura II) was used and images were captured by sCMOS camera (Andor Zyla 5.5, 2560 × 2160 px). Holographic data were numerically reconstructed with Fourier transform method (described in [3]) and phase unwrapping was used on phase image. As a result we obtain Quantitative phase image (QPI) and amplitude image, which is practically a Bright-field (BF). Both QPI and BF images are spatially registered on fluorescence images. Ordinarily, only QPI image is used for image analysis, thanks to its contrast and desirable properties, but we decided to test addition of BF image (by-product of holographic QPI) to improve our model.

2.2 Used Models

There are plenty of CNN's pixel-to-pixel models, where the most popular are the encoder-decoder type. First, SegNet [4] network (its SegNet-Basic version) was employed, because of its ease of training, but afterwards U-net [2], which is widely used for biological tasks, has shown to have better results. Both of these networks are encoder-decoder type, where SegNet uses unpooling and U-net uses transposed convolution with concatenation of decoder data with encoder data of same degree. This block concatenation allow a better combination of high and low level features. For both networks, the original topologies from those papers were used and both networks were optimized identically as described below.

2.3 Preprocessing

One of the main problem in fluorescence data analysis is the fluctuation of intensities of the fluorescence between different cells, moreover between experiments. CNN has no chance to recognize how much fluorescence staining was captured by each cell, thus we must somehow locally normalize. Similar problem is in QPI image, where highly adhered cells have much less contrast than mitotic/apoptic cells, which are less adhered and round-shape. This issue was tested to solve with local histogram equalization using CLAHE method [5], applied on both source (QPI/BF) and desired (fluorescence) images. CLAHE is widely used as a preprocessing of CNNs (e.g. [6]), but we even use it on the

fluorescence (label) images. The disadvantage of this approach is that resulting "synthetic" fluorescence is equalized-like and the original fluorescence can not be reconstructed. Both QPI and BF pixel intensities were z-scored with mean and standard deviation computed from whole training database (QPI has exactly quantified values, thus single image z-score would lead to loss of information).

2.4 Network Implementation

For training we constructed image triples of QPI, BF and fluorescence images—where 10/14 fields of view (FOVs) were used for training and 4/14 FOVs were used for testing and evaluation (each FOV contains 30 time-lapse images—1.5 h of recording, all FOVs and time points were mixed together). Network were trained with Adam optimizer [7] (learning rate 0.001, $\beta_1 = 0.9$ and $\beta_2 = 0.99$—which is all the default settings from the paper) and Mean Squared Error (MSE) loss (L2 loss) was used as an optimization criteria. Small 320 × 320 px randomly selected patches were used for training, which were cropped from original 600 × 600 px images. PyTorch 0.3.0 was used for network implementation and training.

Many test with a dropout and data augmentation with rotation, shearing and scaling were done, but neither leads to good convergence of the network. However, these techniques can significantly improve network generalization. For this reason, a modified two step learning was employed— learning without data augmentation (only random choosing of patches were employed) for pre-training of the network and re-training with the data augmentation (flipping, scaling, shearing and rotation before patch selection). The typical progress of MSE during learning is shown on Fig. 1, where test data MSE was 0.304 and 0.364 for the two step learning and learning without the augmentation, respectively. Moreover we tested L1 and Huber (L2 for small and L1 for large values) loss instead of L2 (MSE), but both lead to visually less sufficient results.
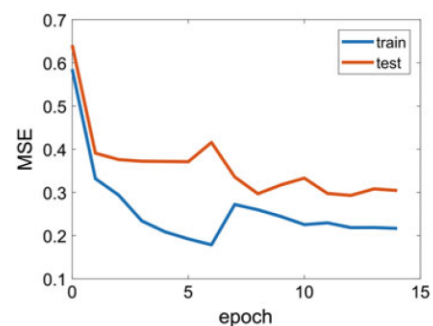
**Fig. 1** Example of model MSE on training and testing datasets for U-Net, QPI + BF images and PNT1A cells

Table 1 MSE and Dice between original and reconstructed nuclear staining images (with U-net unless otherwise stated), * value is not comparable with others

Value	Cell line	QPI	BF	QPI + BF	QPI + BF SegNet	QPI + BF CLAHE
MSE	DU145	0.311	0.451	0.285	0.336	0.0028*
	PNT1A	0.335	0.590	0.304	0.381	0.0024*
Dice	DU145	0.758	0.622	0.784	0.767	0.752
	PNT1A	0.712	0.542	0.764	0.758	0.781

2.5 Nucleus Segmentation

From the "synthetic" staining, a final nucleus segmentation was obtained by thresholding with an automatic threshold method based on Poison distribution of the histogram [8] (better for cell images than Otsu), followed by morphol-ogical operations—morphological closing and elimination of small objects and holes (<50 px). Original staining was segmented similarly. This segmentation step has been performed for both, the comparison of the reconstruction results and proving the segmentability of the "synthetic" fluorescence data.
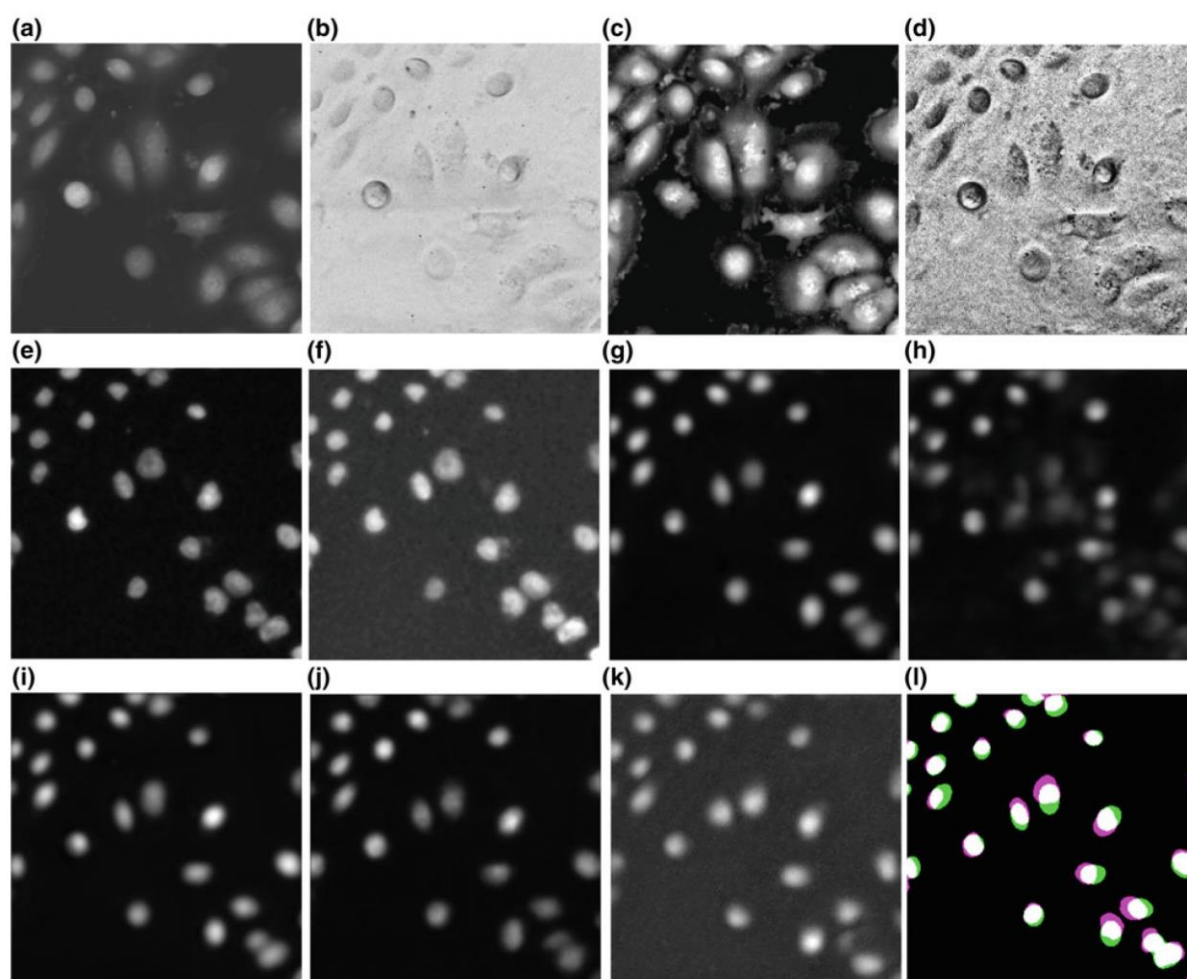
Fig. 2 Example of results for a patch of DU145 cells reconstructed with U-net unless otherwise stated. **a** QPI, **b** BF, **c** equalized QPI, **d** equalized BF, **e** fluorescence, **f** equalized fluorescence, **g–k** "synthetic" fluorescence for QPI, BF, QPI + BF, QPI + BF SegNet, QPI + BF CLAHE, (L) segmentation results from original (purple) and synthetic fluorescence (green) (dice 0.752 and for QPI + BF data used), 10 × magnification and image width 200 μm (color figure online)

3 Results

The aim of this study was to (1) create artificial masks for nuclei for further segmentation and (2) to reconstruct the structure of the nuclei. With this regard, first the accuracy of different networks can be well evaluated in term of MSE, which can be well compared between different settings. Disadvantage of MSE is data dependency and as such different cell lines or data with equalization are not comparable. As shown in Table 1, addition of BF image leads to improvement 0.026 and 0.031 for DU145 and PNT1A, respectively. U-net performed better for this task as expected. The results of non-equalized images are incomparable with equalized images, because MSE is image value-dependent, however without using of an equalization the convergence of the network was slower during the training and results were worse in images with both distinctive cells and less visible cells.

One of the main motivations for nuclear staining reconstruction is nucleus segmentation. Segmentation was evaluated in term of dice coefficient (see e.g. [9]), which is also much less data dependent and as such, thus is also better for comparison of different data sets than original MSE. As shown in Table 1, very similar results for both cell lines were achieved. Despite the fact that the images reconstructed with CLAHE are visually better, so CLAHE leads to better results for PNT1A (by 0.018 of dice), but worse results for DU145 (by 0.032 of dice). Maximal achieved dice (0.784 for DU145 and 0.781 for PNT1A) can be considered sufficient for further analysis, moreover if we consider lack of clarity of nuclei in QPI images. As you can see in Fig. 2, the main inaccuracy arises at the point of nearby nuclei, where they will be interconnected in "synthetic" fluorescence image.

4 Discussion

Overall, reconstructed "synthetic" fluorescence leads to blurry images, which may be used for localization of cell nuclei and nuclei segmentation, but their usability for precise nuclei segmentation is limited. However it is possible to consider using higher magnification. Another improvement might be done with enlargement of training database, which was relatively limited for such easy to obtain data. Using a more precise nuclei segmentation method must also be considered.

Another possible use of "synthetic" florescence could be found in cell detection (cell counting). Further analysis should be done for another staining for segmentation of other cell organelles. Other possibility is to use similar approach with staining signaling phases of cell cycle or ongoing apoptosis for detection of such states.

5 Conclusions

The proposed method can provide an easy-to-obtain annotated dataset for CNN training, which is then able to produce fluorescence-like images usable for numerous biological applications. Application of CLAHE on both source and desirable images shown to be usable approach for fluorescence image contrast normalization. The data augmentation prevents the network convergence, but two step learning approach was presented to enable the use of data augmentation. Reconstructed staining has proven to be useful for the nuclei segmentation.

Conflict of Interest The authors declare that they have no conflict of interest.

References

1. Wang, Z., Millet, L., Chan, V., Ding, H., Gillette, M.U., Bashir, R., Popescu, G.: Label-free intracellular transport measured by spatial light interference microscopy. Journal of Biomedical Optics 16(2), 026019–026019–9 (2011), http://dx.doi.org/10.1117/1.3549204
2. Ronneberger, O., Fischer, P., Brox, T.: U-net: Convolutional networks for biomedical image segmentation. In: International Conference on Medical image computing and computer-assisted intervention. pp. 234–241. Springer (2015)
3. Slaby, T., Kolman, P., Dostal, Z., Antos, M., Lostak, M., Chmelik, R.: Off-axis setup taking full advantage of incoherent illumination in coherence-controlled holographic microscope. Optics Express 21 (12), 14747–14762 (2013)
4. Badrinarayanan, V., Kendall, A., Cipolla, R.: Segnet: A deep convolutional encoder-decoder architecture for image segmentation. IEEE transactions on pattern analysis and machine intelligence 39 (12), 2481–2495 (2017)
5. Reza, A.M.: Realization of the contrast limited adaptive histogram equalization (clahe) for real-time image enhancement. Journal of VLSI signal processing systems for signal, image and video technology 38(1), 35–44 (2004)
6. Cireşan, D., Meier, U., Masci, J., Schmidhuber, J.: A committee of neural networks for traffic sign classification. In: Neural Networks (IJCNN), The 2011 International Joint Conference on. pp. 1918–1921. IEEE (2011)
7. Kingma, D.P., Ba, J.: Adam: A method for stochastic optimization. arXiv preprint arXiv:1412.6980 (2014)
8. Al-Kofahi, Y., Lassoued, W., Lee, W., Roysam, B.: Improved automatic detection and segmentation of cell nuclei in histopathology images. IEEE Transactions on Biomedical Engineering 57(4), 841–852 (2010)
9. Zou, K.H., Warfield, S.K., Bharatha, A., Tempany, C.M., Kaus, M.R., Haker, S.J., Wells, W.M., Jolesz, F.A., Kikinis, R.: Statistical validation of image segmentation quality based on a spatial overlap index1: scientific reports. Academic radiology 11(2), 178–189 (2004)

4.2.2 Quantitative phase nuclei reconstruction from unpaired images

The approach presented in chapter 4.2.1, however, needs a paired training image (correlative imaging of the same field of view acquired label-free and with staining), which is not always doable. There might exist limitations related to different sample preparation conditions, or construction aspects of microscopes disabling the correlative imaging.

Cycle-consistent generative adversarial network [79] (CycleGAN) is a machine learning technique overcoming this limitation – it is suitable for learning on non-paired data (e.g. one dataset of brightfield microscopy, the second dataset of atomic force microscopy, fluorescent or other technique). In addition to the U-Net based paired approach shown in chapter chapter 4.2.1 , this CycleGAN-based approach demonstrates that nuclear image reconstruction is possible from another dataset of quantitative phase imaging. Specifically – DU-145 cells stained with Hoechst 33258. Generation of virtual fluorescence from QPI is doable using CycleGAN: Improved Wasserstein loss [80] was used for training of dataset and results were compared to a standard supervised U-Net (Figure 1). We determined mean squared error 3.23 x 10^{-4} for U-Net and just slightly lower, but sufficient performance of CycleGAN 5.1 x 10^{-4} verifying the possibility of such approach [60].
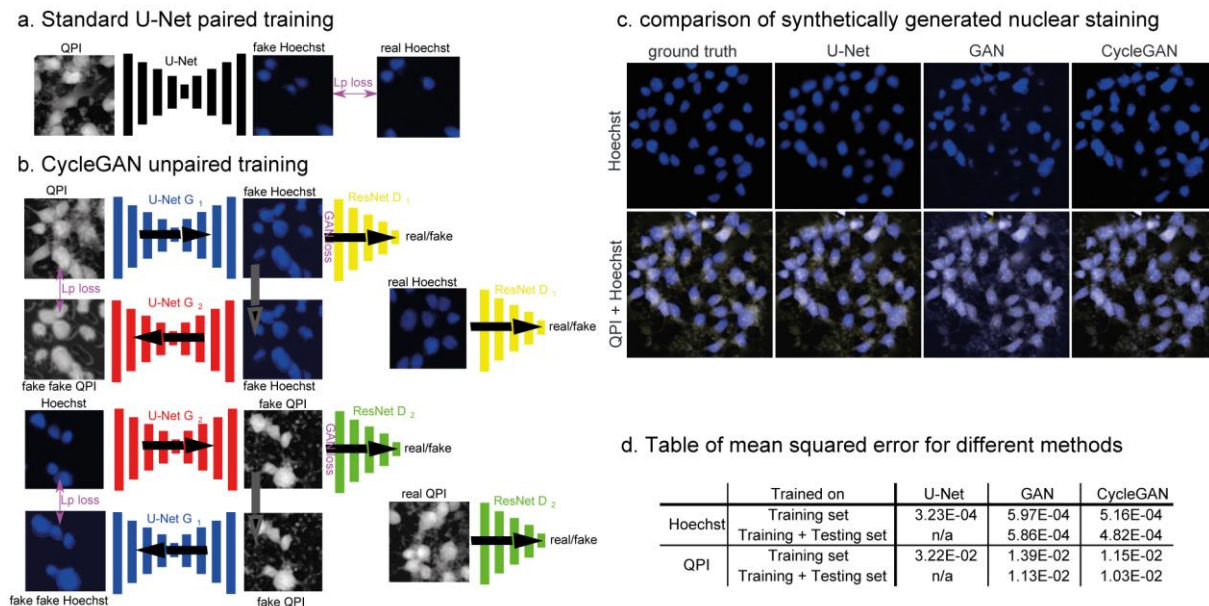

Figure 1 Generation of synthetic nuclei from quantitative phase image. a. architecture of standard paired network. b. network design of unpaired network. c. comparison of real staining and synthetic image-based on quantitative phase image. d. performance of the network. Taken from Vicar, Gumulec et al, [60],

4.3 Imaging to characterize cell mechanics

This chapter is based on the hypothesis that quantitative phase imaging provides information on cell mechanics. The rationale of such hypothesis is based on the physical properties of quantitative phase imaging (chapter 2.5.1) and the motivation is based on a fact that, compared to atomic force microscopy, QPI is faster and less invasive. In the following chapters, QPI is correlated with atomic force microscopy, Brillouin spectroscopy, confocal imaging of cytoskeleton, and related to molecular phenotype, cell migration and invasiveness.

4.3.1 Quantitative phase imaging correlates with Young modulus

In the Majercik et al. study [62] we provided a piece of evidence that prostate cancer cells characteristic by higher degree of in vitro aggressiveness (PC-3 zinc-resistant) differ from their wild-type counterparts (PC-3) in physical composition – its quantitative phase image. These findings however do not provide any clue how the cell dry mass distribution differs between wild-type and zinc-resistant cells nor what is the underlying mechanism of this finding.

With this regard, a study which further became a crucial part of this thesis was performed: In a Raudenska et al. [81] paper we focused on how cell dry mass scales with Young modulus determined by atomic force microscopy and with cytoskeletal rearrangement and therefore to provide evidence how cell dry mass is linked with cell biomechanics. Furthermore, the molecular basis of this process was explained.

Tumor cells are usually softer (of lower Young modulus as determined by AFM) compared to non-tumor counterparts and more aggressive tumor cells are usually softer than less aggressive ones [19], which is useful as an indicator of malignant potential. In the following study, we observed a disagreement with this concept: metastatic cell lines (PC-3 and LNCaP) characteristic by increased aggressiveness *in vitro* and *in vivo* were significantly stiffer than cells derived from the primary tumor (22Rv1) [2]. The Young modulus of these cells scaled with cell dry mass and with the expression of membrane protein caveolin, implicating its involvement in mechanotransduction and confirming the predictive value of QPI for biomechanical studies.

This study provides one other implication: either Young modulus or cell dry mass is in relation to the gene expression of Caveolin-1. The function of this pleotropic protein includes metabolic reprogramming, mechanotransduction, cell migration and mechanical stress responses and are in depth discussed in chapter 2.3. Here the data indicate that cells expressing high CAV1 are stiffer compared to CAV1-non-expressing cells.
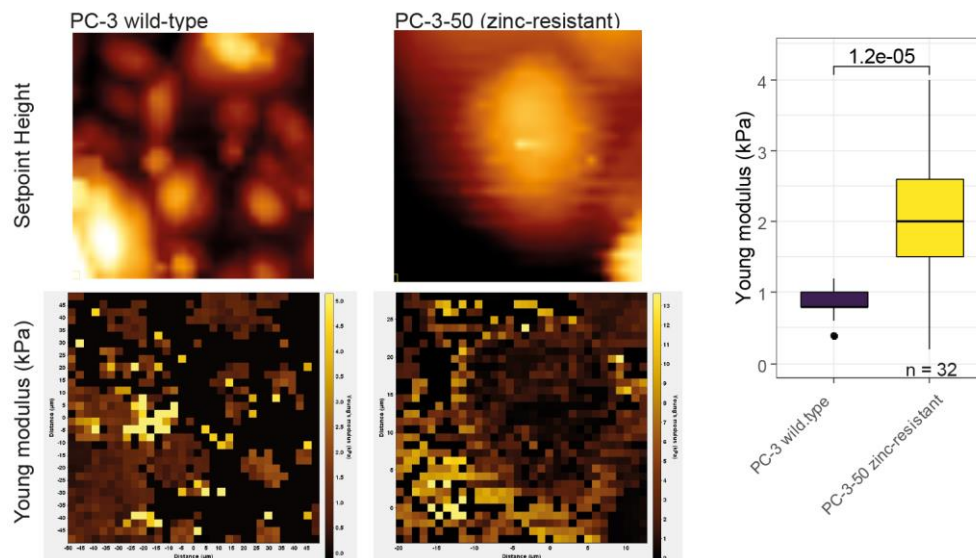
Figure 2 Young moduli and setpoint height maps determined using atomic force microscopy, representative FOVs of wild-type and zinc-resistant PC-3 cells and per-cell-average Young modulus values of 32 measured cells. From Gumulec et al. [1] and Raudenska et al. [2]

Furthermore, in the next experiment we compared the Young modulus of wild-type PC-3 and zinc-resistant PC-3-50 cells using AFM with 5 µm silica sphere probe qp-SCONT (0,01 N/m). The Young moduli calculated using Derjaguin-Muller-Toporov model were 0.99 and 2.0 kPa for wild-type and zinc-resistant PC-3 cells (Figure 2), suggesting that the zinc resistant counterparts characteristic by higher migration and invasiveness rates in vitro are stiffer, being in agreement with Kim et al study on docetaxel-resistant prostate cancer cells [2].

Mechanical properties of cells affect cell migration, adhesion, differentiation and subcellular organelle transport as well as cell metabolic state[82]. These properties are not only related to physiological functions but are also linked to a pathophysiological mechanism of diseases, cancer development in particular. One of the key features of cancer cells is the ability to migrate and invade tissues – cancer spreading, which leads to the development of metastatic tumors in distant organs [83]. More deformable cells are favoured for key cancer spreading processes – extravasation and extravasation [10]. As compared to non-tumor cells, a decrease in stiffness of cancer cells was accordingly described by numerous studies in a spectrum of tumor types [10]. Accordingly, such change of mechanical properties of cancer cells is a promising indicator of malignant potential[19], because it is a direct measurement of the cells` phenotype. This contrasts with a number of molecular markers, which, despite their high predictive value, do not correspond with the actual development of the disease. For instance, although prostatic specific antigen is a powerful diagnostic tool for prostate cancer, its function is not cancer-specific, instead, it is needed for sperm liquefaction.

However, the increase in deformability remains controversial. It is not clear whether all cells or just some subpopulation of cancer cells is softer [84], and how this depends on tumor type and tumor progression. Also, mechanisms leading to cell softening are still not explained satisfactorily.

In our lab we studied a prostate cancer model and observed a disagreement with this concept: metastatic cell lines (PC-3 and LNCaP) characteristic by increased aggressiveness *in vitro* and *in vivo* were significantly stiffer than cells derived from the primary tumor (22Rv1) [2]. In a spite of the fact that zinc plays an important role in prostate cancer development, we further developed a zinc-resistant metastatic prostate tumor cells "PC-3-res-50" [85], which demonstrated to be even stiffer (to have higher Young modulus determined by atomic force microscopy, AFM) and even more aggressive, as determined by wound-healing, colony-forming, migration assays and partly by growth speed in animal models and higher levels of glycolysis and respiration (Kratochvilova *et al*, in preparation). Gene expression profiling of those cells revealed enrichment of pathways associated with stress response, positive regulation of metabolic processes, DNA repair and cell ageing mediated mostly by RAS signalling. Moreover, our results also suggest a positive correlation between cell stiffness and cell dry mass density as determined by quantitative phase imaging and an association between Caveolin-1 expression and the total stiffness of prostate cancer cells [2]. In prostate cancer cells, an increase of stiffness in more aggressive cells was described similarly in literature [37; 38]. However, as shown by Raudenska et al study, this stiffening was not attributed to the change in actin cytoskeleton network architecture, one of the major factors determining the cell stiffness [2].

RAUDENSKA, M., M. KRATOCHVILOVA, T. VICAR, J. GUMULEC, et al. Cisplatin enhances cell stiffness and decreases invasiveness rate in prostate cancer cells by actin accumulation. Scientific Reports, 2019/02/07 2019, 9(1), 1660.

SCIENTIFIC REP⚙RTS

OPEN

Cisplatin enhances cell stiffness and decreases invasiveness rate in prostate cancer cells by actin accumulation

Martina Raudenska [1], Monika Kratochvilova[1], Tomas Vicar [2,3], Jaromir Gumulec [1,2,4], Jan Balvan [1,2,4], Hana Polanska[2], Jan Pribyl[5] & Michal Masarik [1,2,4]

We focused on the biomechanical and morphological characteristics of prostate cancer cells and their changes resulting from the effect of docetaxel, cisplatin, and long-term zinc supplementation. Cell population surviving the treatment was characterized as follows: cell stiffness was assessed by atomic force microscopy, cell motility and invasion capacity were determined by colony forming assay, wound healing assay, coherence-controlled holographic microscopy, and real-time cell analysis. Cells of metastatic origin exhibited lower height than cells derived from the primary tumour. Cell dry mass and *CAV1* gene expression followed similar trends as cell stiffness. Docetaxel- and cisplatin-surviving cells had higher stiffness, and decreased motility and invasive potential as compared to non-treated cells. This effect was not observed in zinc(II)-treated cells. We presume that cell stiffness changes may represent an important overlooked effect of cisplatin-based anti-cancer drugs. Atomic force microscopy and confocal microscopy data images used in our study are available for download in the Zenodo repository (https://zenodo.org/, Digital Object Identifiers:10.5281/zenodo.1494935).

Atomic force microscopy (AFM) is a three-dimensional high-resolution topographic technique suitable for biological applications in native conditions[1] with the ability to measure cantilever probe bending with an extremely high precision[2]. Moreover, AFM emerged as a powerful tool to obtain biomechanical properties of biological samples including biomolecules and cells[1,3–6]. The method of nanomechanical mapping of cell surfaces is based on works published by Nikolaev and Thomas[7,8].

It was shown that cell stiffness determined by AFM can be used as a marker for cancer progression and metastatic potential[9–11]. Different cancer types feature distinct cell stiffness[12] and a connection between attenuated cell stiffness and increased invasion capacity was also observed[13]. Furthermore, cytoskeletal architecture changes induced by stress (anti-cancer drugs or fluid shear stress in the circulatory system during metastatic processes) were shown to influence biomechanical features of cancer cells significantly[4,14,15]. Since the cellular bio-mechanical characteristics including cell stiffness are very important for cell motility[9], changes in the cytoskeletal architecture and consequent changes in the cell stiffness, cell dry mass, and motility could represent important secondary effects of many cytostatic drugs.

We studied the effect of two widely used anticancer drugs docetaxel and cisplatin on a panel of prostate cancer cell lines by using AFM, quantitative phase imaging and assays analyzing migratory and invasiveness potentials. Furthermore, the effect of zinc supplementation on the biomechanical characteristics of prostate cancer cells was also tested because zinc(II) ions play a key role in the prostate gland metabolism and contribute to the number of biological processes such as apoptosis, signal transduction and cell invasiveness[16–18]. Docetaxel

[1]Department of Physiology, Faculty of Medicine, Masaryk University/Kamenice 5, CZ-625 00, Brno, Czech Republic. [2]Department of Pathological Physiology, Faculty of Medicine, Masaryk University/Kamenice 5, CZ-625 00, Brno, Czech Republic. [3]Department of Biomedical Engineering, Faculty of Electrical Engineering and Communication, Brno University of Technology, Technicka 3058/10, CZ-616 00, Brno, Czech Republic. [4]Central European Institute of Technology, Brno University of Technology, Technicka 3058/10, CZ-616 00, Brno, Czech Republic. [5]Central European Institute of Technology, Masaryk University/Kamenice 5, CZ-625 00, Brno, Czech Republic. Martina Raudenska and Monika Kratochvilova contributed equally. Correspondence and requests for materials should be addressed to M.M. (email: masarik@med.muni.cz)

is a second-generation taxane derived from the needles of *Taxus baccata*. The primary mechanism of action for docetaxel is to promote and stabilize microtubulin assembly, thereby blocking microtubule dynamics. Consequences include impairment of mitotic progression, cell cycle arrest, and inhibition of cell proliferation[19]. Furthermore, some studies indicate that DNA is not the only cellular target for cisplatin, but that it may also affect cytoskeleton[20,21]. These additional interactions could enhance the anti-proliferative effect and contribute to the anti-cancer effects of cisplatin such as inhibition of growth and migration. An important aim of this study was to reveal changes in the cell stiffness after treatment (zinc, docetaxel, cisplatin) and to assess the effect of this changed cell stiffness on cell invasiveness and migration of prostate cancer cells in different stages of cancer disease progression. The second question we wanted to answer was whether the expression of *CAV1* gene in prostate cancer cells reflects their bio-mechanical phenotypes because Cav1 has been recently linked to cell stiffness through the regulation of actin remodelling and focal adhesions[22,23].

Methods

Chemical and biochemical reagents. RPMI-1640 medium, Ham's F12 medium, fetal bovine serum (FBS) (mycoplasma-free), penicillin/streptomycin, and trypsin were purchased from Sigma Aldrich Co. (St. Louis, MO, USA). Phosphate buffered saline PBS was purchased from Invitrogen Corp. (Carlsbad, CA, USA). Ethylenediaminetetraacetic acid (EDTA), zinc(II) sulphate (BioReagent grade, suitable for cell cultures) and all other chemicals of ACS purity including docetaxel were purchased from Sigma Aldrich Co. (St. Louis, MO, USA) unless noted otherwise.

Cell cultures. Four human prostatic cell lines were used in this study. The PNT1A human cell line is derived from normal adult prostatic epithelial cells immortalized by transfection with a plasmid containing SV40 genome with defective replication origin. The primary culture was obtained from the normal prostatic tissue of a 35-year old male *post-mortem*. PNT1A is PTEN positive non-tumorigenic epithelial cell line[24]. PNT1A cells harbour wild-type p53. However, SV40 induced T-antigen expression inhibits the activity of p53[25,26]. This cell line had lost the expression of androgen receptor (AR) and prostate-specific antigen (PSA)[27,28]. 22Rv1 is the human prostate carcinoma epithelial cell line derived from a xenograft serially propagated in mice after castration. The cell line expresses prostate specific antigen (PSA). Growth is weakly stimulated by dihydroxytestosterone and lysates are immunoreactive with AR antibody. 22Rv1 is PTEN and p53 positive[29,30]. The PC-3 human epithelial cell line was established from a 4-grade prostatic adenocarcinoma, androgen-independent and unresponsive metastatic site in the bone. PC-3 is PTEN-, AR-, PSA-, and p53-negative[26,28,29]. The LNCaP cell line was established from a lymph node metastasis of the hormone-refractory patient and contains a mutation in the AR gene. This mutation creates a promiscuous AR that can bind to different types of steroids. LNCaP are AR-positive, PSA-positive, PTEN-negative and harbor wild-type p53[28,30]. All cell lines used in this study were purchased from HPA Culture Collections (Salisbury, UK).

Cell cultivation. The PNT1A, LNCaP, and 22Rv1 cells were cultured in the RPMI-1640 medium with 10% FBS. The PC-3 cells were cultured in the Ham's F12 medium with 10% FBS. Both media were supplemented with antibiotics (penicillin 100 U/ml and streptomycin 0.1 mg/ml). The cells were maintained at 37 °C in the humidified (60%) incubator with 5% CO_2 (Sanyo, Japan).

MTT viability assay. The MTT assay was used to determine the cell viability. After a passage, the suspension of cells in growth media was diluted to a concentration of 2 000–10 000 cells/200 ul and transferred into 96-well plate. On each plate, positive and negative control was carried out. The plates were incubated for 2 days at 37 °C to ensure cell adhesion. Docetaxel and cisplatin were added in fresh media at increasing concentrations (0–400 nM for docetaxel and 0–150 μmol/l for cisplatin). The plates with the treatment were incubated for 24 h. Subsequently, the medium was changed to a fresh medium with MTT (4:1, MTT 5 mg/ml in PBS) and incubated for 4 h in the incubator in the dark. DMSO was used to dissolve MTT – formazan crystals and absorbance was measured at 570 nm (VersaMax microplate reader, USA).

Cisplatin and docetaxel treatment of cell cultures. Cells confluent up to 50–60% were washed with a FBS-free medium and treated with a fresh medium with FBS and required antineoplastic drug concentration (IC50 concentration for the particular cell line). The cells were treated with 93 μM (PC-3), 38 μM (PNT1A), and 24 μM (22Rv1) of cisplatin (Sigma-Aldrich, St. Louis, Missouri), respectively. IC50 concentrations used for treatment with docetaxel (Sigma-Aldrich, St. Louis, Missouri) were 200 nM for PC-3, 70 nM for PNT1A, and 150 nM for 22Rv1. The cells were cultivated under these conditions for 24 h. Subsequently, the cells were washed with an FBS-free medium and treated with a fresh medium with FBS. Non-viable cells were washed out and the viability of remaining cells was checked by microscopy. AFM, coherence-controlled holographic microscopy, invasion assay, colony forming assay and wound healing assay followed.

Long-term zinc (II) treatment of cell cultures. Cells were cultivated in the constant presence of zinc(II) ions. Concentrations of zinc(II) sulphate in the medium were increased gradually by small changes of 25 or 50 μM. The cells were cultivated at each concentration no less than one week before harvesting and their viability was checked before adding more zinc. This process was used to select zinc resistant cells naturally and to ensure better accumulation of zinc within the cells (accumulation of zinc is usually poor during the short-term treatment of prostate cancer cells)[18]. Total time of the cultivation of cell lines in the zinc(II)-containing media exceeded one year. Resulting concentrations of zinc(II) in the media (IC50 for the particular cell line) were 50 μM for the PC-3 cell line, 150 μM for the PNT1A cell line, and 400 μM for the 22Rv1 cell line. The concentrations of zinc(II) in the media and FBS were taken into account. The cells were washed with an FBS-free medium and treated with a fresh

medium with FBS. AFM, coherence-controlled holographic microscopy, invasion assay, colony forming assay and wound healing assay followed.

RNA isolation, cDNA preparation. The cultivation medium was removed and the cells were washed with PBS and trypsinized. TriPure Isolation Reagent (Roche, Basel, Switzerland) was used for RNA isolation. RNA samples without reverse transcription were used as negative control for qRT-PCR to exclude DNA contamination. The isolated RNA was used for the cDNA synthesis. RNA (1000 ng) was transcribed using the transcriptor first strand cDNA synthesis kit (Roche, Switzerland) according to manufacturer's instructions. The cDNA (20 μl) prepared from the total RNA was diluted with RNase free water to 100 μl and the amount of 5 μl was analyzed directly.

Quantitative real-time polymerase chain reaction (qRT-PCR). The qRT-PCR was performed using TaqMan gene expression assays with the LightCycler®480 II System (Roche, Basel, Switzerland). The amplified DNA was analyzed by the comparative Ct method using β-actin as a reference. The primer and probe sets for *ACTB* (assay ID: Hs99999903_m1), and CAV1 (assay ID: Hs00971716_m1) were selected from the TaqMan gene expression assays (Life Technologies, USA). The qRT-PCR was performed under following amplification conditions: total volume of 20 μl, initial incubation at 50 °C/2 min followed by denaturation at 95 °C/10 min, then 45 cycles at 95 °C/ 15 sec and at 60 °C/1 min.

Actin and tubulin staining. β-tubulin was labeled with anti- β tubulin antibody [EPR1330] (ab108342) at a working dilution of 1/300. The secondary antibody used was Alexa Fluor® 555 donkey anti-rabbit (ab150074) at a dilution of 1/1000. Actin was labeled with Alexa Fluor™ 488 Phalloidin (A12379, Invitrogen); 1 unit per slide. For mounting Duolink® *In Situ* Mounting Medium with DAPI (DUO82040) was used. The cells were fixed in 3.7% paraformaldehyde and permeabilized using 0.1% Triton X-100.

Confocal microscopy. The microscopy of samples was performed at the Institute of Biophysics, Czech Academy of Sciences, Brno, Czech Republic. Leica DM RXA microscope (equipped with DMSTC motorized stage, Piezzo z-movement, MicroMax CCD camera, CSU-10 confocal unit and 488, 562, and 714 nm laser diodes with AOTF) was used for acquiring detailed cell images (100 × oil immersion Plan Fluotar lens, NA 1.3). Total 50 Z slices was captured with Z step size 0.3 μm.

AFM measurements. We used the bioAFM microscope JPK NanoWizard 3 (JPK, Berlin, Germany) placed on the inverted optical microscope Olympus IX-81 (Olympus, Tokyo, Japan) equipped with the fluorescence and confocal module, thus allowing a combined experiment (AFM-optical combined images). The maximal scanning range of the AFM microscope in X-Y-Z range was 100-100-15 μm. The typical approach/retract settings were identical with a 15 μm extend/retract length, Setpoint value of 1 nN, a pixel rate of 2048 Hz and a speed of 30 μm/s. The system operated under closed-loop control. After reaching the selected contact force, the cantilever was retracted. The retraction length of 15 μm was sufficient to overcome any adhesion between the tip and the sample and to make sure that the cantilever had been completely retracted from the sample surface. Force-distance (FD) curve was recorded at each point of the cantilever approach/retract movement. AFM measurements were obtained at 37 °C (Petri dish heater, JPK) with force measurements recorded at a pulling speed of 30 μm/s (extension time 0.5 sec).

The Young's modulus (E) was calculated by fitting the Hertzian-Sneddon model on the FD curves measured as force maps (64 × 64 points) of the region containing either a single cell or multiple cells. JPK data evaluation software was used for the batch processing of measured data. The adjustment of the cantilever position above the sample was carried out under the microscope by controlling the position of the AFM-head by motorized stage equipped with Petri dish heater (JPK) allowing precise positioning of the sample together with a constant elevated temperature of the sample for the whole period of the experiment. Soft uncoated AFM probes HYDRA-2R-100N (Applied NanoStructures, Mountain View, CA, USA), i.e. silicon nitride cantilevers with silicon tips are used for stiffness studies because they are maximally gentle to living cells (not causing mechanical stimulation). Moreover, as compared with coated cantilevers, these probes are very stable under elevated temperatures in liquids – thus allowing long-time measurements without nonspecific changes in the measured signal.

Wound healing assay. After the passage process, each cell line was re-suspended and seeded into a 24-well plate, the cell amount per well in 500 μl media being optimized to 150,000 for PC-3, 150,000 for PNT1A and 200,000 for 22Rv1. After 48 h, the cells were 100% confluent and scratched into the cell monolayer. After gentle wash and change of media, each well was photographed at time 0 and after 24 h on the same spot. The photos were analyzed according to instructions from the software creator[31]. The software computed the percentage of the open wound area. Each cell line was analyzed in min. twenty four repetitions.

Real-time impedance-based cell proliferation and invasiveness assay. The impedance-based real-time cell analysis (RTCA) xCELLigence system was used according to supplier's (Roche Applied Science and ACEA Biosciences, San Diego, CA, USA) instructions. The xCELLigence system consists of four main components: RTCA DP station, RTCA computer with integrated software and disposable CIM-plate 16. Firstly, seeding concentration optimal for proliferation and invasion assay was determined. Response optimal for the proliferation assay was found in the well containing 10,000 cells. After seeding a total number of cells in 200 μl of medium to each well in E-plate 16, attachment and proliferation of the cells were monitored every 15 min. For the invasiveness assay, optimal response was found in the well containing 20,000 cells. After coating the upper wells with Matrigel and after adding FBS as a chemoattractant, a total number of cells in 100 μl of medium to each well in CIM-plate 16 was seeded. Attachment and growth of the cells through the matrigel were monitored every 15 min.

Duration of all experiments was 150 h. Relative invasiveness rate was defined as the cell index for matrigel-coated wells (cells need to decompose matrigel to produce signal) at a given time point. The impedance of electron flow caused by adherent cells is reported using a unitless parameter called Cell Index (CI), where CI = (impedance at time point n – impedance in the absence of cells)/nominal impedance value). In order to compare between cell lines/treatments, those cell indices were normalized to value 1.0 at the time when treatment was added.

Colony forming assay. Colony forming assay is a method of choice to determine cell reproductive death after cytotoxic treatment. Only a fraction of seeded cells retains the capacity to produce colonies. Cells were harvested with trypsin in EDTA and centrifuged at 2700 rpm/7 min. Then the cells were re-suspended in the fresh medium and counted using CASY® Cell Counter. The cells were seeded onto 6–well plates. Each well contained 2 ml media and 100, 500, 1,000 or 2,000 cells. The plates were cultivated for 1–3 weeks. Optimal seeding was 500 cells. Any shaking or moving with plates was prevented to obtain clear colonies. The cells were subsequently fixed with cold methanol and visualised with the trypan blue.

Quantitative phase imaging. Quantitative phase imaging was performed by using Tescan multimodal holographic microscope Q-PHASE. Cells were cultivated in Flow chambers µ-Slide I Lauer Family (Ibidi, Martinsried, Germany). To image a sufficient number of cells in one field of view, lens Nikon Plan 10/0.30 were chosen. Holograms were captured by CCD camera (XIMEA MR4021 MC-VELETA). Complete image reconstruction and image processing were performed in Q-PHASE control software. Cell dry mass values were derived according to[32,33] from the phase, eq. (1)

$$m = \frac{\varphi\lambda}{2\pi\alpha} \tag{1}$$

where m is cell dry mass density (in pg/µm²), φ is detected phase (in rad), λ is wavelength in µm (0.65 µm in Q-PHASE), and α is specific refraction increment ($\approx$0.18 µm³/pg). All values in the formula except the Phi are constant. Phi (Phase) is the value measured directly by microscope.

Statistical analysis and image processing. Quantitative phase images were analyzed with Q-PHASE control software, which includes segmentation based on watershed with region merging, followed by feature extraction (mass, circularity and position) for the following analysis. AFM and colony forming assay images were analyzed with MATLAB custom scripts. For the AFM images, segmentation masks were created by watershed segmentation of Setpoint Height images with manual corrections, then the masks were used for the extraction of mean cell values of both Setpoint Height and Young's modulus images. For the colony forming assays, regions of interest were chosen by registration of each image to the reference image (with manually labeled area of interest). Next, the colonies were segmented by thresholding of the blue component of image transformed into Lab color space, where single fixed threshold was used. Finally, the fraction of areas covered by colonies was computed.

Fluorescence microscopy data were analyzed in ImageJ 1.52h and Python 3.7.1 as follows: cells were manually segmented using actin fluorescence channel, two regions were created for analysis: whole cell and cell periphery, lining a 4 µm thick region around cell border and including most of periphery actin cytoskeleton. In these two regions following parameters were measured for both actin and tubulin fluorescence: Integrated intensity, median intensity, and following regions were measured to describe cell morphology: Cell area, Maximum caliper (max feret diameter), roundness, and aspect ratio. Moreover, stress fibers were manually segmented in every cell and following parameters were measured: number of fibers per cell, feret angle of fiber, integrated intensity, fiber length, mean intensity. Next, a standard deviation of feret angles of individual fibers was calculated relatively to mean of feret angle using a circstd function from scipy package for Python.

Data were checked for normality, based on which either paired ANOVA or Kruskal–Wallis test were applied in order to test the impact of the tested factors (cell line, resistance, treatment), and either Pearson or Spearman correlation were applied in order to test dependency between variables. MATLAB 2017a (Statistics and Machine Learning Toolbox) was used for this statistical analysis with p < 0.05 considered as significant.

Results

Biomechanical profiling of non-treated prostate cells. Force-indentation curves were successfully acquired for 68 LNCaP, 42 PC-3, 20 22Rv1 and 64 PNT1A non-treated cells to which the Hertz model was fitted. The Hertz model worked well in the used indentation range (example in Fig. 1e for PC-3 cells). Coherence-controlled holograms were successfully acquired for 104 LNCaP, 17 PC-3, 99 22Rv1 and 77 PNT1A cells. Figure 1a,b (AFM) and Fig. 1c,d (coherence-controlled holographic microscopy) show representative profiles of each of the cell lines used in this work. The median Young's moduli values, cell mass values and *CAV1* gene expression obtained for these four cell lines are shown in Fig. 1f. The values of Young's moduli were within the range reported in the literature[9]. The median values of Young's moduli were E = 997 Pa for LNCaP, 1210 Pa for PC-3, 1153 Pa for PNT1A and 671 Pa for 22Rv1. The Young's moduli obtained for the 22Rv1 cells were significantly lower than those obtained for the PC-3, PNT1A and LNCaP cells (p ≤ 0.009 in all cases, for details, see Supplementary Tab. S1). On the other hand, no significant changes in cell stiffness were found between the PC-3, PNT1A and LNCaP cells. The observed values of Young's moduli followed similar trends with cell dry mass measured by coherence-controlled holographic microscopy and with *CAV1* gene expression (see Fig. 1f).

Significant cell height (Setpoint Height) differences were observed between the PNT1A and PC-3 cells (p ≤ 0.001), PNT1A and LNCaP cells (p = 0.001) and between 22Rv1 and PC-3 cells (p = 0.039). Cells of metastatic origin were significantly flatter than cells derived from a primary tumour or benign tissue (p ≤ 0.001, Fig. 1g). The LNCaP cells also showed correlation between cell height and cell stiffness stronger than the other types of cells (Fig. 1b).

111
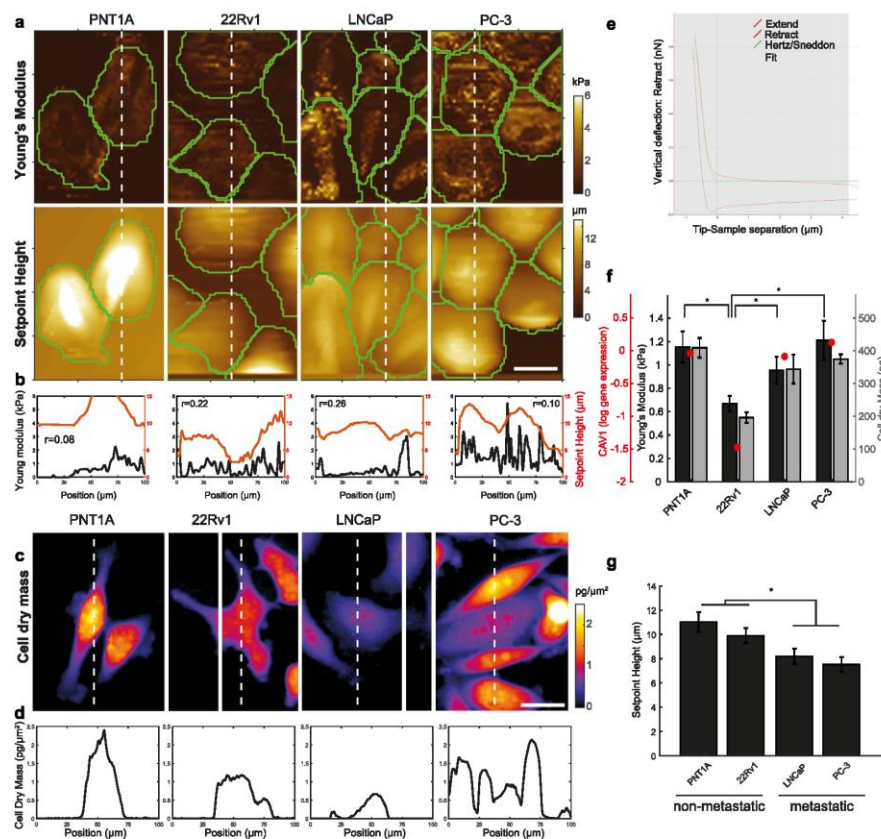
Figure 1. Cell stiffness, cell dry mass and CAV1 expression of untreated prostate cancer cell lines. (**a**) Cell stiffness maps determined by indentation (Young's modulus) of prostatic cells (first row) and cell height (displayed as Setpoint Height, second row). (**b**) Profile of Setpoint Height/Young's modulus of red/blue lines shown in A together with pixel Pearson correlation values. (**c**) Cell dry mass. (**d**) Profile of cell dry mass in the corresponding cutting point (white line). (**e**) Hertz model fitting to a force curve obtained on PC-3 cells. (**f**) Values of Young's modulus, Cell dry mass, CAV1 gene expression for prostatic cells. Statistical significance shown for Young's modulus only. (**g**) Setpoint Height of cells. Significance between metastatic and non-metastatic cells highlighted. Calibration bars for A and C represent 25 μm. Error bars denote standard errors. Asterisk indicates statistical significance at p < 0.05. For detailed statistics see Supplementary Table S1.

Effect of cytostatics on cell biomechanics and morphology. We analyzed cell stiffness, cell dry mass, and cell height in cells that had survived the chosen 24 h treatments (1x IC50 of zinc(II), cisplatin, and docetaxel; for MTT see Fig. 2a). Force-indentation curves were successfully acquired for 27 PC-3, 41 22Rv1 and 84 PNT1A cisplatin-treated cells, for 23 PC-3, 23 22Rv1 and 23 PNT1A zinc(II) treated cells, and for 83 PC-3, 26 22Rv1 and 61 PNT1A docetaxel-treated cells. Figure 2b shows representative profiles for each treatment. Coherence-controlled holograms were successfully acquired for 118 PC-3, 187 22Rv1 and 33 PNT1A cisplatin-treated cells, for 61 PC-3, 67 22Rv1 and 37 PNT1A zinc(II) treated cells, and for 19 PC-3, 107 22Rv1 and 39 PNT1A docetaxel-treated cells.

Because no significant changes in cell stiffness, cell flatness, and cell dry mass were found between the metastatic cell lines PC-3 and LNCaP, only the more aggressive PC-3 cell line was included in further experiments. In all tested cell lines (PNT1A, 22Rv1 and PC-3), cells treated with the cytostatic drugs (cisplatin or docetaxel) had a higher Young's modulus (were stiffer) as compared to non-treated cells (p ≤ 0.007 in all tested cell lines). Docetaxel increased cell stiffness more effectively than cisplatin (p ≤ 0.001). On the other hand, this effect was not observed in the zinc(II) treated cells (see Fig. 2b,c and Supplementary Tab. S1). Consequently, changes in cell stiffness due to cisplatin treatment do not result from simple metal accumulation in the cells (platinum or zinc) but are connected with changes in the cytoskeletal organization (for illustration see Fig. 3 and Supplementary Fig. S1 with fluorescent staining of tubulin and actin). Using an image analysis, it was observed, that cisplatin causes significant increase of actin density (determined by increased integrated density of actin fluorescence)
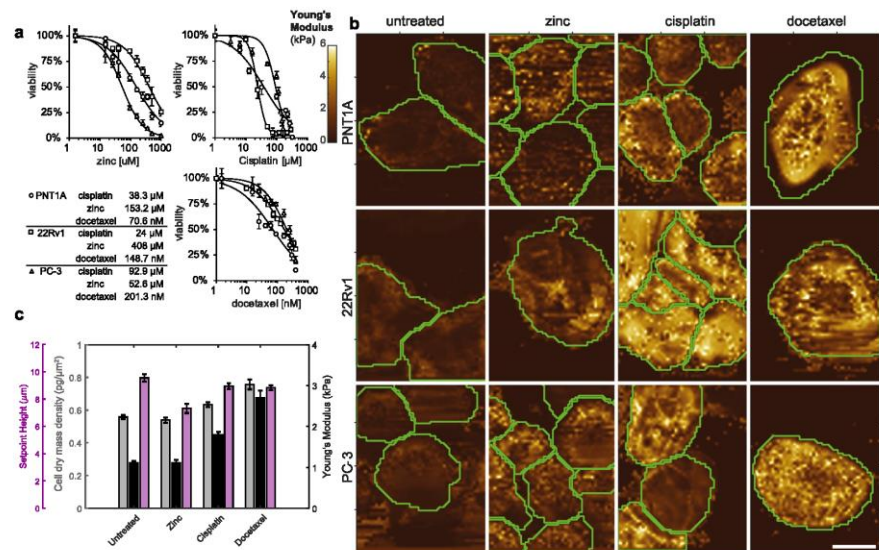
Figure 2. Changes in biomechanical features; effect of treatment. (**a**) MTT test and respective IC50 concentration values. For detailed statistics see Supplementary Table S1. (**b**) Representative Young's moduli maps of cell lines treated with zinc(II), docetaxel, and cisplatin. (**c**) Young's moduli (cell stiffness), Setpoint Height, and cell dry mass density changes after zinc(II), docetaxel and cisplatin treatment. All tested cell lines (PNT1A, 22Rv1 and PC-3) assessed together. Error bars denote standard errors.

and in particular, increased number of stress fibers, their increased length and fluorescent intensity (Fig. 3b,c and Supplementary Table S2). With regard to tubulin, no increase of cell periphery tubulin content was observed after cisplatin treatment. On the other hand, docetaxel treatment caused distinct accumulation of tubulin in cell periphery (described by increased median and integrated fluorescence density). Elongation of actin fibers was observed as a non-specific marker of cell stress, caused by all types of treatments used in this study.

Cell dry mass density values measured by coherence-controlled holographic microscopy followed the trend of Young's modulus. On the other hand, no significant changes were observed in cell height due to the cytostatic treatment (values of Setpoint Height) (Fig. 2c).

Next, the association was analyzed between morphological parameters, cell treatment and the cell type (Fig. 4). Cell circularity differed distinctly and tended to be significantly lower due to the zinc treatment and higher due to the cisplatin and docetaxel treatments in the 22Rv1 and PNT1A cells. However, no significant association between the treatments and cell circularity was observed in the metastatic PC-3 cells.

Migration, invasiveness and cytostatic treatment. To establish the relationship between the changes in cell stiffness and the metastatic potential of prostate cancer cells, we performed invasion assay, colony forming assay and wound healing assay of cells that had survived the cisplatin, docetaxel and zinc treatment, and of non-treated cells. Simple migration ability was tested by wound healing assay and verified by real-time coherence-controlled holographic microscopy (Fig. 5). Due to the cisplatin and docetaxel treatment, a significant reduction of cell migration was observed in all tested cell lines according to the wound-healing assay. This trend was observable also in the coherence-controlled migration assay, but did not gain statistical significance for PNT1A and PC-3. On the other hand, the zinc treatment enhanced the migration speed in the PNT1A cells (Fig. 5a,b). The circularity of the cells was in the negative correlation with the migration speed after the zinc and cytostatic treatments ($r_{Sp} = -0.33$; $p = 0.0001$ for zinc and $r_{Sp} = -0.48$; $p = 0.0001$ for cytostatic drugs). On the other hand, the cell circularity showed no association with the cell migration speed in the non-treated cells.

Furthermore, the ability of cancer cells to spread to the surrounding tissues was tested by using the label-free impedance-based real-time cell analysis, where the cells must be able to go through the matrigel. Due to the cisplatin and docetaxel treatment, a significant reduction of cell invasion was observed (Fig. 6a). Conversely, the long-term zinc treatment enhanced the ability to invade, for the PC-3 cells in particular. To determine the reproductive death of cells that had survived the cytotoxic treatment, the colony forming assay was used. A significant reduction in colony formation was observed due to the cisplatin and docetaxel treatment, where no formation of new colonies was observed. Conversely, the long-term zinc treatment enhanced the ability to form colonies in the metastatic PC-3 cells (Fig. 6b,c).
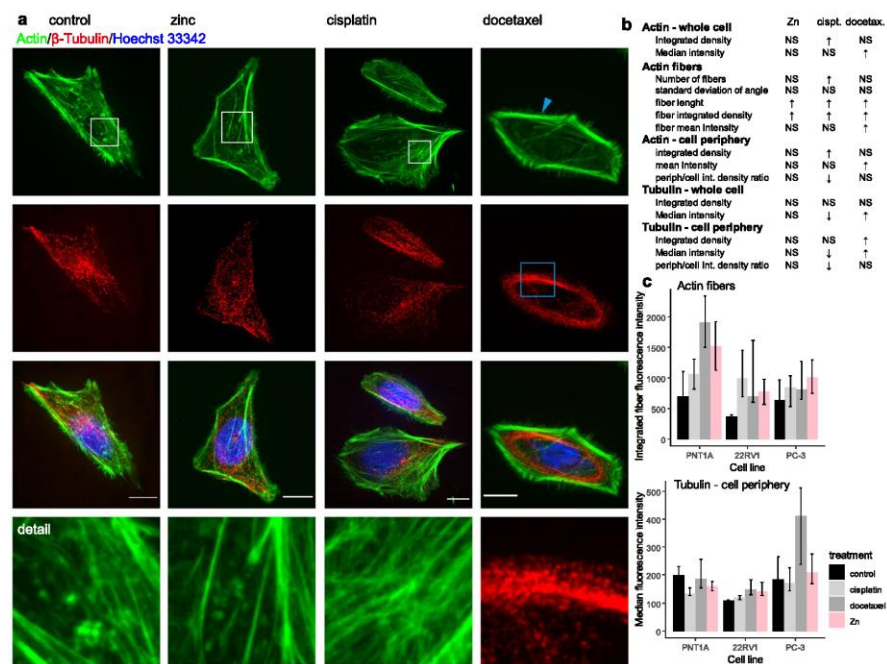
Figure 3. β-Tubulin; effect of treatment, PNT1A cells. (**a**) Tubulin fibers form a thick cables and dense shell due to docetaxel treatment (see blue square). In contrast to docetaxel that caused significant changes in microtubules, cisplatin affected actin cytoskeleton more fundamentally. Accumulation of stress fibers and/or changes in actin organization were observed. All three treatments (zinc, cisplatin, and docetaxel) caused stress fibers accumulation and/or actin disintegration in some cells (see and compare areas in the white squares), but cisplatin was the most effective in this process (all images (N = 242) and data analyses are accessible on (https://zenodo.org/, Digital Object Identifiers: 10.5281/zenodo.1494935). For remaining cell lines see Supplementary Fig. S1. Cells are shown at 100x magnification, calibration bar indicates 10 μm, detail square width 10 μm. (**b**) Results of image analysis for actin and tubulin structures, shown results for all cell lines, for detailed results of all cell lines see Supplementary Table S2 (**c**) Actin fibers, Tubulin in cell periphery (defined as a region 4 μm from the cell border). Intensity of actin fibers localized in cytoplasm (i.e. those fibers not in periphery) is increased by cisplatin treatment, tubulin fluorescence is pronounced in cell periphery after docetaxel treatment. Displayed as median and interquartile range.

Discussion

Tumour transformed cells differ from normal tissue-connected cells in many features. Significant observable differences were shown in biomechanical properties such as cell adhesion and mechanical stiffness[12,34–36]. Accordingly, cell stiffness studies showed that cancerous cells are usually less stiff than their normal counterparts[37–39]. This observation was only partially confirmed in our study. Whereas tumour cells derived from the primary tumour tissue (22Rv1 cells) were significantly softer than cells derived from the normal prostatic tissue (PNT1A cells), this was not true for metastatic cell lines (PC-3 and LNCaP).

In many studies, it was demonstrated that the low cell stiffness could serve as a marker for cell motility and malignant potential[9–11]. Nevertheless, in our case, both types of cells derived from metastatic sites (PC-3-high invasiveness, LNCaP-low invasiveness) were stiffer and flatter than tumour cells derived from the primary tumour tissue. Our results also suggest some role of CAV1 in the total stiffness of prostate cancer cells and a positive correlation between cell stiffness and cell dry mass in the non-treated cells and between cell stiffness and cell dry mass density in the treated cells. The influence of CAV1 could be managed by modulating the Rho/ROCK pathways[22]. Other studies focused on the prostate-derived cells had similar results regarding the cell stiffness[11,34,40,41].

According to our results, cytoskeleton plays a key role in the changes of biomechanical features of cancer cells, because the treatment with docetaxel that stabilizes microtubule and blocks their dynamics caused a significant enhancement of the cell stiffness. This observation is in a good agreement with other studies[4,14,15] and interestingly, the cytochalasin that is known to depolymerize the actin filaments, caused a decrease of the cell stiffness[12,42]. Furthermore, the treatment with cisplatin caused also a significant increase in the cell stiffness of prostate cancer cells and the effect of cisplatin on cytoskeleton as mentioned in[20] and[21] was confirmed. Changes in cell stiffness due to cisplatin treatment probably do not result from simple metal accumulation in the cells because no such increase was shown in the zinc-treated cells. The observed reorganization of the cell cytoskeleton
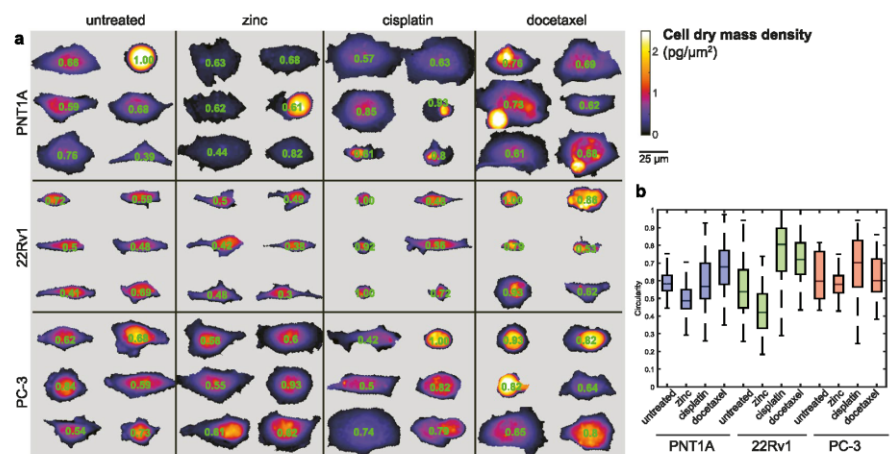
Figure 4. Cell dry mass distribution and morphology; effect of treatment. (**a**) Matrix of representative cells, coherence-controlled holographic microscopy. Longer axis orientation of the cells was unified. Numbers inside cells represent circularity, $4\pi(\text{area/perimeter}^2)$. (**b**) Circularity of the cells. Boxes and error bars represent interquartile range and 95% percentile.
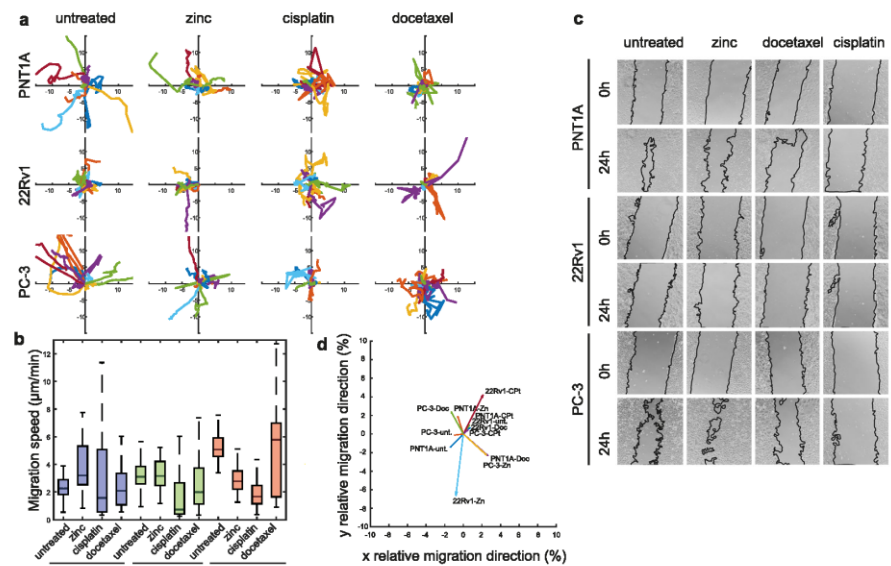
Figure 5. Changes in motility of prostate cancer cells; effect of treatment. (**a**) Rose diagram of cell migration speed obtained by coherence-controlled holographic microscopy and corresponding bar charts, (**b**) Boxes and error bars represent interquartile range and 95% percentile. (**c**) Wound-healing assay in $t = 0$ and 24 h. (**d**) Summary vector of the movements of all cells after respective treatments divided by migrated path length.

implies changes in cancer cell motility and invasiveness. Accordingly, a significant decrease in cell migration, invasion and forming of colonies was observed in cells that had survived the docetaxel and cisplatin treatments in all tested cell lines. We can speculate that this decrease is among other things a consequence of increasing cell stiffness because highly invasive cells need to be rather more pliable[9,13,37]. Consequently, changes in cell stiffness could be an important overlooked effect of antineoplastic drugs. Conversely, the zinc(II) treatment did not show such clear trends as the treatments with cisplatin and docetaxel. The effect of zinc treatment was highly influenced by the type of cell line.
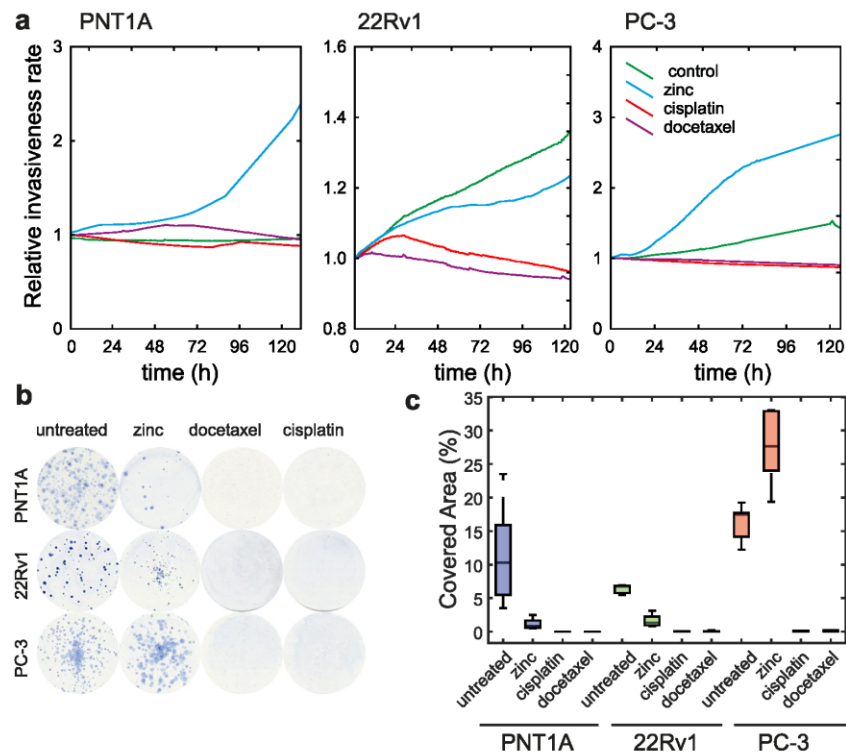
Figure 6. Changes in the invasive potential of prostate cancer cells; effect of treatment. (**a**) Impedance-based real-time cell analysis (xCELLigence invasion assay); effect of zinc(II), docetaxel, and cisplatin treatment. (**b**) Representative images of colony forming assays and calculated covered area, (**c**) Boxes and error bars represent interquartile range and 95% percentile.

Conclusions

In this study, we demonstrated AFM together with coherence-controlled holographic microscopy to bring a promising approach that helps understand the correlation between the cell structure, cell mechanics, and function (changes in migration speed, cell dry mass, cell circularity, etc.). Despite the differences in the absolute value of Young's modulus across biomechanical studies, the obtained relative changes of Young's modulus were shown to be consistent.

Both cisplatin and docetaxel treatments caused a significant increase in the cell stiffness of prostate cancer cells that had survived the treatment. Hence, we presume the effect of cisplatin on the cytoskeleton. Consequently, the decrease in cell migration, invasion and forming of colonies observed in cells surviving the docetaxel and cisplatin treatment was associated with the increasing cell stiffness. We maintain therefore that changes in the cell stiffness could be an important overlooked effect of cisplatin-based anti-cancer drugs.

Data Availability

Atomic force microscopy and confocal microscopy data images used in our study are available for download in the Zenodo repository (https://zenodo.org/, Digital Object Identifiers: 10.5281/zenodo.1494935).

References

1. Vahabi, S., Nazemi Salman, B. & Javanmard, A. Atomic force microscopy application in biological research: a review study. *Iran J Med Sci* **38**, 76–83 (2013).
2. Sundararajan, S. & Bhushan, B. Development of AFM-based techniques to measure mechanical properties of nanoscale structures. *Sensors and Actuators a-Physical* **101**, 338–351 (2002).
3. Pesl, M. *et al.* Atomic force microscopy combined with human pluripotent stem cell derived cardiomyocytes for biomechanical sensing. *Biosensors & Bioelectronics* **85**, 751–757 (2016).
4. Sharma, S. *et al.* Correlative nanomechanical profiling with super-resolution F-actin imaging reveals novel insights into mechanisms of cisplatin resistance in ovarian cancer cells. *Nanomedicine-Nanotechnology Biology and Medicine* **8**, 757–766 (2012).
5. Wang, J. *et al.* Atomic force microscope study of tumor cell membranes following treatment with anti-cancer drugs. *Biosens Bioelectron* **25**, 721–727 (2009).
6. Zhang, L., Yang, F., Cai, J. Y., Yang, P. H. & Liang, Z. H. *In-situ* detection of resveratrol inhibition effect on epidermal growth factor receptor of living MCF-7 cells by Atomic Force Microscopy. *Biosensors & Bioelectronics* **56**, 271–277 (2014).

116

7. Nikolaev, N. I., Mueller, T., Williams, D. J. & Liu, Y. Changes in the stiffness of human mesenchymal stem cells with the progress of cell death as measured by atomic force microscopy. *Journal of Biomechanics* **47**, 625–630 (2014).
8. Thomas, G., Burnham, N. A., Camesano, T. A., Wen, Q. Measuring the mechanical properties of living cells using atomic force microscopy. *J Vis Exp*, (2013).
9. Luo, Q., Kuang, D. D., Zhang, B. Y. & Song, G. B. Cell stiffness determined by atomic force microscopy and its correlation with cell motility. *Biochimica Et Biophysica Acta-General Subjects* **1860**, 1953–1960 (2016).
10. Cross, S. E., Jin, Y. S., Rao, J. & Gimzewski, J. K. Nanomechanical analysis of cells from cancer patients. *Nat Nanotechnol* **2**, 780–783 (2007).
11. Cross, S. E. *et al.* AFM-based analysis of human metastatic cancer cells. *Nanotechnology* **19** (2008).
12. Rotsch, C. & Radmacher, M. Drug-induced changes of cytoskeletal structure and mechanics in fibroblasts: An atomic force microscopy study. *Biophysical Journal* **78**, 520–535 (2000).
13. Osborne, L. D. *et al.* TGF-beta regulates LARG and GEF-H1 during EMT to affect stiffening response to force and cell invasion. *Molecular Biology of the Cell* **25**, 3528–3540 (2014).
14. Lam, W. A., Rosenbluth, M. J. & Fletcher, D. A. Chemotherapy exposure increases leukemia cell stiffness. *Blood* **109**, 3505–3508 (2007).
15. Chivukula, V. K., Krog, B. L., Nauseef, J. T., Henry, M. D. & Vigmostad, S. C. Alterations in cancer cell mechanical properties after fluid shear stress exposure: a micropipette aspiration study. *Cell Health Cytoskelet* **7**, 25–35 (2015).
16. Gumulec, J. *et al.* Insight to Physiology and Pathology of Zinc(II) Ions and Their Actions in Breast and Prostate Carcinoma. *Current Medicinal Chemistry* **18**, 5041–5051 (2011).
17. Franklin, R. B. & Costello, L. C. The Important Role of the Apoptotic Effects of Zinc in the Development of Cancers. *Journal of Cellular Biochemistry* **106**, 750–757 (2009).
18. Kratochvilova, M. *et al.* Amino Acid Profiling of Zinc Resistant Prostate Cancer Cell Lines: Associations With Cancer Progression. *Prostate* **77**, 604–616 (2017).
19. Herbst, R. S. & Khuri, F. R. Mode of action of docetaxel - a basis for combination with novel anticancer agents. *Cancer Treatment Reviews* **29**, 407–415 (2003).
20. Kopemaier, P., Muhlhausen, S. K. & Changes, I. N. The Cytoskeleton Pattern of Tumor-Cells by Cisplatin Invitro. *Chemico-Biological Interactions* **82**, 295–316 (1992).
21. Boekelheide, K., Arcila, M. E. & Eveleth, J. Cis-diamminedichloroplatinum (ii) (cisplatin) alters microtubule assembly dynamics. *Toxicology and Applied Pharmacology* **116**, 146–151 (1992).
22. Lin, H. H. *et al.* Mechanical phenotype of cancer cells: cell softening and loss of stiffness sensing. *Oncotarget* **6**, 20946–20958 (2015).
23. Yang, B., Radel, C., Hughes, D., Kelemen, S. & Rizzo, V. p190 RhoGTPase-activating protein links the beta1 integrin/caveolin-1 mechanosignaling complex to RhoA and actin remodeling. *Arterioscler Thromb Vasc Biol* **31**, 376–383 (2011).
24. Sharrard, R. M. & Maitland, N. J. Regulation of protein kinase B activity by PTEN and SHIP2 in human prostate-derived cell lines. *Cell Signal* **19**, 129–138 (2007).
25. Schmieg, F. I. & Simmons, D. T. Characterization of the *in vitro* interaction between SV40 T antigen and p53: mapping the p53 binding site. *Virology* **164**, 132–140 (1988).
26. Gumulec, J. *et al.* Cisplatin-resistant prostate cancer model: Differences in antioxidant system, apoptosis and cell cycle. *Int J Oncol* **44**, 923–933 (2014).
27. Berthon, P. *et al.* Androgens are not a direct requirement for the proliferation of human prostatic epithelium *in vitro* **73**, 910–916 (1997).
28. Mitchell, S., Abel, P., Ware, M., Stamp, G. & Lalani, E. N. Phenotypic and genotypic characterization of commonly used human prostatic cell lines. *Bju International* **85**, 932–944 (2000).
29. Fraser, M. *et al.* PTEN deletion in prostate cancer cells does not associate with loss of RAD51 function: implications for radiotherapy and chemotherapy. *Clin Cancer Res* **18**, 1015–1027 (2012).
30. Skjoth, I. H. & Issinger, O. G. Profiling of signaling molecules in four different human prostate carcinoma cell lines before and after induction of apoptosis. *Int J Oncol* **28**, 217–229 (2006).
31. Gebaeck, T., Schulz, M. M. P., Koumoutsakos, P. & Detmar, M. TScratch: a novel and simple software tool for automated analysis of monolayer wound healing assays. *Biotechniques* **46**, 265–+ (2009).
32. Prescher, J. A. & Bertozzi, C. R. Chemistry in living systems. *Nat Chem Biol* **1**, 13–21 (2005).
33. Wayne, R. Interference Microscopy. In: *Light and Video Microscopy* (ed^(eds Wayne, R.). Elsevier Inc (2014).
34. Bastatas, L. *et al.* AFM nano-mechanics and calcium dynamics of prostate cancer cells with distinct metastatic potential. *Biochimica Et Biophysica Acta-General Subjects* **1820**, 1111–1120 (2012).
35. Denais, C., Lammerding, J. Nuclear Mechanics in Cancer. In: *Cancer Biology and the Nuclear Envelope: Recent Advances May Elucidate Past Paradoxes* (ed^(eds Schirmer, E. C., DeLasHeras, J. I.) (2014).
36. Rao, K. M. K. & Cohen, H. J. Actin cytoskeletal network inaging and cancer. *Mutation Research* **256**, 139–148 (1991).
37. Thoumine, O. & Ott, A. Comparison of the mechanical properties of normal and transformed fibroblasts. *Biorheology* **34**, 309–326 (1997).
38. Lekka, M. *et al.* Elasticity of normal and cancerous human bladder cells studied by scanning force microscopy. *European Biophysics Journal with Biophysics Letters* **28**, 312–316 (1999).
39. Alibert, C., Goud, B. & Manneville, J. B. Are cancer cells really softer than normal cells? *Biology of the Cell* **109**, 167–189 (2017).
40. Faria, E. C. *et al.* Measurement of elastic properties of prostate cancer cells using AFM. *Analyst* **133**, 1498–1500 (2008).
41. Zhu, M.-L. & Kyprianou, N. Role of androgens and the androgen receptor in epithelial-mesenchymal transition and invasion of prostate cancer cells. *The FASEB Journal* **24**, 769–777 (2010).
42. Wu, H. W., Kuhn, T. & Moy, V. T. Mechanical properties of l929 cells measured by atomic force microscopy: Effects of anticytoskeletal drugs and membrane crosslinking. *Scanning* **20**, 389–397 (1998).

Acknowledgements

Author Contributions

M.R.: Study design, preparation of manuscript, experiment coordination, qRT-PCR. M.K.: Cell experiments management. T.V.: Image analysis, statistics. J.G.: Statistics, manuscript preparation. J.B.: Quantitative phase imaging. H.P.: Fluorescent microscopy. J.P.: Atomic-force microscopy. M.M.: Study design, manuscript preparation.

117

Additional Information

Supplementary information accompanies this paper at https://doi.org/10.1038/s41598-018-38199-7.

Competing Interests: The authors declare no competing interests.

Publisher's note: Springer Nature remains neutral with regard to jurisdictional claims in published maps and institutional affiliations.

118

4.3.2 Shear modulus estimation using quantitative phase imaging

Previous study revealed an association between cell cry mass and cell Young modulus [2], chapter 4.3.1. To further examine the possibilities of using QPI to analyse the mechanical properties of cells, QPI was employed in a microfluidic setup with cells exposed to shear stress [86]. The approach is used to estimate cell viscoelastic properties upon fluid shear tress induction. In this system QPI is used because it enables optical path length measurement as higher objects cause higher phase shifts. Approach is based on a study by Eldridge et al. [24] and is further improved by a possibility to extract refractive index and to estimate cell height in a single measurement. In addition, the proposed method highly benefits from a parametric deconvolution of a flow signal measured by flow meter; this parameter is highly dependent on a fluidics and syringes used, adding a capacity to the system. Therefore, cell viscosity estimation in particular can be highly distorted. To suppress this effect, we applied a correction method utilizing parametric deconvolution of the flow system's optimized impulse response [87]. Achieved results were compared with the direct fitting of the Kelvin-Voigt viscoelastic model and the basic steady-state model. The results showed that our novel parametric deconvolution approach is more robust and provides a more reliable estimation of viscosity with respect to changes in the syringe's compliance compared to Kelvin-Voigt model [87].

We demonstrated that this setup is suitable for high throughput and robust cell viscoelasticity estimation and work even in a time-lapse scenario. The great advantage if of the system is that apart from the viscoelastic properties estimation per cell also parameters derived from quantitative phase image can be extracted – cell morphology, cell dry mass, or parameters like circularity or others. Simultaneous measurement of refractive index, which is used to calculate the cell height, further complements a number of determinable parameters for individual cells [86].

4.3.3 Complementarity of Brillouin spectroscopy and quantitative phase imaging

In the chapter 4.3.1, a correlation between cell dry mass and Young modulus of prostatic cells was described [2]. In an Elsayad et al [88] study, we focused on an alternative approach of measurement of cell mechanical properties based on Brillouin spectroscopy. Compared to AFM, the advantages of Brillouin microscopy are that it is a completely non-invasive, non-contact method that can measure mechanical properties in short acquisition times. Spontaneous scattering is based on the inelastic scattering of light from acoustic phonons that are inherently present in the probed material [88]. It enables to calculate the storage modulus and thus elastic properties of the sample by the relation

$$\nu_B \sim n \sqrt{\frac{M'}{\rho}}$$

where ν_B is a Brillouin peak frequency shift, n is a refractive index of a material, M' is a storage modulus and ρ is the mass density. Critical in this relation is a need for knowing the refractive index of the sample. As ρ and n are directly coupled in most samples, there is no need to measure both. Quantitative phase imaging extracts the phase shift from which cell dry mass can be approximated. Another quantitative phase technique – optical diffraction tomography enables to separate two components of the cell dry mass – that is the physical (optical) property of the sample (its refractive index) and sample height.

In this study, we have effectively demonstrated that a combination of both techniques in a correlative setup provides a more accurate way of estimating storage modulus – estimating the mechanical properties of the sample. Brillouin microspectroscopy was performed on a custom-build setup in Vienna Biocenter Advanced microscopy core facility, while the refractive index was determined in our lab.

In sum, the paper shows the complementary roles of Brillouin spectroscopy and quantitative phase imaging. Therefore, in this experiment instead of living prostate cancer cells, the imaging was performed on simple-to analyse non-moving objects – cellulose fibres, as the acquisition of correlative dataset of fast-migrating cells is still a challenging issue.

ELSAYAD, K., G. URSTOGER, C. CZIBULA, C. TEICHERT, et al. Mechanical Properties of cellulose fibers measured by Brillouin spectroscopy. Cellulose, May 2020, 27(8), 4209-4220.

ORIGINAL RESEARCH

Mechanical Properties of cellulose fibers measured by Brillouin spectroscopy

Kareem Elsayad · Georg Urstöger · Caterina Czibula · Christian Teichert · Jaromir Gumulec · Jan Balvan · Michael Pohlt · Ulrich Hirn

Abstract We investigate the potential of Brillouin Light Scattering (BLS) Microspectroscopy for fast non-invasive all-optical assessment of the mechanical properties of viscose fibers and bleached softwood pulp. Using an optimized Brillouin spectrometer, we demonstrate fast spatial mapping of the complex longitudinal modulus over extended areas (> 100 μm). Our results reveal that while the softwood pulp has a relatively uniform moduli, the viscous fibers have significant spatial heterogeneous in the moduli. Specifically, the viscose fibers exhibited a regular pattern of increasing and decreasing modulus normal to the fiber axis. The potential influence of a locally changing refractive index is investigated by holographic phase microscopy and ruled out. We discuss our results in light of the anisotropic mechanical properties of the fibers and are able to estimate the relative difference between the modulus along the fiber axis and that perpendicular to it. Results are presented alongside reference measurements of the quasi-static mechanical properties transverse to the fiber axes obtained using AFM-nanoindentation which reveal a similar trend, hinting at the potential usefulness of BLS for mechanical characterization applications. However, more detailed investigations are called for to uncover all the factors influencing the measured high-frequency BLS modulus and its significance in relation to physical properties of the fiber that may be of practical interest.

Keywords Storage modulus · Young's modulus · Loss modulus · Brillouin spectroscopy · Viscoelasticity · Cellulose fiber

K. Elsayad
Advanced Microscopy, Vienna Biocenter Core Facilities, Vienna Biocenter, Dr. Bohr-Gasse 3, Vienna 1030, Austria

G. Urstöger · U. Hirn (✉)
Institute of Bioproducts and Paper Technology, Graz University of Technology, Graz, Austria
e-mail: ulrich.hirn@tugraz.at

G. Urstöger · C. Czibula · C. Teichert · U. Hirn
Christian Doppler Laboratory for Fiber Swelling and Paper Performance, Vienna, Austria

C. Czibula · C. Teichert
Institute of Physics, Montanuniversität Leoben, Leoben, Austria

J. Gumulec · J. Balvan
Department of Pathophysiology, Masarykova Univerzita, Brno, Czech Republic

M. Pohlt
Canon Production Printing, Poing, Germany

Introduction

The mechanical properties of pulp fibers have been investigated using numerous different approaches. Longitudinal (i.e. along the fiber axis) measurements of fiber properties like the E-modulus and the breaking strength are usually studied using fiber tensile testing (Kompella and Lambros 2002; Burgert et al. 2005; Fischer et al. 2012; Jajcinovic et al. 2018) [see also Fischer (2013) and Jajcinovic (2017) for extensive reviews]. In contrast the transverse properties of fibers (i.e. perpendicular to the fiber axis) were initially investigated via compressive measurements on wet fibers (Hartler and Nyren 1970; Dunford and Wild 2002; Wild et al. 2005). Bergander et al. carried out tests on radial double-wall cut wood strips in an environmental scanning electron microscope (Bergander and Salmen 2000). Atomic Force Microscopy (AFM) based methods have also been used to investigate fiber properties such as flexibility and conformability (Nilsson et al. 2000; Pettersson et al. 2017) as well as transverse mechanical properties (Ganser et al. 2013; Ganser and Teichert 2017). A comprehensive list of literature on the topic can be found in Czibula et al. (2019).

While the viscoelastic nature of cellulosic fibers has been known for a long time, earlier studies focused predominantly on the creep behaviour of fibers in the longitudinal direction (Stanzl-Tschegg and Navi 2008; Cisse et al. 2015). The viscoelastic behaviour of wood has been characterized for pine specimens along the grain direction (Penneru et al. 2006) and for green wood in the transverse direction (Bardet and Gril 2002). However, only recently has fiber viscoelasticity in the transverse direction been addressed using an AFM-Nano-Indentation (NI) based method (Ganser et al. 2018) at varying levels of relative humidity (RH) (Czibula et al. 2019).

In this work spontaneous Brillouin Light Scattering (BLS) Microspectroscopy is applied to probe the mechanical properties of cellulosic fibers. Spontaneous BLS is based on the inelastic scattering of light from acoustic phonons that are inherently present in the probed material. Acoustic phonons are collective molecular excitations, which unlike optical phonons, have a significantly lower energy (in the GHz range) and will extend over many molecules. BLS measures the effective velocity of these excitations, by measuring the frequency shift of the so-called BLS peaks

relative to the probing laser. In a typical BLS microspectroscopy experiment when one couples to a single acoustic phonon mode, one observes *two* Brillouin scattering peaks on either side of the probing laser frequency, which correspond to the "creation" and "annihilation" of a phonon. The shift of these peaks relative to the elastic scattering peak (i.e. frequency of the probing laser) is directly proportional to the hypersonic velocity of the phonons via Eq. (1). The velocity can in turn be used to calculate the elastic storage modulus at the corresponding frequency via the Christoffel equation [Eq. (2)].

Key advantages of BLS microscopy are that it is a completely non-invasive, non-contact method that can measure mechanical properties in short acquisition times (~ 100 ms or less per position). This is particularly useful for investigation of pulp fibers, as their small size (length 0.6–3 mm, width 15–40 µm) require elaborate sample preparation and intricate micromachinery for mechanical testing. Another potentially promising aspect of BLS microscopy is that it can be used to evaluate the full elastic tensor of anisotropic materials. Due to the fibril orientation in the S2 wall and the misalignment between the fibril orientation angle and the fiber axis, the fiber should be described by an orthotropic material model of the fiber wall, explicitly taking into account also the fibril orientation angle (Magnusson and Östlund 2013). As thus the fibers can be characterized by either performing mechanical measurements in the longitudinal and the transverse direction—i.e. two tensile plus two shear moduli—together with the fibril angle, or, by performing direct orthogonal measurements of the three tensile moduli plus the three shear moduli. Measurement of pulp fiber shear moduli is even more complicated than tensile moduli, and to the best of our knowledge has not been done. BLS has routinely been used to measure mechanical properties and even the complete elastic tensor of biological fibers such as for spider silk (Koski et al. 2013), proteins (Randall et al. 1979; Speziale et al. 2003), collagens (Harley et al. 1977; Cusack and Miller 1979; Edginton et al. 2016), muscle fibers (Berovic et al. 1989), or recently bamboo wood splinters (Williams et al. 2019). Being a non-contact method able to measure the full elastic tensor (i.e. the elastic moduli and shear moduli in all three spatial directions) BLS has the potential to provide substantial progress for mechanical testing of cellulosic fibers and, at the same time, resolve the

laborious and complicated issues in fiber handling during mechanical testing.

In this work we demonstrate the applicability of the method for cellulosic fibers by analyzing the BLS-measured mechanical properties of pulp- and viscose fibers. Specifically, the elastic modulus (storage modulus) representing the elastic behavior and the loss modulus (dampening coefficient) representing the viscous behavior are evaluated. By adjusting the effective solid angle over which we are probing and detecting (via the effective numerical aperture of the objective lens) we are able to transition between coupling to predominantly acoustic phonon modes perpendicular to the fiber axis and acoustic phonon modes both perpendicular and parallel to the fiber axis. We note that because of the employed back-scattering geometry and polarization of detection we are exclusively measuring *longitudinal acoustic phonons*, which in turn yield the so-called *longitudinal moduli*. In this brief communication we also for the first time to our knowledge demonstrate the feasibility of using a Virtual Imaged Phase Array (VIPA)-based imaging spectrometer for studying such fibers. While having a lower spectral resolution and finesse than the traditionally employed multi-pass Fabry–Perot spectrometers (Sandercock 1970), it also has some advantages in regard to required acquisition time and illumination intensity, as well as affordability, which would be important for wider research and potentially also industrial applications.

Materials and methods

Fibers

The two different fibers investigated were hand ribbon shaped viscose fibers (Leonardo fiber from Kelheim Fibers) and fully bleached softwood kraft pulp fiber from industrial production (Sappi). For the BLS measurements two viscose fibers and two softwood fibers were investigated. Reference measurements, by AFM-NI, were carried out on fully bleached Canadian softwood kraft pulp (Canfor) at about 50% RH. AFM-NI data of round shaped viscose fibers from Kelheim were used as the second reference.

Calculation of elastic modulus from BLS measurements

The measured BLS frequency shift v_B (GHz) is in general related to the speed of the probed acoustic phonons $V_{\hat{q}}$ for a given scattering wavevector $\hat{q}$ via:

$$v_B = \pm 2\mathbf{n} \cdot \hat{q} c^{-1} v_0 V_{\hat{q}} \tag{1}$$

where $\mathbf{n}$ is the refractive index (written here as a tensor for the general anisotropic case), v_0 is the frequency of the probing laser, and c is the vacuum speed of light. (In the backscattering geometry this reduces to $v_B = \pm 2nc^{-1}v_0V$). The propagation of phonons in the $\hat{x}_i$ direction is described by (Berne and Pecora 2000):

$$\rho \frac{\partial^2 u_i}{\partial t^2} = c_{ijkl} \frac{\partial}{\partial x_j}\left(\frac{\partial u_l}{\partial x_k}\right) \tag{2}$$

where ρ is the mass density and c_{ijkl} is the *stiffness tensor*. It follows that the components of the latter can be calculated from the measured acoustic velocity (Eq. 1) via (Berne and Pecora 2000):

$$\left| (\hat{x}_k \cdot \hat{q})(\hat{x}_l \cdot \hat{q}) c_{ijkl} - \rho V_{\hat{q}}^2 \right| = 0 \tag{3}$$

For the case of an isotropic material in the back-scattering geometry one would probe the first three diagonal components ($c_{1111} = c_{2222} = c_{3333}$), such that the position of the BLS peaks directly yield the longitudinal storage modulus M':

$$M' = \rho V^2 \tag{4}$$

The corresponding loss modulus (M'') can be obtained from the lifetime of the phonons—which is manifested in the homogeneous broadening of the BLS peak Γ_B-via (Carroll and Patterson 1984; Floudas et al. 1991)

$$M'' = \rho V^2 \frac{\Gamma_B}{v_B} \tag{5}$$

The case of anisotropic samples—as is the case with the studied fibers—is more subtle, given the distinct elastic moduli in different directions. For the studied fibers we may assume a transverse anisotropic symmetry such that measurements will yield a linear combination of the modulus parallel and perpendicular to the fiber axis ($M_{\parallel}$ and $M_{\perp}$. respectively). The respective contribution of these can be calculated from

Eqs. 1 and 3 by considering the projection of the scattering wavevector on the stiffness tensor.

Finite numerical aperture

In order to achieve a high lateral spatial resolution, one needs to probe with a correspondingly large numerical aperture (NA). Finite NA measurements will in the studied case result in two modifications to the measured spectrum. Firstly, one would observe an inherent effective broadening and slight shift in the peak position of the BLS signal resulting from the frequency dependence of the scattering wavevector (Eq. 1) (Antonacci et al. 2013). This can readily be calculated by integrating Eq. 1 over the probed solid angles. Secondly, one may observe an effective broadening due to the anisotropy of the sample, namely that the phonon speed is dependent on direction. To illustrate the latter for the samples studied here, let us assume the fibers are orientated in the $\hat{x}_1$ direction and we probe along the perpendicular $\hat{x}_3$-axis, such that $c_{1111}\left(= M_{\parallel}\right) \neq c_{2222} = c_{3333}(= M_{\perp})$. By increasing the effective probing NA from ≈ 0 one will thus transition from probing exclusively $M_{\perp}$ to probing a linear combination of $M_{\perp}$ and $M_{\parallel}$. Given that $M_{\parallel} \neq M_{\perp}$ this will result in an effective broadening with increasing NA and a shift in the measured v_B to lower (higher) frequencies if $M_{\parallel} < M_{\perp}$ ($M_{\parallel} > M_{\perp}$). The exact dependence can again be obtained by integrating Eq. 1 over the probed solid angles, this time taking these symmetry conditions into account and noting that there will also likely be an associated anisotropy in the refractive index (i.e. $n_{\parallel} \neq n_{\perp}$). Since we do not have access to the latter, in this study we calculate an *effective* elastic modulus ($\bar{M}$). This is obtained by calculating a single effective acoustic velocity ($V_{\hat{q}} = V$) from Eq. 1 assuming the back-scattering geometry and an effective refractive index ($\mathbf{n} \cdot \hat{q} = n$), and subsequently calculating the complex modulus from Eqs.'s 4 and 5. Prior to fitting the BLS spectra to obtain v_B and Γ_B the results are deconvolved with the elastic scattering peak and corrected for broadening exclusively due to the finite NA as described below. The effective refractive index (1.3–1.4) was taken from holographic phase microscopy measurements (see below) on the same samples, and a density of 1500 kg/m^3 was assumed throughout.

Measurements on the same samples using a very small NA (< 0.01) were used to estimate the contribution of $M_{\perp}$ to the total high-NA measured Modulus, since the former can be assumed to exclusively probe in the direction transverse to the fiber axis. The ratio of the elastic modulus along the fiber axis to that perpendicular to the fiber axis was also estimated via:

$$\frac{M'_{\perp}}{M'_{\parallel}} = \left[1 + 2n \left[\left(\frac{v_B}{v_B^{\perp}} \right)^2 - 1 \right] \right]^{-1} \tag{6}$$

where v_B is measured BLS-shift with NA = 1, and $v_B^{\perp}$ is that measured for NA < 0.01.

An effective loss tangent is also calculated from the measured effective storage and loss moduli as $\tan(\delta) = \bar{M}'' / \bar{M}'$ for each of the measured samples.

BLS setup

The employed setup consists of a self-built confocal sample scanning Brillouin microscope as described in e.g. Elsayad et al. (2016). In particular this consisted of an inverted microscope frame (iX73 by Olympus, Japan) with the laser and spectrometer coupled to the lower right port. Samples were mounted on standard microscopy slides and imaged through standard 170 μm glass coverslips. An objective (numerical aperture (NA) = 1.3, 60×, Si-immersion oil, Olympus, Japan) was employed for all BLSM measurements. The aperture of which was only partially filled yielded an effective NA ~ 1.0. The measured (optical) lateral and axial resolution (corresponding to the probing volume) were 290 nm and 650–700 nm as determined from the Full Width Half Maximum of the Point Spread Function. To assure optimum confocality the physical pinhole was fixed at 100 μm, corresponding to just over one Airy unit with the employed tube lens. Excitation was performed via a solid state single-mode 532 nm laser (Torus by Quantum Laser, Germany), passed through an optical isolator, expanded, and coupled into the optical path via a 90:10 non-polarizing beam splitter. The sample was scanned using a long travel range 3-axis piezo stage (Physik Instrumente, Germany) and for each position one spectrum was acquired. Average laser power at the sample was kept low and measured to be below 3 mW. The dwell time per scanned point was fixed at 100 ms. After the pinhole the beam passed through a polarizer and 2 nm narrow band pass filter centered at 532 nm.

The Brillouin spectrometer consisted of a cross dispersion Virtual Imaged Phased Array (VIPA) spectrometer similar to the one described in Scarcelli et al. (2015) with the elastic scattering peaks blocked by masks at intermediate imaging planes. The employed VIPAs (Light Machinery, Canada) each had a free spectral range of 30 GHz. Also employed were self-fabricated gradient apodization filters prior to each VIPA. The resulting spectral projection was subsequently Fourier filtered using a Lyot stop (Edrei et al. 2017) and magnified. Finally, the Brillouin spectra consisting of only the Brillouin peaks, was imaged on a cooled EM-CCD camera (ImageEM II, Hamamatsu, Japan) which was read out for each scan point. Measurements on distilled water and spectroscopic grade ethanol before and after each scan where used for scaling the dispersion axis of the spectral projection. All spectra were fitted with Lorentzian functions with a quadratic background correction term, using a standard least-squares fitting algorithm in Matlab as described in Elsayad et al. (2016).

To account for the instrumental spectral response as well as the contribution from multiple-scattering in the sample, the spectra was deconvolved with a measurement of the elastic Rayleigh scattering peak measured in each respective sample. This was performed by optically attenuating the laser and opening the slits of the spatial masks in the spectrometer. Since our laser line has a line-width (kHz–MHz) that is orders of magnitude smaller than the spectral resolution, a straight forward deconvolution can be assumed to accurately capture the spectral response of our setup. This however will not account for the spectral broadening induced by the finite NA (see below).

To account for this, measurements were performed at different effective NAs by placing a ring-actuated iris diaphragm (Thorlabs, Germany) immediately behind the objective lens. By closing the iris (which could be done with an accuracy of several hundred microns) we could tune the effective NA from < 0.01 up to the maximum of the objective lens. We note that this would equally affect the probing and detection NA. The effective NA (NA_{eff}) was calculated from the radius (R) of the iris aperture via: $NA_{eff} = nR(w^2 + R^2)^{-1/2}$, where w is the working distance of the objective lens. The results on distilled water showed an increase in the line width by a factor of $1.9(\pm 0.1)$ from NA ~ 0 to NA = 1.0, with a small shift in the peak position to lower frequencies of 310 MHz ($\sim 4\%$).

The effect of changing the effective NA from ~ 0 to 1.0 was also measured on each of the samples using the same approach. To determine the contribution from the anisotropy to the observed broadening, the measured frequency shift and line width at each NA was corrected in the sample measurements by a multiplicative factor corresponding to the effective modification in the peak position and linewidth (see above) measured in distilled water for the same corresponding NA relative to the low-NA limit.

BLS measurement time

The total time consumed by the sample preparation and the BLSM measurements amounted to approx. 3–4 h. During this time calibration measurements were performed and multiple areas of approx. 100×100 μm were measured, each of which were divided into 21×5 measurement spots.

Testing conditions

It is important to note that BLSM measurements are very sensitive to the level of hydration (Wu et al. 2018) as well as temperature. Also, cellulose fiber mechanical properties are strongly affected by relative humidity under ambient conditions (Jajcinovic et al. 2018). Special care was thus taken that these were kept at the same level (25 °C, 30–50% RH) for all measured samples.

Holographic phase microscopy

Refractive index tomograms were acquired on a commercial holographic phase microscope with rotating scanner (3D Cell Explorer, Nanolive SA, Lausanne, Switzerland) with a Nikon BE Plan 60 × NA 0.8 objective lens. The size of acquired tomogram was $93.1 \times 93.1 \times 35.7$ μm (XYZ). Water was used as the reference refractive index (1.330) in all measurements. The software "Steve 1.6.3496" (Nanolive SA) was used for image acquisition and reconstruction, and maximum intensity projections were plotted using FIJI/ImageJ.

AFM nanoindentation

All AFM measurements were performed with an Asylum Research MFP-3D AFM. The instrument is equipped with a closed-loop planar x–y-scanner with a scanning range of 85 × 85 μm² and a z-range of about 15 μm. For the experiments, four-sided pyramidal, full diamond probes (ND-DYIRS, Advanced Diamond Technology) with a tip apex radius of about 50 nm have been used. The spring constant of the cantilever was about 60 N/m and calibration of the cantilever was performed according to Hutter and Bechhoefer (1993). In AFM-NI, the sample surface is plastically deformed and according to the Oliver–Pharr method (Oliver and Pharr 1992) the reduced modulus E_r and the hardness H can be obtained. The method has been successfully established for pulp and viscose fibers before and is thoroughly described in Ganser et al. (2013) and Ganser and Teichert (2017).

Results and discussion

Figure 1 shows spatial maps of the measured BLS frequency shift v_B of the viscose and bleached softwood Kraft fibers and the calculated effective transversal storage modulus ($\bar{M}$) and widefield transmitted light pictures of each fiber. While the pulp fibers seem to have a quite uniform elastic modulus the viscose fibers exhibit a regular longitudinal stripe pattern. Along the fiber axis there are elongated regions with lower (low region, 4.2 GPa) and higher (high region, 5.4 GPa) effective transversal moduli.

Figure 2 shows the effect of increasing the effective numerical aperture (NA = 0.01–1) for the viscose (high region and low region separately) and bleached softwood Kraft fibers. The plotted storage and loss modulus have in each case been corrected for the effect of finite NA excitation/detection by a linear coefficient determined from measuring distilled water with the corresponding NA (see above). As such the observed changes with NA can be attributed to the anisotropy of the sample. In all cases one sees an increase in both the loss modulus (line width) and the storage modulus (frequency shift) with increasing NA. The latter suggests that the component of the storage modulus along the fiber axis is larger than that perpendicular to the fiber axis. This corresponds to the anisotropic nature of both, viscose (strong orientation of cellulose due to stretching during the spinning process) and wood fibers (strong orientation of fibrils in S2 wall). The loss modulus as well as the loss tangent also show an increasing trend with increasing NA, however the errors on the measurements are quite high.

As the BLS frequency shift scales linearly with the refractive index (Eq. 1) we used holographic phase microscopy to investigate whether there are any significant differences in n (between and within samples) which could account for any observed variations in the frequency shift. Maximum intensity projections of the reconstructed refractive index holograms are shown for two different representative sample types in Fig. 3. The local variation of the refractive index is in each case rather low and therefore cannot in itself explain the differences in the calculated longitudinal modulus (see above). Interestingly similar longitudinal patterns in the viscose fiber can be observed for the refractive index maps (Fig. 3a) as for the storage modulus (Fig. 2c, e), which might be the result of the drawing of the filaments during the spinning process.

Table 1 summarizes the results for the refractive index n, BLS frequency shift v_B, the measured effective longitudinal storage and loss moduli ($\bar{M}'$ and $\bar{M}''$) and the loss tangent for the two fiber types. Also shown is the derived ratio of the storage modulus perpendicular and along the fiber axis ($M'_\perp/M'_\parallel$), calculated from the point measurements at different NA's (see above). We note that for this calculation an isotropic refractive index is assumed for each of the sample regions (as referenced in table), which is likely not the case. The calculations for all NA's can be found in the ESI.

As also evident from the spatial maps (Fig. 1) the low region of the viscose fibers and the softwood pulp have comparable values for $\bar{M}'$ while the (longitudinal) "stripes" in the viscose fiber (high region) have a significantly larger $\bar{M}'$. We suspect the differences may be related to either a local densification of the material or a local hardening of the structure.

Table 1 also shows reference data for the reduced modulus in the transverse fiber direction obtained from AFM-NI of viscose and bleached softwood pulp fibers. In comparison the measurements from AFM-NI are higher for the viscose and lower for softwood pulp.
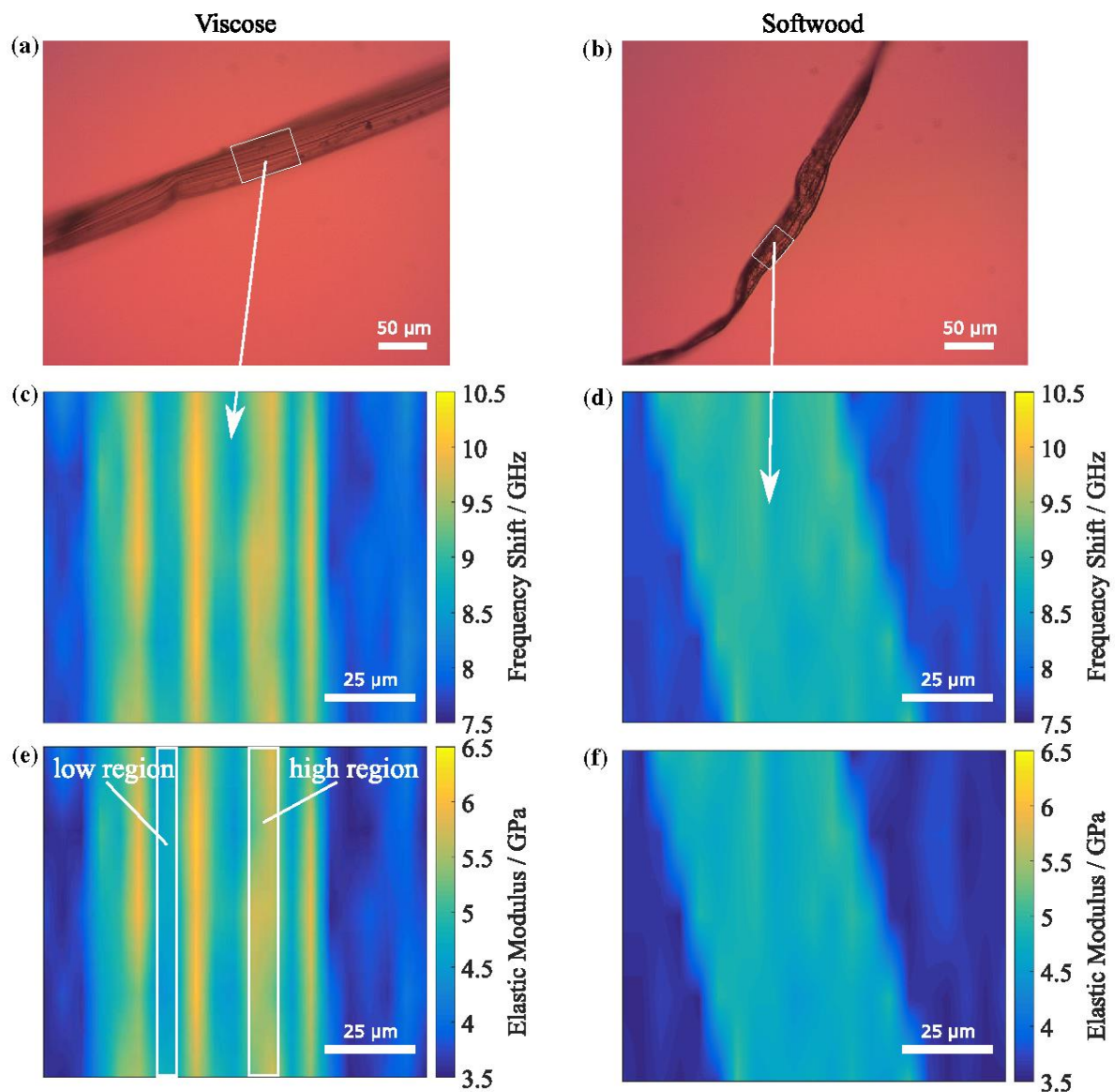
Fig. 1 **a**, **b** Transmitted light widefield microscopy images of the viscose and bleached softwood Kraft fibers respectively. **c**, **d** confocal spatial maps of the BLS-frequency shift. **e**, **f** the calculated effective transversal storage modulus (see main text) from **a**, **b**. *Note* The widefield pictures in **a**, **b** were taken through a different microscope port and with a different magnification, and are thus not spatially aligned with the confocal BLS-maps in **c**–**f**

While these show a similar trend to the average effective longitudinal storage moduli measured with BLS, the percentage difference is significantly larger between the two types of fiber. It is often the case when attempting to perform correlative AFM and BLS studies that relatively large changes in the AFM measured (Young's) moduli will correspond to only subtle changes in the BLS-measured (longitudinal) moduli—in many cases scaling in a roughly semi-logarithmic fashion (e.g. Scarcelli et al. 2015). It should be noted though that currently such relations are empirical and lacking theoretical foundation, given the different boundary conditions of the measured moduli and the vastly different frequency regimes probed (quasi-static vs. GHz) which will be sensitive to distinct mechanical relaxation processes.
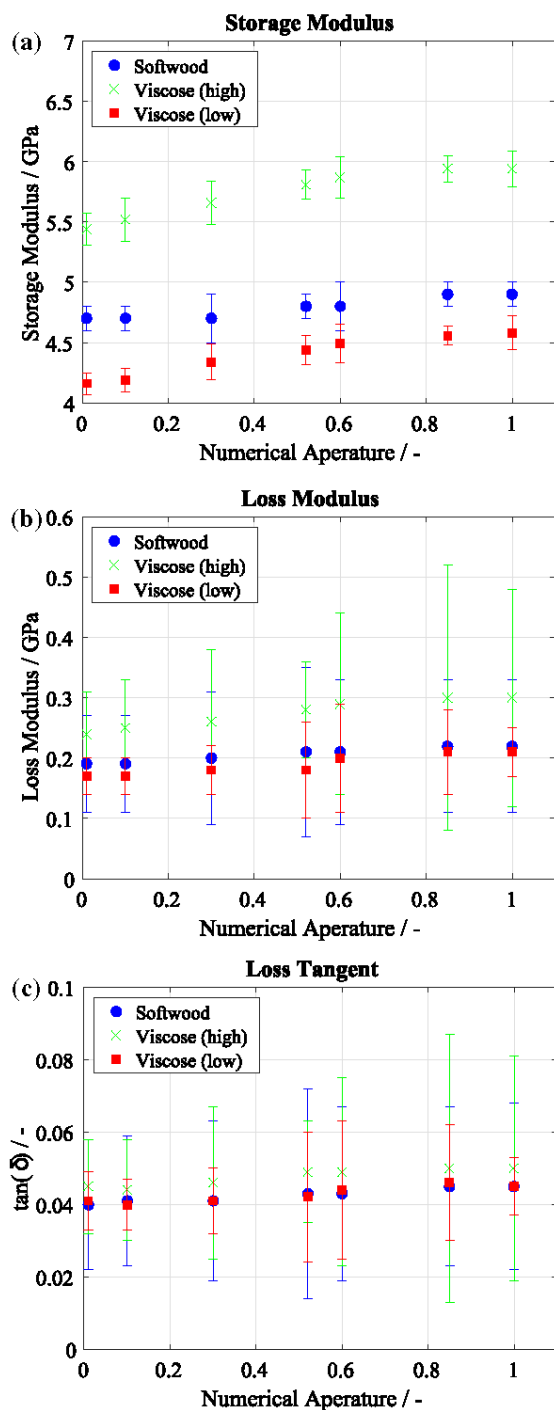
◄ **Fig. 2** Measurements of the properties over a changing NA. The storage modulus **a** shows a consistent trend to higher moduli at higher NA. These results show that, as expected, the storage modulus along the fiber axis is higher than perpendicular to it. The loss modulus (**b**) and the loss tangent (**c**) also appear to show a similar trend but the associated uncertainties are too large to draw any definitive conclusions

In the context of the current study it is also necessary to emphasize that the references were not measured on the same fibers. The counterintuitive result that the quasi-static AFM measurements yield an effectively lower modulus may possibly be due to the effective length scales probed with BLS. Since the probed phonons have a wavelength of approximately 100–200 nm with decay lengths on the order of 1 μm, they probe an effective collective response. Aside from more detailed knowledge of molecular level interactions, interpretation of the BLS spectra would for the case of heterogeneous media also require (ultra-)structural considerations on these scales especially for the viscous fibers.

The loss tangent (tan(δ)) relates the storage and the loss modulus and is a measure of how well energy is dissipated in the material. A tan(δ) = 0 would mean that the material is fully elastic while a number > 1 means that more energy is dissipated than stored. Importantly in the case of BLS measurements the loss tangent will be independent of the density and refractive index (which cancel out—Eqs. 4 and 5) which means that a change in loss modulus indicates a "true" change in the moduli of the structure. Within experimental uncertainties the loss tangent was similar between the two fiber types, with the values being in the same range than quasi-static measurements (Zhou et al. 2001; Csóka et al. 2012).

Given the frequency of the probed phonons in BLS, the most relevant mechanical relaxation times probed will be on the scale of picoseconds. It is possible to extract effective mechanical relaxation times (τ) from BLS measurements by driving the sample across a thermodynamic phase transition (at which $v_B \tau \sim 1$), e.g. Carroll and Patterson (1984). It is however in general challenging to obtain the relaxation times from the BLS measurements, as they will also depend to a large degree on the distribution (model) of relaxation times (Floudas et al. 1991). A detailed investigation of this would also benefit from complementary lower

It is also understood that under high hydration levels (> 90%) the solvent can dominate the contribution to the modulus measured with BLS and such an apparent correlation breaks down (Wu et al. 2018).
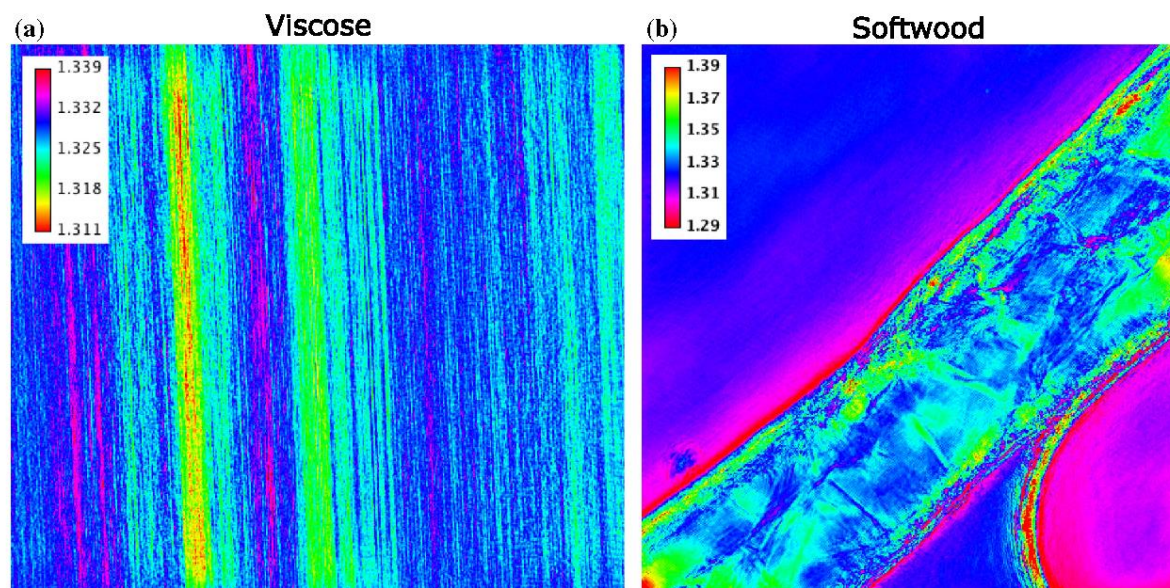
Fig. 3 Refractive index n of the Viscose (**a**) and bleached softwood Kraft (**b**) fibers (colorbar $= n$), suggesting only relatively small variations between and within the samples

frequency broader-bandwidth techniques (such as photon correlation spectroscopy), which is beyond the scope of the current study.

Conclusions

We have demonstrated spatial mapping of the high-frequency effective transversal storage and loss modulus for viscose and softwood pulp fibers using a VIPA based Brillouin Microscope. Reference measurements with AFM-NI revealed a similar trend—namely a larger elastic modulus for viscous than softwood pulp fibers, although a direct comparison between the two moduli is at this point unjustified given the different mechanical relaxation processes probed.

Our results suggest that Brillouin microscopy can serve as a fast and reliable technique to investigate the high-frequency mechanical properties of cellulosic fibers. One demonstrated advantage is the ability to map the properties in different directions (longitudinal and transverse to the fiber axis). In addition it has the ability to rapidly and all-optically map properties over larger areas using a VIPA based spectrometer such as was employed here. In this regard we see much potential for BLS microscopy for understanding and testing the mechanical properties of cellulose fibers as

it is also less cumbersome and a lot faster than direct mechanical testing. Extensions of the technique to e.g. consecutively probing at different angles (scattering wavevectors) can also be used to investigate the full elastic (stiffness) tensor of the fiber material, i.e. tension stiffness and shear stiffness in all three spatial directions, as has been demonstrated for other natural fiber materials (Koski et al. 2013; Edginton et al. 2016). It is however important to note that the measured properties with BLS are by construction different than those probed with most other mechanical testing techniques. This will be due to the high-frequency regime probed (where coupling of constituents/solutes to liquids will be much stronger and the latter will have a high modulus) and the different boundary conditions associated with deriving the elastic modulus from the speed of acoustic phonons. While there is ongoing active research in the direction of both empirically and theoretically relating the BLS measured moduli to more familiar structural and physical parameters and shedding light on their relevance in assessing otherwise relevant chemical/physical properties, the current study demonstrates the practical feasibility and potential of Brillouin microscopy for studying the anisotropic mechanical properties of cellulosic fibers.

Table 1 Data obtained from the measurements presented in Figs. 1 and 2

Sample	Refractive index: n	Frequency shift v_B (GHz)	Measured effective storage modulus: $\bar{M}'$ (GPa)	Measured effective loss modulus: $\bar{M}''$ (GPa)	Tan(δ)	Estimated ratio of storage modulus transverse to fiber axes and storage modulus along fiber axis: $M'_\perp/M'_\parallel$	Reduced modulus (GPa)
Viscose (region high)	1.31	9.4 ± 0.1	5.4 ± 0.13	0.24 ± 0.07	0.045 ± 0.013	0.81 ± 0.16	5.6–7.3[a] (50–30) %RH
Viscose (region low)	1.34	8.40 ± 0.1	4.2 ± 0.1	0.17 ± 0.03	0.041 ± 0.008	0.79 ± 0.04	
Bleached softwood Kraft	1.34 ± 0.02	8.7 ± 0.1	4.5 ± 0.1	0.18 ± 0.08	0.040 ± 0.018	0.88 ± 0.17	1.3 ± 0.7 (50) %RH N = 3

Values were calculated as described in the main text

[a]Data from Ganser (2014)

References

Antonacci G, Foreman MR, Paterson C, Török P (2013) Spectral broadening in Brillouin imaging. Appl Phys Lett 103:221105. https://doi.org/10.1063/1.4836477

Bardet S, Gril J (2002) Modelling the transverse viscoelasticity of green wood using a combination of two parabolic elements. Comptes Rendus Mécanique 330:549–556. https://doi.org/10.1016/S1631-0721(02)01503-6

Bergander A, Salmen L (2000) The transverse elastic modulus of the native wood fibre wall. J Pulp Pap Sci 26:234

Berne BJ, Pecora R (2000) Dynamic light scattering: with applications to chemistry, biology, and physics. Courier Corporation, North Chelmsford

Berovic N, Thomas N, Thornhill RA, Vaughan JM (1989) Observation of Brillouin scattering from single muscle fibres. Eur Biophys J 17:69–74. https://doi.org/10.1007/BF00257104

Burgert I, Frühmann K, Keckes J et al (2005) Microtensile testing of wood fibers combined with video extensometry for efficient strain detection. Holzforschung 57:661–664. https://doi.org/10.1515/HF.2003.099

Carroll PJ, Patterson GD (1984) Rayleigh–Brillouin spectroscopy of simple viscoelastic liquids. J Chem Phys 81:1666–1675. https://doi.org/10.1063/1.447892

Cisse O, Placet V, Guicheret-Retel V et al (2015) Creep behaviour of single hemp fibres. Part I: viscoelastic properties and their scattering under constant climate. J Mater Sci 50:1996–2006. https://doi.org/10.1007/s10853-014-8767-1

Csóka L, Božanić DK, Nagy V et al (2012) Viscoelastic properties and antimicrobial activity of cellulose fiber sheets impregnated with Ag nanoparticles. Carbohydr Polym 90:1139–1146. https://doi.org/10.1016/j.carbpol.2012.06.065

Cusack S, Miller A (1979) Determination of the elastic constants of collagen by Brillouin light scattering. J Mol Biol 135:39–51. https://doi.org/10.1016/0022-2836(79)90339-5

Czibula C, Ganser C, Seidlhofer T et al (2019) Transverse viscoelastic properties of pulp fibers investigated with an atomic force microscopy method. J Mater Sci 54:11448. https://doi.org/10.1007/s10853-019-03707-1

Dunford J, Wild P (2002) Cyclic transverse compression of single wood-pulp fibres. J Pulp Pap Sci 28:136–141

Edginton RS, Mattana S, Caponi S et al (2016) Preparation of extracellular matrix protein fibers for Brillouin spectroscopy. J Vis Exp. https://doi.org/10.3791/54648

Edrei E, Gather MC, Scarcelli G (2017) Integration of spectral coronagraphy within VIPA-based spectrometers for high extinction Brillouin imaging. Opt Express 25:6895–6903. https://doi.org/10.1364/OE.25.006895

Elsayad K, Werner S, Gallemí M et al (2016) Mapping the subcellular mechanical properties of live cells in tissues with fluorescence emission–Brillouin imaging. Sci Signal 9:rs5. https://doi.org/10.1126/scisignal.aaf6326

Fischer WJ (2013) A novel direct method for mechanical testing of individual fibers and fiber to fiber joints. Technische Universität Graz, Graz

Fischer WJ, Hirn U, Bauer W, Schennach R (2012) Testing of individual fiber–fiber joints under biaxial load and simultaneous analysis of deformation. Nord Pulp Pap Res J 27:237–244. https://doi.org/10.3183/npprj-2012-27-02-p237-244

Floudas G, Fytas G, Alig I (1991) Brillouin scattering from bulk polybutadiene: distribution of relaxation times versus single relaxation time approach. Polymer 32:2307–2311. https://doi.org/10.1016/0032-3861(91)90065-Q

Ganser C (2014) Influence of water on mechanical properties of cellulosic materials studied by AFM based methods. University of Leoben, Leoben

Ganser C, Teichert C (2017) AFM-based Nanoindentation of cellulosic fibers. In: Tiwari A, Natarajan S (eds) Applied nanoindentation in advanced materials. Wiley, New York, pp 247–267

Ganser C, Hirn U, Rohm S et al (2013) AFM nanoindentation of pulp fibers and thin cellulose films at varying relative humidity. Holzforschung 68:53–60. https://doi.org/10.1515/hf-2013-0014

Ganser C, Czibula C, Tscharnuter D et al (2018) Combining adhesive contact mechanics with a viscoelastic material model to probe local material properties by AFM. Soft Matter 14:140–150. https://doi.org/10.1039/C7SM02057K

Harley R, James D, Miller A, White JW (1977) Phonons and the elastic moduli of collagen and muscle. Nature 267:285–287. https://doi.org/10.1038/267285a0

Hartler N, Nyren J (1970) Transverse compressibility of pulp fibers. 2. Influence of cooking method, yield, beating, and drying. Tappi 53:820

Hutter JL, Bechhoefer J (1993) Calibration of atomic-force microscope tips. Rev Sci Instrum 64:1868–1873. https://doi.org/10.1063/1.1143970

Jajcinovic M (2017) Strength of individual fibres and fibre to fibre joints—influence of the pulp type, environmental conditions and the degree of refining. Technische Universität Graz, Graz

Jajcinovic M, Fischer WJ, Mautner A et al (2018) Influence of relative humidity on the strength of hardwood and softwood pulp fibres and fibre to fibre joints. Cellulose 25:2681–2690. https://doi.org/10.1007/s10570-018-1720-8

Kompella MK, Lambros J (2002) Micromechanical characterization of cellulose fibers. Polym Test 21:523–530. https://doi.org/10.1016/S0142-9418(01)00119-2

Koski KJ, Akhenblit P, McKiernan K, Yarger JL (2013) Non-invasive determination of the complete elastic moduli of spider silks. Nat Mater 12:262–267. https://doi.org/10.1038/nmat3549

Magnusson MS, Östlund S (2013) Numerical evaluation of interfibre joint strength measurements in terms of three-dimensional resultant forces and moments. Cellulose 20:1691–1710. https://doi.org/10.1007/s10570-013-9939-x

Nilsson B, Wågberg L, Gray D (2000) Conformability of wet pulp fibres at small length scales. FSCN, Mitthögskolan, Sundsvall

Oliver WC, Pharr GM (1992) An improved technique for determining hardness and elastic modulus using load and displacement sensing indentation experiments. J Mater Res 7:1564–1583. https://doi.org/10.1557/JMR.1992.1564

Penneru AP, Jayaraman K, Bhattacharyya D (2006) Viscoelastic behaviour of solid wood under compressive loading. Holzforschung 60:294–298. https://doi.org/10.1515/HF.2006.047

Pettersson T, Hellwig J, Gustafsson P-J, Stenström S (2017) Measurement of the flexibility of wet cellulose fibres using atomic force microscopy. Cellulose 24:4139–4149. https://doi.org/10.1007/s10570-017-1407-6

Randall JT, Vaughan JM, Buckingham AD et al (1979) Brillouin scattering in systems of biological significance. Philos Trans R Soc Lond Ser A Math Phys Sci 293:341–348. https://doi.org/10.1098/rsta.1979.0101

Sandercock JR (1970) Brillouin scattering study of SbSI using a double-passed, stabilised scanning interferometer. Opt Commun 2:73–76. https://doi.org/10.1016/0030-4018(70)90047-7

Scarcelli G, Polacheck WJ, Nia HT et al (2015) Noncontact three-dimensional mapping of intracellular hydro-mechanical properties by Brillouin microscopy. Nat Methods 12:1132–1134. https://doi.org/10.1038/nmeth.3616

Speziale S, Jiang F, Caylor CL et al (2003) Sound velocity and elasticity of tetragonal lysozyme crystals by Brillouin spectroscopy. Biophys J 85:3202–3213. https://doi.org/10.1016/S0006-3495(03)74738-9

Stanzl-Tschegg SE, Navi P (2008) Fracture behaviour of wood and its composites. A review COST action E35 2004–2008: wood machining—micromechanics and

fracture. Holzforschung 63:139–149. https://doi.org/10.1515/HF.2009.012

Wild P, Omholt I, Steinke D, Schuetze A (2005) Experimental characterization of the behaviour of wet single wood-pulp fibres under transverse compression. J Pulp Pap Sci 31:116–120

Williams DR, Nurco DJ, Rahbar N, Koski KJ (2019) Elasticity of bamboo fiber variants from Brillouin spectroscopy. Materialia 5:100240. https://doi.org/10.1016/j.mtla.2019.100240

Wu P-J, Kabakova IV, Ruberti JW et al (2018) Water content, not stiffness, dominates Brillouin spectroscopy measurements in hydrated materials. Nat Methods 15:561–562. https://doi.org/10.1038/s41592-018-0076-1

Zhou Tashiro K, Hongo T et al (2001) Influence of water on structure and mechanical properties of regenerated cellulose studied by an organized combination of infrared spectra, X-ray diffraction, and dynamic viscoelastic data measured as functions of temperature and humidity. Macromolecules 34:1274–1280. https://doi.org/10.1021/ma001507x

4.3.4   Mitochondrial network increases mass density in zinc resistant cells

Changes in cellular biomechanical properties play a crucial role in the development of metastases in cancers. Although cell stiffness decrease is described in most tumor types, in a model of prostate cancer we previously described an increase of stiffness of metastatic tumor-derived cells compared to primary tumor-derived cells and increase of cell stiffness in a more aggressive zinc-resistant variant of PC-3 cells (chapter 4.3.1). As this stiffening was not related to actin cytoskeleton organisation, the most predominant factor affecting cell mechanics, we next aim to explain the underlying mechanism by using a combination of microscopical methods (coherence-controlled holographic microscopy, confocal microscopy of actin and tubulin and refractive index tomography).

In the wild-type PC-3 cells individual mitochondria are well discernible in refractive index tomograms (Figure 3A) from rest of perinuclear structures [1]. On the other hand, in zinc-resistant cells, individual mitochondria are barely visible compared to wild-type cells due to
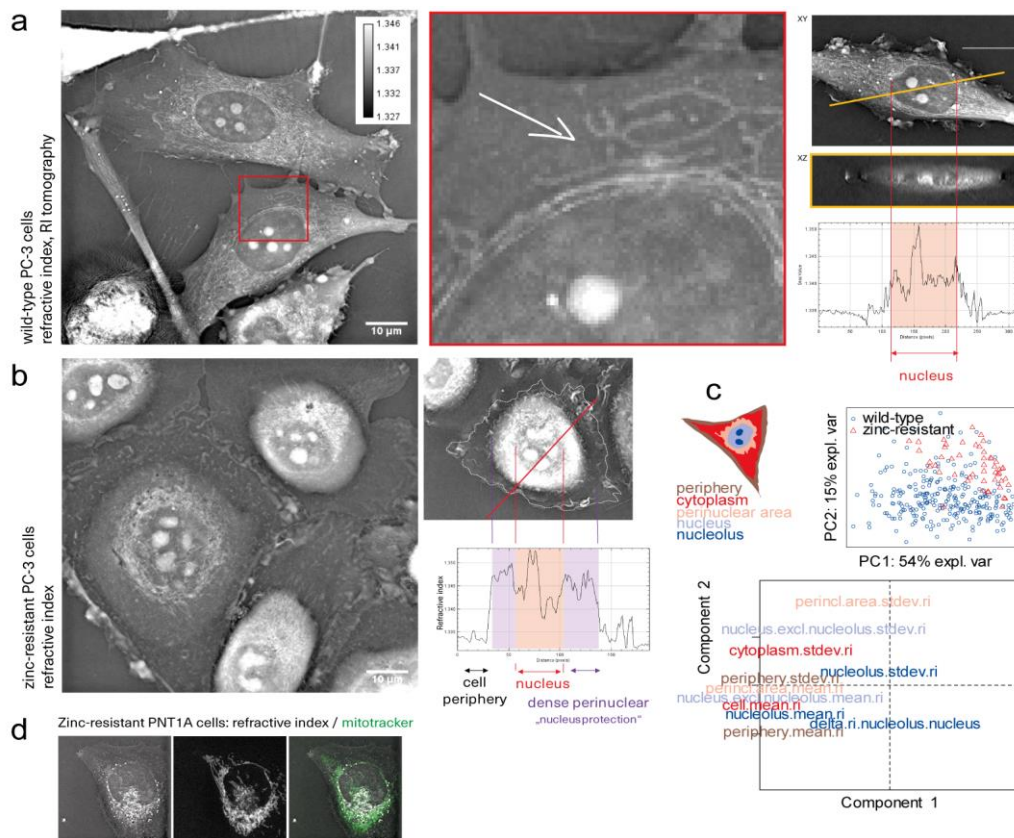
Figure 3 Mitochondrial network is predominantly altered in zinc-resistant cells. a. refractive index tomography (optical diffraction tomography) of wild-type cells with evident mitochondrial network. Single slice of tomogram. White arrow indicates mitochondrial branching. right: profile of RI map of cell, nucleoli are the most prominent structures regarding refractive index. b. tomograms of more aggressive zinc resistant PC-3 cells and respective profile. Evident density increase in perinuclear region. c. principal component analysis of parameters extracted from multiple zones of the cells illustrated in a cartoon cell. These parameters are suitable (N=235 cells) to distinguish PC-3 cell variants with increased aggressiveness. d. correlative imaging of RI tomography with fluorescent staining of mitochondria (mitoTracker Green FM). From Gumulec et al [1]

accumulation of these organelles (Figure 3B). Based on parameters extracted from refractive index tomograms, quantitative phase microscopy can be used to distinguish between more metabolically active and more aggressive „zinc-resistant" PC-3 cells and wild-type counterparts (Figure 3C). Combination of refractive index tomography, AFM and confocal microscopy provided more robust evidence that mass redistribution and increase of metabolic plasticity is characteristic for aggressive prostate cancer model rather than just increase of cell stiffness as seen by AFM.

Based on these findings, the attention was directed on a metabolic reprogramming of cancer cells, and specifically, on the dysregulation of use of metabolic substrates, amino acids, and, on the mitochondria [1; 89; 90].

4.4 Mechanical phenotype is linked also with metabolic phenotype

Metabolic reprogramming is an important prostate cancer hallmark as indicated by multiple evidence. First, malignant cells derived from prostatic tumors show a decrease in zinc accumulation and thus mitochondrial aconitase-mediated increased OXPHOS and no Warburg effect in primary tumors [7]. Based on our experiments, zinc levels differ dramatically in tumorous tissue of patients and benign prostate [91] and cell line models derived from aggressive tumors are highly sensitive to zinc ions [39]. Second, as indicated by refractive index tomography, the mitochondrial network architecture is altered in zinc-resistant prostate cancer cells [1]. With this regard, the focus on oxidative metabolism was given in the next steps.

4.4.1 Amino acid metabolism in prostate cancer

In a study by Raudenska et al [2] on highly aggressive prostate cancer cells discussed in chapter 4.3.1 it is shown that cells derived from metastatic site are stiffer, of higher cell dry mass, and expressing CAV1 compared to the primary tumor-derived cells of low aggressiveness. To further explain which energy-rich compounds are predominantly metabolised, the following study was performed. Here we show a link between changes in amino acid utilization and aggressiveness of the prostate cancer cells.

The non-tumor prostatic cells accumulate citrate due to inhibitory effect of zinc to mitochondrial aconitase. Therefore, citrate metabolization to alpha-ketoglutarate is inhibited and citrate cannot be used as a source of protons in Krebs cycle in non-tumor cells. Although glucose cannot be effectively transferred to energy in cancer cells, other substrates can enter the Krebs cycle. Glucogenic amino acids in particular. In prostate cells, Accumulation of high amount of citrate is manged via acetyl-CoA through pyruvate and oxalacetate regeneration in the end of the Krebs

cycle. Oxalacetate is synthesized from aspartate, which is in turn increasingly imported to the prostatic cells. For the prostate cells, aspartate can therefore be considered an "essential" amino acid [92]. Prostate cancer, on the other hand, loses the ability of citrate accumulation as the inhibitory effect of zinc diminishes. As a result, mitochondrial aconitase is disinhibited and this results from an increased metabolic effectiveness of cancer cells [93; 94] (reviewed in Gumulec et al. [36]).

In a Kratochvilova et al. [95] study, shifts in amino acid pattern were described in relation to the aggressiveness and degree of zinc resistance [85]. Higher aspartate accumulation and lower levels of alanine, methionine leucine, lysine and threonine were present in aggressive cells (characteristic by high Young modulus, high cell dry mass, more stemness-like phenotype and higher migration rates) compared to less aggressive primary tumor-derived cells of low Young modulus and low cell dry mass. Results of the amino acid profiling in prostate cancer are summarized in Kratochvilova et al.

In sum, here we demonstrated that alanine, methionine leucine, lysine and threonine are "essential" for zinc-resistant PC-3 cells and the results also confirm that enzymes of citrate cycle are intact in these cells, otherwise no Asp increase would not be possible.

KRATOCHVILOVA, M., M. RAUDENSKA, Z. HEGER, L. RICHTERA, et al. Amino Acid Profiling of Zinc Resistant Prostate Cancer Cell Lines: Associations With Cancer Progression. Prostate, May 2017, 77(6), 604-616.

Amino Acid Profiling of Zinc Resistant Prostate Cancer Cell Lines: Associations With Cancer Progression

Monika Kratochvilova,[1,2] Martina Raudenska,[1,2] Zbynek Heger,[2,3] Lukas Richtera,[2,3] Natalia Cernei,[2,3] Vojtech Adam,[2,3] Petr Babula,[1] Marie Novakova,[1] Michal Masarik,[1,2,4] and Jaromir Gumulec[1,4]*

[1]Faculty of Medicine, Department of Physiology, Masaryk University, Brno, Czech Republic
[2]Central European Institute of Technology, Brno University of Technology, Brno, Czech Republic
[3]Department of Chemistry and Biochemistry, Mendel University in Brno, Brno, Czech Republic
[4]Faculty of Medicine, Department of Pathological Physiology, Masaryk University, Brno, Czech Republic

BACKGROUND. Failure in intracellular zinc accumulation is a key process in prostate carcinogenesis. Nevertheless, epidemiological studies of zinc administration have provided contradicting results. In order to examine the impact of the artificial intracellular increase of zinc(II) ions on prostate cancer metabolism, PNT1A, 22Rv1, and PC-3 prostatic cell lines— depicting different stages of cancer progression—and their zinc-resistant counterparts were used. To determine "benign" and "malignant" metabolic profiles, amino acid patterns, gene expression, and antioxidant capacity of these cell lines were assessed.
METHODS. Amino acid profiles were examined using an ion-exchange liquid chromatography. Intracellular zinc content was measured by atomic absorption spectrometry. Metallothionein was quantified using differential pulse voltammetry. The content of reduced glutathione was determined using high performance liquid chromatography coupled with an electrochemical detector. Cellular antioxidant capacity was determined by the ABTS test and gene expression analysis was performed by qRT-PCR.
RESULTS AND CONCLUSIONS. Long-term zinc treatment was shown to reroute cell metabolism from benign to more malignant type. Long-term application of high concentration of zinc(II) significantly enhanced cisplatin resistance, invasiveness, cellular antioxidant capacity, synthesis of glutathione, and expression of treatment resistance- and stemness-associated genes (SOX2, POU5F1, BIRC5). Tumorous cell lines universally displayed high accumulation of aspartate and sarcosine and depletion of essential amino acids. Increased aspartate/threonine, aspartate/methionine, and sarcosine/serine ratios were associated with cancer phenotype with high levels of sensitivity and specificity. Prostate 77: 604–616, 2017.
© 2017 Wiley Periodicals, Inc.

KEY WORDS: zinc; resistance; amino acid; aspartate; metabolomics

INTRODUCTION

Metabolism of prostate gland cells is unique and different from metabolism of other cells in human body. Secretory epithelial cells in the prostate are highly specialized in citrate production and are able to secrete high amounts of citrate into the prostatic fluid. This happens due to their capability to accumulate high levels of zinc that inhibit m-aconitase and citrate oxidation in the Krebs cycle. As a consequence, normal prostate glandular epithelial cells exhibit low respiration, unfinished Krebs cycle, low citrate oxidation, and

are therefore worse ATP producers as compared to benign epithelial cells in other tissues [1].

In majority of tumors, tumorigenesis is usually associated with a metabolic switch from respiration to glycolysis and reduced catabolic Krebs cycle activity (Warburg effect) which attenuates effectivity of ATP production. Conversely, due to a failure in intracellular zinc accumulation in tumor prostate cells, a metabolic switch from citrate-accumulating, energy-inefficient benign cells to energy-efficient tumor cells occurs [2]. Citrate can be oxidized to carbon dioxide and oxaloacetate for the production of ATP in mitochondria; another possibility is its preferable export to the cytosol, where acetyl coenzyme A (acetyl-CoA) and oxaloacetate is formed due to ATP citrate lyase action. Acetyl-CoA is used for the synthesis of fatty acids and cholesterol, whereas oxaloacetate is an amino acid precursor [3]. Accordingly, prostate cancer cells were shown to contain higher levels of amino acids, fatty acids, and cholesterol [3–6]. Furthermore, N-methyl derivative of glycine (sarcosine) can be accumulated in cells during prostate cancer progression to metastasis [7]. Changes in intracellular concentrations of particular metabolites can influence cancer cell growth and metastatic invasion [8,9]. Many oncogenes—such c-Myc, Ras, or Src—provide cancer cells with alternative metabolic pathways and unconventional use of amino acids [10,11]. Consequently, changes in amino acid profiles may serve as a valuable biomarker for screening, diagnosis, and prognosis, since they are easily measurable in body fluids.

It is obvious that failure in intracellular zinc accumulation is a key process in prostate carcinogenesis. Nevertheless, epidemiological studies of zinc administration have provided rather contradicting results [12]. In order to examine the impact of excessive zinc concentrations on intracellular zinc accumulation and prostate cancer metabolism, PNT1A, 22Rv1, and PC-3 prostatic cell lines—depicting different stages of the cancer disease progression—and their previously created zinc-resistant counterparts have been used in this study [13]. The main focus of this work has been to assess "benign" and "malignant" metabolic profiles. Furthermore, amino acid profiles of each cell line in relation to a degree of zinc accumulation and zinc resistance have been determined.

MATERIALS AND METHODS

Chemical and Biochemical Reagents

RPMI-1640 medium, Ham's F12 medium, fetal bovine serum (FBS) (mycoplasma-free), penicillin/streptomycin, and trypsin were purchased from Sigma Aldrich Co. (St. Louis, MO). Phosphate buffered saline PBS was purchased from Invitrogen Corp. (Carlsbad, CA). Ethylenediaminetetraacetic acid (EDTA), zinc(II) sulphate (BioReagent grade, suitable for cell cultures) and all other chemicals of ACS purity were purchased from Sigma Aldrich Co., unless noted otherwise.

Cell Cultures

Three human prostatic cell lines were used in this study. PNT1A human cell line is derived from normal adult prostatic epithelial cells immortalized by transfection with a plasmid containing SV40 genome with defective replication origin. The primary culture was obtained from the normal prostatic tissue of a 35-year old male post mortem. PNT1A is PTEN positive non-tumorigenic epithelial cell line [14]. 22Rv1 is human prostate carcinoma epithelial cell line derived from a xenograft serially propagated in mice after castration. The cell line expresses prostate specific antigen (PSA). Growth is weakly stimulated by dihydroxytestosterone and lysates are immunoreactive with androgen receptor antibody. 22Rv1 is PTEN positive [15]. PC-3 human epithelial cell line was established from a four grade prostatic adenocarcinoma, androgen independent, and unresponsive metastatic site in bone. PC-3 is PTEN- and p53-negative [15,16]. All cell lines used in this study were purchased from HPA Culture Collections (Salisbury, UK).

Cell Cultivation

PNT1A and 22Rv1 cells were cultured in RPMI-1640 medium with 10% FBS. PC-3 cells were cultured in Ham's F12 medium with 10% FBS. Both media were supplemented with antibiotics (penicillin 100 U/ml and streptomycin 0.1 mg/ml). Cells were maintained at 37°C in a humidified (60%) incubator with 5% CO_2 (Sanyo, Japan). The passages of PNT1A and 22Rv1 cell lines ranged from 25 to 35, the passages of PC-3 cell line ranged from 15 to 25.

Zinc(II) Treatments of Cell Cultures

Two different treatments were used in this study. The first one was short-term treatment. Cells confluent up to 50–60% were washed with FBS-free medium and treated with fresh medium with FBS and required zinc concentration (onefold to threefold the value of IC50 for the cell line). Cells were cultivated under these conditions for 24 hr. The resulting samples are called zinc-treated "wild type" in this study. The second type of treatment was long-term. Cells were cultivated with the constant presence of zinc(II) ions.

The concentrations of zinc(II) sulphate in the medium were increased gradually by small changes of 25 or 50 μM. Cells were cultivated at each concentration no less than 1 week before harvesting and the viability was checked before adding more zinc. This process naturally selected zinc resistant cells. Cells with long-term exposure are called "resistant" in this study. Total time of cultivation of cell lines in zinc(II)-containing media exceeded one year. Resulting concentrations of zinc(II) in media (onefold to threefold the value of IC50 for particular cell line) were 50; 100 and 150 μM for PC-3 cell line, 150; 300 and 450 μM for PNT1A cell line, and 400; 800 and 1200 μM for 22Rv1 cell line. Concentrations of zinc(II) in media and FBS were taken into account.

RNA Isolation, cDNA Preparation

Cultivation medium was removed, cells were washed with PBS and trypsinized. TriPure Isolation Reagent (Roche, Basel, Switzerland) was used for RNA isolation. RNA samples without reverse transcription were used as negative control for qRT-PCR to exclude DNA contamination. The isolated RNA was used for the cDNA synthesis. RNA (1,000 ng) was transcribed using the transcriptor first strand cDNA synthesis kit (Roche, Switzerland) according to manufacturer's instructions. The cDNA (20 μl) prepared from the total RNA was diluted with RNase free water to 100 μl and the amount of 5 μl was directly analyzed.

Quantitative Real-Time Polymerase Chain Reaction (qRT-PCR)

qRT-PCR was performed using the TaqMan gene expression assays with the LightCycler®480 II System (Roche, Basel, Switzerland). The amplified DNA was analyzed by the comparative Ct method using β-actin as a reference. The primer and probe sets for *ACTB* (assay ID: Hs99999903_m1), *MT2A* (Hs02379661_g1), *ZNT1* (Hs00253602_m1), *SOX2* (Hs01053049_s1), *HIF1A* (Hs00153153_m1), *NANOG* (Hs04260366_g1), *BIRC5* (Hs00153353_m1), and *POU5F1* (Hs04260367_gH) were selected from TaqMan gene expression assays (Life Technologies). qRT-PCR was performed under the following amplification conditions: total volume of 20 μl, initial incubation at 50°C/2 min followed by denaturation at 95°C/10 min, then 45 cycles at 95°C/15 sec and at 60°C/1 min.

Preparation of Cells for Determination of Amino Acid Profiles and Zinc Content

Five miligram of cells was digested by Microwave system 3,000 (Anton Paar GmbH, Graz, Austria) using

rotor MG-65 in nitric acid (65% v/v) and hydrogen peroxide (30 v/v) in ratio 7:3. Microwave power was set to 100 W (30 min) at a temperature of 140°C.

Amino Acids Profiling

Amino acid profiles were examined using an ion-exchange liquid chromatography (AAA-400, Ingos, Prague, Czech Republic) with post-column derivatization by ninhydrin and absorbance detector in visible light range (IEC-Vis). Measurements were carried out under conditions optimized in our previous study [17].

Zinc Quantitation by Atomic Absorption Spectrometry

Measurements were carried out on 280Z atomic absorption spectrometer (Agilent, Technologies, Santa Clara, CA) with electrothermal atomization and Zeeman background correction. Zinc was measured on primary wavelength: Zn 213.9 nm (spectral bandwidth 0.5 nm, lamp current 10 mA) in the presence of Pd chemical modifier.

Preparation of Cells Prior Sarcosine Analyses

The cells were frozen by liquid nitrogen to disrupt their structure. The frozen samples were further homogenized using ultrasonic homogenizer SONO-PLUS mini20 (Bandelin electronic, Berlin, Germany). Then 1 ml of 0.2 M phosphate buffer (pH = 7.0) was added and the sample was homogenized again for 5 min. The cell homogenates were further analyzed using IEC-Vis according to our previous study [17].

Preparation of Cells for Determination of Total Protein, Metallothionein, Glutathione, and Antioxidant Capacity

The cells were frozen by liquid nitrogen and homogenized using ultrasonic homogenizer SONO-PLUS mini20 (Bandelin electronic). Subsequently, 1 ml of 0.2 M phosphate buffer (pH 7.0) was added and the sample was homogenized for 5 min. The homogenates were further centrifuged using Microcentrifuge 5417R (Eppendorf, Hamburg, Germany) at 4°C, 15,000g, for 15 min. Finally, the supernatant was filtered through a membrane filter (0.45 μm nylon filter disk; Millipore, Billerica, MA) and analyzed.

Determination of Total Protein Content

The total proteins were utilized for results normalization and were performed using SKALAB

CBT 600T kit (Skalab, Svitavy, Czech Republic) according to manufacturer's instructions, using BS-400 automated spectrophotometer (Mindray, Schenzhen, China).

Determination of Amount of Metallothionein

MT was quantified using differential pulse voltammetry (747 VA Stand, connected to the 693 VA processor and 695 Autosampler, Metrohm, Herissau, Switzerland), under the conditions used in our previous study [18].

Determination of Reduced Glutathione

The content of reduced glutathione (GSH) was determined using high performance liquid chromatography coupled with an electrochemical detector (HPLC-ED) system under the conditions used in our previous study [19].

Determination of Antioxidant Capacity by the ABTS Test

Antioxidant capacity was analyzed using the neutralization of a radical-cation arising from one-electron oxidation of the synthetic chromophore 2,2'-azino-bis(3-ethylbenzothiazoline-6-sulfonic acid (ABTS). The reaction was monitored spectrophotometrically by the change of the absorption value at 660 nm using spectrophotometer BS-400 (Mindray).

Real-Time Impedance Based Cell Migration and Invasivity Assay

The impedance-based real-time cell analysis (RTCA) xCELLigence system was used according to the instructions of the supplier (Roche Applied Science and ACEA Biosciences, San Diego, CA). The xCELLigence system consists of four main components: RTCA DP station, RTCA computer with integrated software and disposable CIM-plate 16. Firstly, the optimal seeding concentration for migration and invasivity assay was determined. Optimal response was found in the well containing 20,000 cells. After coating the upper wells with Matrigel and adding FBS as chemoattractant, a total number of cells in 100 μl of medium to each well in CIM-plate 16 was seeded. The cell attachment and growth through the matrigel were monitored every 15 min. Duration of all experiments was 80 hr. Results are expressed as relative impedance using manufacturer's software (Roche Applied Science and ACEA Biosciences) [20].

Statistical Analysis

Data were checked for normality and log-normal data were transformed. Univariate general regression models with all three factors (cell line, resistance, zinc concentration) as categorial predictors were performed in the first step. Consequently, planned comparisons were performed. In the next step, all values were standardized and dependencies were analyzed using principal component analysis on a two-factor plane based on amino-acid levels (oxidative parameters and genes were plotted as supplementary variables), (c) using hierarchical clustering using Ward's method showing linkage distance between cases (cell lines). Finally, receiver-operator statistic using easyROC 1.3 (http://www.biosoft.hacettepe.edu.tr/easyROC/) was performed to assess area under the curve, sensitivity and specificity of selected variables as predictors of tumor presence. Unless noted otherwise, P level <0.05 was considered significant and software Statistica 12 (Dell Inc., Tulsa, OK) was used.

RESULTS

Zinc Accumulation

In previous experiments, IC50 for zinc sulphate of wild-type cell lines was determined as follows: 150.8 μM, 369.1 μM, and 55.5 for PNT1A, 22Rv1, and PC-3, respectively [13].

The levels of accumulated (measured) intracellular zinc in wild-type and resistant cell lines exposed to 0–3-fold of its IC50 concentrations of zinc sulphate were compared (see experimental section for details). Intracellular zinc was accumulated more intensively in resistant cell lines in comparison with wild-type cell lines ($P = 0.01$, see Supplementary Table S1) when exposed to zinc treatment. Nevertheless, cell-line specific differences in zinc accumulation were observed; intracellular zinc(II) content increased extensively and proportionally to added zinc sulphate in all resistant cell lines and also in the wild-type 22Rv1. On the other hand, only a small increase in intracellular levels of zinc due to zinc sulphate treatment was observed in wild-types PC-3 and PNT1A. Maximal increase in intracellular zinc concentration was achieved in zinc-resistant 22Rv1 cultured in threefold IC50 (up to 1,800 μg/g); see Figure 1A.

General Mechanisms of Coping With Increasing Zinc(II) Concentrations

Changes in antioxidant capacity, expression of selected genes, and accumulation of particular amino acids caused by increasing zinc(II) concentration are
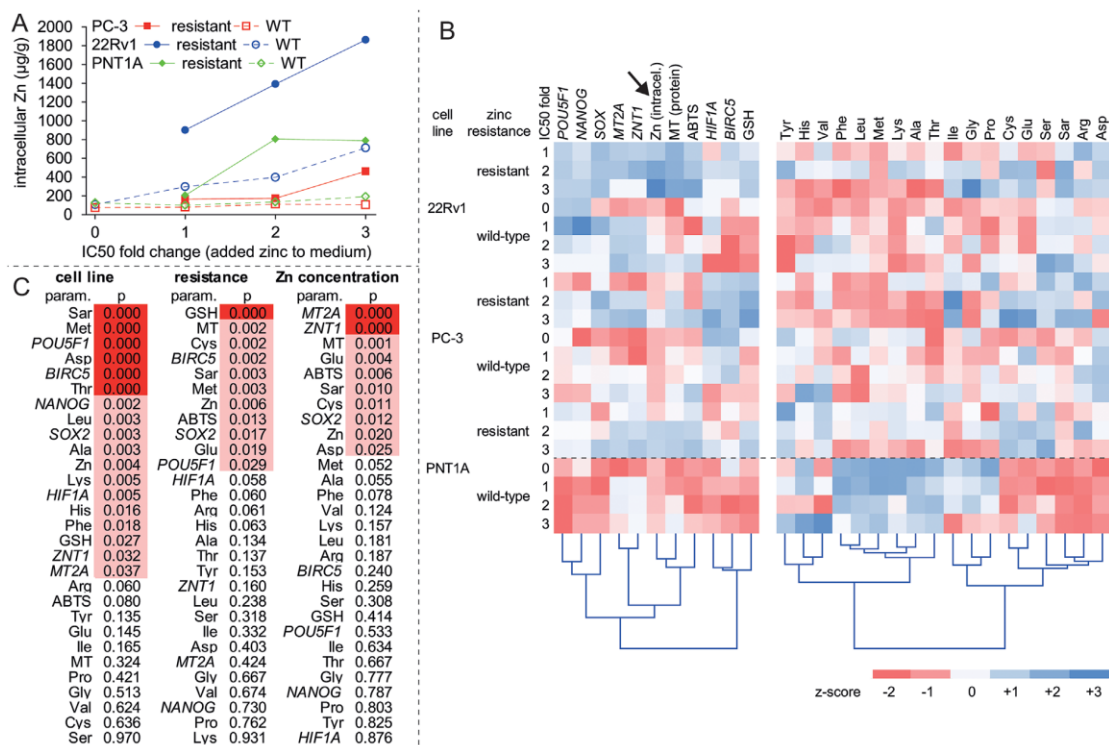
Fig. 1. Concentrations of amino acids, gene expression levels and other parameters in zinc-resistant prostatic cell lines and wild-type counterparts. (**A**) absolute concentration of intracellular (measured) zinc versus concentration of zinc in medium (0, 1, 2, and 3 correspond to IC-50 fold changes). (**B**) Heatmap showing relative amounts of parameters in cells. Displayed as z-scores with mean = 0 and standard deviation = 1. Note the distinctive differences between wild-type PNT1A cells and tumorous counterparts. ``IC50 fold'' indicate fold change of half-maximal concentration of zinc used for treatment, ``Zn'' indicate amount of intracellular zinc (measured). (**C**) results of univariate test, P-values for individual variables for three independent predictors—cell line, resistance, and zinc concentration. Sorted based on P-level (parameters most significantly affected by cell line/resistance or Zn concentration are dark red, topmost in table).

shown in Figure 1B. According to multivariate ANOVA, MT gene, and protein, *ZnT1*, and *SOX2* genes significantly increased their expression in cells treated with zinc(II)ions ($P \leq 0.001$, $P \leq 0.001$, $P = 0.002$, see supplementary Table S1). Furthermore, zinc(II) treatment significantly enhanced cellular concentrations of sarcosine ($P = 0.03$), aspartate ($P = 0.01$), glutamate ($P = 0.01$), cysteine ($P = 0.005$), valine ($P = 0.03$), and arginine ($P = 0.04$) as well as antioxidant capacity of cells (2,2′-azino-bis(3-ethylbenzothiazoline-6-sulphonic acid, ABTS, $P = 0.05$). On the other hand, cellular concentrations of alanine ($P = 0.04$), methionine ($P = 0.01$), and phenylalanine ($P = 0.04$) significantly decreased due to zinc(II) treatment.

In conclusion, universal mechanisms of coping with increasing zinc concentrations (common to both resistant and wild-type cell lines) were observed. These mechanisms involved chelation of free zinc ions by metallothionein (an increasing trend in MT expression was observed), efflux of zinc(II) ions from the cytoplasm by the ZnT1 transporter and enhancement of the antioxidant capacity (measured by ABTS) followed by the accumulation or depletion of particular amino acids.

Effect of Cell Line

In this step, the effect of the cell line was analyzed after adjustment of zinc concentration and zinc resistance. Using univariate test, there was a significant effect of cell line on the gene expression and amino acid profile $F_{(30,6)} = 16.97$; $P \leq 0.001$ (see Fig. 1C). Among the parameters most distinctly affected by cell line are cellular concentrations of sarcosine, methionine, aspartate, and threonine and gene expression levels of *POU5F1*, *NANOG*, and *BIRC5*.

Subsequent planned comparisons (multivariate testing) revealed that tumorous 22Rv1 cell line (compared to non-tumor PNT1A) exhibited up-regulation of the gene expression of *SOX2* ($P = 0.001$), *MT2A*

($P = 0.02$), *NANOG* ($P = 0.004$), and *POU5F1* ($P < 0.001$); higher accumulation of zinc ($P = 0.01$), aspartate ($P = 0.002$), and sarcosine ($P < 0.001$) and higher antioxidant capacity ($P = 0.04$). Conversely, intracellular concentrations of threonine ($P = 0.005$), alanine ($P = 0.002$), methionine ($P < 0.001$), leucine ($P = 0.003$), phenylalanine ($P = 0.02$), histidine ($P = 0.005$), and lysine ($P = 0.002$) were lower in 22Rv1 cell line. Secondly, characteristics of the cell line derived from metastasis (PC-3) were analyzed. Compared to PNT1A, there was a significant up-regulation of GSH ($P = 0.01$), *BIRC5* ($P < 0.001$), *SOX2* ($P = 0.03$), and *HIF1A* ($P = 0.002$). Higher accumulation of aspartate ($P < 0.001$), sarcosine ($P < 0.001$), and arginine ($P = 0.03$) was also observed in PC-3. Conversely, intracellular concentrations of threonine ($P < 0.001$), alanine ($P = 0.01$), methionine ($P < 0.001$), leucine ($P = 0.002$), phenylalanine ($P = 0.01$), and lysine ($P = 0.02$) were lower in PC-3 cell line.

In conclusion, tumorous cell lines were characteristic by higher expression of *SOX2*, higher accumulation of aspartate, and sarcosine and lower levels of essential amino acids, in particular: threonine, methionine, leucine, phenylalanine, lysine, and alanine. Primary tumor-derived 22Rv1 was characteristic by depletion of histidine and increased expression of *MT2A*, *NANOG*, and *POU5F*. Bone metastasis-derived PC-3 was typical by increased accumulation of arginine and higher expression of *HIF1A* and *BIRC5*.

Effect of Long-Term Treatment (Zinc Resistance)

In this step, the effect of "zinc resistance" (i.e., long-term vs. short-term treatment) was assessed.

Resistant cells markedly increased their IC50 for cisplatin: by 1.4-, 1.6-, and 1.6-fold for PNT1A, 22Rv1, and PC-3, respectively [21]. Furthermore, morphological changes and increased numbers of polyploid giant cancer cells (PGCCs) in zinc-resistant PC-3 cell line were observed (Fig. 2A). Also, cellular concentrations of metallothionein, cysteine, sarcosine, methionine, glutamine, and GSH were significantly affected by the zinc resistance. Resulting zinc accumulation, antioxidant capacity (ABTS) and higher gene expression of *BIRC5* ($P = 0.002$), *POU5F1* ($P = 0.03$), and *SOX2* ($P = 0.02$) were other consequences of zinc-resistant phenotype (Fig. 1C and supplementary Table SI). Higher accumulation of zinc in resistant cells (see section Zinc Accumulation) could be a direct result of their higher antioxidant capacity (ABTS) ($P = 0.01$) and higher GSH ($P = 0.001$), and metallothionein (MT) production ($P = 0.002$). Resistant cells accumulate also higher levels of sarcosine ($P = 0.003$), cysteine ($P = 0.002$), and glutamate ($P = 0.02$) and relatively lower levels of methionine ($P = 0.003$). The ability of

cells to spread in the surrounding tissues was tested by using real-time, label-free monitoring xCELLigence invasivity assay. Higher invasiveness of all tested zinc resistant cell lines (PC-3, PNT1A, 22Rv1) in comparison with their non-resistant counterparts was demonstrated (Fig. 2B).

To reveal the complex connection patterns between long- and short-term treatments and thus to illustrate the involvement of amino acids in zinc resistance, principal component analysis (PCA) was performed. This analysis combines the advantages of correlation analysis with cluster analysis by projecting the variables (amino acids, genes, etc.) on a two-factor plane. The "importance" of the variables increases with their distance from the center of the diagram. A two-factor plane was constructed based on amino acid patterns ("active" variables). This approach explained 66.4% and 59.7% of data heterogeneity in wild-type and resistant cells. In the next step, other parameters (genes, oxidative stress-related parameters) were plotted into this factor plane as supplementary variables. Following associations were evident: (i) The central effect of GSH and its association with amino acid metabolism is typical for zinc-resistant cells (compare the distance of GSH from the PCA center in WT and resistant cells, Fig. 3A); (ii) On the other hand, antioxidant capacity measured by ABTS played a more central role in wild-type cells (compare distances from PCA center accordingly). Because GSH was not in a positive correlation with ABTS, we assume another important role of GSH in resistant metabolism; (iii) Furthermore, "pro-survival and/or antioxidant" markers (such as ABTS, GSH, MT, HIF1A, cysteine, glutamine) are clustered together in wild-type cells (lower left quadrant of PCA), while markers associated with "pluripotency" (*NANOG*, *SOX2*, *POU5F1*) are located in a different (upper left) quadrant in wild-type cells. However, this is not evident in zinc-resistant cells, where all those parameters are clustered together.

Amino Acid Patterns as Predictors of Cancer Phenotype

Previous analyses highlighted amino acids specifically related to zinc resistance, cell lines, or zinc concentration. However, these data do not bring the evidence whether or how the individual amino acids are related to the advancement of the disease. Therefore, hierarchical cluster analysis was performed using amino acid concentrations as variables. Based on interrelationships between amino acids, linkage distance between wild-type untreated PNT1A cell line and others was calculated (Fig. 3B). As expected, remaining wild-type PNT1As (exposed
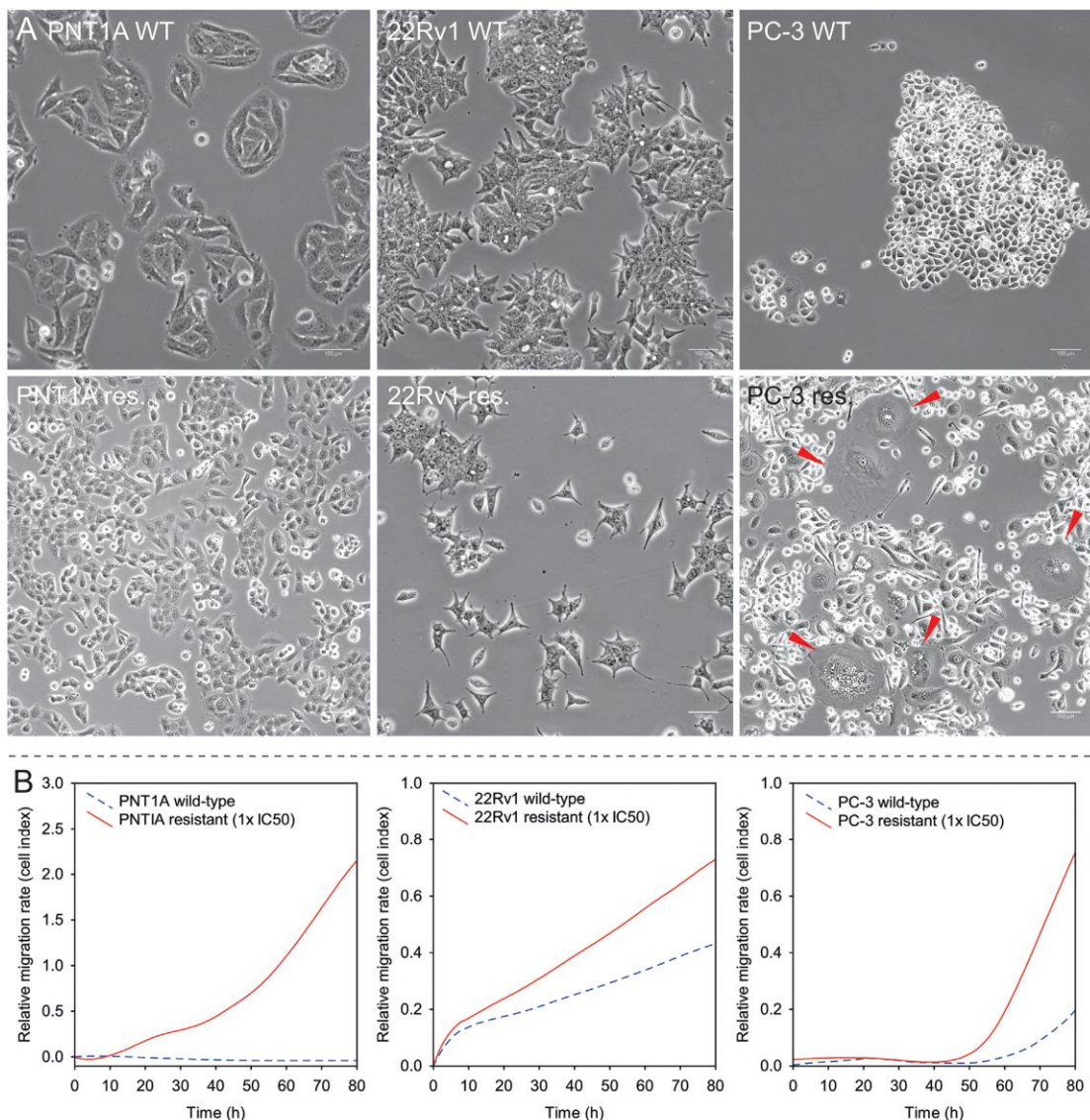
Fig. 2. Cell morphology and invasivity changes due to long-term zinc treatment. (**A**) Morphology of wild-type and zinc-resistant cells. Red arrow indicate polyploid giant cancer cells. (**B**) real-time label-free monitoring of invasivity. See higher invasiveness of all tested zinc resistant cell lines (PC-3, PNT1A, 22Rv1) in comparison with their non-resistant counterparts.

to zinc) were clustered closely to the untreated one followed by a cluster of tumorous cell lines (see the setting of the plateau on a linkage distance curve in Fig. 3B "tumorous metabolism" characteristic for tumorous cells). Distinct contribution of zinc treatment was also evident: higher concentrations of zinc, as well as resistant variants of particular cell lines, were at greater distance from benign untreated PNT1A. Moreover, another cluster characteristic by the highest linkage distances to PNT1A was

observed and designated as "highly resistant metabolism"; this cluster was composed of resistant tumorous cell lines treated by the highest zinc(II) concentrations. This trend was verified using receiver-operator statistics (ROC), showing that linkage distance based on amino acid profiles is highly specific and sensitive indicator of malignant behavior (Fig. 3C). This trend was also in a correlation with pluripotency marker *SOX2* (r = 0.72, P < 0.001, highlighted as green dots in the chart).

The Prostate
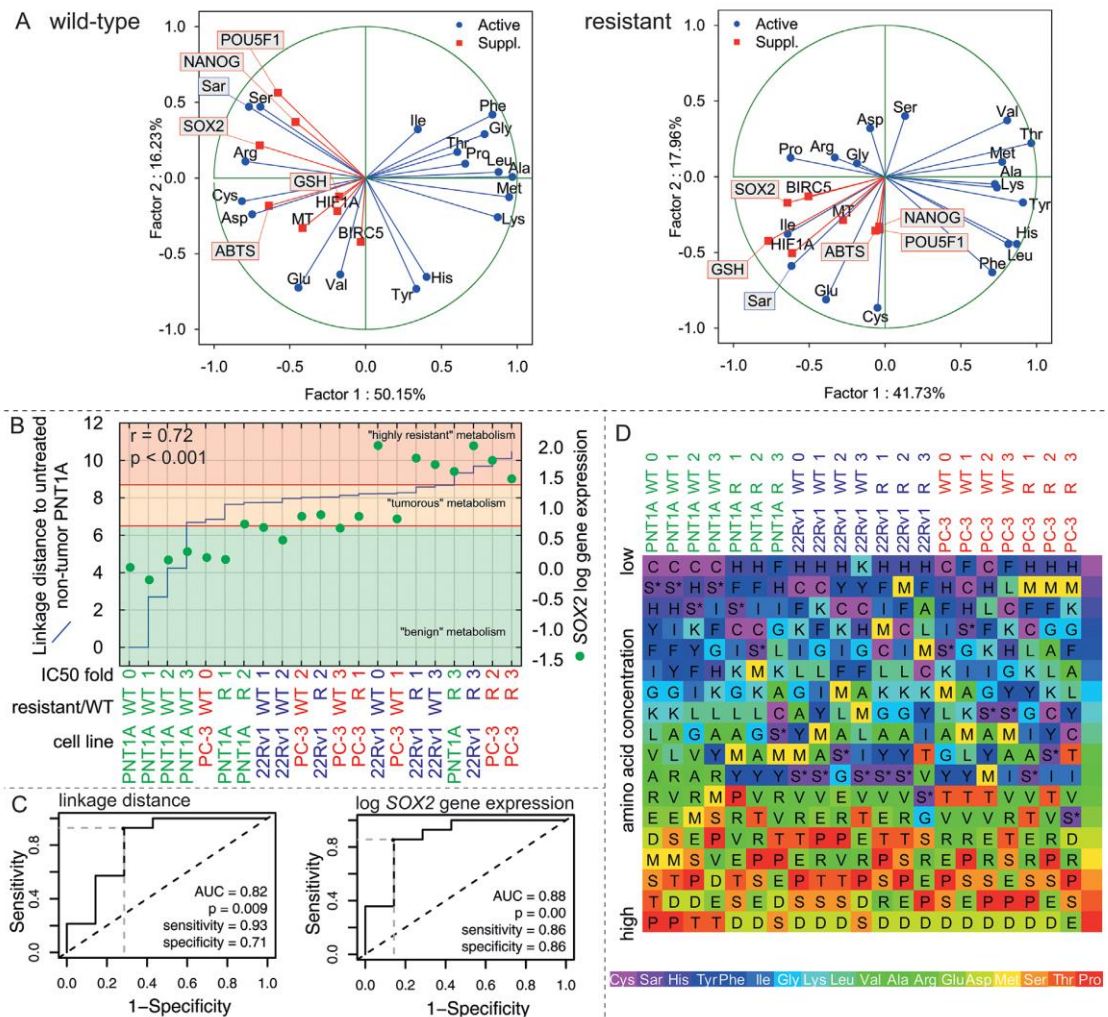
Fig. 3. Amino acid patterns and tumor progression. (**A**) Principal component analysis, projection of variables on two-factor plane based on amino acid concentrations (other parameters plotted on a chart as a supplementary variables). Note that pluripotency-associated genes *NANOG*, *SOX2*, and *POU5F1* are clustered together with pro-survival and oxidative stress parameters in resistant cells (lower left quadrant) and clustered separately in WT cells. (**B**) linkage distance determined by cluster analysis based on amino acid patterns. Linkage distance illustrates level of dissimilarity from non-tumor wild-type untreated PNT1A cells, for whose linkage distance = zero. 0, 1, 2, and 3 correspond to IC-50 fold changes. See that resistance and/or tumorous phenotype enhance linkage distance from PNT1A cells. Based on a linkage distance, benign, tumorous and highly resistant cells were distinguished. Linkage distance correlated with *SOX2* expression in cells (green dots). (**C**) receiver-operator curves and its subsequent statistics for determination of benign/malignant cell lines. (**D**) chart showing relative abundance of particular amino acid in particular cells, sorted from low to high concentrations. 0, 1, 2, and 3 correspond to IC-50 fold changes. Rainbow color order coding based on untreated wild-type PNT1A cells. See the rainbow-colored heatmap distracts by relative increase/decrease of specific amino acids amounts (see online for color). See gradual decrease of Met (high concentrations in non-tumor cells vs. low concentrations in resistant tumorous cells) and increasing concentrations of Sar, Cys, and Asp in relation to the progression of zinc resistance and malignance. S* indicate sarcosine. WT, wild-type; R, resistant.

In order to highlight which of the amino acids contribute to this "model of gradual increase of aggressiveness," a heatmap based on amino acid concentrations was created (Fig. 3D). Several specific phenomena were evident: (i) gradual decrease of methionine (high concentrations in non-tumor cells as compared to low methionine concentrations in resistant tumorous cells) and (ii) increasing concentrations of sarcosine, cysteine, and aspartate in relation to the progression of zinc resistance and malignance. Based

on these data, following product/precursor ratios were calculated: cysteine/methionine and sarcosine/serine. The association of these ratios with malignant phenotype was verified by ROC and multivariate ANOVA (Table I), where both of them demonstrated high levels of sensitivity and specificity. Thus, high cysteine/methionine and sarcosine/serine ratios were shown to be a promising marker of malignant metabolism.

Excessive accumulation of aspartate was accompanied by a depletion of some essential amino acids (threonine, lysine, leucine, phenylalanine, and methionine) in prostate cancer cells. This fact indicated a boosting of aspartate synthesis pathways. Various molecules could serve as a substrate for synthesis of aspartate, including essential amino acids (Fig. 4). In accordance with observed increasing/decreasing trends of amino acids (Fig. 3D), ratios between Asp and other amino acids were calculated and the effect of cell line on the level of these ratios was analyzed using multivariate ANOVA and receiver-operator statistic (Table I). Aspartate/tyrosine, aspartate/methionine, and aspartate/threonine ratios were shown to be promising markers of malignant metabolism. Furthermore, ROC analysis provided evidence that aspartate synthesis pathway is specifically altered in tumorous cell line and thus it is involved in the prostate cancer progression.

DISCUSSION

The key biochemical feature of prostate cancer cells is a steep decrease in intracellular zinc(II) and citrate levels. Metabolic transformation leading to the attenuation of zinc concentration with subsequent triggering of citrate oxidation is fundamental for the manifestation of malignant phenotype [22]. Consequently, it is intriguing to apply this relationship to treatment or prevention of prostate cancer. Our approach in this study was to constitute conditions that would enforce the accumulation of zinc(II) into the malignant cells and to assess consequences of such accumulation for malignant metabolism (Will an artificial intracellular increase of zinc cause a change towards a benign metabolism?). PNT1A, 22Rv1, and PC-3 prostatic cell lines— depicting different stages of the cancer disease progression—and their previously created zinc-resistant counterparts have been used [13]. We have confirmed the higher ability of zinc-accumulation in resistant cell lines (see Fig. 1A). It can be assumed that long-term exposure to excessive zinc(II) is able to exhaust the capacity of cellular zinc(II) exporters and cells are then forced to accumulate this metal and to trigger intrinsic mechanism for coping with it. Universal mechanisms of coping with increasing

intracellular zinc(II) concentrations include free zinc ions chelation by metallothionein and an enhancement of the antioxidant capacity. These effects were previously observed in several laboratories, including ours [13,23,24]. The maximal increase in intracellular zinc concentration was achieved in zinc-resistant 22Rv1 derived from primary tumor of prostate (up to 1,800 μg/g). High zinc tolerance in primary tumor cells (especially in comparison with metastatic counterparts) may result from adoption and enhancement of inherited capabilities of benign secretory epithelial cells. These cells are highly specialized and evolved for zinc accumulation [25]; therefore, they can exploit protective mechanisms against the toxic effects of zinc. On the contrary, prostate cancer cells derived from bone metastasis (PC-3 cells) no longer need to cope with high zinc concentrations in prostate gland and hence are more sensitive to zinc(II).

The main focus of this study was to assess "benign" and "malignant" metabolic profiles. Clarifying of metabolic shifts triggered by carcinogenesis is relevant for diagnostic purposes and can also elucidate the molecular basis of malignant processes, which could possibly result in new therapeutic options. In this study, tumorous cell lines displayed higher expression of *SOX2* gene, higher accumulation of aspartate and sarcosine and lower levels of threonine, alanine, methionine, leucine, phenylalanine, and lysine as compared to benign PNT1A. SOX2 is a core transcription factor involved in self-renewal and pluripotency of tumor cells and was reported to be involved in malignant transformation of prostate tissue [26,27] which is in full accordance with our results. *SOX2* expression plays a significant role in cancer phenotype, as it was in a strong correlation with linkage distance depicting the degree of deviation from benign metabolism represented by PNT1A cells (see Fig 3B). With regard to sarcosine and aspartate, we have previously shown that these amino acids affect the progression and migration capacity of prostate cancer cells [9]. Aspartate is usually synthesized in the mitochondrial matrix with the help of malate dehydrogenase (MDH2) and glutamic-oxaloacetic transaminase 2 (GOT2). Nevertheless, the shift in the NAD+/NADH balance after OXPHOS attenuation in healthy prostate secretory cells can inhibit MDH2 and consequently aspartate synthesis in mitochondria [28,29]. Accordingly, aspartate was considered as an essential amino acid for healthy prostate cells [30,31]. Moreover, healthy prostate cells utilize large amounts of aspartate as the carbon source for citrate production [32]. Support of aspartate biosynthesis in proliferating cells was recently revealed as a key activity of respiration [28,33]. Excessive aspartate accumulation accompanied by depletion of

TABLE I. The Effect of Cell Line on Amino Acid Levels and Amino Acid Ratios

Amino acid	Absolute concentration (estimate and 95%CI)		Aspartate[a]/amino acid ratio				
	22Rv1 vs. PNT1A	PC-3 vs. PNT1A	22Rv1 vs. PNT1A (estimate and 95% CI)	PC-3 vs. PNT1A	Benign vs. tumorous (AUC and 95% CI)	Sensitivity	Specificity
Asp	1.62 (−2.36 to 5.60)	8.55* (3.68 to 13.42)	—	—	—	—	—
Thr	−2.46 (−5.78 to 0.86)	−6.29* (−10.35 to −2.22)	2.00* (1.32 to 3.04)	2.95* (1.95 to 4.47)	0.97* (0.9 to 1.04)	99%	100%
Ser	1.83 (−1.92 to 5.57)	0.54 (−4.05 to 5.13)	1.38 (0.97 to 1.96)	1.48* (1.04 to 2.11)	0.85* (0.67 to 1.02)	86%	86%
Glu	4.48* (0.84 to 8.13)	0.20 (−4.27 to 4.67)	1.43* (1.03 to 1.98)	1.22 (0.88 to 1.69)	0.78* (0.56 to 0.99)	93%	57%
Pro	0.84 (−4.92 to 6.6)	−4.44 (−11.49 to 2.62)	1.59 (0.95 to 2.64)	1.54 (0.92 to 2.57)	0.77 (0.49 to 1.04)	86%	71%
Gly	0.41 (−1.56 to 2.37)	−0.46 (−2.87 to 1.94)	1.52 (0.82 to 2.81)	2.22* (1.2 to 4.12)	0.76* (0.52 to 0.99)	71%	86%
Ala	−0.98 (−2.28 to 0.33)	−2.84* (−4.44 to −1.23)	2.47* (1.47 to 4.15)	2.54* (1.51 to 4.27)	0.87* (0.68 to 1.06)	93%	71%
Cys	1.07* (0.46 to 1.67)	0.29 (−0.46 to 1.03)	0.74 (0.35 to 1.59)	0.92 (0.43 to 1.97)	0.51 (0.18 to 0.84)	93%	43%
Val	−0.49 (−2.92 to 1.93)	−1.38 (−4.35 to 1.6)	1.56* (1.15 to 2.1)	1.6* (1.19 to 2.16)	0.92* (0.75 to 1.08)	100%	86%
Met	−2.93* (−4.7 to −1.17)	−6.26* (−8.42 to −4.1)	4.10* (2.86 to 5.88)	5.71* (3.98 to 8.19)	0.92* (0.79 to 1.04)	100%	71%
Ile	0.83 (−0.92 to 2.57)	−0.15 (−2.28 to 1.98)	1.21 (0.5 to 2.93)	0.79 (0.33 to 1.9)	0.49 (0.18 to 0.8)	86%	43%
Leu	−0.77 (−2.09 to 0.56)	−2.68* (−4.29 to −1.06)	2.46* (1.22 to 4.97)	3.63* (1.8 to 7.32)	0.89* (0.72 to 1.06)	86%	86%
Tyr	0.95 (−0.39 to 2.29)	−1.64 (−3.28 to 0.00)	2.65* (1.61 to 4.35)	1.94* (1.18 to 3.18)	0.95* (0.86 to 1.04)	79%	100%
Phe	−0.61 (−1.25 to 0.03)	−0.98* (−1.75 to −0.2)	2.13* (1.09 to 4.17)	2.78* (1.42 to 5.45)	0.82* (0.61 to 1.02)	100%	57%
His	−0.49 (−1.01 to 0.03)	−0.99* (−1.63 to −0.35)	3.19* (1.68 to 6.06)	2.31* (1.22 to 4.39)	0.89* (0.75 to 1.03)	79%	100%
Lys	0.05 (−1.16 to 1.26)	−2.61* (−4.09 to −1.14)	3.21* (1.85 to 5.58)	2.32* (1.33 to 4.03)	0.92* (0.79 to 1.05)	93%	86%
Arg	3.17 (−0.16 to 6.49)	3.85 (−0.22 to 7.92)	0.98 (0.66 to 1.48)	1.02 (0.68 to 1.53)	0.52 (0.24 to 0.80)	93%	29%
Sar[b]	1.70* (0.68 to 2.72)	4.49* (3.24 to 5.73)	0.30* (0.19 to 0.46)	0.49* (0.31 to 0.76)	0.91* (0.78 to 1.03)	71%	100%
Sar/ser	—	—	4.65* (3.77 to 5.74)	3.04* (2.47 to 3.76)	0.99* (0.96 to 1.02)	93%	100%
Cys/met	—	—	5.51* (2.52 to 12.06)	6.2* (2.83 to 13.57)	0.77* (0.52 to 1.01)	100%	57%

CI, confidence interval; AUC, area under curve.
Differences in absolute concentrations between cell lines (first two columns), differences in amino acid ratios ([a]ratios between aspartate and particular amino acid except Sar/Ser and Cys/Met ratios), second two columns. Determined by multivariate ANOVA. Last three columns show results of receiver-operator statistics (difference in ratios between benign and tumorous cell lines). [b]ROC statistics for all amino acids calculated as Asp/amino acids calculated as Asp/amino acid apart from Sarcosine (calculated as Sar/Asp ratio).
Asterisk (*) indicate significant trend at $P < 0.05$.
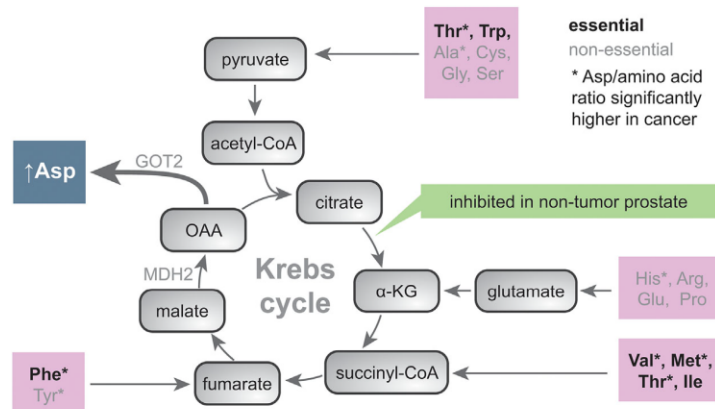
Fig. 4. Crucial role of aspartate in prostate cancer metabolism. Amino acid contributors for Asp synthesis based on amino acid ratios and receiver operator statistics (see Fig. 3 and Table I). Asterisk indicates amino acid whose Asp/amino acid ration differs significantly between non-tumor and tumorous cells. α-KG, α-ketoglutarate; OAA, oxaloacetate; MDH2, malate dehydrogenase; GOT2, glutamic-oxaloacetic transaminase 2.

several essential amino acids (threonine, lysine, leucine, phenylalanine, and methionine) suggests activation of aspartate biosynthesis through enhancement of MDH2/GOT2 activity in prostate cancer cells with renewed Krebs cycle and OXPHOS [28,29]; see Figure 4. In accordance, oncogenic KRAS, a common feature of prostate cancer, plays a role in redirecting of glutamine metabolism toward aspartate production [34,35]. Moreover, high levels of MDH2 were associated with poor prognosis in prostate cancer patients [36]. Based on our previous data, we examined selected product/precursor ratios for associations with a malignant phenotype by multifactorial ANOVA and ROC analysis. Aspartate/threonine, aspartate/methionine, and sarcosine/serine ratios demonstrated high levels of sensitivity and specificity in distinguishing cancer and benign metabolism. Our observation also confirmed the potential for threonine, tyrosine, and methionine restriction as a promising approach in prostate cancer treatment [37–42], especially because methionine is limiting factor for GSH and metallothionein synthesis [43] associated with cisplatin resistance [16].

Last, but not least, short- and long-term zinc treatments were shown to redirect cell metabolism from benign to more malignant type (see Fig. 3B). Zinc has long been associated with prostate health [22], but our findings contradict this statement as well as results of some other studies [44–46]. According to our results, resistant cells markedly increased their IC50 for cisplatin: by 1.4-, 1.6-, and 1.6-fold for PNT1A, 22Rv1, and PC-3, respectively [21] and their ability to invade. Moreover, long-term application of high concentration of zinc significantly enhanced synthesis of glutathione

(GSH) (see Fig. 1C), which could result in triggering of molecular mechanisms underlying the stemness and pluripotency [47–49]. Accordingly, we observed increasing number of polyploid giant cancer cells (PGCCs) in our zinc-resistant PC-3 cell line. Due to their possible stem cell-like properties, these PGCCs cells could represent an escape route to survive a genotoxic stress and to enhance aggressiveness of cancer cells [50–52]. Increased cellular antioxidant capacity and higher gene expression of treatment resistance-, pluripotency-, and stemness-associated genes BIRC5, POU5F1, and SOX2 were other consequences of zinc-resistant phenotype showing potential danger of long-term zinc supplementation.

CONCLUSIONS

In this study, we demonstrated that an intriguing idea to reestablish intracellular zinc concentrations in prostatic tumors does not restore benign phenotype in malignant prostate cells. Conversely, this approach drives tumor cells toward a higher level of aggressiveness and resistance through the activation of pluripotency- and stemness-associated regulatory molecules. Furthermore, changes of amino acid levels triggered by carcinogenesis and/or resistance are relevant for diagnostic purposes and may elucidate the molecular basis of malignant processes, which could possibly result in new therapeutic options. Ratios of certain logically-related amino acids may then be a sensitive indicator of the malignant phenotype. Moreover, the restriction of essential amino acids, such as threonine or methionine, or the inhibition of aspartate synthesis may be a promising

The Prostate

approach for the prostate cancer therapy with minimal toxic side effects.

ACKNOWLEDGMENT

REFERENCES

1. Costello LC, Franklin RB, Feng P. Mitochondrial function, zinc, and intermediary metabolism relationships in normal prostate and prostate cancer. Mitochondrion 2005;5(3):143–153.

2. Massie CE, Lynch A, Ramos-Montoya A, Boren J, Stark R, Fazli L, Warren A, Scott H, Madhu B, Sharma N, Bon H, Zecchini V, Smith D-M, DeNicola GM, Mathews N, Osborne M, Hadfield J, MacArthur S, Adryan B, Lyons SK, Brindle KM, Griffiths J, Gleave ME, Rennie PS, Neal DE, Mills IG. The androgen receptor fuels prostate cancer by regulating central metabolism and biosynthesis. EMBO J 2011;30(13):2719–2733.

3. Lloyd SM, Arnold J, Sreekumar A. Metabolomic profiling of hormone-dependent cancers: a bird's eye view. Trends Endocrinol Metab 2015;26(9):477–485.

4. Putluri N, Shojaie A, Vasu VT, Nalluri S, Vareed SK, Putluri V, Vivekanandan-Giri A, Byun J, Pennathur S, Sana TR, Fischer SM, Palapattu GS, Creighton CJ, Michailidis G, Sreekumar A. Metabolomic profiling reveals a role for androgen in activating amino acid metabolism and methylation in prostate cancer cells. PLoS ONE 2011;6(7):e21417.

5. Kaushik AK, Vareed SK, Basu S, Putluri V, Putluri N, Panzitt K, Brennan CA, Chinnaiyan AM, Vergara IA, Erho N, Weigel NL, Mitsiades N, Shojaie A, Palapattu G, Michailidis G, Sreekumar A. Metabolomic profiling identifies biochemical pathways associated with castration-Resistant prostate cancer. J Proteome Res 2014;13(2):1088–1100.

6. Dasgupta S, Putluri N, Long WW, Zhang B, Wang JH, Kaushik AK, Arnold JM, Bhowmik SK, Stashi E, Brennan CA, Rajapakshe K, Coarfa C, Mitsiades N, Ittmann MM, Chinnaiyan AM, Sreekumar A, O'Malley BW. Coactivator SRC-2-dependent metabolic reprogramming mediates prostate cancer survival and metastasis. J Clin Invest 2015;125(3):1174–1188.

7. Sreekumar A, Poisson LM, Rajendiran TM, Khan AP, Cao Q, Yu JD, Laxman B, Mehra R, Lonigro RJ, Li Y, Nyati MK, Ahsan A, Kalyana-Sundaram S, Han B, Cao XH, Byun J, Omenn GS, Ghosh D, Pennathur S, Alexander DC, Berger A, Shuster JR, Wei JT, Varambally S, Beecher C, Chinnaiyan AM. Metabolomic profiles delineate potential role for sarcosine in prostate cancer progression. Nature 2009;457(7231):910–914.

8. Arakaki AK, Mezencev R, Bowen NJ, Huang Y, McDonald JF, Skolnick J. Identification of metabolites with anticancer properties by computational metabolomics. Mol Cancer 2008;7.

9. Heger Z, Gumulec J, Cernei N, Polanska H, Raudenska M, Masarik M, Eckschlager T, Stiborova M, Adam V, Kizek R. Relation of exposure to amino acids involved in sarcosine

10. Pavlova NN, Thompson CB. The emerging hallmarks of cancer metabolism. Cell Metab 2016;23(1):27–47.

11. Wang JB, Erickson JW, Fuji R, Ramachandran S, Gao P, Dinavahi R, Wilson KF, Ambrosio AL, Dias SM, Dang CV, Cerione RA. Targeting mitochondrial glutaminase activity inhibits oncogenic transformation. Cancer Cell 2010;18(3):207–219.

12. Kolenko V, Teper E, Kutikov A, Uzzo R. Zinc and zinc transporters in prostate carcinogenesis. Nat Rev Urol 2013;10 (4):219–226.

13. Holubova M, Axmanova M, Gumulec J, Raudenska M, Sztalmachova M, Babula P, Adam V, Kizek R, Masarik M. KRAS NF-kappaB is involved in the development of zinc resistance and reduced curability in prostate cancer. Metallomics 2014;6(7):1240–1253.

14. Sharrard RM, Maitland NJ. Regulation of protein kinase B activity by PTEN and SHIP2 in human prostate-derived cell lines. Cell Signal 2007;19(1):129–138.

15. Fraser M, Zhao H, Luoto KR, Lundin C, Coackley C, Chan N, Joshua AM, Bismar TA, Evans A, Helleday T, Bristow RG. PTEN deletion in prostate cancer cells does not associate with loss of RAD51 function: Implications for radiotherapy and chemotherapy. Clin Cancer Res 2012;18(4):1015–1027.

16. Gumulec J, Balvan J, Sztalmachova M, Raudenska M, Dvorakova V, Knopfova L, Polanska H, Hudcova K, Ruttkay-Nedecky B, Babula P, Adam V, Kizek R, Stiborova M, Masarik M. Cisplatin-resistant prostate cancer model: Differences in antioxidant system, apoptosis and cell cycle. Int J Oncol 2014;44(3):923–933.

17. Heger Z, Cernei N, Gumulec J, Masarik M, Eckschlager T, Hrabec R, Zitka O, Adam V, Kizek R. Determination of common urine substances as an assay for improving prostate carcinoma diagnostics. Oncol Rep 2014;31(4):1846–1854.

18. Tmejova K, Hynek D, Kopel P, Gumulec J, Krizkova S, Guran R, Heger Z, Kalina M, Vaculovicova M, Adam V, Kizek R. Structural effects and nanoparticle size are essential for quantum dots-metallothionein complex formation. Colloids Surf B Biointerfaces 2015;134:262–272.

19. Kominkova M, Michalek P, Cihalova K, Guran R, Cernei N, Nejdl L, Smerkova K, Dostalova S, Chudobova D, Heger Z, Vesely R, Gumulec J, Kynicky J, Xhaxhiu K, Zitka O, Adam V, Kizek R. Study of linkage between glutathione pathway and the antibiotic resistance of escherichia coli from patients' swabs. Int J Mol Sci 2015;16(4):7210–7229.

20. Masarik M, Gumulec J, Hlavna M, Sztalmachova M, Babula P, Raudenska M, Pavkova-Goldbergova M, Cernei N, Sochor J, Zitka O, Ruttkay-Nedecky B, Krizkova S, Adam V, Kizek R. Monitoring of the prostate tumour cells redox state and real-time proliferation by novel biophysical techniques and fluorescent staining. Integr Biol 2012;4(6):672–684.

21. Holubova M, Axmanova M, Gumulec J, Raudenska M, Sztalmachova M, Babula P, Adam V, Kizek R, Masarik M. KRAS NF-kappa B is involved in the development of zinc resistance and reduced curability in prostate cancer. Metallomics 2014;6(7):1240–1253.

22. Costello LC, Feng P, Milon B, Tan M, Franklin RB. Role of zinc in the pathogenesis and treatment of prostate cancer: Critical issues to resolve. Prostate Cancer Prostatic Dis 2004;7(2):111–117.

23. Hardyman JE, Tyson J, Jackson KA, Aldridge C, Cockell SJ, Wakeling LA, Valentine RA, Ford D. Zinc sensing by metal-responsive transcription factor 1 (MTF1) controls metallothionein and ZnT1 expression to buffer the sensitivity of the transcriptome response to zinc. Metallomics 2016;8(3):337–343.

24. Raudenska M, Gumulec J, Podlaha O, Sztalmachova M, Babula P, Eckschlager T, Adam V, Kizekb R, Masarik M. Metallothionein polymorphisms in pathological processes. Metallomics 2014;6(1):55–68.

25. Costello LC, Franklin RB. Novel role of zinc in the regulation of prostate citrate metabolism and its implications in prostate cancer. Prostate 1998;35(4):285–296.

26. Bae KM, Dai Y, Vieweg J, Siemann DW. Hypoxia regulates SOX2 expression to promote prostate cancer cell invasion and sphere formation. Am J Cancer Res 2016;6(5):1078–1088.

27. Russo MV, Esposito S, Tupone MG, Manzoli L, Airoldi I, Pompa P, Cindolo L, Schips L, Sorrentino C, Di Carlo E. SOX2 boosts major tumor progression genes in prostate cancer and is a functional biomarker of lymph node metastasis. Oncotarget 2016;7(11):12372–12385.

28. Birsoy K, Wang T, Chen WW, Freinkman E, Abu-Remaileh M, Sabatini DM. An essential role of the mitochondrial electron transport chain in cell proliferation is to enable aspartate synthesis. Cell 2015;162(3):540–551.

29. Yang H, Zhou LS, Shi Q, Zhao YZ, Lin HP, Zhang ML, Zhao SM, Yang Y, Ling ZQ, Guan KL, Xiong Y, Ye D. SIRT3-dependent GOT2 acetylation status affects the malate-aspartate NADH shuttle activity and pancreatic tumor growth. EMBO J 2015;34(8):1110–1125.

30. Franklin RB, Zou J, Yu Z, Costello LC. EAAC1 is expressed in rat and human prostate epithelial cells; functions as a high-affinity L-aspartate transporter; and is regulated by prolactin and testosterone. BMC Biochem 2006;7:10.

31. Costello LC, Franklin RB. The clinical relevance of the metabolism of prostate cancer; zinc and tumor suppression: Connecting the dots. Mol Cancer 2006;5.

32. Costello LC, Franklin RB. Prostate epithelial-cells utilize glucose and aspartate as the carbon-sources for net citrate production. Prostate 1989;15(4):335–342.

33. Sullivan LB, Gui DY, Hosios AM, Bush LN, Freinkman E, Vander Heiden MG. Supporting aspartate biosynthesis is an essential function of respiration in proliferating cells. Cell 2015;162(3):552–563.

34. Ahn CS, Metallo CM. Mitochondria as biosynthetic factories for cancer proliferation. Cancer Metab 2015;3:1.

35. Ngalame NNO, Tokar EJ, Person RJ, Waalkes MP. Silencing KRAS overexpression in arsenic-Transformed prostate epithelial and stem cells partially mitigates malignant phenotype. Toxicol Sci 2014;142(2):489–496.

36. Liu Q, Harvey CT, Geng H, Xue CH, Chen V, Beer TM, Qian DZ. Malate dehydrogenase 2 confers docetaxel resistance via regulations of JNK signaling and oxidative metabolism. Prostate 2013;73(10):1028–1037.

37. Fu YM, Yu ZX, Li YQ, Ge XK, Sanchez PJ, Fu X, Meadows GG. Specific amino acid dependency regulates invasiveness and viability of androgen-independent prostate cancer cells. Nutr Cancer 2003;45(1):60–73.

38. Lu S, Hoestje SM, Choo EM, Epner DE. Methionine restriction induces apoptosis of prostate cancer cells via the c-Jun N-terminal kinase-mediated signaling pathway. Cancer Lett 2002;179(1):51–58.

39. Shiraki N, Shiraki Y, Tsuyama T, Obata F, Miura M, Nagae G, Aburatani H, Kume K, Endo F, Kume S. Methionine metabolism regulates maintenance and differentiation of human pluripotent stem cells. Cell Metab 2014;19(5):780–794.

40. Fu YM, Yu ZX, Ferrans VJ, Meadows GG. Tyrosine and phenylalanine restriction induces G0/G1 cell cycle arrest in murine melanoma in vitro and in vivo. Nutr Cancer 1997; 29(2):104–113.

41. Abdallah RM, Starkey JR, Meadows GG. Dietary restriction of tyrosine and phenylalanine: Inhibition of metastasis of three rodent tumors. J Natl Cancer Inst 1987;78(4):759–769.

42. Zhang J, Nuebel E, Daley GQ, Koehler CM, Teitell MA. Metabolic regulation in pluripotent stem cells during reprogramming and self-Renewal. Cell Stem Cell 2012;11(5):589–595.

43. Stein AF, Bracken WM, Klaassen CD. Utilization of methionine as a sulfhydryl source for metallothionein synthesis in rat primary hepatocyte cultures. Toxicol Appl Pharmacol 1987;87(2):276–283.

44. Leitzmann MF, Stampfer MJ, Wu KN, Colditz GA, Willett WC, Giovannucci EL. Zinc supplement use and risk of prostate cancer. J Natl Cancer Inst 2003;95(13):1004–1007.

45. Ko YH, Woo YJ, Kim JW, Choi H, Kang SH, Lee JG, Kim JJ, Park HS, Cheon J. High-dose dietary zinc promotes prostate intra-epithelial neoplasia in a murine tumor induction model. Asian J Androl 2010;12(2):164–170.

46. Makhov P, Golovine K, Uzzo RG, Rothman J, Crispen PL, Shaw T, Scoll BJ, Kolenko VM. Zinc chelation induces rapid depletion of the X-linked inhibitor of apoptosis and sensitizes prostate cancer cells to TRAIL-mediated apoptosis. Cell Death Differ 2008;15(11):1745–1751.

47. Marsboom G, Zhang GF, Pohl-Avila N, Zhang YM, Yuan Y, Kang HJ, Hao B, Brunengraber H, Malik AB, Rehman J. Glutamine metabolism regulates the pluripotency transcription factor OCT4. Cell Rep 2016;16(2):323–332.

48. Lu HQ, Samanta D, Xiang LS, Zhang HM, Hu HX, Chen I, Bullen JW, Semenza GL. Chemotherapy triggers HIF-1-dependent glutathione synthesis and copper chelation that induces the breast cancer stem cell phenotype. Proc Natl Acad Sci USA 2015;112(33):E4600–E4609.

49. Hu J, Yang ZY, Wang JB, Yu J, Guo J, Liu SY, Qian CM, Song LW, Wu Y, Cheng JJ. Zinc chloride transiently maintains mouse embryonic stem cell pluripotency by activating stat3 signaling. PLoS ONE 2016;11(2):e0148994.

50. Ivanov A, Cragg MS, Erenpreisa J, Emzinsh D, Lukman H, Illidge TM. Endopolyploid cells produced after severe genotoxic damage have the potential to repair DNA double strand breaks. J Cell Sci 2003;116(20):4095–4106.

51. Zhang D, Wang YJ, Zhang SW. Asymmetric cell division in polyploid giant cancer cells and low eukaryotic cells. Biomed Res Int 2014;2014:432652.

52. Zhang S, Mercado-Uribe I, Xing Z, Sun B, Kuang J, Liu J. Generation of cancer stem-like cells through the formation of polyploid giant cancer cells. Oncogene 2014;33(1):116–128.

SUPPORTING INFORMATION

Additional supporting information may be found in the online version of this article at the publisher's web-site.

4.4.2 Cellular Amino acid levels associated with cancer progression

A dysregulation of amino acid profiles was described in a previous study [95], chapter 4.4.1, highlighting specifically a role of alanine, methionine leucine, lysine and threonine for prostate cancer cells characteristic by high aggressiveness in vitro. In the following study an effect of amino acids on prostate tumors is analysed from a different perspective: Recently, a role of non-coding amino acid *N*-methyl glycine (sarcosine) was related to prostate cancer progression [96]. Specifically, an elevated levels of this amino acid were described in metastatic tumors. Therefore, exogenous supplementation of amino acids – precursors of sarcosine metabolic pathway – was performed and levels of the coding amino acids were monitored together with analysis of cancer cell migration and division rate *in vitro*.

The data observed in this study [97] indicate that the production of sarcosine by prostate cancer cells is inducible by its amino acid precursors – glycine, and, in particular dimethylglycine. The treatments by these precursors further modify the levels of coding amino acids in cancer cells, enabling to differentiate cell lines of different degree of *in vitro* aggressiveness. In both, treated and untreated PC-3 cells significantly higher levels of serine, glutamic acid, and aspartate, linked with prostate cancer progression were found. These phenomena followed migration rates of these cells: The highest migration of metastatic cancer cells PC-3 was induced by sarcosine and glycine. The highest cell division was achieved after treatment of 22Rv1 and PC-3 cells with sarcosine [97].

In the context of the previous study focusing on the association of amino acid patterns and prostate cancer aggressiveness [95] and together with the findings that the cells differ also in Young modulus, cell dry mass, stemness-like phenotype and higher migration rates, data indicate that alterations of amino acid metabolites is inextricably associated with the changes in cell mechanical properties in prostate tumors.

HEGER, Z., J. GUMULEC, N. CERNEI, H. POLANSKA, et al. Relation of exposure to amino acids involved in sarcosine metabolic pathway on behavior of non-tumor and malignant prostatic cell lines. Prostate, May 2016, 76(7), 679-690.

Relation of Exposure to Amino Acids Involved in Sarcosine Metabolic Pathway on Behavior of Non-Tumor and Malignant Prostatic Cell Lines

Zbynek Heger,[1,2] Jaromir Gumulec,[2,3] Natalia Cernei,[1,2] Hana Polanska,[2,3] Martina Raudenska,[2,3] Michal Masarik,[2,3] Tomas Eckschlager,[4] Marie Stiborova,[5] Vojtech Adam,[1,2] and Rene Kizek[1,2]*

[1]Department of Chemistry and Biochemistry, Mendel University in Brno, Brno, Czech Republic, European Union
[2]Central European Institute of Technology, Brno University of Technology, Brno, Czech Republic, European Union
[3]Faculty of Medicine, Department of Physiology, Masaryk University, Brno, Czech Republic, European Union
[4]2nd Faculty of Medicine, Department of Paediatric Haematology and Oncology, Charles University and University Hospital Motol, Czech Republic, European Union
[5]Faculty of Science, Department of Biochemistry, Charles University, Czech Republic, European Union

BACKGROUND. Sarcosine (N-methylglycine) was previously delineated as a substantial oncometabolite of prostate cancer (PCa) and its metabolism seems to be significantly involved in PCa development and behavior.
METHODS. We focused on investigation whether the exposure of prostate cells (PNT1A, 22Rv1, and PC-3) to sarcosine-related amino acids (glycine, dimethylglycine, and sarcosine) affects their aggressiveness (cell mobility and division rates, using real-time cell based assay). The effect of supplementation on expression of glycine-N-methyltransferase (GNMT) mRNA was examined using qRT-PCR. Finally, post-treatment amino acids patterns were determined with consequent statistical processing using the Ward's method, factorial ANOVA and principal component analysis ($P < 0.05$).
RESULTS. The highest migration induced sarcosine and glycine in metastatic PC-3 cells (a decrease in relative free area about 53% and 73%). The highest cell division was achieved after treatment of 22Rv1 and PC-3 cells with sarcosine (time required for division decreased by 65% or 45%, when compared to untreated cells). qRT-PCR revealed also significant effects on expression of GNMT. Finally, amino acid profiling shown specific amino acid patterns for each cell line. In both, treated and untreated PC-3 cells significantly higher levels of serine, glutamic acid, and aspartate, linked with prostate cancer progression were found.

CONCLUSIONS. Sarcosine-related amino acids can exceptionally affect the behavior of benign and malignant prostate cells. *Prostate 76:679–690, 2016.*   © 2016 Wiley Periodicals, Inc.

INTRODUCTION

The amino acid sarcosine is currently studied as a potential biomarker for the early stages of prostate carcinoma (PCa). Even though the linkage of sarcosine with PCa development and its potential in a diagnosis of early stages of tumors was described [1,2], its usage as a marker remains still unclear [3,4]. Hence, it is necessary to study the fate of sarcosine and other amino acids, which act as the intermediate products of tumor metabolism in PCa. Formation and oxidation of sarcosine occurs in mitochondria and are provided by two basic pathways (schematically depicted in Fig. 1), where sarcosine can be simultaneously produced from dimethylglycine (Dmg) or glycine. The first pathway involves repeated methylation of phosfatidylethanolamine (PE) by S-adenosylmethionine (SAM) to form phosphatidylcholine (PC) with the resulting intermediate product betaine. This reaction forms Dmg and regenerates methionine from homocysteine. The Dmg is subsequently converted to sarcosine via dimethylglycine dehydrogenase (DMGDH) [5]. The second metabolic pathway creates sarcosine during the transformation of the methyl group of S-adenosylmethionine catalyzed by the enzyme glycine N-methyltransferase (GNMT) [6,7]. These two reactions ultimately produce 5,10-methylenetetrahydrofolate and are dependent on oxidized flavine cofactors (e.g., flavine adenine dinucleotide) [5].

GNMT acts as an essential enzyme that influences synthesis of sarcosine [8]. Due to properties of GNMT, its excessive production causes conversion of glycine

Fig. I. Scheme of metabolical pathway of sarcosine biosynthesis and degradation to its non-methylated precursor—glycine and its connection to other important metabolical pathways. Enzymes in scheme are numbered and depicted as follows: 1, DMGDH, dimethylglycine dehydrogenase; 2, GNMT, glycine-N-methyltransferase; 3, SARDH, sarcosine dehydrogenase; 4, SHMT1/2, serine hydroxymethyltransferase; 5, 11, MTHFR, 5,10-methylenetetrahydrofolate reductase; 6, MTR, methionine synthase; 7, BHMT, betaine-homocysteine methyltransferase; 8, CHDH, choline oxidase; 9, MAT, methionine adenosyltransferase; 10, SAM-dependent methyltransferase; 11, PEMT, phosphatidylethanolamine methyltransferase; 12, AHCY, S-adenosylhomocysteine hydrolase; 13, CBS, cystathionine β-synthase; 14, CTH, cystathionase; 15, GCL, glutamate-cysteine ligase; 16, GSS, glutathione synthetase; 17, CDO1, cysteine dioxygenase 1; 18, CSAD, cysteine sulfinic acid decarboxylase; 19, GOT1, glutamate oxaloacetate transaminase 1. Dmg stays for dimethylglycine, SAM for S-adenosyl-methionine, SAH for S-adenosyl-homocysteine, PE for phosphatidylethanolamine, PC for phosphatidylcholine, and THF for tetrahydrofolate.

to sarcosine and elevates the sarcosine levels in urine. This makes sarcosine interesting in the field of non-invasive cancer biomarkers. Thus, sarcosine appears to be not only a non-proteogenic amino acid but also an important metabolite in oncogenesis. According to Sreekumar et al., the elevated levels of sarcosine correlated with progression of prostate cancer and metastatic process [9] and accordingly, it has been revealed that supplementation of sarcosine to prostate cancer cell lines induced a selection of invasive phenotype in culture [10]. Nevertheless, the explanation for these phenomena remains unclear. Moreover, the metabolic fate of sarcosine in prostate cancer cells has not been fully resolved yet.

Therefore, the insight into the metabolic pathways of sarcosine and the mechanisms of its regulation are required to be investigated. This study is aimed to evaluate the effects of treatment of three prostatic cell lines (a "non-tumor" PNT1A, a primary tumor-derived 22Rv1 and metastasis-derived PC-3) with three sarcosine-pathway-related amino acids (glycine, dimethylglycine, and sarcosine) on the cell cancer-geneous status. The evaluation was carried out using as a combination of assays determining the effects of these amino acids on the expression of GNMT mRNA, cell migration, invasiveness, their division and growth capabilities.

EXPERIMENTAL SECTION

Chemical Compounds

All standards and other chemicals were purchased from Sigma–Aldrich (St. Louis, MO) in ACS purity, unless noted otherwise.

Prostatic Cell Lines

Three human prostatic cell lines were used in this study: (i) the PNT1A human cell line established by immortalization of normal adult prostatic epithelial cells by transfection with a plasmid containing SV40 genome with a defective replication origin. The primary culture was obtained from the prostate of a 35-year-old male post mortem; (ii) 22Rv1 which is a human prostate carcinoma epithelial cell line derived from a xenograft that was serially propagated in mice after castration-induced regression and relapse of the parental, androgen-dependent CWR22 xenograft. (iii) The PC-3 human cell line established from a grade 4 androgen independent and unresponsive prostatic adenocarcinoma from 62-year-old Caucasian male and derived from metastatic site in bone. All cell lines used in this study were purchased from Health Protection Agency Culture Collections (Salisbury, UK).

Culture Conditions

PNT1A and 22Rv1 cells were cultured in RPMI-1640 medium with 10% fetal bovine serum (FBS). PC-3 cells were cultured in Ham's F12 medium with 7% fotel bovine serum (FBS). All media were supplemented with penicillin (100 U/ml) and streptomycin (0.1 mg/ml), and the cells were maintained at 37°C in a humidified incubator (Sanyo, Moriguchi, Japan) with 5% CO_2. The treatment with amino acids was initiated after cells reached ~60–80% confluence. Cells were then harvested and washed four times with PBS, pH 7.4.

Cell Content Quantification

Total cell content was analyzed using Casy model TT system (Roche Applied Science, Penzberg, Germany). To prepare a viable cell standard, 100 µl cell suspension was mixed with 10 ml Casy Tone. All subsequent measurements were performed on 100× diluted 100 µl cell suspension. Prior each measurement, background was subtracted.

Measurements of Cell Viability—MTT Assay

The suspension of 10,000 cells was added to each well of standard microtiter plates (E-plates 16). After addition of medium (200 µl), plates were incubated for 2 days at 37°C to ensure cell growth. To determine the effects on cell viability, the amino acids (sarcosine, glycine, and dimethylglycine) in concentration 0–3 mmol/l were used. Plates were incubated for 24 hr; then, media were removed and replaced by a fresh medium, three times a day. Further, a medium was replaced by 200 µl of fresh medium containing 50 µl of MTT (5 mg/ml in PBS) and incubated in a humidified atmosphere for 4 hr at 37°C, wrapped in aluminum foil. After the incubation, MTT-containing medium was replaced by 200 µl of 99.9% dimethyl sulphoxide to dissolve MTT-formazan crystals. Then, 25 µl of glycine buffer (pH 10.5) was added to all wells and absorbance at 570 nm was immediately determined (VersaMax microplate reader, Molecular Devices, Sunnyvale, CA).

In Vitro Wound-Healing Assay

The cells were pipetted into 16-well plate to reach the confluence ~80%. After seeding of cells on the bottom of a plate, a pin was used to scratch and remove cells from a discrete area of the confluent monolayer to form a cell-free zone. After that, cells were re-suspended in a fresh medium enriched with sarcosine, glycine, and dimethylglycine (1.5 mmol/l). After 24 hr, the pictures of cells were taken and compared with pictures obtained in 0 hr, using TScratch software (CSElab, Zurich, Switzerland).

Growth and Proliferation Assay Using Real-Time Cell-Based Assay

The real-time cell-based assay (RTCA) was carried out using the xCELLigence system (Roche Applied Science and ACEA Biosciences, San Diego, CA). After seeding the total number of cells (10,000) in 100 µl medium to each well in E-plate, the attachment, proliferation and spreading of the cells was monitored every 15 min. After 24 hr, amino acids (1.5 mmol/l) or MiliQ water (control measurements) were added and cell impedance was monitored for 250 h. For evaluation of exposure, a "doubling time" function, describing the cell division rate, was employed.

Isolation of RNA and Reverse Transcription

High pure total-RNA isolation kit (Roche, Basel, Switzerland) was used for isolation of cellular RNA. The medium was removed and samples were twice washed with 5 ml of ice-cold PBS. Cells were scraped off, transferred to clean tubes and centrifuged at 20,800g for 5 min at 4°C. After this step, lysis buffer was added and RNA isolation was carried out from 22Rv1, PNT1A, and PC-3 according to manufacturer's instructions. Isolated RNA was used for cDNA synthesis. RNA (500 ng) was transcribed using transcriptor first strand cDNA synthesis kit (Roche) according to manufacturer's instructions. Prepared cDNA (20 µl) from total-RNA was diluted with RNase-free water to a total volume of 100 µl and 5 µl of this solution was directly analyzed by q-PCR.

Quantitative Polymerase Chain Reaction (q-PCR)

q-PCR was performed using the TaqMan gene expression assay system with the Lightcycler 480 II RT-PCR system (Roche, Basel, Switzerland) and the amplified DNA was analyzed by the comparative Ct method using β-actin as a housekeeping gene. The primer and probe sets for β-actin (assay ID: Hs99999903_ m1) and GNMT (Hs00219089-m1) were selected from TaqMan gene expression assays (Life Technologies, Carlsbad, CA). q-PCR was performed under the following amplification conditions: total volume of 20 µl, initial incubation 50°C/2 min followed by denaturation 94°C/10 min, then 40 cycles 94°C/10 sec, 60°C/1 min.

Preparation of Cell Lines for Determination of Patterns of Cellular Amino Acids

The harvested cells were frozen in liquid nitrogen to disrupt their structure. The frozen sample was homogenized using ultrasonic homogenizer SONOPLUS

mini20 (Bandelin Electronic, Berlin, Germany). Subsequently, 1 ml of 0.2 M phosphate buffer (pH, 7.0) was added and the sample was homogenized for 5 min. The homogenate was further centrifuged using Microcentrifuge 5417R under the following conditions at 4°C for 15 min. Finally, the supernatant was filtered through a membrane filter (0.45-µm nylon filter disk; Millipore, Billerica, MA) and analyzed.

Ion-Exchange Chromatography

Amino acids including sarcosine were determined using ion-exchange chromatography with Vis detection after post-column derivatization with ninhydrin (AAA-400, Ingos, Prague, Czech Republic), following conditions employed in our previous study [3].

Quantification of Total Protein in Cell Lines

Total protein was determined using the SKALAB CBT 600T kit (Skalab, Svitavy, Czech Republic), on automatic spectrophotometer BS-400 (Mindray, Shenzhen, China), following the manufacturer's instructions.

Statistical Analysis

Prior all analyses, data were standardized. Correlation analysis followed by hierarchical clustering using the Ward's method was exploited to reveal dependencies between variables. To analyze the effects of cell line, amino acid used for treatment and the concentration of amino acid used for treatment, factorial ANOVA was used. To reveal dependences in complex data, principal component analysis was employed. Unless noted otherwise, the threshold for significance was $P < 0.05$. For analyses Software Statistica 12 (StatSoft, Tulsa, OK) was employed.

RESULTS

Cytotoxicity of Sarcosine, Glycine, and Dimethylglycine on Prostate Cells

In the first step, prostatic cell lines were tested for their susceptibility to applied amino acids using MTT assay. Figure 2A–C illustrates that treatment with glycine (Gly), sarcosine (Sar), and dimethylglycine (Dmg), respectively, resulted in low or no inhibition of cell lines growth, observed particularly by the highest applied concentration or above the used concentration range (2.0–3.5 mmol/l). The found data were further employed to design the experimental workflow. Because the undesired cytotoxicity can affect performance of further analyses, concentrations not exceeding 1.5 mmol/l were utilized for subsequent treatments only.
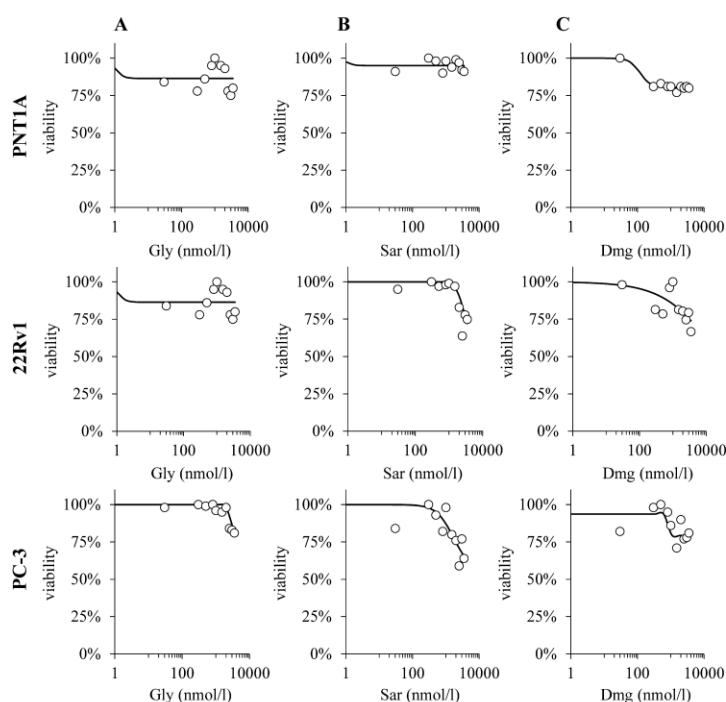
Fig. 2. Viability assay data of (**A**) PNT1A, (**B**) 22Rv1, and (**C**) PC-3 cells after application of glycine, sarcosine, and dimethylglycine (0.0–3.5 mmol/l). Growth inhibition in each treatment is expressed as a percentage of the control (untreated) cells. The data shown were obtained by the MTT assay. Values are means of three independent replicates (n = 3).

An Effect of Sarcosine, Glycine, and Dimethylglycine on Growth Properties of Prostate Cells

The growth of the cells were tested using wound-healing assay (Fig. 3A), which is an easy, low-cost and well-developed method to measure cell migration in vitro [11]. After formation of a new artificial gap on a confluent cell monolayer and subsequent supplementation with 1.5 mmol/l of sarcosine, glycine, or dimethylglycine, it was found that the cell migration was induced distinctly by sarcosine and glycine in PC-3 (relative free area of 53% and 73%, respectively) and 22Rv1 cells (57% and 87%), which is shown in Figure 3B. Contrary to that, dimethylglycine treatment suppressed migration in 22Rv1 and PC-3 (150% in 22Rv1 and 202% in PC-3), whereas the treatment of PNT1A led to increase in cell migration (80%). Using the real-time cell-based assay, we also focused on investigation of the effects of sarcosine, glycine, and dimethylglycine on the division rates of the tested prostate cells. As shown in Figure 3C, the most significant effects were achieved after cultivation with exogenously added sarcosine, which resulted in elevation of a division rate of 22Rv1 and PC-3 cell lines (time required for their division was 65% and 45%, respec-

tively). Furthermore, the 22Rv1 cells were also boosted by treatment with glycine and dimethylglycine.

An Effect of Treatment of Prostate Cells With Sarcosine, Glycine, and Dimethylglycine on Expression of mRNA of Cellular GNMT

The results shown in Figure 4A demonstrate that relative expression of GNMT mRNA differs among the tested cell lines. The lowest GNMT mRNA expression was identified in non-malignant PNT1A cells, followed by metastatic PC-3 and primary tumor 22Rv1 cells, which corresponds to the known fact that GNMT over-expression is associated with the cancer cells more than with the non-tumor ones [12]. In the case of PC-3 cells, glycine treatment induced significant down-regulation of GNMT mRNA. Similar effect was observed in 22Rv1 cells, where 0.1 and 0.5 mmol/l of glycine stimulated expression of GNMT, however, higher applied concentrations resulted in down-regulation as in PC-3 cells. The highest increase in GNMT mRNA expression by glycine was found in PNT1A cells; nevertheless, the higher concentration (1.0 and 1.5 mmol/l) led to a decrease in GNMT mRNA expression (Fig. 4B). Contrary to relatively low effects of glycine, sarcosine

The Prostate
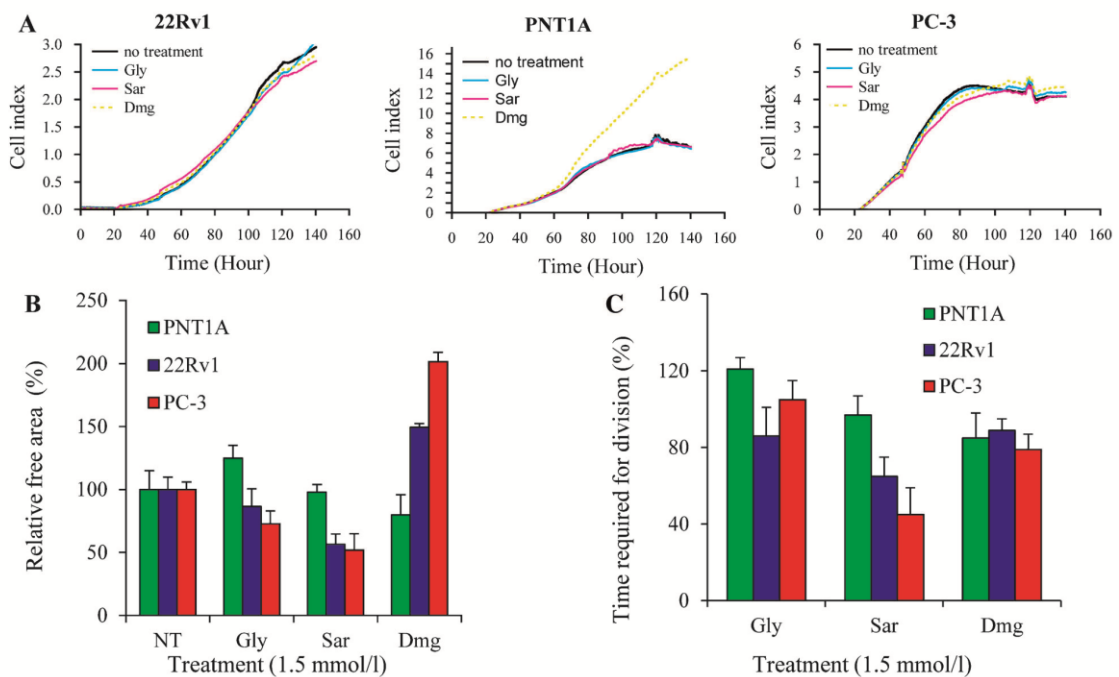
Fig. 3. Cell growth and invasiveness. (**A**) Growth of cell lines after treatment of amino acids compared to untreated cells. Displayed as a relative impedance (cell index). The effect of amino acids on (**B**) cell mobility, assessed by wound-healing assay, NT stands for no amino acid treatment (as reference free areas in NT cell lines were employed) and (**C**) the cell division rate (related to cell division rate of cells without treatment. Cells were seeded at a density of 10,000 cells per well in microtiter E-Plates 16. The cell index was monitored after application of 1.5 mmol/l of each amino acid. Values are means of three independent replicates (n = 3). Vertical bars indicate standard error.

supplementation mostly induced down-regulation of *GNMT* gene among all tested cell lines (PNT1A > PC-3 > 22Rv1) (Fig. 4C). Dimethylglycine treatment stimulated expression of GNMT mRNA in PNT1A cells, whereas this amino acid inhibited expression of mRNA of this enzyme in primary tumor (22Rv1) and metastatic cell lines (PC-3) (Fig. 4D). Taken together, the results demonstrate that supplementation of cells with even low concentrations of sarcosine and its pathway-related amino acids is able to trigger over-expression of GNMT (particularly in the case of dimethylglycine in PNT1A cells) or its down-regulation during treatment of PC-3 cells with glycine, sarcosine and dimethylglycine or, 22Rv1 cells supplemented with sarcosine and dimethylglycine.

Analysis of the Effect of Treatment of Prostate Cells With Sarcosine, Glycine, and Dimethylglycine on Patterns of Cellular Amino Acids

In the next step, the effect of treatment with glycine, dimethylglycine and sarcosine on the spec-

trum of amino acids in the tested prostate cell lines was analyzed. The correlation heatmap showing the response of cellular amino acid spectra to exposure of cells with sarcosine, glycine, and dimethylglycine is shown in Figure 5A. There was a significant positive correlation of all supplemented amino acids with intracellularly measured ones; $r = 0.62$, 0.38, and 0.48 at $P < 0.05$ for glycine, dimethylglycine, and sarcosine, respectively. Based on factorial ANOVA, a significant effect of all prediction factors on the amino acid pattern was found as follows: cell line $F(28, 144) = 136.6$, $P < 0.001$ (Fig. 5C), amino acid used for treatment $F(38, 144) = 28.66$, $P < 0.001$ (Fig. 5D) and the concentration of treatment $F(76, 286) = 7.2$, $P < 0.001$ (Fig. 5E). The combined effect of all three variables was significant, $F(304, 930) = 2.7$, $P < 0.001$, too. Noteworthy, the highest sarcosine levels were found in 22Rv1 (mean in untreated cells 3.12 µmol/mg of total protein), followed by PC-3 (1.78 µmol/mg of total protein) and PNT1A (0.84 µmol/mg of total protein), which corresponds to the expression of the *GNMT* gene. Inasmuch, glycine, sarcosine, and dimethylglycine treatment led to large
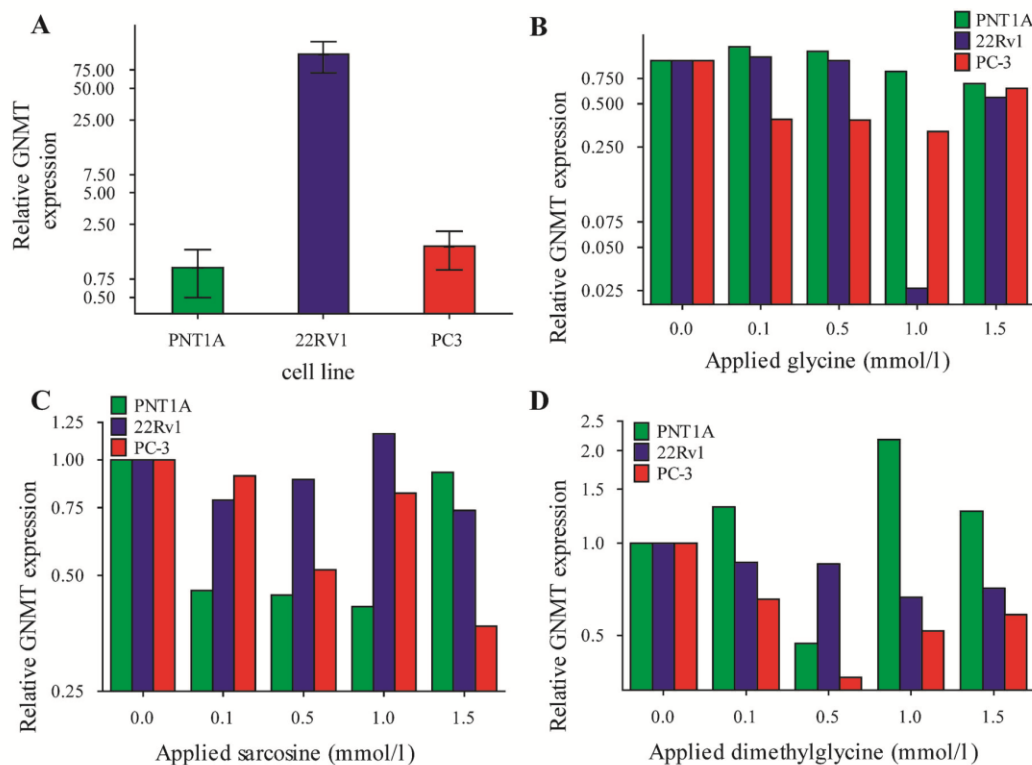
Fig. 4. Glycine-*N*-methyltransferase (GNMT) mRNA expression determined in (**A**) untreated cell lines (PNT1A, 22Rv1, and PC-3), related to *β-actin* as housekeeping and the same cell lines after application of 0.1–1.5 mmol/l (**B**) glycine, (**C**) sarcosine, and (**D**) dimethylglycine, assessed by qRT-PCR. Values are expressed using the delta-delta Ct method to derive relative fold change compared to untreated cell lines GNMT expression. Values are means of three independent replicates (n = 3).

changes in amino acid patterns in the cells (for details, see Table S1 in supplementary data). The obtained data indicate that the cell line type is highly specific for its amino acid pattern and this pattern is significantly influenced by amino acid supplementation.

Characterization of Patterns of Cellular Amino Acids

The previous analyses did not sufficiently highlight trends and relationships in the complex amino acid profile of the cell lines. Therefore, correlations among the individual amino acids detected in the cells were performed (Fig. 5B). Based on the results found by correlation analyses, amino acids can be divided into three clusters: cluster Lys, His, Dmg, Sar, Cys (cluster 1 in Fig. 5B), which is characterized by minimal correlations between these amino acids. The other two clusters, Phe, Ile, Ala, Arg, Thr (cluster 2 in Fig. 5B) and Tyr, Leu, Gly, Val, Met, Pro, Glu, Ser, Asp (cluster 3 in Fig. 5B) are characterized by strong correlation between those amino acids. A specific correlation pattern is apparent for sarcosine and cysteine, which demonstrate a negative correlation with all other amino acids except themselves.

Nevertheless, the correlation analysis did not allow to interpret complex multidimensional relationships between the amino acids' levels after the treatment of cells with sarcosine, glycine, and dimethylglycine—so called "amino acid patterns" of cell lines. Therefore, the principal component analysis was used. The component analysis allowed us to detect the structure in relationships between amino acid levels, and thus helped us to reveal characteristic patterns for the respective cell lines—non-tumor, primary tumor, and secondary/metastatic tumor cells. A two-factor model was employed with the eigenvalue 3.61, thus 49.4% of total variability of data (30.4 and 19.0 for factors 1 and 2, respectively) is explained. First, cases (cell lines, and amino acids used for supplementation) were projected into a factor plane (Fig. 6A). A color-coding by the cell line revealed a significant clustering of cell lines by a factor 2, whereas non-tumor PNT1A cells are clustered rather by positive values of factor 2, metastatic PC-3
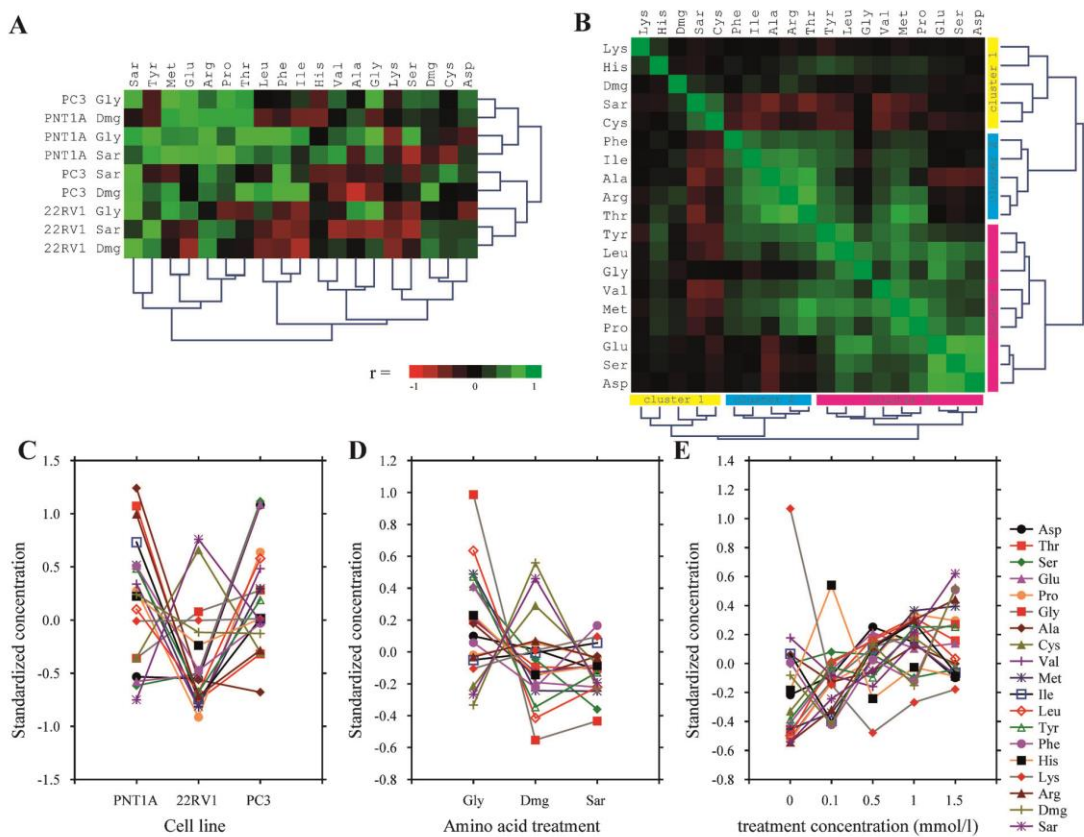
Fig. 5. Effect of treatment with glycine, dimethylglycine, and sarcosine on the cellular amino acid profile. (**A**) Heatmap showing clustered correlation analysis of amino acids used for treatment and amino acids profile measured in cells. Note the differential response of individual cell lines. (**B**) Heatmap showing correlation of amino acid profile measured in all three cell lines. Notice the differential negative correlation of sarcosine and cysteine with the majority of other amino acids. (**C**) Effect of the cell line on the level of amino acids, factorial ANOVA. Notice the differential response of cysteine, sarcosine, dimethylglycine, glycine, lysine, and alanine compared to the remaining amino acids. (**D**) Effect of amino acid used for treatment, factorial ANOVA. (**E**) Effect of concentration of the amino acids used for treatment, factorial ANOVA. Error bars not displayed for purposes of clarity.

are associated rather with negative values of this factor. Primary tumor 22Rv1 cluster is located between PNT1A and PC-3. Thus, the second factor is considered as "non-malignant—aggressive tumor cluster." In the next step, cases were color-coded by the amino acid used for treatment of prostate cell lines. This correlated with factor 1 on a factor plane; for each cell line the precursors—notably glycine was associated with more negative values than sarcosine. Thus, this factor was further designated as "precursor-product" (Fig. 6B). When variables (i.e., determined amino acids) were plotted to this factor plane, a similar shift is apparent (Fig. 6C). Whereas an amino acid pattern of the non-tumor PNT1A cell line is associated rather with negative values of factor 1, a metastatic-derived PC-3 amino acid pattern is associated with positive values of this factor, which corresponds also to

"precursor" factor in Fig. 6B demonstrating sarcosine connection to prostate cancer.

DISCUSSION

The metabolic abnormalities of prostate cancer cells have not yet been fully elucidated [13]. Amino acids play an important role in cellular physiology, since they are involved in a number of fundamental metabolic processes [14,15]. Thus, we have focused on determination of response of the prostate cell biomolecules involved in a sarcosine metabolic pathway to supplementation of these cells with amino acids with emphasis on sarcosine, a widely discussed biomarker of PCa.

Only the high concentrations of sarcosine, glycine, and dimethylglycine are toxic to the tested prostate
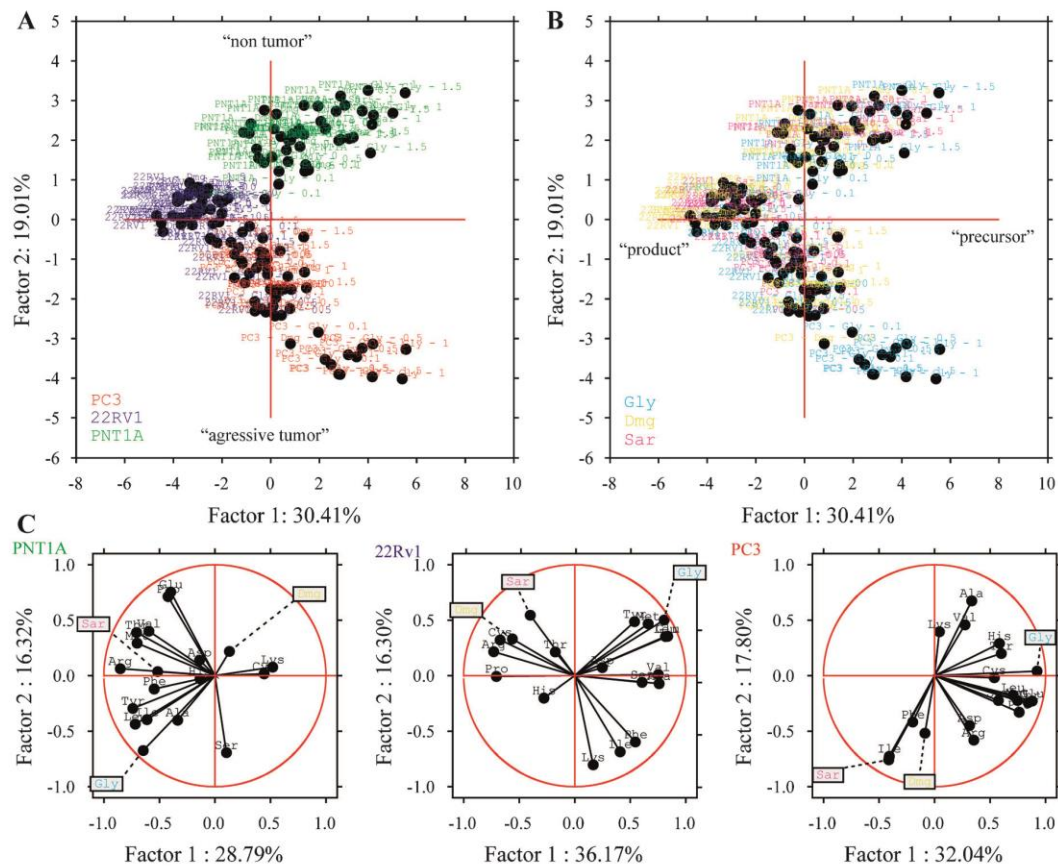
Fig. 6. Fingerprinting of prostate cells according to amino acid patterns, principal component analysis. (**A**) Projection of cases on a two-factor plane, color coded according to the cell line. Notice apparent clustering of cell lines by factor 2, thus this factor is considered "non-tumor–tumor." (**B**) Identical projection as (**A**), color coded by amino acid used for treatment. Notice the clustering for each cell line by Factor 1 so Sar precursors are more to the right from Sar for each cell line, so this factor is considered as "precursor–product." (**C**) Projection of variables (cellular amino acids) on two-factor plane identical as (**A**) and (**B**). See differential distribution of amino acids between cell lines (PNT1A, 22Rv1, and PC-3)—"left-to-right" shift on factor 1.

cells. Their cytotoxic concentrations are in conformity with those described by Stachlewitz et al., who have found that only the high concentrations of glycine (units of mM) are able to prevent increases in Ca^{2+} in cells, thereby inhibiting cell proliferation [16]. Likewise, we have found in our previous study, focused on possible effects of sarcosine on PC-3 cells, that only the high concentrations of sarcosine are able to inhibit cell growth, as a result of disruption of redox equilibrium [14]. Importantly, throughout our study, supplementation of prostate cells with tested amino acids did not exceed the concentrations of 1.5 mmol/l.

Sarcosine metabolism is suspicious to be an important part of malignant transformation of prostate cells. According to the changes in the cell mobility and division rates, sarcosine and glycine, but not dimethylglycine, can stimulate the migration of malignant cell lines (22Rv1 and PC-3). These findings are in agreement with a study carried out by Sreekumar et al., who have found that direct addition of sarcosine imparted an invasive phenotype to benign prostate cells and the number of motile prostate cells was significantly higher upon sarcosine treatment ($P = 6.997^{-6}$, n = 10) [9]. Similar, to that, Khan et al. demonstrated that addition of sarcosine to prostatic GNMT knockdown cells partially rescued their invasive properties, while addition of a sarcosine isomer, alanine, failed to rescue the invasive phenotype [17]. Notably, both studies highlighted the role of glycine, inducing invasion in the cells, however, to a lesser degree than sarcosine. It is plausible that this phenomenon is linked with the conversion of glycine to sarcosine catalyzed by GNMT.

Song et al. have reported that GNMT activity is connected with the progression of prostate cancer [12]. In agreement with their data, we have shown that GNMT mRNA expression is low predominantly in benign prostate cells, whereas high in the malignant cells. Hence, our results support the finding that sarcosine, generated from glycine by GNMT could be exploited as a PCa biomarker [3,9]. The GNMT enzyme is expected to play a substantial role in modulating prostate cancer cells invasion [18], and thus can be involved in promotion of the oncogenic potential of prostate cells with subsequent facilitating conversion of glycine to sarcosine. We demonstrated that dimethylglycine causes inhibition of GNMT mRNA expression in malignant cells, however, benign PNT1A were affected in a different manner. Increased amount of endogenously added dimethylglycine can stimulate sarcosine formation through action of dimethylglycine dehydrogenase (DMGDH), utilizing dimethylglycine as a substrate, instead of GNMT; nevertheless, whether the activity of DMGDH is disturbed in prostate cancer cells is unknown. The data found in the present work further illustrate that applied sarcosine significantly inhibited expression of GNMT in PNT1A cells, and to a lower extent in malignant PC-3 and 22Rv1. Thus, it can be hypothesized that by this kind of blocking, GNMT is not able to catalyze transformation of sarcosine to glycine and sarcosine can be thus accumulated in cancerous cells, as was shown in many studies [2,9,19]. However, plausible mechanism of this phenomenon is still not defined. Treatment of cells with glycine triggered only slight expression differences in GNMT, thus it can be stated that its expression is not glycine inducible. Our results illustrate the divergent significance of GNMT among the prostate cell lines and confirm the role of free amino acid pool as important metabolic factor, influencing PCa cells as was suggested by Fu et al. [15].

It has been shown that amino acids are substantial for cellular physiology [20–22] and our results demonstrate that free glycine and sarcosine can influence the GNMT expression in PCa cells. Jain et al. have revealed increased reliance of cancer cells on glycine mitochondrial metabolic pathway, which involves sarcosine and dimethylglycine [23]. Importantly, recent works have identified that sarcosine and related metabolites or their associated metabolic pathways, are central to cancer metastasis [9], cellular transformation [24,25], or murine embryonic stem cell proliferation [26]. Hence, we focused on patterns of amino acids in prostate cell lines and on the effect of exogenous supplementation with sarcosine-related amino acids on amino acid patterns in these cells. Our profiling revealed unique amino acid patterns,

exhibiting exceptional specificity toward prostate cell types. This phenomenon is likely connected with disturbances in carbohydrate, lipid, and protein metabolism during oncogenesis. Considering the Warburg effect [27], metabolic shifts in tumor cells from respiration to fermentation should result in an increased demand for consumption of amino acids and complex metabolic derangements reflected by alteration in amino acid patterns. Noteworthy, statistical processing of amino acid patterns revealed that malignant cell lines (22Rv1 and PC-3) exhibit common features in increased (Glu, Sar, Gly, Asp, Ser) and decreased (Ala, Thr, Arg, Ile, Phe, Dmg) amino acids, when compared to benign PNT1A cells (Fig. 5C).

First, our interest was caught by differences in glutamic acid. This amino acid is a precursor for glutamine in its interconvertible biosynthesis. In cancer cells, glutamine is the primary mitochondrial substrate, maintaining mitochondrial membrane potential and integrity [28]. Moreover, it provides support for the NADPH production required for redox control and macromolecular synthesis [29]. Our results show that oncogenesis results in elevated level of intracellular glutamic acid. This phenomenon is likely connected with the fact that many of the signaling pathways promoting oncogenesis also reprogramms the glutamine metabolism. For instance, Myc coordinates the reprogramming of metabolism to depend on glutamine and to sustain cellular viability and the citric acid cycle (TCA) anaplerosis through carbon donation [30,31]. Interestingly, glycine supplementation led to a significant elevation of glutamic acid levels within the cell lines; however, the reason explaining this phenomenon is not yet clear. Taken together, divergence in glutamic acid metabolism supports the idea that interventions into metabolism could be a potential therapeutic approach in PCa management, as was shown by Wang et al. [32].

Figure 6C illustrates that contrary to benign prostate cells, in malignant cells, glutamic acid essentially shares similar distribution with glycine and serine. Serine and glycine are linked biosynthetically. They provide the precursors for the synthesis of proteins, nucleic acids, and lipids [33]. Our results show that cancer cells benefit from higher levels of these amino acids. Serine biosynthesis is a component of glycolysis-diverting pathways, resulting in expression of phosphoglycerate dehydrogenase (PHGDH), which is necessary to sustain cancer growth and oncogenic transformation through production of anaplerotic intermediate of TCA α-ketoglutarate [34]. Serine also supports aerobic glycolysis and lactate production by affecting the activity of pyruvate kinase M2 (PKM2), converting phosphoenolpyruvate to pyruvate and one molecule

of ATP [35]. Glycine promotes tumorigenesis and its upregulation correlates with cell proliferation and poor prognosis. Its conversion significantly contributes to the biosynthetic requirements of purines, ATP and NADPH in cancer cells [23].

Elevated levels of aspartate in both types of malignant prostate cells are likely related to glutaminolysis, which lyses glutamine to citrate [36]. Such process takes place in all proliferating cells and especially in tumor cells, where the TCA is truncated due to an inhibition of aconitase [37]. Aspartic acid, produced from oxaloacetate during conversion of glutamate to α-ketoglutarate is utilized as a precursor for synthesis of nucleic acids and serine [38]. Taken together, both malignant prostate cell lines exhibited high dependency on glutamine metabolism, when compared to benign ones.

Our data further indicate that glycine supplementation influences all prostate cell amino acid patterns most effectively, which is likely due to a linkage with serine biosynthesis. Glycine treatment also resulted in elevation of amounts of amino acids connected to glutamine metabolism. Hence, we put evidence that glycine plays substantial role in prostate cells and glycine deprivation (dietetic or enzymatic depletion) may be a new strategy for human cancer therapy as was described earlier [23,33,39]. On the contrary, the highest increase in sarcosine concentrations was found after supplementation with exogenous dimethylglycine, whose role in prostate cancer development is not yet well elucidated. Elevated sarcosine levels during prostate cancer progression [3,9,17,19] are thus likely associated with action of both substrates—glycine and dimethylglycine and catalytic actions of corresponding enzymes—GNMT and DMGDH. One may speculate that inhibition of those enzymes may be used in prevention of prostate cancer.

CONCLUSION

The present study illustrates that exogenous supplementation of prostate cells with amino acids, closely related to sarcosine metabolism, can significantly affect the expression of GNMT mRNA in tested cells as well as their growth attributes. The results found indicate that sarcosine production is triggered by dimethylglycine treatment more than by glycine; however, glycine, a well-known cancer-related metabolite, significantly influences the prostate cell amino acid patterns. Above-mentioned data support the studies, which demonstrate that the deprivation of some amino acids can be helpful in management of cancer and furthermore proves the elevated levels of sarcosine in primary and secondary tumor cell lines when compared with non-tumor ones, which

corresponds to their GNMT expression levels. We anticipate that sarcosine metabolic pathway is highly important in prostate cancer behavior, and thus further studies, dealing with involved amino acids and their enzymes and also with inhibition of their activity in relation to physical and molecular parameters of prostate cells are strongly required to elucidate this phenomenon. Moreover, it was shown that amino acid patterns unequivocally describe if the prostate cells demonstrate malignant or non-tumor parameters.

REFERENCES

1. Armstrong AJ, Eisenberger MA, Halabi S, Oudard S, Nanus DM, Petrylak DP, Sartor AO, Scher HI. Biomarkers in the management and treatment of men with metastatic castration-resistant prostate cancer. Eur Urol 2012;61(3):549–559.

2. Lucarelli G, Fanelli M, Larocca AMV, Germinario CA, Rutigliano M, Vavallo A, Selvaggi FP, Bettocchi C, Battaglia M, Ditonno P. Serum sarcosine increases the accuracy of prostate cancer detection in patients with total serum PSA less than 4.0ng/ml. Prostate 2012;72(15):1611–1621.

3. Zitka O, Heger Z, Kominkova M, Skalickova S, Krizkova S, Adam V, Kizek R. Preconcentration based on paramagnetic microparticles for the separation of sarcosine using hydrophilic interaction liquid chromatography coupled with coulometric detection. J Sep Sci 2014;37(5):465–475.

4. Cernei N, Heger Z, Gumulec J, Zitka O, Masarik M, Babula P, Eckschlager T, Stiborova M, Kizek R, Adam V. Sarcosine as a potential prostate cancer biomarker—A review. Int J Mol Sci 2013;14(7):13893–13908.

5. Metallo CM. Expanding the reach of cancer metabolomics. Cancer Prev Res 2012;5(12):1337–1340.

6. Luka Z, Pakhomova S, Loukachevitch LV, Newcomer ME, Wagner C. Differences in folate-protein interactions result in differing inhibition of native rat liver and recombinant glycine N-methyltransferase by 5-methyltetrahydrofolate. Biochim Biophys Acta 2012;1824(2):286–291.

7. Mitchell AD, Benevenga NJ. Importance of sarcosine formation in methionine methyl carbon oxidation in rat. J Nutr 1976;106(12):1702–1713.

8. Soriano A, Castillo R, Christov C, Andres J, Moliner V, Tunon I. Catalysis in glycine N-methyltransferase: Testing the electrostatic stabilization and compression hypothesis. Biochemistry 2006;45(50):14917–14925.

9. Sreekumar A, Poisson LM, Rajendiran TM, Khan AP, Cao Q, Yu JD, Laxman B, Mehra R, Lonigro RJ, Li Y, Nyati MK, Ahsan A, Kalyana-Sundaram S, Han B, Cao XH, Byun J, Omenn GS, Ghosh D, Pennathur S, Alexander DC, Berger A, Shuster JR, Wei JT, Varambally S, Beecher C, Chinnaiyan AM. Metabolomic profiles delineate potential role for sarcosine in prostate cancer progression. Nature 2009;457(7231):910–914.

10. Cao DL, Ye DW, Zhang HL, Zhu Y, Wang YX, Yao XD. A multiplex model of combining gene-based, protein-based,

and metabolite-based with positive and negative markers in urine for the early diagnosis of prostate cancer. Prostate 2011;71(7):700–710.

11. Liang CC, Park AY, Guan JL. In vitro scratch assay: A convenient and inexpensive method for analysis of cell migration in vitro. Nat Protoc 2007;2(2):329–333.

12. Song YH, Shiota M, Kuroiwa K, Naito S, Oda Y. The important role of glycine N-methyltransferase in the carcinogenesis and progression of prostate cancer. Mod Pathol 2011;24(9):1272–1280.

13. Fu YM, Lin HM, Fang WG, Meadows GG. Cell death of prostate cancer cells by specific amino acid restriction depends on alterations of glucose metabolism. J Cell Physiol 2010;224(2):491–500.

14. Heger Z, Cernei N, Kudr J, Gumulec J, Blazkova I, Zitka O, Eckschlager T, Stiborova M, Adam V, Kizek R. A novel insight into the cardiotoxicity of antineoplastic drug doxorubicin. Int J Mol Sci 2013;14(11):21629–21646.

15. Fu YM, Yu ZX, Li YQ, Ge XK, Sanchez PJ, Fu X, Meadows GG. Specific amino acid dependency regulates invasiveness and viability of androgen-independent prostate cancer cells. Nutr Cancer 2003;45(1):60–73.

16. Stachlewitz RF, Li XL, Smith S, Bunzendahl H, Graves LM, Thurman RG. Glycine inhibits growth of T lymphocytes by an IL-2-independent mechanism. J Immunol 2000;164(1):176–182.

17. Khan AP, Rajendiran TM, Ateeq B, Asangani IA, Athanikar JN, Yocum AK, Mehra R, Siddiqui J, Palapattu G, Wei JT, Michailidis G, Sreekumar A, Chinnaiyan AM. The role of sarcosine metabolism in prostate cancer progression. Neoplasia 2013;15(5):491–501.

18. Huang YC, Lee CM, Chen M, Chung MY, Chang YH, Huang WJS, Ho DMT, Pan CC, Wu TT, Yang S, Lin MW, Hsieh JT, Chen YMA. Haplotypes, loss of heterozygosity, and expression levels of glycine N-methyltransferase in prostate cancer. Clin Cancer Res 2007;13(5):1412–1420.

19. Heger Z, Cernei N, Krizkova S, Masarik M, Kopel P, Hodek P, Zitka O, Adam V, Kizek R. Paramagnetic nanoparticles as a platform for FRET-based sarcosine picomolar detection. Sci Rep 2015;5:1–7.

20. Bar-Peled L, Sabatini DM. Regulation of mTORC1 by amino acids. Trends Cell Biol 2014;24(7):400–406.

21. Torrente M, Guetg A, Sass JO, Arps L, Ruckstuhl L, Camargo SMR, Verrey F. Amino acids regulate transgene expression in MDCK cells. PLoS ONE 2014;9(5):1–13.

22. Mann GE, Yudilevich DL, Sobrevia L. Regulation of amino acid and glucose transporters in endothelial and smooth muscle cells. Physiol Rev 2003;83(1):183–252.

23. Jain M, Nilsson R, Sharma S, Madhusudhan N, Kitami T, Souza AL, Kafri R, Kirschner MW, Clish CB, Mootha VK. Metabolite profiling identifies a key role for glycine in rapid cancer cell proliferation. Science 2012;336(6084):1040–1044.

24. Zhang WC, Shyh-Chang N, Yang H, Rai A, Umashankar S, Ma SM, Soh BS, Sun LL, Tai BC, Nga ME, Bhakoo KK, Jayapal SR, Nichane M, Yu Q, Ahmed DA, Tan C, Sing WP, Tam J, Thiruganaanam A, Noghabi MS, Pang YH, Ang HS, Robson P, Kaldis P, Soo RA, Swarup S, Lim EH, Lim B. Glycine decarboxylase activity drives non-small cell lung cancer tumor-initiating cells and tumorigenesis. Cell 2012;148(1–2):259–272.

25. Locasale JW, Grassian AR, Melman T, Lyssiotis CA, Mattaini KR, Bass AJ, Heffron G, Metallo CM, Muranen T, Sharfi H, Sasaki AT, Anastasiou D, Mullarky E, Vokes NI, Sasaki M,

Beroukhim R, Stephanopoulos G, Ligon AH, Meyerson M, Richardson AL, Chin L, Wagner G, Asara JM, Brugge JS, Cantley LC, Vander MG, Heiden. Phosphoglycerate dehydrogenase diverts glycolytic flux and contributes to oncogenesis. Nat Genet 2011;43(9):869–874.

26. Wang J, Alexander P, Wu LJ, Hammer R, Cleaver O, McKnight SL. Dependence of mouse embryonic stem cells on threonine catabolism. Science 2009;325(5939):435–439.

27. Warburg O, Wind F, Negelein E. The metabolism of tumors in the body. J Gen Physiol 1927;8(6):519–530.

28. Barger JF, Plas DR. Balancing biosynthesis and bioenergetics: Metabolic programs in oncogenesis. Endocr Relat Cancer 2010;17(4):287–304.

29. Wise DR, Thompson CB. Glutamine addiction: A new therapeutic target in cancer. Trends Biochem Sci 2010;35(8):427–433.

30. Wise DR, DeBerardinis RJ, Mancuso A, Sayed N, Zhang XY, Pfeiffer HK, Nissim I, Daikhin E, Yudkoff M, McMahon SB, Thompson CB. Myc regulates a transcriptional program that stimulates mitochondrial glutaminolysis and leads to glutamine addiction. Proc Natl Acad Sci USA 2008;105(48):18782–18787.

31. Dang CV. Rethinking the Warburg effect with Myc micromanaging glutamine metabolism. Cancer Res 2010;70(3):859–862.

32. Wang Q, Hardie RA, Hoy AJ, van Geldermalsen M, Gao D, Fazli L, Sadowski MC, Balaban S, Schreuder M, Nagarajah R, Wong JJL, Metierre C, Pinello N, Otte NJ, Lehman ML, Gleave M, Nelson CC, Bailey CG, Ritchie W, Rasko JE, Holst J. Targeting ASCT2-mediated glutamine uptake blocks prostate cancer growth and tumour development. J Pathol 2015;236(3):278–289.

33. Amelio I, Cutruzzola F, Antonov A, Agostini M, Melino G. Serine and glycine metabolism in cancer. Trends Biochem Sci 2014;39(4):191–198.

34. DeBerardinis RJ. Serine metabolism: Some tumors take the road less traveled. Cell Metab 2011;14(3):285–286.

35. Chaneton B, Hillmann P, Zheng L, Martin ACL, Maddocks ODK, Chokkathukalam A, Coyle JE, Jankevics A, Holding FP, Vousden KH, Frezza C, O'Reilly M, Gottlieb E. Serine is a natural ligand and allosteric activator of pyruvate kinase M2. Nature 2012;491(7424):458–462.

36. Moreadith RW, Lehninger AL. The pathways of glutamate and glutamine oxidation by tumor-cell mitochondria—Role of mitochondrial NADP(P)+-dependent malic enzyme. J Biol Chem 1984;259(10):6215–6221.

37. Kim KH, Rodriguez AM, Carrico PM, Melendez JA. Potential mechanisms for the inhibition of tumor cell growth by manganese superoxide dismutase. Antioxid Redox Signal 2001;3(3):361–373.

38. Newsholme P, Lima MMR, Porcopio J, Pithon-Curi TC, Doi SQ, Bazotte RB, Curi R. Glutamine and glutamate as vital metabolites. Braz J Med Biol Res 2003;36(2):153–163.

39. Maddocks ODK, Berkers CR, Mason SM, Zheng L, Blyth K, Gottlieb E, Vousden KH. Serine starvation induces stress and p53-dependent metabolic remodelling in cancer cells. Nature 2013;493(7433):542–546.

SUPPORTING INFORMATION

Additional supporting information may be found in the online version of this article at the publisher's web-site.

4.4.3 Modulation of cell metabolic and mechanical properties as a drug target

Targeting of cancer cell migration and adhesion accompanied by or resulting in changes of cell stiffness, as well as changes in differentiation and metabolic state is commonly used as an anti-cancer strategy. Interestingly, the mechanism of action of some of the commonly used anticancer agents exceeds their canonical mechanism. For instance, data indicate DNA damage is not the only mechanism cisplatin; our previous study [2] in agreement with literature data points out that that cisplatin induces the formation the actin stress fibers and thereby affects the cytoskeleton and membrane mechanical properties [98-101]. The ability of cisplatin to modify microtubule disassembly by direct tubulin modification was also shown [102]. Moreover, also cancer cell metabolism is affected by this drug. In proliferating cancer cells, pyruvate is shifted away from the tricarboxylic acid cycle and fermented into lactate. Cisplatin exerts an inhibiting effect on glucose transport, glycolysis and lactate production and stimulates ROS generation by OXPHOS which contributes to the mitochondrial dysfunction and cell death. Evidence on these mechanisms are discussed in a following review [103].

RAUDENSKA, M., J. BALVAN, M. FOJTU, J. GUMULEC, et al. Unexpected therapeutic effects of cisplatin. Metallomics, Jul 2019, 11(7), 1182-1199.

CRITICAL REVIEW

Check for updates

Unexpected therapeutic effects of cisplatin

Martina Raudenska, [a] Jan Balvan, [abc] Michaela Fojtu, [a] Jaromir Gumulec [abc] and Michal Masarik [*abd]

Cisplatin is a widely used chemotherapeutic agent that is clinically approved to fight both carcinomas and sarcomas. It has relatively high efficiency in treating ovarian cancers and metastatic testicular cancers. It is generally accepted that the major mechanism of cisplatin anti-cancer action is DNA damage. However, cisplatin is also effective in metastatic cancers and should, therefore, affect slow-cycling cancer stem cells in some way. In this review, we focused on the alternative effects of cisplatin that can support a good therapeutic response. First, attention was paid to the effects of cisplatin at the cellular level such as changes in intracellular pH and cellular mechanical properties. Alternative cellular targets of cisplatin, and the effects of cisplatin on cancer cell metabolism and ER stress were also discussed. Furthermore, the impacts of cisplatin on the tumor microenvironment and in the whole organism context were reviewed. In this review, we try to reveal possible causes of the unexpected effectiveness of this anti-cancer drug.

Introduction

cis-Diamminedichloroplatinum(II) (NSC 119875), more often called cisplatin, is a platinum coordination compound with a planar geometry. Platinum is bound to two amine groups and two chloride ions. Cisplatin is called the "penicillin of cancer" because it is widely used in clinics and it was also the first relevant chemotherapy drug in cancer therapy (FDA approved cisplatin under the name of Platinol® for cancer treatment in 1978). Cisplatin has a water solubility of 2.53 g L^{-1} at 25 °C, a melting point of 270 °C, a molecular weight of 300.01 mg mol^{-1}, and a density of 3.74 g cm^{-3}.[1] Cisplatin is clinically approved to fight both carcinomas and sarcomas and has relatively high efficiency in treating ovarian cancers and metastatic testicular cancers. Nevertheless, other tumor types such as head and neck cancer, bladder cancer, lung cancer, or breast cancer also benefit from a therapeutic regimen that includes this drug.[1–3] Cellular accumulation of cisplatin happens by different mechanisms, including passive diffusion and multiple transport systems such as high-affinity copper uptake transporter 1 (hCTR1/*SLC31A1*) or some members of the *SLC22* family.[4]

It is generally accepted that the major mechanism of cisplatin anti-cancer action is binding of platinum to DNA by forming intra-stranded and inter-stranded crosslinks. This DNA damage then arrests the cell cycle and initiates cell death in fast proliferating cells.[2] Nevertheless, before interaction with DNA, cisplatin has to undergo the activation step which consists of the chloro-ligand(s) replacement, usually by water molecules. Depending on the pH value of the environment, the hydrated complexes can be subsequently stabilized by deprotonation of the aqua ligands or again passivated in the alkaline solution.[219] Various values of pK_a were determined for cisplatin hydrates in several studies. For example, the pK_a value of *cis*-[PtCl(H$_2$O)(NH$_3$)$_2$]$^+$ was 6.41 in ref. 220 or 6.6 in ref. 219, the pK_a value of *cis*-[Pt(H$_2$O)2(NH$_3$)$_2$]$^{2+}$ was 5.37 in ref. 220 or 5.5 in ref. 219, and the pK_a value of *cis*-[PtCl(H$_2$O)(OH)(NH$_3$)$_2$]$^+$ was 7.21 in ref. 220 or 7.3 in ref. 219. Furthermore, when cisplatin is administered as an anti-cancer treatment, it is exposed to various endogenous sulfur-containing molecules such as glutathione, metallothioneins and thioredoxins, and it has been found that in 180 minutes almost all the ligands are substituted by sulfur ligands.[221] In the cell, cisplatin is co-localized with sulfur-rich and phosphorus-rich regions in the nucleus and cytoplasm. In the nucleus, most of the platinum was associated with the nucleolus. Within the cytoplasm, platinum mainly accumulated in the acidic organelles.[222] Probably only 1–10% of intracellular cisplatin ends up in the nucleus and reacts with DNA which leads to the cell cycle arrest and initiates cell death in fast proliferating cells.[71,222,223] However, cancer stem cells (CSCs) maintain a quiescent slow-cycling state which protects them from the type of therapy targeting fast proliferating cells. Quiescent CSCs have been proven in many human malignancies and are probably the major cause of

[a] *Department of Physiology, Faculty of Medicine, Masaryk University, Kamenice 5, CZ-625 00 Brno, Czech Republic. E-mail: masarik@med.muni.cz; Fax: +420-5-4949-4340; Tel: +420-5-4949-3631*

[b] *Department of Pathological Physiology, Faculty of Medicine, Masaryk University, Kamenice 5, CZ-625 00 Brno, Czech Republic*

[c] *Central European Institute of Technology, Brno University of Technology, Purkynova 656/123, CZ-612 00 Brno, Czech Republic*

[d] *BIOCEV, First Faculty of Medicine, Charles University, Průmyslová 595, CZ-252 50 Vestec, Czech Republic*
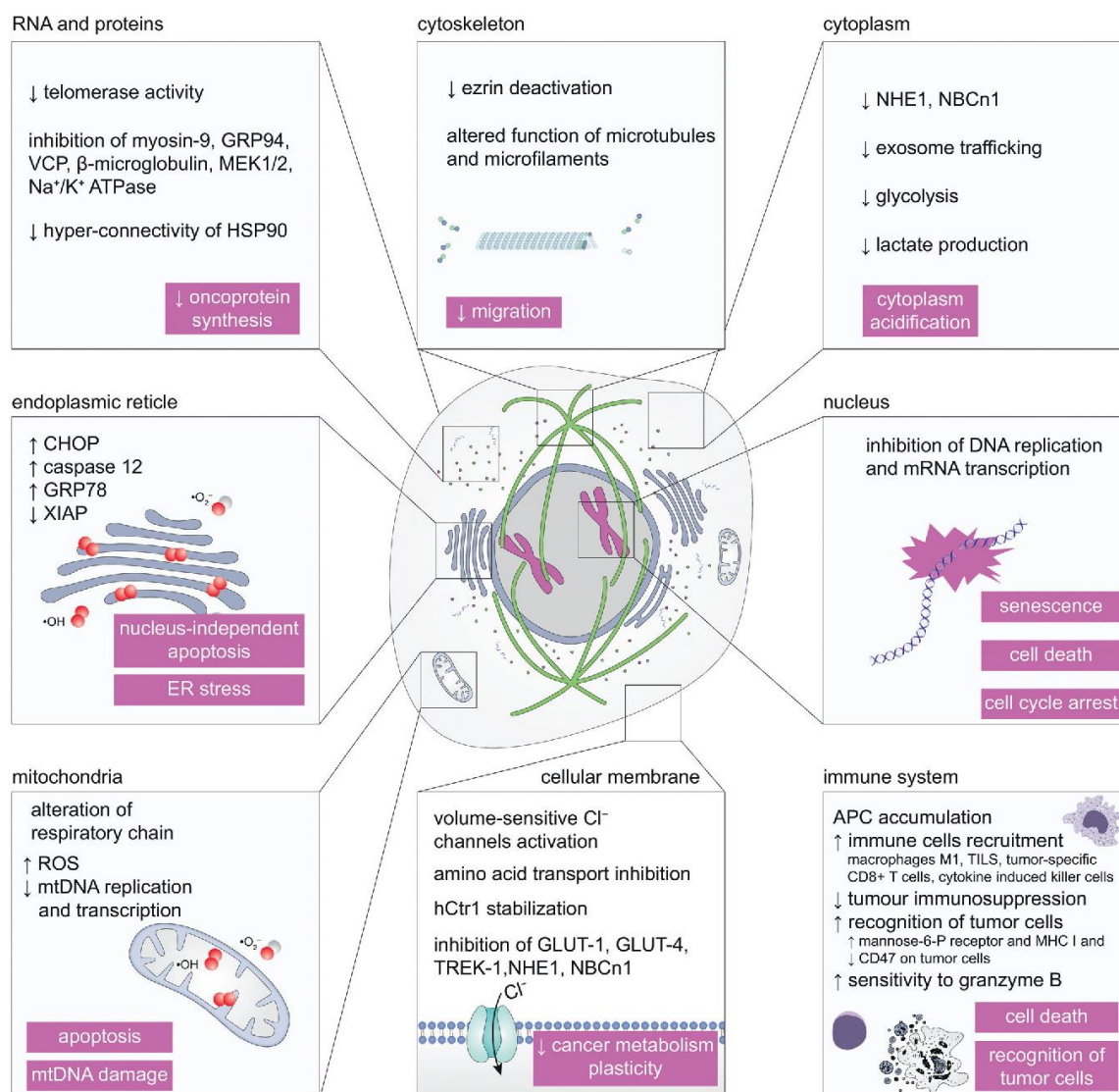
Fig. 1 Alternative effects of cisplatin. Cisplatin is known as a cytotoxic drug which kills cancer cells by damaging DNA. However, other interesting mechanisms such as acidification of the cytoplasm, ER stress, disruption of RNA transcription, inhibition of important oncogenic proteins and decrease in metabolic plasticity of cancer cells as well as changes in their mechanobiology should be considered as cisplatin has a pleiotropic effect on cellular proteins significantly affecting their conformation and function. Cisplatin may also exert antitumor immunomodulation.

treatment resistance in metastatic cancers[5–7] because CSCs can survive chemotherapy with increased tumorigenic and invasive potential.[8] Nevertheless, about 80% of patients with metastatic testicular germ-cell tumors can be cured using cisplatin-based chemotherapy.[3,9] Why is cisplatin so effective? Recent studies suggest that cisplatin could have other mechanisms of action and more variable cellular targets beyond nuclear DNA. Therefore, we will focus on the alternative effects of cisplatin that can reflect its good therapeutic response in this review. First, we will pay attention to the effects of cisplatin at the cellular level; then the whole organism context will be reviewed. Uncovering

of the cellular pathways that could be influenced by cisplatin may provide an important clue for the design of new cancer treatment strategies. The alternative effects of cisplatin discussed in this review are summarized in Fig. 1.

Cisplatin and intracellular pH of tumor cells

The acid–base balance of tumor tissues is fundamentally different from that in healthy tissues. Cancer cells tend to have

more alkaline intracellular pH (pH_i = 7.12–7.7) compared to healthy cells (pH_i = 6.99–7.05) while producing acidic extra-cellular pH (pH_e = 6.2–6.9). In healthy tissues, the pH_e value is in the range of 7.3–7.4.[10] This situation leads to an inverse pH gradient (ΔpH_i to ΔpH_e) between the outside and inside space of the cell, which can enhance proliferation, metabolic adaptation, apoptosis resistance, migration, and invasion of cancer cells.[11] Moreover, the inverse pH_e/pH_i gradient influences the effectivity of antineoplastic drugs. Many of them, such as doxorubicin, mitoxantrone, paclitaxel, and vinblastine are weak bases which are inactivated by protonation in the acidic microenvironment surrounding the cancer cells. On the other hand, cisplatin which is a weak acid has a better chance to concentrate on the more alkaline intracellular space of tumor cells.[12,13]

The aberrant regulation of hydrogen ion dynamics in tumor tissues can be considered as one of the hallmarks of cancer.[13] Rapid cytoplasmic alkalization seems to be an oncogene-dependent early event in the malignant transformation and accounts for the increased activity of hydrogen ion extruders such as the Na^+/H^+ exchangers of the *SLC9* family.[14–16] An increase in pH_i above 7.2 facilitates the cell cycle progression through the S and G2/M phases by increasing the activity of the key mitotic regulators such as cyclin-dependent kinase 1 (*CDK1*) and cyclin B1 (*CCNB1*).[17,18] Changes in pH_i seem to be a con-served evolutionary mechanism for the regulation of mitosis and meiosis.[19] Furthermore, an alkaline pH_i promotes glycolysis,[20] which may depend on the pH-sensitive activity of several glycolytic enzymes. Optimal pH at 30 °C (pH_{30} optimum) for the activity of lactate dehydrogenase (LDH) by conversion of pyruvic acid to lactate is within the range of 7.20–7.40 for all the LDH isoenzymes.[21] The LDH activity is elevated in many types of cancers and has been linked to tumor growth and invasion.[22,23] Moreover, intracellular alkaline pH prevents the progression of apoptosis because pH_i acidification is essential for the activa-tion of caspases and endonucleases.[24,25]

Recently, it was shown that cisplatin could significantly affect the intracellular pH of cancer cells. Acidification of the cytoplasm was described as a result of cisplatin treatment, as demonstrated by *in vitro* and *in vivo* experiments.[26,27] Although the exact causes of this cytoplasmic acidification are yet to be clarified, it is possible that this effect is associated with cisplatin-caused inhibition of the proton extrusion and seems to be independent of cisplatin–DNA adduct formation.[26,27] Indeed, non-competitive inhibition of the Na^+/H^+ exchanger 1 (NHE-1/ *SLC9A1*) by cisplatin was confirmed in the HT29 cells and fibroblasts from the PS120 cell line.[27,28] The activity of NHE-1 is typically increased in cancer cells[13] and steadily increased pH_i has been shown in the cisplatin-resistant cell lines.[29–31] The role of NHE-1 in tumorigenesis may be essential because NHE-1-deficient cells showed severe acidification of pH_i and cell death due to Ras oncogene overactivation.[32] Thus, NHE-1 inhibition by cisplatin can play an important role in its antineoplastic effect.

Further evidence that cisplatin has a significant effect on the intracellular and extracellular pH of tumor cells is that proton pump inhibition,[33] and also carbonic anhydrase 9 (CAIX/*CA9*)-targeted therapy enhance the anti-cancer effects of cisplatin.[34]

CAIX is a dimeric protein belonging to a family of zinc-containing enzymes that catalyze the reversible hydration of carbon dioxide (CO_2) to bicarbonate and protons ($CO_2 + H_2O \leftrightarrow HCO_3^- + H^+$). CAIX can effectively utilize CO_2 to produce bicarbonate that is delivered through the plasma membrane by the bicarbonate transporter protein family NBC (*NBC2/SLC4A5* and others).[12,35] The protons produced by CAIX stay outside and increase the acidosis of the tumor microenvironment. The intracellular bicarbonate is converted back to CO_2 by cytoplasmic carbonic anhydrase 2 (*CA2*) in a reaction that scavenges protons and helps neutralize the intracellular pH. In summary, the CAIX activity protects the cytosol from acidification, while contributing to the acidosis of the extracellular microenvironment.[36] Cisplatin can also intervene in this mechanism, as sodium bicarbonate cotransporter NBCn1 (NBC3/*SLC4A7*) might be made unfunc-tional by cisplatin treatment, for example, by its reduced plasma membrane localization.[37]

In conclusion, the induction and maintenance of intracellular alkalization and extracellular acidification has an important role in the progression of the neoplastic transformation.[38] Further-more, low microenvironmental pH is a key factor for exosome trafficking in tumor cells[39,40] and some cancer cell-derived exo-somes can increase treatment resistance of recipient cells.[41,42] Due to cisplatin treatment, the pH gradient reversal in cancer tissues can be abolished, and this can mean a major contribu-tion to the treatment efficacy.

Cisplatin and cell metabolism

It is generally accepted that binding of cisplatin to the nuclear DNA is mainly responsible for its antineoplastic effect. However, cisplatin also forms a high amount of adducts in mitochondrial DNA (mtDNA), because mitochondria are not able to carry out nucleotide excision repair, and to effectively remove cisplatin–mtDNA adducts compared to the nucleus. So, the possibility shall not be excluded that mitochondrial DNA may also be an important target of cisplatin. Actually, it has been shown that the level of DNA adducts in mtDNA is higher than that in nuclear DNA. This may be a consequence of both higher initial platinum binding and inefficient removal of cisplatin–mtDNA adducts.[43,44]

Mitochondria are important for the energy supply and reg-ulation of apoptosis. Apart from mtDNA adducts, cisplatin also stimulates ROS generation, prompting oxidative alterations in mitochondrial lipids, proteins, and mtDNA and inducing apoptosis.[45] Mitochondrial ROS generation is independent of the amount of cisplatin-induced damage of nuclear DNA. The cytotoxic effect of cisplatin varies among cells and depends on the mitochondrial redox status and integrity of mitochondrial DNA.[44] Cisplatin may induce serious mitochondrial damage[46] and tumor cells with such damaged mtDNA showed delayed tumor growth. Further tumorigenesis was conditioned by the acquisition of mtDNA from the host cells.[47]

Cancer cells were found to switch their cellular metabolism to glycolysis. Moreover, glycolysis is uncoupled from the mitochondrial tricarboxylic acid (TCA) cycle and oxidative

phosphorylation in such cells. Consequently, lactate formation increases. This metabolic phenotype is called the Warburg effect. By restricting the input of pyruvate into oxidative metabolism in mitochondria, the Warburg effect decreases the mitochondrial ROS generation and increases the cell death resistance and survival advantage for metastasis.[48] Originally, increased glycolysis in cancer cells under aerobic conditions was misinterpreted as evidence for respiration damage. However, we now understand that it reflects an altered regulation of glycolysis, not respiration damage directly. The metabolic flexibility of cancer cells allows the possibility to alternate between glycolysis and oxidative phosphorylation.[49,50] However, cisplatin generates a high level of oxidative stress which is accompanied by cytosolic and mitochondrial acidification, rapid shifts in carbon metabolism and severe decrease of cancer cell metabolic plasticity.[26,51,52] Cytosolic acidification is known to inhibit glycolysis in many ways, for example by the reduction of the glucose transporters expression, and by the inhibition of phosphofructokinase (PFK) and other glycolytic enzymes, while activating oxidative phosphorylation.[22,26,53] Forced stimulation of oxidative phosphorylation in cancer cells with cisplatin-damaged mitochondria raises ROS production and oxidative stress and can restore cancer cells' sensitivity to cell death.[48] Accordingly, antioxidants and mitochondrial uncoupling proteins neutralize cisplatin-induced cytotoxicity in tumor cells and on the contrary, lactate dehydrogenase or pyruvate dehydrogenase kinase 1 (PDK1) inhibitors can further sensitize cancer cells to cisplatin.[45,46,54–57]

Cisplatin down-regulates the expression of many glycolysis-related proteins, including hexokinases, phosphofructokinases, pyruvate kinases, glucose transporters 1 and 4 (GLUT-1/*SLC2A1* and GLUT-4/*SLC2A4*), and lactate dehydrogenase B (*LDHB*).[58,59] Consequently, lactate production is reduced after cisplatin treatment in cancer cells.[51,59] Lactate is probably a key signaling molecule in the tumor microenvironment necessary for all main hallmarks of carcinogenesis, including immune escape, angiogenesis, cell migration, metastasis and self-sufficient metabolism.[40,60] The lactate levels are highly correlated with cancer aggressiveness, and poor survival and reduction of lactate may have a beneficial effect on the cancer therapy.[61,62] The effect of cisplatin on glucose metabolism is summarized in Fig. 2.

Other key signaling molecules in the cancer microenvironment are ATP and adenosine. The ATP levels in the resting/healthy tissues are very low (in the nanomolar range), whereas it can reach hundreds of μmol L^{-1} in stimulated or cancer tissues.[63] Cell death-inducing chemotherapeutic agents such as etoposide, oxaliplatin, cisplatin, staurosporine, and doxorubicin may trigger the release of ATP from the tumor and dendritic cells.[64] Virtually, all tumor cell lines and many primary human tumors express purinergic receptors and are sensitive to ATP.[63] Nevertheless, the activation of purinergic receptors has very heterogeneous and contradictory effects on tumorigenesis.[64] Some results suggest that cisplatin can induce a Cl$^-$ current by activating volume-sensitive chloride channels through the
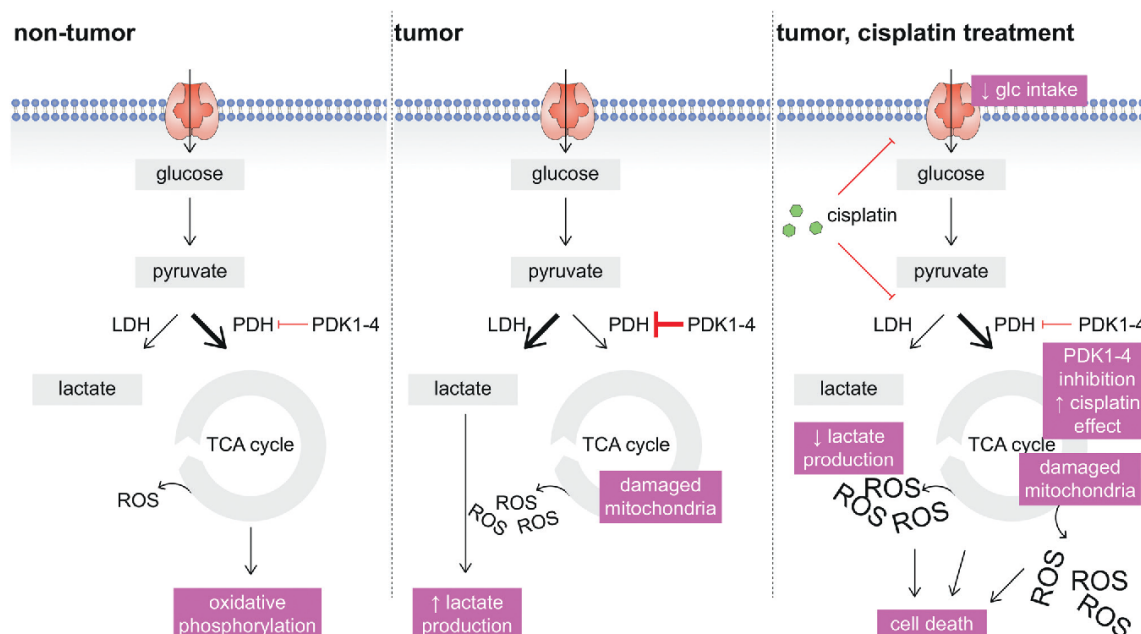
Fig. 2 Changes in cancer metabolism; effect of cisplatin. In most healthy cells with ample oxygen supply, glucose is metabolized to pyruvate which is transformed to acetyl-CoA by pyruvate dehydrogenase (PDH) for entering the respiratory chain. In proliferating cancer cells, increased expression of pyruvate dehydrogenase kinases (PDKs) shifts the pyruvate away from the tricarboxylic acid (TCA) cycle by inhibiting its conversion to acetyl-CoA. 85% pyruvate in malignant cells is fermented into lactate and only 5% pyruvate goes into the TCA cycle by the Warburg effect. Cisplatin exerts an inhibiting effect on glucose transport, glycolysis and lactate production and stimulates ROS generation by OXPHOS which contributes to the mitochondrial dysfunction and cell death. Pyruvate dehydrogenase kinase 1 (PDK1) inhibitors can sensitize cancer cells to cisplatin.

P2Y purinergic receptor pathway.[65] Volume-sensitive chloride channels are involved in the apoptotic cellular volume decrease and cell death after cisplatin treatment.[66-68] Interestingly, ATP suppresses the antiproliferative activity of paclitaxel and etoposide, while it enhances the antineoplastic effect of cisplatin in human lung epithelial tumor cells.[69]

Taken together, cisplatin exerts an inhibiting effect on glycolysis and lactate production;[51] it stimulates ROS generation and purinergic signaling and contributes to mitochondrial dysfunction and cell death.[44,70] Targeting mitochondria and lactate production seem to be an important contribution to the treatment efficacy of cisplatin.

Cisplatin, endoplasmic reticulum, and nucleus-independent apoptosis

Cisplatin can react with nucleophiles other than DNA. It was reported that cisplatin could trigger apoptotic signaling independently of nuclear DNA damage even in enucleated cells through increased cytosolic calcium and calpain-dependent activation of the ER-specific caspase-12.[71,72] Cisplatin-mediated activation of calpain protease was found to occur early in the apoptotic process and to coincide with BH3-interacting domain death agonist (*BID*) cleavage.[73] In contrast to cisplatin, etoposide, which is also a DNA-damaging agent, failed in inducing apoptosis in these enucleated cells.[71] Moreover, the inhibition of ER-specific caspase-12 with the anti-caspase-12 antibody significantly decreased cisplatin-induced apoptosis, indicating that ER stress is involved in the cisplatin-induced cell death.[74] Accordingly, the expression of chaperone glucose regulated-protein 78 (GRP-78/*HSPA5*), which is an ER stress marker, is up-regulated after cisplatin treatment.[75] This phenomenon is probably not caused by reactive oxygen species (ROS), because ROS scavenger *N*-acetyl cysteine (NAC) failed to inhibit calpain activation and apoptosis in cisplatin-treated cells and the presence of NAC did not affect the up-regulation of GRP-78 levels after cisplatin treatment.[71] These facts suggest that the endoplasmic reticulum (ER) might be a non-nuclear target of cisplatin. Disturbances in the normal functions of the ER lead to a stress response because protein folding in the ER is sensitive to various deleterious conditions such as calcium concentrations, the redox state, misglycosylation of glycoproteins, and low ATP levels.[76] The ER stress mechanism is a key response to deleterious environmental factors and triggers the unfolded protein response (UPR). A moderate UPR activation enables compensation for damage and has an anti-apoptotic role that enhances tumor cell survival and drug resistance.[77] However, the compensatory phase of the ER stress response is not limitless. When ER stress becomes severe, cell death is triggered even in the presence of high levels of GRP-78.[78] The key factor in this phenomenon is the transcription factor CCAAT-enhancer-binding protein homologous protein (CHOP/*DDIT3*). The increased expression of CHOP triggers the activation of pro-apoptotic pathways.[79] Apparently, cisplatin treatment induces significant ER stress followed by the up-regulation of pro-apoptotic signaling molecules CHOP or protein disulfide

isomerase (PDI).[80-82] Furthermore, cisplatin inhibits the expression of X-chromosome-linked inhibitor of apoptosis protein (XIAP).[83,84]

Adaptation to ER stress depends not only on the activation of the UPR but also on autophagy.[85] Knockdown of p62 (adaptor for autophagic degradation, *SQSTM1*) or the autophagy inhibitors 3-methyladenine and chloroquine increases the level of ubiquitinated proteins, which elevates the ER stress and results in a higher apoptotic rate of cancer cells treated with cisplatin.[86,87] In conclusion, the activation of UPR and CHOP in various cancer cell lines indicates that cisplatin may induce apoptosis through the ER stress pathways.

Cisplatin and mechanical properties of tumor cells

The cell has a complex internal structure that changes in response to its microenvironment as well as to the physiological state. Altered cellular functions can markedly remodel the cellular biomechanical properties. The cellular shape, mechanical response, and mechanical deformability are primarily determined by the cytoskeleton. In concert with accessory proteins, the cytoskeleton also plays a key role in important cellular processes such as mechanotransduction, migration, and mitosis.[88] The structures of the cytoskeleton, cellular membrane, and extracellular matrix are transformed during cancer progression, which changes the deformability of the cancer cells. As a result, the motility of cancer cells can be different from that of normal cells, causing them to migrate through the tissue to different sites in the human body and inducing metastasis.[89,90] It was also shown that cytoskeletal remodelling is a key process in the formation of cancer stem cells (CSCs).[91] It seems that cisplatin can strongly influence the actin stress fiber formation and affects the cytoskeleton.[91-96] The actin cytoskeleton strongly influences the membrane mechanical properties and is connected to mechanosensitive channels and transporters, such as NHE-1.[97] The significance of this sodium/hydrogen exchanger in carcinogenesis was discussed in the previous text. The ability of cisplatin to modify microtubule disassembly by direct tubulin modification was also shown. In contrast to cisplatin, carboplatin did not produce microtubule disassembly abnormalities.[96] Accordingly, the treatment with cisplatin caused a significant increase in the cell stiffness of the prostate cancer cells.[92] Changes in the cell stiffness due to cisplatin treatment probably do not result from metal accumulation in the cells because no such increase was shown in the zinc-treated cells. Under cisplatin treatment, the cytoskeletal tubules and filaments, which are normally distributed as a gently organized network spreading through the whole cytoplasm and forming delicate protrusions such as filopodia, aggregated to dense areas on the leading edge of the cell or to the cap-like structures around the nucleus. These phenomena are dependent on the dose of cisplatin applied.[92,95] This effect of cisplatin was observable also in breast cancer cells, where cisplatin produced changes in the cell morphology and the actin cytoskeleton. These changes were manifested as a loss of lamellipodia/filopodia and the appearance of membrane ruffles.

The activation of acid sphingomyelinase (ASMase/*SMPD1*) was shown to be required upstream of these morphological changes.[93] Cisplatin activates ASMase and ceramide production, which triggers the redistribution of CD95 into the plasma membrane rafts. Such redistribution sensitizes tumor cells to CD95-mediated apoptosis.[98] Furthermore, cisplatin induces dephosphorylation of the actin-binding protein ezrin (*EZR*), and its relocation from the membrane to the cytosol.[93] Cytosolic non-phosphorylated ezrin represents a dormant form of ezrin,[99] while phosphorylated (active) ezrin regulates the cytoskeletal dynamics by cross-linking the actin filaments to the plasma membrane. The membrane localization of ezrin plays a pivotal role in the progression of malignant diseases.[100,101] Ezrin has been shown to support cancer dissemination by several mechanisms including changes in proliferative signaling, cell motility, and anoikis resistance. Ezrin probably regulates these processes through the influence on the expression levels of E-cadherin and CD44. The suppression of ezrin active state also sensitized cells to anti-cancer drugs.[99,100]

Nevertheless, the tumor-suppressive effect of cisplatin through cytoskeletal remodeling is probably context dependent. Some types of cancer cells such as prostate cancer cells and ovarian cancer cells surviving cisplatin treatment are stiffer with a cytoskeleton composed of long actin stress fibers created due to RhoA activation.[92,102] These stiffer cells are more resistant but less aggressive showing a significant decrease in cell migration, invasion, and formation of colonies.[92] On the other hand, cisplatin-treated melanoma cells exhibit a significant decrease in cell stiffness and the up-regulation of FAK-mediated and MAPK-mediated signaling promoting the malignancy, chemoresistance, and invasiveness of these cells.[94,103] Accordingly, cisplatin is not effective against melanoma.[103] We can speculate that highly aggressive cells need to be rather more pliable[89,90,104,105] with low levels of Rho GTPase activation and low stress fiber formation,[88,106,107] because tumor cells with high deformability and low RhoA activation preferentially engulf and outcompete neighboring cells with low deformability in heterogeneous cancer cell populations.[107] Accordingly, changes in cell stiffness may be a promising marker of the cisplatin treatment response of individual cancer cells.

Other cellular targets and binding sites of cisplatin

Recent studies suggest that cisplatin has multiple cellular targets beyond DNA. Cisplatin could inactivate essential RNA molecules such as the RNA components of ribosomes and splicing machineries, catalytic RNA motifs, or tRNA and also membrane lipids, proteins, and cellular enzymes.[27,108–112] 65–98% of cisplatin molecules have formed adducts with proteins such as hemoglobin, serum albumin, transferrin, metallothionein, and glutathione after 24 h of cisplatin administration to the patient.[113,114] However, it is possible that upon several ligand exchange reactions, cisplatin may exchange the chlorido/aquo and both ammine ligands with nucleophilic amino acids of a protein and may form a Pt-adduct while causing functional disruption of the targeted molecules. Accordingly, cisplatin reduced telomerase activity in a specific and concentration-dependent manner in human testicular tumor cells, while bleomycin, doxorubicin, methotrexate, or melphalan had no effect. The telomerase inhibition could be a decisive reason for cisplatin's success in the therapy of testicular cancer.[115,116]

In addition to telomerase, there are other cancer-associated proteins identified as cisplatin binding sites, including high-affinity copper transporter 1 (hCtr1/*SLC31A1*), non-muscle myosin IIA (Myosin-9, *MYH9*), heat shock protein 90 (HSP90), endoplasmin (GRP-94/*HSP90B1*), valosin-containing protein (*VCP*), or β_2-microglobulin (*B2M*).[117–119]

High-affinity copper transporter 1 functions as homotrimer having three transmembrane domains forming a pore through the plasma membrane. hCTr1 mediates cellular copper uptake, but has also been shown to be involved in the cellular import of cisplatin.[120–122] Whereas Cu triggers internalization of hCTr1 from the plasma membrane, cisplatin does not.[123] Conversely, cisplatin may stabilize hCTr1 trimeric pores by spanning the methionine-rich motifs of the interacting hCtr1 subunits facilitating the cisplatin cross through the membrane into the cytoplasm.[119] Cisplatin also induces the expression of hCtr1 in time- and concentration-dependent manners. Abundance and multimeric state of hCtr1 in various tumors reflect their response to cisplatin.[124] Other cisplatin binding sites were found on copper chaperone Cox17, copper chaperone Atox-1 and the Cu-ATPase ATP7B.[114,224] The ability of cisplatin to form protein dimers was observed in the case of Atox-1. Since Atox-1 is transferred to the nucleus after copper exposure, it may be also involved in the transport of cisplatin to DNA. Furthermore, cisplatin bound to Atox-1 may alter copper homeostasis and cellular defense against oxidative stress, therefore providing an alternative route to cell killing.[225] Cox17 seems to be involved in cisplatin transfer to mitochondria.[114] Cisplatin bound to ATP7B stimulates its catalytic phosphorylation with the formation of a transient acyl-phosphate intermediate (which is unstable at basic pH, but stable at acidic conditions).[224] Hyperphosphorylation is associated with the transfer of ATP7B from the trans-Golgi network to vesicles.[226]

Another cisplatin-binding protein, whose activity could be changed by cisplatin is myosin-9.[117] Myosin-9 is a class II non-muscle myosin that regulates cell motility and maintains an equilibrium between the actomyosin and microtubule systems.[125] Elevated myosin-9 expression was associated with poor prognosis, lymph node positivity, and advanced tumor stage in oesophagal squamous cell carcinoma patients.[126] Myosin-9 was also found as a key protein for the invasion of MCF-7 breast cancer cells.[127] On the other hand, p53 failed to accumulate and/or remain in the nucleus in the absence of endogenous myosin-9 activity in squamous-cell carcinoma cells.[128] Myosin-9 also interacts with the cytoplasmic tail of Golgi glycosyltransferases and creates a force for Golgi disorganization, which is typical for colon and prostate cancer progression. Myosin-9 is more stably associated with the Golgi of androgen-refractory prostate cancer cells than androgen-sensitive cells

and inhibition of myosin-9 restored compact Golgi morphology in prostate and colon cancer cells.[129] Myosin-9 inhibitors (such as cisplatin) could also block the development of tolerogenic dendritic cells.[130]

Cisplatin also binds heat shock protein 90 (HSP90) and inhibits its activity.[117] HSP90 is a molecular chaperone that is generally thought to function in assisting protein folding, and degradation of misfolded proteins. Nevertheless, a critical role of HSP90 in cancer was also revealed. HSP90 can protect mutated and overexpressed oncoproteins from degradation, facilitating cancer cell survival.[131] HSP90 was also identified as an inhibitor of the mammalian pro-apoptotic protein inositol hexakisphosphate kinase 2 (IP6K2) in cancer cells. Consequently, HSP90 inhibition should be cytotoxic for cancer cells.[132] Furthermore, HSP90 inhibition caused by cisplatin halts adipogenesis and differentiation of adipocytes.[133,134] Adipocytes secrete a great number of pro-inflammatory adipokines, which support tumorigenesis and metastasis.[135] Also, the adipocyte mediated conversion of androgens to estrogen contributes to the development of endometrial cancer.[136] Cisplatin binds to the C-domain and N-domain of the human HSP90 and inhibits HSP90 chaperone activity.[137,138] Because the HSP90 N-domain is the binding site of the aryl hydrocarbon receptor (AhR), AhR is dissociated from the HSP90 chaperone complex in the presence of cisplatin and is degraded through the 26S proteasome. AhR is a transcription factor and induces an enzyme of the cytochrome P450 family, CYP1A1. In the presence of cisplatin, the CYP1A1 mRNA level was strongly reduced.[139] CYP1A1 was shown to regulate breast cancer proliferation and survival, and its knockdown decreased colony formation and cell proliferation, and increased apoptosis associated with a reduction of survival.[140] HSP90 is stable as a dimer; however, oncogene-induced stress, such as MYC hyperactivation, can lead to chaperone oligomerization and hyper-connectivity. The oligomerization may activate functions that are normally silent including NF-κB signaling and autophagy. Cisplatin could disrupt oligomerization by binding to HSP90 and impair the formation of signaling loops in cancer cells that enable resistance to kinase inhibitors.[141]

Another cisplatin binding protein is GRP-94 (HSP90B1), the HSP90-like chaperone functioning in the lumen of the endoplasmic reticulum.[117] An elevated level of GRP-94 has been reported in many types of cancer such as breast cancer,[142] lung cancer,[143] esophageal adenocarcinoma,[144] and colon, and gastric cancer.[145,146] GRP94 overexpression is probably involved in the migration and proliferation of cancer cells.[147]

Cisplatin further binds valosin-containing protein (VCP; or p97). VCP is an ATPase belonging to the AAA family which is involved in the ubiquitin/proteasome degradation pathways.[148] VCP influences both increased cell proliferation and the attenuation of cell death in cancer cells by regulating NF-κB signaling.[149] High VCP expression in tumor tissue was correlated with poor prognosis in patients with non-small cell lung carcinoma, hepatocellular carcinoma, gastric carcinoma, follicular thyroid and prostate cancer.[150–154]

Cisplatin binding sites also contain β_2-microglobulin. β_2-microglobulin is a component of major histocompatibility complex class 1 molecules and can act as a growth factor and signaling molecule inducing epithelial to mesenchymal transition in cancer.[155] β_2-microglobulin expression increases during the progression of many human cancers such as breast cancer,[156] prostate cancer,[157] lung cancer,[158] or colon cancer.[159] β_2-microglobulin was also proved as a proaging factor that impairs cognitive functions and neurogenesis.[160] Inhibition of β_2-microglobulin improved radiation sensitivity in prostate cancer cells.[161]

Other important cisplatin binding sites were found on cytochrome c, calmodulin, insulin, ribonuclease A, cytochrome c oxidase, insulin growth factor, α_2-macroglobulin, α_1-anti-trypsin, apolipoprotein A1 and A2, superoxide dismutase, specificity protein 1 (SP1), or on ribosomal protein L5.[114,117,162–164] Furthermore, cisplatin binds to the CXXC motif of proteins containing a ferrodoxin-like fold.[165] Cisplatin is also able to induce the formation of higher oligomers of proteins via crosslinking. The ability of cisplatin to form protein dimers was observed in the case of human serum albumin and is suggested for insulin.[114] Furthermore, acute inhibition of mechanosensitive transporters and channels such as Na^+/H^+ exchanger NHE-1 and K^+ channel TREK-1 (KCNK2) was observed after cisplatin treatment.[28] TREK-1 is abundantly expressed in the PC-3 and LNCaP prostate cancer cell lines but is not detectable in healthy prostate epithelial cells. The overexpression of TREK-1 resulted in a significant increase in cell proliferation in normal prostate epithelial cells and Chinese hamster ovary cells.[166] TREK-1 overexpression was also related to shorter castration resistance free survival in prostate cancer patients.[167] Cisplatin also interacts with proteins that comprise high-mobility-group domains, such as upstream binding factor (UBF), and in this way influences ribosomal RNA transcription by RNA polymerase I. Cisplatin causes a redistribution of UBF, TATA-binding protein (TBP), TBP-associated factors for RNA polymerase I, and RNA polymerase I. Consequently, cisplatin blocks the synthesis of ribosomal RNA, while the activity of RNA polymerase II stays intact.[168] Furthermore, clinically relevant concentrations of cisplatin inhibit MEK1 and MEK2 activity.[165] MEK1 and MEK2 are protein kinases that are the gatekeepers of ERK1/2 activity.[169] Many types of tumor cells exhibit hyperactivation of ERK, and a range of MEK inhibitors are in late-stage clinical trials.[170] Moreover, cisplatin can inhibit the Na^+/K^+-ATPase (NKA).[171] Several reports suggest that the alpha subunits of the NKA could be interesting anti-cancer targets.[172,173]

In conclusion, cisplatin has a pleiotropic effect on cellular proteins significantly affecting their conformation and function and takes part in the disruption of rRNA synthesis, which is stimulated in proliferating cells. Cisplatin can also influence the transport of amino acids, which are the basic building units of proteins.[174] As some cancer cells are auxotrophic for special amino acids, the inhibition of essential amino acid transporters by cisplatin may be an important part of the clinical success of cisplatin as well as the inhibition of key oncoproteins. Nevertheless, in the above-mentioned studies, cisplatin or cisplatin derivatives were usually prepared by challenging the drug with one purified protein. This is not a realistic situation because cisplatin is simultaneously challenged with a huge variety of different

proteins in a real organism. Consequently, the biological actions of cisplatin will be most probably the result of thousands of cisplatin–protein interactions and their functional consequences. Competitive binding experiments can give valuable insight into the selectivity of platinum-based drugs with mixtures of small molecules, proteins or peptides and oligonucleotides.[227]

Cisplatin and the immune system

According to the FDA prescribing information (https://www.drugs.com/pro/cisplatin.html), platinum concentrations in tumors after cisplatin treatment are usually somewhat lower than the concentrations in the organ where a tumor is located. Consequently, some effect exceeding simple damage of tumor cells should be considered. Recent studies suggest that an important part of the antitumor effect of cisplatin occurs through mechanisms counteracting cancer immune evasion.[175,176] It is well known that an immune escape of tumor cells is associated with the major histocompatibility complex class I (MHC-I) down-regulation and the capacity to induce upregulation of MHC class I cell surface expression is a critical step in the tumor rejection.[177] Some studies have recently demonstrated that cisplatin may upregulate the tumor cells' MHC-I expression and may boost CD8+ T cell-mediated anti-cancer immunity.[178–181] Such MHC class I recovery might well synergize with some forms of immunotherapy.[177,178,182] Interestingly, cisplatin chemotherapy broadened the range of tumor antigens recognized by cytotoxic CD8+ T cells.[183] The cancer immune editing of the host's immune system represents one of the major mechanisms by which tumors evade anti-cancer immunity. The cancer immune editing includes T cell anergy, regulatory T cells and their immune suppressive mediators, and systemic defects of antigen presenting cells. The ability of the immune system to fight against tumor cells is highly dependent on the accumulation and activation of immune effector cells.[184] Some studies suggest that low-dose cisplatin could promote the accumulation of antigen presenting cells such as CD11c+ dendritic cells in tumor loci[185] and support the recruitment and proliferation of immune effector cells such as M1 macrophages, tumor-specific CD8+ T cells,[181,186] and cytokine-induced killer cells.[187,188] Cisplatin can also activate murine peritoneal macrophages to the tumoricidal state[189] and cisplatin-treated monocytes enhance the proliferation of CD4+ T cells by the increased production of IFN-β. No such effect was seen in dexamethasone, doxorubicin, or irinotecan-treated monocytes.[190] Cisplatin can also enhance the immuno-stimulatory potential of dendritic cells (DCs) and decrease the immunosuppressive capability of tumor cells.[191] This immuno-modulatory activity is based on the inhibition of STAT6-mediated expression of co-inhibitory molecule PD-L2. Decreased PD-L2 expression led to the increased activation and proliferation of T cells by DCs and enhanced recognition of tumor cells by T cells.[192] Cisplatin also sensitizes tumor cells to attack of cytotoxic T cells.[193] This attack may be mediated by the up-regulation of mannose-6-phosphate receptors on the surface of tumor cells, which makes the tumor cells sensitive to granzyme B,[194] or by

enhanced expression of death receptor Fas/CD95 on the cancer cells.[195] Stimulation of the anti-cancer immune response is also mediated by the exposure of calreticulin, which is a dominant pro-phagocytic signal, on the surface of the cancer cells facilitating their uptake by dendritic cells and the following presentation of tumor-associated antigens to T lymphocytes.[196] In contrast to oxaliplatin, cisplatin probably fails to induce the translocation of calreticulin to the cell surface.[196] Nevertheless, the calreticulin effect is counterbalanced by CD47 in multiple human cancers[197] and a significant reduction in CD47 surface expression occurs after cisplatin treatment.[198] The enhanced expression of the CD47 molecule on cancer cells has been found in many cancers, including malignant blood tumors.[199]

Cisplatin is also able to modulate immune-suppressive milieu of tumor tissues. Treatment with cisplatin significantly reduced the levels of myeloid-derived suppressor cells (MDSCs) and regulatory T cells (Tregs) in the tumor microenvironment.[181,182,186–188,200] Inflammatory mediators including cytokines can participate in tumor progression, as the important component of the tumor microenvironment, inflammatory mediators including cytokines can participate in tumor promotion and progression. Cisplatin inhibits the growth, migration, and invasion of cervical cancer cells by downregulating the IL-17E/IL-17RB pathway[201] and enhances the tumoricidal activity of bone marrow-derived macrophages through the production of extracellular and membrane-associated interleukin-1 (IL-1) and tumor necrosis factor (TNF-α).[189] Furthermore, cisplatin-treated phytohemagglutinin-stimulated human peripheral blood lymphocytes displayed enhanced IL-2, IL-2R, IFN-γ and TNF-α mRNA levels compared to non-treated controls.[202] IL-1 is known to be required for tumor eradication mediated by tumor-specific Th1 cells and was also shown to synergize with IFN-γ for induction of tumoricidal activity in tumor-infiltrating macrophages.[203] Simultaneous administration of TNF-α with IFN-γ resulted in synergistic effects manifested by the retardation of tumor growth[204] and local combined treatments with IL-1 and IL-2 can induce T cell-mediated anti-cancer effects.[205]

In conclusion, cisplatin promotes the antigen presentation and function of effector immune cells while simultaneously counteracting numerous immune-suppressive mechanisms which stay behind cancer immune evasion. Although cisplatin does not induce immunogenic cell death per se, which is probably caused by the lack of calreticulin exposure after cisplatin treatment, cisplatin could still potentiate immunogenic cell death by coadministration with another kind of therapy, such as radiotherapy. Radiotherapy is a potent inducer of calreticulin exposure and combining cisplatin with induced calreticulin exposure consequently leads to immunogenic cell death.[175,196]

Cisplatin and the microbiome

In the previous chapter, we have shown that cisplatin may exert its anti-cancer effect by influencing the immune system. Some studies indicate that the ROS required for platinum toxicity *in vivo* is mostly derived from tumor-associated inflammatory

cells.[206] Recently, it was shown that anti-cancer immunity could also be significantly influenced by the intervention of the intestinal microbiota.[207,208] Compared with controls with a normal gut microbiome, the antibiotic-treated and germ-free mice reacted poorly to immunotherapy and chemotherapy by cisplatin. It is possible that cisplatin influences gut microbes to make immune cells ready to produce reactive oxygen species (ROS), which then kill tumor cells.[209] Accordingly, the absence of gut microbiota in mice was shown to prevent the paracrine production of ROS by tumor-infiltrating myeloid cells.[206] Conversely, administration of antibiotic-treated mice with *Lactobacillus acidophilus* renews the cisplatin anti-cancer effect and restores some of the cisplatin-induced inflammatory gene expression that is observed in ordinarily raised mice.[210] The ROS production in intra-tumor myeloid cells after platinum treatment seems to be managed by signaling through myeloid differentiation primary response 88 (*MYD88*)-associated innate immune receptors also known as pattern recognition receptors (PRRs) which detect molecules typical for the pathogens.[206,211] Microbes highly influence the effect of cisplatin, but this effect is two-sided. Cisplatin can also modify proliferation and the resulting effect of microbes. It was shown that cisplatin protects macrophages from lysis by *Bacillus anthracis* lethal toxin (LT).[212] Cisplatin also inhibits protein splicing in *Mycobacteria* by decreasing the activation of inteins. In addition to *M. tuberculosis*, self-splicing inteins are critical proteins in *Mycobacterium leprae*, *Coxiella burnetii*, and *Cryptococcus neoformans*. Moreover, cisplatin is a potent inhibitor of RecA intein splicing and DNA gyrase in *Escherichia coli*.[213,214] It has been shown that *Escherichia coli* (B2 phylogenetic group) promotes the pro-tumoral activities of macrophages in colon cancer by inducing sustained COX-2 expression.[215] Furthermore, *E. coli* (B2 phylogenetic group) harbours the pks island (pks+ *E. coli*) coding colibactin.[216] Colibactin is a bacterial genotoxin promoting colon tumor growth by inducing a senescence-associated secretory phenotype while simultaneously making the epithelial cells that line the gut more prone to DNA damage.[217] Colonization of mice with the pks+ strain of *E. coli* was sufficient to drive tumorigenesis, whereas germ-free mice were protected,[218] hence inhibition of *E. coli* by cisplatin may also contribute to its treatment effect.

Conclusion

Cisplatin is one of the most effective anti-cancer drugs extensively used for the cure of different types of neoplasms (ovarian, head and neck, lung, breast, leukaemia, brain, kidney, and testicular cancers). Generally, cisplatin is known as a cytotoxic drug which kills cancer cells by damaging DNA, inhibiting mitosis, and triggering cell death. However, other interesting mechanisms should be considered such as immunomodulation and interference in the communication between the tumor cells and their microenvironment. Cisplatin can also change the mechanical properties of cancer cells and significantly encroach on cancer cell metabolism. Recently the modulating effect of cisplatin on the intestinal microbiome was also

proved. Uncovering of the cellular pathways that could be influenced by cisplatin may provide us with an important clue for designing new cancer treatment strategies by finding new potential targets for therapeutic intervention. The mechanisms of cisplatin action in the context of the whole body are weakly studied in humans and need further elucidation and deep cooperation between biologists, chemists and clinicians. Study of cisplatin may also benefit from competitive binding experiments and from global omics studies which can give valuable insight into the non-DNA binding sites of cisplatin.

List of abbreviations

AhR	Aryl hydrocarbon receptor
ASMase/SMPD1	Acid sphingomyelinase
Atox-1	Antioxidant 1 copper chaperone
ATP	Adenosine triphosphate
B2M	β_2-Microglobulin
BID	BH3-interacting domain death agonist
CA2	Cytoplasmic carbonic anhydrase 2
CAIX/CA9	Carbonic anhydrase 9
CCNB1	Cyclin B1
CD47	Cluster of differentiation 47
CD95	Cluster of differentiation 95; fas receptor, also known as apoptosis antigen 1
CDK1	Cyclin-dependent kinase 1
CHOP/DDIT3	CCAAT-enhancer-binding protein homologous protein
Cl current	Chloride current
Cox17	Cytochrome *c* oxidase copper chaperone
CSCs	Cancer stem cells
CYP1A1	Cytochrome P450, family 1, subfamily A, polypeptide 1
DCs	Dendritic cells
ER	Endoplasmic reticulum
ERK	Extracellular signal-regulated kinase
EZR	Ezrin
FAK	Focal adhesion kinase
GLUT-1/SLC2A1	Glucose transporters 1
GLUT-4/SLC2A4	Glucose transporters 4
GRP-78/HSPA5	Glucose regulated-protein 78
GRP-94/HSP90B1	Heat shock protein 90 kDa beta member 1 also known as endoplasmin
hCtr1/SLC31A1	High affinity copper transporter 1
HSP90	Heat shock protein 90
IFN	Interferon
IFN-β	Interferon beta
IL	Interleukin
IP6K2	Inositol hexakisphosphate kinase 2
LDH	Lactate dehydrogenase
LDHB	Lactate dehydrogenase B
MAPK	Mitogen-activated protein kinase
MDSC	Myeloid-derived suppressor cells
MEK	Mitogen-activated protein kinase kinase
MHC-I	Histocompatibility complex class I

mtDNA	Mitochondrial DNA
MYC	Myelocytomatosis proto-oncogene
MYD88	Myeloid differentiation primary response 88
MYH9	Non-muscle myosin IIA
NAC	N-Acetyl cysteine
NBC	Sodium bicarbonate cotransporter family
NBC2/SLC4A5	Sodium bicarbonate cotransporter, member 5
NBCn1 (NBC3/SLC4A7)	
	Sodium bicarbonate cotransporter, member 7
NHE-1/SLC9A1	Na^+/H^+ exchanger 1
NKA	Na^+/K^+-ATPase
P2Y receptors	Purinergic G protein-coupled receptors
PDI	Disulfide isomerase
PDK1	Pyruvate dehydrogenase kinase
PD-L2	Programmed death ligand-2
PFK	Phosphofructokinase
pH_i	Intracellular pH
RhoA	Ras homolog gene family, member A
ROS	Reactive oxygen species
SLC22	Solute carrier family 22
SLC9	Solute carrier family 9
SP1	Specificity protein 1
STAT6	Signal transducer and activator of transcription 6
TBP	TATA-binding protein
TCA cycle	Tricarboxylic acid cycle
TNF	Tumor necrosis factor
Tregs	Regulatory T cells
TREK-1/KCNK2	Potassium two pore domain channel subfamily K member 2
UBF	Upstream binding factor
UPR	Unfolded protein response
VCP	Valosin-containing protein
XIAP	X-Chromosome-linked inhibitor of apoptosis protein

Authors' contributions

MR review design, writing; JB writing, mechanobiology section; MF writing, cisplatin targets; JG pathway analyses, illustrations; MM review design.

Funding

Conflicts of interest

None declared.

References

1 S. Dasari and P. B. Tchounwou, Cisplatin in cancer therapy: molecular mechanisms of action, *Eur. J. Pharmacol.*, 2014, **740**, 364–378.
2 L. Kelland, The resurgence of platinum-based cancer chemotherapy, *Nat. Rev. Cancer*, 2007, **7**, 573–584.
3 L. H. Einhorn, Curing metastatic testicular cancer, *Proc. Natl. Acad. Sci. U. S. A.*, 2002, **99**, 4592–4595.
4 M. D. Hall, M. Okabe, D. W. Shen, X. J. Liang and M. M. Gottesman, The role of cellular accumulation in determining sensitivity to platinum-based chemotherapy, *Annu. Rev. Pharmacol. Toxicol.*, 2008, **48**, 495–535.
5 E. Batlle and H. Clevers, Cancer stem cells revisited, *Nat. Med.*, 2017, **23**, 1124.
6 W. Chen, J. Dong, J. Haiech, M.-C. Kilhoffer and M. Zeniou, Cancer Stem Cell Quiescence and Plasticity as Major Challenges in Cancer Therapy, *Stem Cells Int.*, 2016, **2016**, 16.
7 I. Baccelli, A. Schneeweiss, S. Riethdorf, A. Stenzinger, A. Schillert, V. Vogel, C. Klein, M. Saini, T. Bauerle, M. Wallwiener, T. Holland-Letz, T. Hofner, M. Sprick, M. Scharpff, F. Marme, H. P. Sinn, K. Pantel, W. Weichert and A. Trumpp, Identification of a population of blood circulating tumor cells from breast cancer patients that initiates metastasis in a xenograft assay, *Nat. Biotechnol.*, 2013, **31**, 539–544.
8 J. L. Dembinski and S. Krauss, Characterization and functional analysis of a slow cycling stem cell-like subpopulation in pancreas adenocarcinoma, *Clin. Exp. Metastasis*, 2009, **26**, 611–623.
9 J. R. Masters and B. Koberle, Curing metastatic cancer: lessons from testicular germ-cell tumours, *Nat. Rev. Cancer*, 2003, **3**, 517–525.
10 S. J. Reshkin, M. R. Greco and R. A. Cardone, Role of pH(i), and proton transporters in oncogene-driven neoplastic transformation, *Philos. Trans. R. Soc., B*, 2014, **369**, 20130100.
11 B. A. Webb, M. Chimenti, M. P. Jacobson and D. L. Barber, Dysregulated pH: a perfect storm for cancer progression, *Nat. Rev. Cancer*, 2011, **11**, 671–677.
12 S. Fais, G. Venturi and B. Gatenby, Microenvironmental acidosis in carcinogenesis and metastases: new strategies in prevention and therapy, *Cancer Metastasis Rev.*, 2014, **33**, 1095–1108.
13 C. Corbet and O. Feron, Tumour acidosis: from the passenger to the driver's seat, *Nat. Rev. Cancer*, 2017, **17**, 577–593.
14 W. Doppler, R. Jaggi and B. Groner, Induction of v-mos and activated Ha-ras oncogene expression in quiescent NIH 3T3 cells causes intracellular alkalinisation and cell-cycle progression, *Gene*, 1987, **54**, 147–153.
15 N. Hagag, J. C. Lacal, M. Graber, S. Aaronson and M. V. Viola, Microinjection of ras p21 induces a rapid rise in intracellular pH, *Mol. Cell. Biol.*, 1987, **7**, 1984–1988.
16 S. J. Reshkin, A. Bellizzi, S. Caldeira, V. Albarani, I. Malanchi, M. Poignee, M. Alunni-Fabbroni, V. Casavola and M. Tommasino, Na^+/H^+ exchanger-dependent intracellular

alkalinization is an early event in malignant transformation and plays an essential role in the development of subsequent transformation-associated phenotypes, *FASEB J.*, 2000, **14**, 2185–2197.

17 J. Pouyssegur, A. Franchi, G. Lallemain and S. Paris, cytoplasmic pH, a key determinant of growth factor-induced DNA-synthesis in quiescent fibroblasts, *FEBS Lett.*, 1985, **190**, 115–119.

18 L. K. Putney and D. L. Barber, Na-H exchange-dependent increase in intracellular pH times G(2)/M entry and transition, *J. Biol. Chem.*, 2003, **278**, 44645–44649.

19 C. Sellier, J. F. Bodart, S. Flament, F. Baert, J. Gannon and J. P. Vilain, Intracellular acidification delays hormonal G2/M transition and inhibits G2/M transition triggered by thiophosphorylated MAPK in Xenopus oocytes, *J. Cell. Biochem.*, 2006, **98**, 287–300.

20 F. Kuwata, N. Suzuki, K. Otsuka, M. Taguchi, Y. Sasai, H. Wakino, M. Ito, S. Ebihara and K. Suzuki, Enzymatic regulation of glycolysis and gluconeogenesis in rabbit periodontal ligament under various physiological pH conditions, *J. Nihon Univ. Sch. Dent.*, 1991, **33**, 81–90.

21 R. J. Gay, R. B. McComb and G. N. Bowers, Jr., Optimum reaction conditions for human lactate dehydrogenase isoenzymes as they affect total lactate dehydrogenase activity, *Clin. Chem.*, 1968, **14**, 740–753.

22 P. Miao, S. L. Sheng, X. G. Sun, J. J. Liu and G. Huang, Lactate Dehydrogenase A in Cancer: A Promising Target for Diagnosis and Therapy, *IUBMB Life*, 2013, **65**, 904–910.

23 R. Liu, J. Cao, X. Gao, J. Zhang, L. Wang, B. Wang, L. Guo, X. Hu and Z. Wang, *Overall survival of cancer patients with serum lactate dehydrogenase greater than 1000 IU/L*, 2016.

24 H. J. Park, J. C. Lyons, T. Ohtsubo and C. W. Song, Acidic environment causes apoptosis by increasing caspase activity, *Br. J. Cancer*, 1999, **80**, 1892–1897.

25 M. F. Counis and A. Torriglia, Acid DNases and their interest among apoptotic endonucleases, *Biochimie*, 2006, **88**, 1851–1858.

26 M. V. Shirmanova, I. N. Druzhkova, M. M. Lukina, V. V. Dudenkova, N. I. Ignatova, L. B. Snopova, V. I. Shcheslavskiy, V. V. Belousov and E. V. Zagaynova, Chemotherapy with cisplatin: insights into intracellular pH and metabolic landscape of cancer cells in vitro and in vivo, *Sci. Rep.*, 2017, **7**, 8911.

27 A. Rebillard, X. Tekpli, O. Meurette, O. Sergent, G. LeMoigne-Muller, L. Vernhet, M. Gorria, M. Chevanne, M. Christmann, B. Kaina, L. Counillon, E. Gulbins, D. Lagadic-Gossmann and M. T. Dimanche-Boitrel, Cisplatin-induced apoptosis involves membrane fluidification via inhibition of NHE1 in human colon cancer cells, *Cancer Res.*, 2007, **67**, 7865–7874.

28 N. Milosavljevic, C. Duranton, N. Djerbi, P. H. Puech, P. Gounon, D. Lagadic-Gossmann, M. T. Dimanche-Boitrel, C. Rauch, M. Tauc, L. Counillon and M. Poet, Nongenomic Effects of Cisplatin: Acute Inhibition of Mechanosensitive Transporters and Channels without Actin Remodeling, *Cancer Res.*, 2010, **70**, 7514–7522.

29 Z. H. Huang and Y. G. Huang, The change of intracellular pH is involved in the cisplatin-resistance of human lung

adenocarcinoma A549/DDP cells, *Cancer Invest.*, 2005, **23**, 26–32.

30 Q. Chau and D. J. Stewart, Cisplatin efflux, binding and intracellular pH in the HTB56 human lung adenocarcinoma cell line and the E-8/0.7 cisplatin-resistant variant, *Cancer Chemother. Pharmacol.*, 1999, **44**, 193–202.

31 T. Murakami, I. Shibuya, T. Ise, Z. S. Chen, S. Akiyama, M. Nakagawa, H. Izumi, T. Nakamura, K. Matsuo, Y. Yamada and K. Kohno, Elevated expression of vacuolar proton pump genes and cellular pH in cisplatin resistance, *Int. J. Cancer*, 2001, **93**, 869–874.

32 B. K. Grillo-Hill, C. Choi, M. Jimenez-Vidal and D. L. Barber, Increased H+ Efflux is Sufficient to Induce Dysplasia and Necessary for Viability with Oncogene Expression, *eLife*, 2015, **4**, e03270.

33 A. Kulshrestha, G. K. Katara, J. Ginter, S. Pamarthy, S. A. Ibrahim, M. K. Jaiswal, C. Sandulescu, R. Periakaruppan, J. Dolan, A. Gilman-Sachs and K. D. Beaman, Selective inhibition of tumor cell associated Vacuolar-ATPase 'a2' isoform overcomes cisplatin resistance in ovarian cancer cells, *Mol. Oncol.*, 2016, **10**, 789–805.

34 J. L. Bryant, R. G. Gieling, S. L. Meredith, T. J. Allen, L. Walker, B. A. Telfer, C. T. Supuran, K. J. Williams and A. White, Novel carbonic anhydrase IX-targeted therapy enhances the anti-tumour effects of cisplatin in small cell lung cancer, *Int. J. Cancer*, 2018, **142**, 191–201.

35 K. Xu, X. Mao, M. Mehta, J. Cui, C. Zhang, F. Mao and Y. Xu, Elucidation of How Cancer Cells Avoid Acidosis through Comparative Transcriptomic Data Analysis, *PLoS One*, 2013, **8**, e71177.

36 S. Parkkila, Significance of pH regulation and carbonic anhydrases in tumour progression and implications for diagnostic and therapeutic approaches, *BJU Int.*, 2008, **101**, 16–21.

37 H. H. Sigurosson, C. W. Olesen, R. Dybboe, G. Lauritzen and S. F. Pedersen, Constitutively Active ErbB2 Regulates Cisplatin-Induced Cell Death in Breast Cancer Cells via Pro- and Antiapoptotic Mechanisms, *Mol. Cancer Res.*, 2015, **13**, 63–77.

38 Y. Kato, S. Ozawa, C. Miyamoto, Y. Maehata, A. Suzuki, T. Maeda and Y. Baba, Acidic extracellular microenvironment and cancer, *Cancer Cell Int.*, 2013, **13**, 89.

39 I. Parolini, C. Federici, C. Raggi, L. Lugini, S. Palleschi, A. De Milito, C. Coscia, E. Iessi, M. Logozzi, A. Molinari, M. Colone, M. Tatti, M. Sargiacomo and S. Fais, Microenvironmental pH is a key factor for exosome traffic in tumor cells, *J. Biol. Chem.*, 2009, **284**, 34211–34222.

40 I. San-Millan and G. A. Brooks, Reexamining cancer metabolism: lactate production for carcinogenesis could be the purpose and explanation of the Warburg Effect, *Carcinogenesis*, 2017, **38**, 119–133.

41 X. Qin, S. Yu, L. Zhou, M. Shi, Y. Hu, X. Xu, B. Shen, S. Liu, D. Yan and J. Feng, Cisplatin-resistant lung cancer cell-derived exosomes increase cisplatin resistance of recipient cells in exosomal miR-100-5p-dependent manner, *Int. J. Nanomed.*, 2017, **12**, 3721–3733.

42 X. Xiao, S. R. Yu, S. C. Li, J. Z. Wu, R. Ma, H. X. Cao, Y. L. Zhu and J. F. Feng, Exosomes: Decreased Sensitivity of Lung Cancer A549 Cells to Cisplatin, *PLoS One*, 2014, **9**, e89534.

43 M. A. Fuertes, C. Alonso and J. M. Pérez, Biochemical Modulation of Cisplatin Mechanisms of Action: Enhancement of Antitumor Activity and Circumvention of Drug Resistance, *Chem. Rev.*, 2003, **103**, 645–662.

44 K. Kohno, K.-Y. Wang, M. Takahashi, T. Kurita, Y. Yoshida, M. Hirakawa, Y. Harada, A. Kuma, H. Izumi and S. Matsumoto, Mitochondrial Transcription Factor A and Mitochondrial Genome as Molecular Targets for Cisplatin-Based Cancer Chemotherapy, *Int. J. Mol. Sci.*, 2015, **16**, 19836–19850.

45 F. M. Santandreu, P. Roca and J. Oliver, Uncoupling protein-2 knockdown mediates the cytotoxic effects of cisplatin, *Free Radical Biol. Med.*, 2010, **49**, 658–666.

46 Y.-M. Choi, H.-K. Kim, W. Shim, M. A. Anwar, J.-W. Kwon, H.-K. Kwon, H. J. Kim, H. Jeong, H. M. Kim, D. Hwang, H. S. Kim and S. Choi, Mechanism of Cisplatin-Induced Cytotoxicity Is Correlated to Impaired Metabolism Due to Mitochondrial ROS Generation, *PLoS One*, 2015, **10**, e0135083.

47 A. S. Tan, J. W. Baty, L. F. Dong, A. Bezawork-Geleta, B. Endaya, J. Goodwin, M. Bajzikova, J. Kovarova, M. Peterka, B. Yan, E. A. Pesdar, M. Sobol, A. Filimonenko, S. Stuart, M. Vondrusova, K. Kluckova, K. Sachaphibulkij, J. Rohlena, P. Hozak, J. Truksa, D. Eccles, L. M. Haupt, L. R. Griffiths, J. Neuzil and M. V. Berridge, Mitochondrial genome acquisition restores respiratory function and tumorigenic potential of cancer cells without mitochondrial DNA, *Cell Metab.*, 2015, **21**, 81–94.

48 J. Lu, M. Tan and Q. Cai, The Warburg effect in tumor progression: Mitochondrial oxidative metabolism as an anti-metastasis mechanism, *Cancer Lett.*, 2015, **356**, 156–164.

49 C. Jose, N. Bellance and R. Rossignol, Choosing between glycolysis and oxidative phosphorylation: a tumor's dilemma?, *Biochim. Biophys. Acta*, 2011, **1807**, 552–561.

50 A. Pasto, C. Bellio, G. Pilotto, V. Ciminale, M. Silic-Benussi, G. Guzzo, A. Rasola, C. Frasson, G. Nardo, E. Zulato, M. O. Nicoletto, M. Manicone, S. Indraccolo and A. Amadori, Cancer stem cells from epithelial ovarian cancer patients privilege oxidative phosphorylation, and resist glucose deprivation, *Oncotarget*, 2014, **5**, 4305–4319.

51 W. Yu, Y. Chen, J. Dubrulle, F. Stossi, V. Putluri, A. Sreekumar, N. Putluri, D. Baluya, S. Y. Lai and V. C. Sandulache, Cisplatin generates oxidative stress which is accompanied by rapid shifts in central carbon metabolism, *Sci. Rep.*, 2018, **8**, 4306.

52 C. Balut, M. VandeVen, S. Despa, I. Lambrichts, M. Ameloot, P. Steels and I. Smets, Measurement of cytosolic and mitochondrial pH in living cells during reversible metabolic inhibition, *Kidney Int.*, 2008, **73**, 226–232.

53 T. F. Sergeeva, M. V. Shirmanova, O. A. Zlobovskaya, A. I. Gavrina, V. V. Dudenkova, M. M. Lukina, K. A. Lukyanov and E. V. Zagaynova, Relationship between intracellular pH, metabolic co-factors and caspase-3 activation in cancer cells during apoptosis, *Biochim. Biophys. Acta*, 2017, **1864**, 604–611.

54 M. Manerba, L. Di Ianni, L. Fiume, M. Roberti, M. Recanatini and G. Di Stefano, Lactate dehydrogenase inhibitors sensitize lymphoma cells to cisplatin without enhancing the drug effects on immortalized normal lymphocytes, *Eur. J. Pharm. Sci.*, 2015, **74**, 95–102.

55 A. L. Stark, A. G. Madian, S. W. Williams, V. Chen, C. Wing, R. J. Hause, Jr., L. A. To, A. L. Gill, J. L. Myers, L. K. Gorsic, M. F. Ciaccio, K. P. White, R. B. Jones and M. E. Dolan, Identification of Novel Protein Expression Changes Following Cisplatin Treatment and Application to Combination Therapy, *J. Proteome Res.*, 2017, **16**, 4227–4236.

56 R. Wang, K. C. MoYung, Y. J. Zhao and K. Poon, A Mechanism for the Temporal Potentiation of Genipin to the Cytotoxicity of Cisplatin in Colon Cancer Cells, *Int. J. Med. Sci.*, 2016, **13**, 507–516.

57 G. Baffy, Z. Derdak and S. C. Robson, Mitochondrial recoupling: a novel therapeutic strategy for cancer?, *Br. J. Cancer*, 2011, **105**, 469–474.

58 R. Zhou, M. G. Vander Heiden and C. M. Rudin, Genotoxic exposure is associated with alterations in glucose uptake and metabolism, *Cancer Res.*, 2002, **62**, 3515–3520.

59 S. Wang, J. Xie, J. Li, F. Liu, X. Wu and Z. Wang, Cisplatin suppresses the growth and proliferation of breast and cervical cancer cell lines by inhibiting integrin β5-mediated glycolysis, *Am. J. Cancer Res.*, 2016, **6**, 1108–1117.

60 F. Hirschhaeuser, U. G. Sattler and W. Mueller-Klieser, Lactate: a metabolic key player in cancer, *Cancer Res.*, 2011, **71**, 6921–6925.

61 D. M. Brizel, T. Schroeder, R. L. Scher, S. Walenta, R. W. Clough, M. W. Dewhirst and W. Mueller-Klieser, Elevated tumor lactate concentrations predict for an increased risk of metastases in head-and-neck cancer, *Int. J. Radiat. Oncol., Biol., Phys.*, 2001, **51**, 349–353.

62 S. Walenta, M. Wetterling, M. Lehrke, G. Schwickert, K. Sundfor, E. K. Rofstad and W. Mueller-Klieser, High lactate levels predict likelihood of metastases, tumor recurrence, and restricted patient survival in human cervical cancers, *Cancer Res.*, 2000, **60**, 916–921.

63 F. Di Virgilio and E. Adinolfi, Extracellular purines, purinergic receptors and tumor growth, *Oncogene*, 2017, **36**, 293–303.

64 G. Burnstock and F. Di Virgilio, Purinergic signalling and cancer, *Purinergic Signalling*, 2013, **9**, 491–540.

65 X. Yang, L. Zhu, J. Lin, S. Liu, H. Luo, J. Mao, S. Nie, L. Chen and L. Wang, Cisplatin activates volume-sensitive like chloride channels via purinergic receptor pathways in nasopharyngeal carcinoma cells, *J. Membr. Biol.*, 2015, **248**, 19–29.

66 Y. Okada, T. Shimizu, E. Maeno, S. Tanabe, X. Wang and N. Takahashi, Volume-sensitive chloride channels involved in apoptotic volume decrease and cell death, *J. Membr. Biol.*, 2006, **209**, 21–29.

67 S. Cai, T. Zhang, D. Zhang, G. Qiu and Y. Liu, Volume-sensitive chloride channels are involved in cisplatin treatment of osteosarcoma, *Mol. Med. Rep.*, 2015, **11**, 2465–2470.

68 X. J. Min, H. Li, S. C. Hou, W. He, J. Liu, B. Hu and J. Wang, Dysfunction of volume-sensitive chloride channels contributes to cisplatin resistance in human lung adenocarcinoma cells, *Exp. Biol. Med.*, 2011, **236**, 483–491.

69 R. Schafer, F. Sedehizade, T. Welte and G. Reiser, ATP- and UTP-activated P2Y receptors differently regulate proliferation of human lung epithelial tumor cells, *Am. J. Physiol.: Lung Cell. Mol. Physiol.*, 2003, **285**, L376–385.

70 R. Marullo, E. Werner, N. Degtyareva, B. Moore, G. Altavilla, S. S. Ramalingam and P. W. Doetsch, Cisplatin Induces a Mitochondrial-ROS Response That Contributes to Cytotoxicity Depending on Mitochondrial Redox Status and Bioenergetic Functions, *PLoS One*, 2013, **8**, e81162.

71 A. Mandic, J. Hansson, S. Linder and M. C. Shoshan, Cisplatin induces endoplasmic reticulum stress and nucleus-independent apoptotic signaling, *J. Biol. Chem.*, 2003, **278**, 9100–9106.

72 F. Yu, J. Megyesi, R. L. Safirstein and P. M. Price, Involvement of the CDK2-E2F1 pathway in cisplatin cytotoxicity in vitro and in vivo, *Am. J. Physiol. Renal. Physiol.*, 2007, **293**, F52–59.

73 A. Mandic, K. Viktorsson, L. Strandberg, T. Heiden, J. Hansson, S. Linder and M. C. Shoshan, Calpain-Mediated Bid Cleavage and Calpain-Independent Bak Modulation: Two Separate Pathways in Cisplatin-Induced Apoptosis, *Mol. Cell. Biol.*, 2002, **22**, 3003–3013.

74 F. Yu, J. Megyesi and P. M. Price, Cytoplasmic initiation of cisplatin cytotoxicity, *Am. J. Physiol. Renal. Physiol.*, 2008, **295**, F44–52.

75 Y. E. Xu, C. Wang and Z. Li, A new strategy of promoting cisplatin chemotherapeutic efficiency by targeting endoplasmic reticulum stress, *Mol. Clin. Oncol.*, 2014, **2**, 3–7.

76 S. Bernales, M. M. Soto and E. McCullagh, Unfolded protein stress in the endoplasmic reticulum and mitochondria: a role in neurodegeneration, *Front. Aging Neurosci.*, 2012, **4**, 5.

77 N. M. Mhaidat, K. H. Alzoubi, O. F. Khabour, M. N. Banihani, Q. A. Al-Balas and S. Swaidan, GRP78 regulates sensitivity of human colorectal cancer cells to DNA targeting agents, *Cytotechnology*, 2016, **68**, 459–467.

78 S. Gaddameedhi and S. Chatterjee, Association between the unfolded protein response, induced by 2-deoxyglucose, and hypersensitivity to cisplatin: a mechanistic study employing molecular genomics, *J. Cancer Res. Ther.*, 2009, **5**(Suppl 1), S61–66.

79 S. Oyadomari and M. Mori, Roles of CHOP/GADD153 in endoplasmic reticulum stress, *Cell Death Differ.*, 2004, **11**, 381–389.

80 D. Rodriguez, D. Rojas-Rivera and C. Hetz, Integrating stress signals at the endoplasmic reticulum: the BCL-2 protein family rheostat, *Biochim. Biophys. Acta*, 2011, **1813**, 564–574.

81 H. Nishitoh, CHOP is a multifunctional transcription factor in the ER stress response, *J. Biochem.*, 2012, **151**, 217–219.

82 B. G. Hoffstrom, A. Kaplan, R. Letso, R. S. Schmid, G. J. Turmel, D. C. Lo and B. R. Stockwell, Inhibitors of protein disulfide isomerase suppress apoptosis induced by misfolded proteins, *Nat. Chem. Biol.*, 2010, **6**, 900.

83 T. Matsumiya, T. Imaizumi, H. Yoshida, H. Kimura and K. Satoh, Cisplatin inhibits the expression of X-chromosome-linked inhibitor of apoptosis protein in an oral carcinoma cell line, *Oral Oncol.*, 2001, **37**, 296–300.

84 T. Nomura, H. Mimata, M. Yamasaki and Y. Nomura, Cisplatin inhibits the expression of X-linked inhibitor of apoptosis protein in human LNCaP cells, *Urol. Oncol.: Semin. Orig. Invest.*, 2004, **22**, 453–460.

85 H. O. Rashid, R. K. Yadav, H. R. Kim and H. J. Chae, ER stress: autophagy induction, inhibition and selection, *Autophagy*, 2015, **11**, 1956–1977.

86 H. Yu, J. Su, Y. Xu, J. Kang, H. Li, L. Zhang, H. Yi, X. Xiang, F. Liu and L. Sun, p62/SQSTM1 involved in cisplatin resistance in human ovarian cancer cells by clearing ubiquitinated proteins, *Eur. J. Cancer*, 2011, **47**, 1585–1594.

87 Y. Xu, H. Yu, H. Qin, J. Kang, C. Yu, J. Zhong, J. Su, H. Li and L. Sun, Inhibition of autophagy enhances cisplatin cytotoxicity through endoplasmic reticulum stress in human cervical cancer cells, *Cancer Lett.*, 2012, **314**, 232–243.

88 S. Suresh, Biomechanics and biophysics of cancer cells, *Acta Biomater.*, 2007, **3**, 413–438.

89 W. Xu, R. Mezencev, B. Kim, L. Wang, J. McDonald and T. Sulchek, Cell Stiffness Is a Biomarker of the Metastatic Potential of Ovarian Cancer Cells, *PLoS One*, 2012, **7**, e46609.

90 J. Guck, S. Schinkinger, B. Lincoln, F. Wottawah, S. Ebert, M. Romeyke, D. Lenz, H. M. Erickson, R. Ananthakrishnan, D. Mitchell, J. Kas, S. Ulvick and C. Bilby, Optical deformability as an inherent cell marker for testing malignant transformation and metastatic competence, *Biophys. J.*, 2005, **88**, 3689–3698.

91 A. Vassilopoulos, C. Xiao, C. Chisholm, W. Chen, X. Xu, T. J. Lahusen, C. Bewley and C. X. Deng, Synergistic therapeutic effect of cisplatin and phosphatidylinositol 3-kinase (PI3K) inhibitors in cancer growth and metastasis of Brca1 mutant tumors, *J. Biol. Chem.*, 2014, **289**, 24202–24214.

92 M. Raudenska, M. Kratochvilova, T. Vicar, J. Gumulec, J. Balvan, H. Polanska, J. Pribyl and M. Masarik, Cisplatin enhances cell stiffness and decreases invasiveness rate in prostate cancer cells by actin accumulation, *Sci. Rep.*, 2019, **9**, 1660.

93 Y. H. Zeidan, R. W. Jenkins and Y. A. Hannun, Remodeling of cellular cytoskeleton by the acid sphingomyelinase/ceramide pathway, *J. Cell Biol.*, 2008, **181**, 335–350.

94 M. L. Kung, C. W. Hsieh, M. H. Tai, C. H. Weng, D. C. Wu, W. J. Wu, B. W. Yeh, S. L. Hsieh, C. H. Kuo, H. S. Hung and S. Hsieh, Nanoscale characterization illustrates the cisplatin-mediated biomechanical changes of B16-F10 melanoma cells, *Phys. Chem. Chem. Phys.*, 2016, **18**, 7124–7131.

95 P. Kopf-Maier and S. K. Muhlhausen, Changes in the cytoskeleton pattern of tumor cells by cisplatin in vitro, *Chem. – Biol. Interact.*, 1992, **82**, 295–316.

96 K. Boekelheide, M. E. Arcila and J. Eveleth, *cis*-diamminedichloroplatinum(II) (cisplatin) alters microtubule assembly dynamics, *Toxicol. Appl. Pharmacol.*, 1992, **116**, 146–151.

97 S. P. Denker, D. C. Huang, J. Orlowski, H. Furthmayr and D. L. Barber, Direct binding of the Na–H exchanger NHE1 to ERM proteins regulates the cortical cytoskeleton and

cell shape independently of H(+) translocation, *Mol. Cell*, 2000, **6**, 1425–1436.

98 S. Lacour, A. Hammann, S. Grazide, D. Lagadic-Gossmann, A. Athias, O. Sergent, G. Laurent, P. Gambert, E. Solary and M. T. Dimanche-Boitrel, Cisplatin-induced CD95 redistribution into membrane lipid rafts of HT29 human colon cancer cells, *Cancer Res.*, 2004, **64**, 3593–3598.

99 V. Horwitz, B. Davidson, D. Stern, C. G. Tropé, T. Tavor Re'em and R. Reich, Ezrin Is Associated with Disease Progression in Ovarian Carcinoma, *PLoS One*, 2016, **11**, e0162502.

100 Q. Liu, C. T. Harvey, H. Geng, C. H. Xue, V. Chen, T. M. Beer and D. Z. Qian, Malate dehydrogenase 2 confers docetaxel resistance via regulations of JNK signaling and oxidative metabolism, *Prostate*, 2013, **73**, 1028–1037.

101 Z. Chen, A. Fadiel, Y. Feng, K. Ohtani, T. Rutherford and F. Naftolin, Ovarian epithelial carcinoma tyrosine phosphorylation, cell proliferation, and ezrin translocation are stimulated by interleukin 1alpha and epidermal growth factor, *Cancer*, 2001, **92**, 3068–3075.

102 S. Sharma, C. Santiskulvong, J. Rao, J. K. Gimzewski and O. Dorigo, The role of Rho GTPase in cell stiffness and cisplatin resistance in ovarian cancer cells, *Integr. Biol.*, 2014, **6**, 611–617.

103 W. Li and D. W. Melton, Cisplatin regulates the MAPK kinase pathway to induce increased expression of DNA repair gene ERCC1 and increase melanoma chemoresistance, *Oncogene*, 2011, **31**, 2412.

104 Q. Luo, D. Kuang, B. Zhang and G. Song, Cell stiffness determined by atomic force microscopy and its correlation with cell motility, *Biochim. Biophys. Acta*, 2016, **1860**, 1953–1960.

105 O. Thoumine and A. Ott, Comparison of the mechanical properties of normal and transformed fibroblasts, *Biorheology*, 1997, **34**, 309–326.

106 J. Katsantonis, A. Tosca, S. B. Koukouritaki, P. A. Theodoropoulos, A. Gravanis and C. Stournaras, Differences in the G/total actin ratio and microfilament stability between normal and malignant human keratinocytes, *Cell Biochem. Funct.*, 1994, **12**, 267–274.

107 Q. Sun, T. Luo, Y. Ren, O. Florey, S. Shirasawa, T. Sasazuki, D. N. Robinson and M. Overholtzer, Competition between human cells by entosis, *Cell Res.*, 2014, **24**, 1299–1310.

108 D. Rhodes, P. W. Piper and B. F. Clark, Location of a platinum binding site in the structure of yeast phenylalanine transfer RNA, *J. Mol. Biol.*, 1974, **89**, 469–475.

109 S. V. Melnikov, D. Söll, T. A. Steitz and Y. S. Polikanov, Insights into RNA binding by the anticancer drug cisplatin from the crystal structure of cisplatin-modified ribosome, *Nucleic Acids Res.*, 2016, **44**, 4978–4987.

110 D. Colangelo, A. L. Ghiglia, I. Viano, G. Cavigiolio and D. Osella, cis-[Pt(Cl)2(pyridine)(5-SO$_3$H-isoquinoline)] complex, a selective inhibitor of telomerase enzyme, *Biometals*, 2003, **16**, 553–560.

111 E. G. Chapman and V. J. DeRose, Site-specific platinum(II) cross-linking in a ribozyme active site, *J. Am. Chem. Soc.*, 2012, **134**, 256–262.

112 C. M. Che and F. M. Siu, Metal complexes in medicine with a focus on enzyme inhibition, *Curr. Opin. Chem. Biol.*, 2010, **14**, 255–261.

113 R. D. Sandlin, C. J. Whelan, M. S. Bradley and K. M. Williams, Effects of amine ligand bulk and hydrogen bonding on the rate of reaction of platinum(II) diamine complexes with key nucleotide and amino acid residues, *Inorg. Chim. Acta*, 2012, **391**, 135–140.

114 L. Messori and A. Merlino, Cisplatin binding to proteins: a structural perspective, *Coord. Chem. Rev.*, 2016, **315**, 67–89.

115 A. M. Burger, J. A. Double and D. R. Newell, Inhibition of telomerase activity by cisplatin in human testicular cancer cells, *Eur. J. Cancer*, 1997, **33**, 638–644.

116 X. Wu, J. C. Yalowich and B. B. Hasinoff, Cisplatin inhibits the catalytic activity of DNA topoisomerase II by binding to critical protein thiol groups and by binding to DNA, *Cancer Res.*, 2004, **64**, 712.

117 T. Karasawa, M. Sibrian-Vazquez, R. M. Strongin and P. S. Steyger, Identification of cisplatin-binding proteins using agarose conjugates of platinum compounds, *PLoS One*, 2013, **8**, e66220.

118 N. B. Zhang, M. Cui, Y. G. Du, Z. Q. Liu and S. Y. Liu, Exploring the interaction of cisplatin with beta 2-microglobulin: new insights into a chemotherapeutic drug, *RSC Adv.*, 2014, **4**, 2300–2305.

119 Y. Guo, K. Smith and M. J. Petris, Cisplatin stabilizes a multimeric complex of the human Ctr1 copper transporter: requirement for the extracellular methionine-rich clusters, *J. Biol. Chem.*, 2004, **279**, 46393–46399.

120 S. Ishida, J. Lee, D. J. Thiele and I. Herskowitz, Uptake of the anticancer drug cisplatin mediated by the copper transporter Ctr1 in yeast and mammals, *Proc. Natl. Acad. Sci. U. S. A.*, 2002, **99**, 14298–14302.

121 I.-S. Song, N. Savaraj, Z. H. Siddik, P. Liu, Y. Wei, C. J. Wu and M. T. Kuo, Role of human copper transporter Ctr1 in the transport of platinum-based antitumor agents in cisplatin-sensitive and cisplatin-resistant cells, *Mol. Cancer Ther.*, 2004, **3**, 1543–1549.

122 X. Du, X. Wang, H. Li and H. Sun, Comparison between copper and cisplatin transport mediated by human copper transporter 1 (hCTR1), *Metallomics*, 2012, **4**, 679–685.

123 C. Y. Tsai, C. A. Larson, R. Safaei and S. B. Howell, Molecular modulation of the copper and cisplatin transport function of CTR1 and its interaction with IRS-4, *Biochem. Pharmacol.*, 2014, **90**, 379–387.

124 Z. D. Liang, Y. Long, H. H. Chen, N. Savaraj and M. T. Kuo, Regulation of the high-affinity copper transporter (hCtr1) expression by cisplatin and heavy metals, *J. Biol. Inorg. Chem.*, 2014, **19**, 17–27.

125 S. Even-Ram, A. D. Doyle, M. A. Conti, K. Matsumoto, R. S. Adelstein and K. M. Yamada, Myosin IIA regulates cell motility and actomyosin-microtubule crosstalk, *Nat. Cell Biol.*, 2007, **9**, 299–309.

126 Z. K. Xia, Y. C. Yuan, N. Yin, B. L. Yin, Z. P. Tan and Y. R. Hu, Nonmuscle myosin IIA is associated with poor

prognosis of esophageal squamous cancer, *Dis. Esophagus*, 2012, **25**, 427–436.

127 L. Derycke, C. Stove, A. S. Vercoutter-Edouart, O. De Wever, L. Dolle, N. Colpaert, H. Depypere, J. C. Michalski and M. Bracke, The role of non-muscle myosin IIA in aggregation and invasion of human MCF-7 breast cancer cells, *Int. J. Dev. Biol.*, 2011, **55**, 835–840.

128 D. R. Raleigh and D. A. Haas-Kogan, Non-Muscle Myosin IIa Heavy Chain Links Squamous-Cell Carcinoma of the Head and Neck to the DNA Damage Response, *Front. Oncol.*, 2014, **4**, 228.

129 A. Petrosyan, Onco-Golgi: Is Fragmentation a Gate to Cancer Progression?, *Biochem. Mol. Biol. J.*, 2015, **1**, 16.

130 D. E. Cheng, J. Y. Hung, M. S. Huang, Y. L. Hsu, C. Y. Lu, E. M. Tsai, M. F. Hou and P. L. Kuo, Myosin IIa activation is crucial in breast cancer derived galectin-1 mediated tolerogenic dendritic cell differentiation, *Biochim. Biophys. Acta*, 2014, **1840**, 1965–1976.

131 J. Trepel, M. Mollapour, G. Giaccone and L. Neckers, Targeting the dynamic HSP90 complex in cancer, *Nat. Rev. Cancer*, 2010, **10**, 537–549.

132 A. Chakraborty, M. A. Koldobskiy, K. M. Sixt, K. R. Juluri, A. K. Mustafa, A. M. Snowman, D. B. van Rossum, R. L. Patterson and S. H. Snyder, HSP90 regulates cell survival via inositol hexakisphosphate kinase-2, *Proc. Natl. Acad. Sci. U. S. A.*, 2008, **105**, 1134–1139.

133 Y.-H. Chang, H.-W. Liu, T.-Y. Chu, Y.-T. Wen, R.-K. Tsai and D.-C. Ding, Cisplatin-Impaired Adipogenic Differentiation of Adipose Mesenchymal Stem Cells, *Cell Transplant.*, 2017, **26**, 1077–1087.

134 M. T. Nguyen, P. Csermely and C. Sőti, Hsp90 chaperones PPARγ and regulates differentiation and survival of 3T3-L1 adipocytes, *Cell Death Differ.*, 2013, **20**, 1654–1663.

135 C. Y. Yeung, A. W. Tso, A. Xu, Y. Wang, Y. C. Woo, T. H. Lam, S. V. Lo, C. H. Fong, N. M. Wat, J. Woo, B. M. Cheung and K. S. Lam, Pro-inflammatory adipokines as predictors of incident cancers in a Chinese cohort of low obesity prevalence in Hong Kong, *PLoS One*, 2013, **8**, e78594.

136 K. M. Nieman, I. L. Romero, B. Van Houten and E. Lengyel, Adipose tissue and adipocytes supports tumorigenesis and metastasis, *Biochim. Biophys. Acta*, 2013, **1831**, 1533–1541.

137 R. Ishida, Y. Takaoka, S. Yamamoto, T. Miyazaki, M. Otaka, S. Watanabe, A. Komatsuda, H. Wakui, K. Sawada, H. Kubota and H. Itoh, Cisplatin differently affects amino terminal and carboxyl terminal domains of HSP90, *FEBS Lett.*, 2008, **582**, 3879–3883.

138 H. Itoh, M. Ogura, A. Komatsuda, H. Wakui, A. B. Miura and Y. Tashima, A novel chaperone-activity-reducing mechanism of the 90-kDa molecular chaperone HSP90, *Biochem. J.*, 1999, **343**(Pt 3), 697–703.

139 E. Sasaki-Kudoh, I. Kudo, Y. Kakizaki, M. Hosaka, S. Ikeda, S. Uemura, E. Grave, S. Togashi, T. Sugawara, H. Shimizu and H. Itoh, Cisplatin Inhibits AhR Activation, *Am. J. Mol. Biol.*, 2018, **8**, 69–82.

140 M. Rodriguez and D. A. Potter, CYP1A1 regulates breast cancer proliferation and survival, *Mol. Cancer Res.*, 2013, **11**, 780–792.

141 S. Joshi, T. Wang, T. L. S. Araujo, S. Sharma, J. L. Brodsky and G. Chiosis, Adapting to stress—chaperome networks in cancer, *Nat. Rev. Cancer*, 2018, **18**, 562–575.

142 L. Bini, B. Magi, B. Marzocchi, F. Arcuri, S. Tripodi, M. Cintorino, J. C. Sanchez, S. Frutiger, G. Hughes, V. Pallini, D. F. Hochstrasser and P. Tosi, Protein expression profiles in human breast ductal carcinoma and histologically normal tissue, *Electrophoresis*, 1997, **18**, 2832–2841.

143 Q. Wang, L. An, Y. Chen and S. Yue, Expression of endoplasmic reticulum molecular chaperon GRP94 in human lung cancer tissues and its clinical significance, *Chin. Med. J.*, 2002, **115**, 1615–1619.

144 X. Chen, Y. Ding, C. G. Liu, S. Mikhail and C. S. Yang, Overexpression of glucose-regulated protein 94 (Grp94) in esophageal adenocarcinomas of a rat surgical model and humans, *Carcinogenesis*, 2002, **23**, 123–130.

145 X. P. Wang, F. R. Qiu, G. Z. Liu and R. F. Chen, Correlation between clinicopathology and expression of heat shock protein 70 and glucose-regulated protein 94 in human colonic adenocarcinoma, *World J. Gastroenterol.*, 2005, **11**, 1056–1059.

146 X. P. Wang, Q. X. Wang and X. P. Ying, Correlation between clinicopathology and expression of heat shock protein 72 and glycoprotein 96 in human gastric adenocarcinoma, *Tohoku J. Exp. Med.*, 2007, **212**, 35–41.

147 N. Dejeans, C. Glorieux, S. Guenin, R. Beck, B. Sid, R. Rousseau, B. Bisig, P. Delvenne, P. Buc Calderon and J. Verrax, Overexpression of GRP94 in breast cancer cells resistant to oxidative stress promotes high levels of cancer cell proliferation and migration: implications for tumor recurrence, *Free Radical Biol. Med.*, 2012, **52**, 993–1002.

148 R. M. Dai and C. C. Li, Valosin-containing protein is a multiubiquitin chain-targeting factor required in ubiquitinproteasome degradation, *Nat. Cell Biol.*, 2001, **3**, 740–744.

149 T. Asai, Y. Tomita, S. Nakatsuka, Y. Hoshida, A. Myoui, H. Yoshikawa and K. Aozasa, VCP (p97) regulates NFkappaB signaling pathway, which is important for metastasis of osteosarcoma cell line, *Jpn. J. Cancer Res.*, 2002, **93**, 296–304.

150 Y. Tsujimoto, Y. Tomita, Y. Hoshida, T. Kono, T. Oka, S. Yamamoto, N. Nonomura, A. Okuyama and K. Aozasa, Elevated expression of valosin-containing protein (p97) is associated with poor prognosis of prostate cancer, *Clin. Cancer Res.*, 2004, **10**, 3007–3012.

151 S. Yamamoto, Y. Tomita, S. Nakamori, Y. Hoshida, H. Nagano, K. Dono, K. Umeshita, M. Sakon, M. Monden and K. Aozasa, Elevated Expression of Valosin-Containing Protein (p97) in Hepatocellular Carcinoma Is Correlated With Increased Incidence of Tumor Recurrence, *J. Clin. Oncol.*, 2003, **21**, 447–452.

152 S. Yamamoto, Y. Tomita, Y. Hoshida, S. Takiguchi, Y. Fujiwara, T. Yasuda, M. Yano, S. Nakamori, M. Sakon, M. Monden and K. Aozasa, Expression Level of Valosin-Containing Protein Is Strongly Associated With Progression and Prognosis of Gastric Carcinoma, *J. Clin. Oncol.*, 2003, **21**, 2537–2544.

153 C. W. Valle, T. Min, M. Bodas, S. Mazur, S. Begum, D. Tang and N. Vij, Critical role of VCP/p97 in the pathogenesis and

progression of non-small cell lung carcinoma, *PLoS One*, 2011, **6**, e29073.

154 S. Yamamoto, Y. Tomita, T. Uruno, Y. Hoshida, Y. Qiu, N. Iizuka, I. Nakamichi, A. Miyauchi and K. Aozasa, Increased expression of valosin-containing protein (p97) is correlated with disease recurrence in follicular thyroid cancer, *Ann. Surg. Oncol.*, 2005, **12**, 925–934.

155 S. Josson, T. Nomura, J.-T. Lin, W.-C. Huang, D. Wu, H. E. Zhau, M. Zayzafoon, M. N. Weizmann, M. Gururajan and L. W. K. Chung, β2-Microglobulin induces epithelial to mesenchymal transition and confers cancer lethality and bone metastasis in human cancer cells, *Cancer Res.*, 2011, **71**, 2600–2610.

156 C. Teasdale, A. M. Mander, R. Fifield, J. W. Keyser, R. G. Newcombe and L. E. Hughes, Serum beta2-microglobulin in controls and cancer patients, *Clin. Chim. Acta*, 1977, **78**, 135–143.

157 M. Gross, I. Top, I. Laux, J. Katz, J. Curran, C. Tindell and D. Agus, Beta-2-microglobulin is an androgen-regulated secreted protein elevated in serum of patients with advanced prostate cancer, *Clin. Cancer Res.*, 2007, **13**, 1979–1986.

158 J. Shuster, P. Gold and M. D. Poulik, beta 2-microglogulin levels in cancerous and other disease states, *Clin. Chim. Acta*, 1976, **67**, 307–313.

159 D. G. Ward, S. Nyangoma, H. Joy, E. Hamilton, W. Wei, C. Tselepis, N. Steven, M. J. Wakelam, P. J. Johnson, T. Ismail and A. Martin, Proteomic profiling of urine for the detection of colon cancer, *Proteome Sci.*, 2008, **6**, 19.

160 L. K. Smith, Y. He, J. S. Park, G. Bieri, C. E. Snethlage, K. Lin, G. Gontier, R. Wabl, K. E. Plambeck, J. Udeochu, E. G. Wheatley, J. Bouchard, A. Eggel, R. Narasimha, J. L. Grant, J. Luo, T. Wyss-Coray and S. A. Villeda, Beta2-microglobulin is a systemic pro-aging factor that impairs cognitive function and neurogenesis, *Nat. Med.*, 2015, **21**, 932–937.

161 S. Josson, Y. Matsuoka, M. Gururajan, T. Nomura, W.-C. Huang, X. Yang, J.-t. Lin, R. Bridgman, C.-Y. Chu, P. A. Johnstone, M. Zayzafoon, P. Hu, H. Zhau, D. Berel, A. Rogatko and L. W. K. Chung, Inhibition of β2-Microglobulin/ Hemochromatosis Enhances Radiation Sensitivity by Induction of Iron Overload in Prostate Cancer Cells, *PLoS One*, 2013, **8**, e68366.

162 S. K. Weidt, C. L. Mackay, P. R. Langridge-Smith and P. J. Sadler, Platination of superoxide dismutase with cisplatin: tracking the ammonia ligands using Fourier transform ion cyclotron resonance mass spectrometry (FT-ICR MS), *Chem. Commun.*, 2007, 1719–1721.

163 N. V. Dolgova, C. Yu, J. P. Cvitkovic, M. Hodak, K. H. Nienaber, K. L. Summers, J. J. H. Cotelesage, J. Bernholc, G. A. Kaminski, I. J. Pickering, G. N. George and O. Y. Dmitriev, Binding of Copper and Cisplatin to Atox1 Is Mediated by Glutathione through the Formation of Metal-Sulfur Clusters, *Biochemistry*, 2017, **56**, 3129–3141.

164 Y. Guo, K. Smith and M. J. Petris, Cisplatin stabilizes a multimeric complex of the human Ctr1 copper transporter - Requirement for the extracellular methionine-rich clusters, *J. Biol. Chem.*, 2004, **279**, 46393–46399.

165 T. Yamamoto, I. F. Tsigelny, A. W. Gotz and S. B. Howell, Cisplatin inhibits MEK1/2, *Oncotarget*, 2015, **6**, 23510–23522.

166 I. Voloshyna, A. Besana, M. Castillo, T. Matos, I. B. Weinstein, M. Mansukhani, R. B. Robinson, C. Cordon-Cardo and S. J. Feinmark, TREK-1 is a novel molecular target in prostate cancer, *Cancer Res.*, 2008, **68**, 1197–1203.

167 G.-M. Zhang, F.-N. Wan, X.-J. Qin, D.-L. Cao, H.-L. Zhang, Y. Zhu, B. Dai, G.-H. Shi and D.-W. Ye, Prognostic significance of the TREK-1 K2P potassium channels in prostate cancer, *Oncotarget*, 2015, **6**, 18460–18468.

168 P. Jordan and M. Carmo-Fonseca, Cisplatin inhibits synthesis of ribosomal RNA in vivo, *Nucleic Acids Res.*, 1998, **26**, 2831–2836.

169 R. Roskoski, Jr., MEK1/2 dual-specificity protein kinases: structure and regulation, *Biochem. Biophys. Res. Commun.*, 2012, **417**, 5–10.

170 C. J. Caunt, M. J. Sale, P. D. Smith and S. J. Cook, MEK1 and MEK2 inhibitors and cancer therapy: the long and winding road, *Nat. Rev. Cancer*, 2015, **15**, 577–592.

171 N. Sakakibara, K. Suzuki, H. Kaneta, Y. Yoshimura, Y. Deyama, A. Matsumoto and H. Fukuda, Inhibition of Na^+,K^+-ATPase by cisplatin and its recovery by 2-mercaptoethanol in human squamous cell carcinoma cells, *Anti-Cancer Drugs*, 1999, **10**, 203–212.

172 T. Mijatovic, L. Ingrassia, V. Facchini and R. Kiss, Na^+/K^+-ATPase alpha subunits as new targets in anticancer therapy, *Expert Opin. Ther. Targets*, 2008, **12**, 1403–1417.

173 K. Alevizopoulos, T. Calogeropoulou, F. Lang and C. Stournaras, Na^+/K^+ ATPase inhibitors in cancer, *Curr. Drug Targets*, 2014, **15**, 988–1000.

174 K. J. Scanlon, R. L. Safirstein, H. Thies, R. B. Gross, S. Waxman and J. B. Guttenplan, Inhibition of amino-acid-transport by cis-diamminedichloroplatinum(II) derivatives in L1210 murine leukemia-cells, *Cancer Res.*, 1983, **43**, 4211–4215.

175 S. V. Hato, A. Khong, I. J. M. de Vries and W. J. Lesterhuis, Molecular Pathways: The Immunogenic Effects of Platinum-Based Chemotherapeutics, *Clin. Cancer Res.*, 2014, **20**, 2831–2837.

176 A. R. de Biasi, J. Villena-Vargas and P. S. Adusumilli, Cisplatin-Induced Antitumor Immunomodulation: A Review of Preclinical and Clinical Evidence, *Clin. Cancer Res.*, 2014, **20**, 5384–5391.

177 F. Garrido, N. Aptsiauri, E. M. Doorduijn, A. M. Garcia Lora and T. van Hall, The urgent need to recover MHC class I in cancers for effective immunotherapy, *Curr. Opin. Immunol.*, 2016, **39**, 44–51.

178 S. R. Gameiro, J. A. Caballero and J. W. Hodge, Defining the Molecular Signature of Chemotherapy-Mediated Lung Tumor Phenotype Modulation and Increased Susceptibility to T-Cell Killing, *Cancer Biother. Radiopharm.*, 2012, **27**, 23–35.

179 Y. Nio, N. Hirahara, Y. Minari, C. Iguchi, K. Yamasawa, T. Toga and K. Tamura, Induction of tumor-specific anti-tumor immunity after chemotherapy with cisplatin in mice bearing MOPC-104E plasmacytoma by modulation of MHC

178

expression on tumor surface, *Anticancer Res.*, 2000, **20**, 3293–3299.

180 S. Ohtsukasa, S. Okabe, H. Yamashita, T. Iwai and K. Sugihara, Increased expression of CEA and MHC class I in colorectal cancer cell lines exposed to chemotherapy drugs, *J. Cancer Res. Clin. Oncol.*, 2003, **129**, 719–726.

181 C.-W. Tseng, C.-F. Hung, R. D. Alvarez, C. Trimble, W. K. Huh, D. Kim, C.-M. Chuang, C.-T. Lin, Y.-C. Tsai, L. He, A. Monie and T. C. Wu, Pretreatment with Cisplatin Enhances E7-Specific CD8(+) T-Cell-Mediated Antitumor Immunity Induced by DNA Vaccination, *Clin. Cancer Res.*, 2008, **14**, 3185–3192.

182 Z. G. Fridlender, J. Sun, S. Singhal, V. Kapoor, G. Cheng, E. Suzuki and S. M. Albelda, Chemotherapy delivered after viral immunogene therapy augments antitumor efficacy *via* multiple immune-mediated mechanisms, *Mol. Ther.*, 2010, **18**, 1947–1959.

183 C. Jackaman, D. Majewski, S. A. Fox, A. K. Nowak and D. J. Nelson, Chemotherapy broadens the range of tumor antigens seen by cytotoxic CD8(+) T cells in vivo, *Cancer Immunol. Immunother.*, 2012, **61**, 2343–2356.

184 D. S. Vinay, E. P. Ryan, G. Pawelec, W. H. Talib, J. Stagg, E. Elkord, T. Lichtor, W. K. Decker, R. L. Whelan, H. Kumara, E. Signori, K. Honoki, A. G. Georgakilas, A. Amin, W. G. Helferich, C. S. Boosani, G. Guha, M. R. Ciriolo, S. Chen, S. I. Mohammed, A. S. Azmi, W. N. Keith, A. Bilsland, D. Bhakta, D. Halicka, H. Fujii, K. Aquilano, S. S. Ashraf, S. Nowsheen, X. Yang, B. K. Choi and B. S. Kwon, Immune evasion in cancer: mechanistic basis and therapeutic strategies, *Semin. Cancer Biol.*, 2015, **35**(Suppl), S185–S198.

185 S. Y. Lee, T. H. Kang, J. Knoff, Z. Huang, R. S. Soong, R. D. Alvarez, C. F. Hung and T. C. Wu, Intratumoral injection of therapeutic HPV vaccinia vaccine following cisplatin enhances HPV-specific antitumor effects, *Cancer Immunol. Immunother.*, 2013, **62**, 1175–1185.

186 C. L. Chang, Y. T. Hsu, C. C. Wu, Y. Z. Lai, C. Wang, Y. C. Yang, T. C. Wu and C. F. Hung, Dose-dense chemotherapy improves mechanisms of antitumor immune response, *Cancer Res.*, 2013, **73**, 119–127.

187 J. Chen, X. Huang, G. Huang, Y. Chen, L. Chen and H. Song, Preconditioning chemotherapy with cisplatin enhances the antitumor activity of cytokine-induced killer cells in a murine melanoma model, *Cancer Biother. Radiopharm.*, 2012, **27**, 210–220.

188 X. Huang, Y. T. Chen, H. Z. Song, G. C. Huang and L. B. Chen, Cisplatin pretreatment enhances anti-tumor activity of cytokine-induced killer cells, *World J. Gastroenterol.*, 2011, **17**, 3002–3011.

189 A. Suresh and A. Sodhi, Production of interleukin-1 and tumor necrosis factor by bone marrow-derived macrophages: effect of cisplatin and lipopolysaccharide, *Immunol. Lett.*, 1991, **30**, 93–100.

190 J. Hu, J. Kinn, A. A. Zirakzadeh, A. Sherif, G. Norstedt, A. C. Wikstrom and O. Winqvist, The effects of chemotherapeutic drugs on human monocyte-derived dendritic cell differentiation and antigen presentation, *Clin. Exp. Immunol.*, 2013, **172**, 490–499.

191 W. J. Lesterhuis, C. J. Punt, S. V. Hato, D. Eleveld-Trancikova, B. J. Jansen, S. Nierkens, G. Schreibelt, A. de Boer, C. M. Van Herpen, J. H. Kaanders, J. H. van Krieken, G. J. Adema, C. G. Figdor and I. J. de Vries, Platinum-based drugs disrupt STAT6-mediated suppression of immune responses against cancer in humans and mice, *J. Clin. Invest.*, 2011, **121**, 3100–3108.

192 S. V. Hato, I. J. de Vries and W. J. Lesterhuis, STATing the importance of immune modulation by platinum chemotherapeutics, *Oncoimmunology*, 2012, **1**, 234–236.

193 E. S. Bergmann-Leitner and S. I. Abrams, Treatment of human colon carcinoma cell lines with anti-neoplastic agents enhances their lytic sensitivity to antigen-specific CD8+ cytotoxic T lymphocytes, *Cancer Immunol. Immunother.*, 2001, **50**, 445–455.

194 R. Ramakrishnan, D. Assudani, S. Nagaraj, T. Hunter, H. I. Cho, S. Antonia, S. Altiok, E. Celis and D. I. Gabrilovich, Chemotherapy enhances tumor cell susceptibility to CTL-mediated killing during cancer immunotherapy in mice, *J. Clin. Invest.*, 2010, **120**, 1111–1124.

195 K. Sundelin, K. Roberg, R. Grenman and L. Hakansson, Effects of cisplatin, alpha-interferon, and 13-*cis* retinoic acid on the expression of Fas (CD95), intercellular adhesion molecule-1 (ICAM-1), and epidermal growth factor receptor (EGFR) in oral cancer cell lines, *J. Oral Pathol. Med.*, 2007, **36**, 177–183.

196 I. Martins, O. Kepp, F. Schlemmer, S. Adjemian, M. Tailler, S. Shen, M. Michaud, L. Menger, A. Gdoura, N. Tajeddine, A. Tesniere, L. Zitvogel and G. Kroemer, Restoration of the immunogenicity of cisplatin-induced cancer cell death by endoplasmic reticulum stress, *Oncogene*, 2011, **30**, 1147–1158.

197 M. P. Chao, S. Jaiswal, R. Weissman-Tsukamoto, A. A. Alizadeh, A. J. Gentles, J. Volkmer, K. Weiskopf, S. B. Willingham, T. Raveh, C. Y. Park, R. Majeti and I. L. Weissman, Calreticulin is the dominant pro-phagocytic signal on multiple human cancers and is counterbalanced by CD47, *Sci. Transl. Med.*, 2010, **2**, 63ra94.

198 D. W. Vermeer, W. C. Spanos, P. D. Vermeer, A. M. Bruns, K. M. Lee and J. H. Lee, Radiation-induced loss of cell surface CD47 enhances immune-mediated clearance of human papillomavirus-positive cancer, *Int. J. Cancer*, 2013, **133**, 120–129.

199 Y.-R. Xiang and L. Liu, Eating Cancer cells by blocking CD47 signaling: cancer therapy by targeting the innate immune checkpoint, *Cancer Transl. Med.*, 2017, **3**, 200–208.

200 K. Wu, M.-Y. Tan, J.-T. Jiang, X.-Y. Mu, J.-R. Wang, W.-J. Zhou, X. Wang, M.-q. Li, Y.-Y. He and Z.-H. Liu, Cisplatin inhibits the progression of bladder cancer by selectively depleting G-MDSCs: a novel chemoimmunomodulating strategy, *Clin. Immunol.*, 2018, **193**, 60–69.

201 J. Cheng, C. J. Gu, B. Zhang, F. Xie, M. M. Yuan, M. Q. Li and J. J. Yu, Cisplatin inhibits the growth, migration and invasion of cervical cancer cells by down-regulating IL-17E/IL-17RB, *International, J. Clin. Exp. Psychopathol.*, 2017, **10**, 9341–9351.

202 K. Riesbeck, Cisplatin at clinically relevant concentrations enhances interleukin-2 synthesis by human primary blood lymphocytes, *Anticancer Drugs*, 1999, **10**, 219–227.

203 O. A. W. Haabeth, K. B. Lorvik, H. Yagita, B. Bogen and A. Corthay, Interleukin-1 is required for cancer eradication mediated by tumor-specific Th1 cells, *Oncoimmunology*, 2016, **5**, e1039763.

204 W. Lasek, A. Wankowicz, K. Kuc, W. Feleszko, J. Golab, A. Giermasz, W. Wiktor-Jedrzejczak and M. Jakobisiak, Potentiation of antitumor effects of tumor necrosis factor alpha and interferon gamma by macrophage-colony-stimulating factor in a MmB16 melanoma model in mice, *Cancer Immunol. Immunother.*, 1995, **40**, 315–321.

205 F. Belardelli, V. Ciolli, U. Testa, E. Montesoro, D. Bulgarini, E. Proietti, P. Borghi, P. Sestili, C. Locardi and C. Peschle, *et al.*, Anti-tumor effects of interleukin-2 and interleukin-1 in mice transplanted with different syngeneic tumors, *Int. J. Cancer*, 1989, **44**, 1108–1116.

206 N. Iida, A. Dzutsev, C. A. Stewart, L. Smith, N. Bouladoux, R. A. Weingarten, D. A. Molina, R. Salcedo, T. Back, S. Cramer, R.-M. Dai, H. Kiu, M. Cardone, S. Naik, A. K. Patri, E. Wang, F. M. Marincola, K. M. Frank, Y. Belkaid, G. Trinchieri and R. S. Goldszmid, Commensal Bacteria Control Cancer Response to Therapy by Modulating the Tumor Microenvironment, *Science*, 2013, **342**, 967.

207 S. Viaud, R. Daillère, I. G. Boneca, P. Lepage, M. J. Pittet, F. Ghiringhelli, G. Trinchieri, R. Goldszmid and L. Zitvogel, Harnessing the Intestinal Microbiome for Optimal Therapeutic Immunomodulation, *Cancer Res.*, 2014, **74**, 4217.

208 M. Yi, S. Yu, S. Qin, Q. Liu, H. Xu, W. Zhao, Q. Chu and K. Wu, Gut microbiome modulates efficacy of immune checkpoint inhibitors, *J. Hematol. Oncol.*, 2018, **11**, 47.

209 R. Spooner and O. Yilmaz, The role of reactive-oxygen-species in microbial persistence and inflammation, *Int. J. Mol. Sci.*, 2011, **12**, 334–352.

210 Q. F. Gui, H. F. Lu, C. X. Zhang, Z. R. Xu and Y. H. Yang, Well-balanced commensal microbiota contributes to anti-cancer response in a lung cancer mouse model, *Genet. Mol. Res.*, 2015, **14**, 5642–5651.

211 S. Roy and G. Trinchieri, Microbiota: a key orchestrator of cancer therapy, *Nat. Rev. Cancer*, 2017, **17**, 271–285.

212 M. Moayeri, J. F. Wiggins, R. E. Lindeman and S. H. Leppla, Cisplatin inhibition of anthrax lethal toxin, *Antimicrob. Agents Chemother.*, 2006, **50**, 2658–2665.

213 L. Zhang, Y. Zheng, B. Callahan, M. Belfort and Y. Liu, Cisplatin Inhibits Protein Splicing, Suggesting Inteins as Therapeutic Targets in Mycobacteria, *J. Biol. Chem.*, 2011, **286**, 1277–1282.

214 S. Neumann, H. Simon, C. Zimmer and A. Quinones, The antitumor agent cisplatin inhibits DNA gyrase and preferentially induces gyrB gene expression in Escherichia coli, *Biol. Chem.*, 1996, **377**, 731–739.

215 J. Raisch, N. Rolhion, A. Dubois, A. Darfeuille-Michaud and M. A. Bringer, Intracellular colon cancer-associated Escherichia coli promote protumoral activities of human

216 Y. Feng, A. Mannion, C. M. Madden, A. G. Swennes, C. Townes, C. Byrd, R. P. Marini and J. G. Fox, Cytotoxic Escherichia coli strains encoding colibactin and cytotoxic necrotizing factor (CNF) colonize laboratory macaques, *Gut Pathog.*, 2017, **9**, 71.

217 A. Cougnoux, G. Dalmasso, R. Martinez, E. Buc, J. Delmas, L. Gibold, P. Sauvanet, C. Darcha, P. Dechelotte, M. Bonnet, D. Pezet, H. Wodrich, A. Darfeuille-Michaud and R. Bonnet, Bacterial genotoxin colibactin promotes colon tumour growth by inducing a senescence-associated secretory phenotype, *Gut*, 2014, **63**, 1932–1942.

218 J. C. Arthur, E. Perez-Chanona, M. Mühlbauer, S. Tomkovich, J. M. Uronis, T.-J. Fan, B. J. Campbell, T. Abujamel, B. Dogan, A. B. Rogers, J. M. Rhodes, A. Stintzi, K. W. Simpson, J. J. Hansen, T. O. Keku, A. A. Fodor and C. Jobin, Intestinal Inflammation Targets Cancer-Inducing Activity of the Microbiota, *Science*, 2012, **338**, 120–123.

219 J. V. Burda, M. Zeizinger and J. Leszczynski, Hydration process as an activation of trans- and cisplatin complexes in anticancer treatment. DFT and ab initio computational study of thermodynamic and kinetic parameters, *J. Comput. Chem.*, 2005, **26**, 907–914.

220 S. J. Berners-Price, T. A. Frenkiel, U. Frey, J. D. Ranford and P. J. Sadler, Hydrolysis products of cisplatin: pKa determinations via[1H, 15N] NMR spectroscopy, *J. Chem. Soc., Chem. Commun.*, 1992, 789–791.

221 M. Obata, M. Harada, H. Ohi, S. Hirohara, M. Gottchaldt and S. Yano, Extended X-ray absorption fine structure study on reaction of anti-tumor platinum complexes with reduced glutathione, *Chem. Pharm. Bull.*, 2009, **57**, 1107–1109.

222 A. A. Legin, A. Schintlmeister, M. A. Jakupec, M. Galanski, I. Lichtscheidl, M. Wagner and B. K. Keppler, NanoSIMS combined with fluorescence microscopy as a tool for subcellular imaging of isotopically labeled platinum-based anticancer drugs, *Chem. Sci.*, 2014, **5**, 3135–3143.

223 C. R. Centerwall, K. A. Tacka, D. J. Kerwood, J. Goodisman, B. B. Toms, R. L. Dubowy and J. C. Dabrowiak, Modification and uptake of a cisplatin carbonato complex by Jurkat cells, *Mol. Pharmacol.*, 2006, **70**, 348–355.

224 K. Leonhardt, R. Gebhardt, J. Mössner, S. Lutsenko and D. Huster, Functional interactions of Cu-ATPase ATP7B with cisplatin and the role of ATP7B in the resistance of cells to the drug, *J. Biol. Chem.*, 2009, **284**, 7793–7802.

225 Y. Hatori and S. Lutsenko, An expanding range of functions for the copper chaperone/antioxidant protein Atox1, *Antioxid. Redox Signaling*, 2013, **19**, 945–957.

226 M. Y. Bartee, M. Ralle and S. Lutsenko, The loop connecting metal-binding domains 3 and 4 of ATP7B is a target of a kinase-mediated phosphorylation, *Biochemistry*, 2009, **48**, 5573–5581.

227 C. Artner, H. U. Holtkamp, W. Kandioller, C. G. Hartinger, S. M. Meier-Menches and B. K. Keppler, DNA or protein? Capillary zone electrophoresis–mass spectrometry rapidly elucidates metallodrug binding selectivity, *Chem. Commun.*, 2017, **53**, 8002–8005.

5 Concluding remarks

Mechanical properties of cells affect cell migration, adhesion, differentiation and subcellular organelle transport as well as cell metabolic state [82]. These properties are not only related to physiological functions but are also linked to a pathophysiological mechanism of diseases, cancer development in particular. One of the key features of cancer cells is the ability to migrate and invade tissues – cancer spreading, which leads to the development of metastatic tumors in distant organs [83]. More deformable cells are favoured for key cancer spreading processes – extravasation and extravasation [10]. As compared to non-tumor cells, a decrease in stiffness of cancer cells was accordingly described by numerous studies in a spectrum of tumor types [10]. Accordingly, such change of mechanical properties of cancer cells is a promising indicator of malignant potential [19], because it is a direct measurement of the cells` phenotype. This contrasts with a number of molecular markers, which, despite their high predictive value, do not correspond with the actual development of the disease. For instance, although prostatic specific antigen is a powerful diagnostic tool for prostate cancer, its function is not cancer-specific, instead, it is needed for sperm liquefaction.

However, the increase in deformability remains controversial. It is not clear whether all cells or just some subpopulation of cancer cells is softer [84], and how this depends on tumor type and tumor progression. Also, mechanisms leading to cell softening are still not explained satisfactorily.

5.1 Metastatic prostate cells are stiffer

In our lab we studied a prostate cancer model and observed a disagreement with this concept: metastatic cell lines (PC-3 and LNCaP) characteristic by increased aggressiveness *in vitro* and *in vivo* were significantly stiffer than cells derived from the primary tumor (22Rv1) [2]. In a spite of the fact that zinc plays an important role in prostate cancer development, we further developed a zinc-resistant metastatic prostate tumor cells "PC-3-res-50" [85], which demonstrated to be even stiffer (to have higher Young modulus determined by atomic force microscopy, AFM) and even more aggressive, as determined by wound-healing, colony-forming, migration assays and partly by growth speed in animal models and higher levels of glycolysis and respiration[1; 90]. Gene expression profiling of those cells revealed enrichment of pathways associated with stress response, positive regulation of metabolic processes, DNA

repair and cell ageing mediated mostly by RAS signalling. Moreover, our results also suggest a positive correlation between cell stiffness and cell dry mass density as determined by quantitative phase imaging and an association between Caveolin-1 expression and the total stiffness of prostate cancer cells [2]. In prostate cancer cells, an increase of stiffness in more aggressive cells was described similarly in literature [37; 38]. However, as shown by Raudenska et al study, this stiffening was not attributed to the change in actin cytoskeleton network architecture, one of the major factors determining the cell stiffness [2].

5.2   Quantitative imaging in mechanobiology

Atomic force microscopy-based determination of cell mechanical properties, however, provides a single value of modulus per cell – the Young modulus. Cells are however highly complex structures and therefore, the description of their mechanical properties just by a single of few moduli is difficult [10]. Moreover, the obtained value is related to the model used in experimental technique, and experimental conditions (temperature, substrate stiffness, etc.) [104]. Furthermore, Young modulus determined from AFM is typically affected by the rigidity of plasma membrane. Nonetheless, higher deformability of this structure is needed just during a specific moment of metastatic dissemination – during migration in confined spaces and during intravasation and extravasation. Only a set of phenotyping methods provides the full picture of cell mechanics: As shown in Holenstein study, in which a combination of atomic force microscopy, tensile biaxial deformation, real-time deformability, and cell traction was measured using two-dimensional and micropost-based traction force microscopy gave a complex picture of the metastatic potential of osteosarcoma cells [19].

As mechanical properties are closer to the viable phenotype of cancer cells compared to indirect evidence provided by flow cytometry or molecular markers, analysis of cell biomechanics is of great interest in diagnostics. However, technical challenges still exist. Although different techniques could provide similar results, they usually differ in the absolute values of the moduli, even if performed on similar equipment. Standardization of the results is therefore limited. Combination of techniques which work on different scales might therefore be promising [10; 105-107].

In this series of commented articles, we combined atomic force microscopy with quantitative phase microscopy techniques –coherence-controlled holographic microscopy. Although the imaging was not performed in a correlative manner, there was an agreement between AFM and

QPI, which suggest a potential of QPI for fast label-free and non-contact cell mechanopheno-typing. The cellular changes range from cytoskeletal rearrangements on the short scale to alteration of gene expression on the long scale, thereby introducing an error to the measurements [108; 109]. QPI was also used in a microfluidic setup where cells were exposed to shear stress induced by fluid flow. By this approach we directly demonstrate that QPI is also suitable to estimate shear modulus of cells, which is in correlation with Young modulus determined by AFM [86; 87].

The robustness of QPI also opens up new possibilities for the image analysis – usage of machine learning. As the acquisition of large FOV numbers is not possible with AFM, rough metrics can be extracted used for cell classification. Modulus of whole cells or prominent subcellular structures like cell nucleus is *de facto* the only (and the most commonly used) metric. On the other hand, measurement of moduli of subtle subcellular structures on a statistically large enough dataset of live cells is not feasible with AFM. Accordingly, focal adhesion protein-mediated transduction of ECM signals, which is linked with cytoskeletal rearrangements and signalling favouring cancer cell migration, proliferation and survival not necessarily affect whole-cell modulus.

However, cancer cells are highly heterogeneous structures by nature and subcellular strucutres might be hidden in this heterogeneity and therefore may not be observable by naked eye [61]. Accordingly, we used the neural network for localization of subcellular areas, notably nucleus and nucleolus [71].

5.3   Caveolin-1 – the crossroad of mechanics and metabolism?

The transcriptomic screening was performed to identify the molecular basis of the metabolic reprogramming and change of mechanic phenotype. Our results point out particularly to one multifunctional protein – caveolin-1. Our results suggest that CAV1 gene expression correlates with the total stiffness of prostate cancer cells. However, this trend was only observable in the wild-type prostate cancer cells. On the other hand, the establishment of zinc resistance, although associated with increased stiffness, was not associated with further CAV1 expression changes. Changes in expression however might not necessarily correlate with altered caveolin regulation. As shown by Jiu study, caveolin cytoplasmic dynamics is preferentially altered upon vimentin depletion, which serves as a physical barrier for this protein. [110]

CAV1 is a component of plasma membrane structures caveolae and also exists in multiple sub-cellular pools (discussed in chapter 2.3). CAV1 was described to affect cellular metabolism [30],

cell migration and mechanical stress responses [31; 32]. Yet the roles of either CAV1 and the caveolae remains enigmatic either in physiology and in disease. [111]. CAV1 was demonstrated to affect both glycolysis and mitochondrial ATP production. Glycolysis is modulated via insulin and IGF1 receptor through AKT signalling. Caveolin also provides a docking site for glycolytic enzymes. This facilitates increased glucose uptake and lactate output and increased glycolysis, and such mechanism is possibly employed in our metastatic *in vitro* model. CAV1 modulates mitochondria through Ca^{++} signalling and via modulation of cholesterol efflux from mitochondria [28]. The causal connection between CAV1 expression and glycolysis was also shown in advanced colon cancer, where high CAV1 expression increased glucose uptake and ATP production by stimulating glucose transporter 3 (*SLC2A3*) transcription in tumor cells [112]. If CAV1 expression in prostate cancer is associated with dependency on glucose [113], then it provides an attractive prospect of using CAV1 expression levels to identify prostate cancer patients who could benefit from inhibitors of glucose transport and inhibitors of OXPHOS or glycolysis. CAV1 crosstalks with the actin cytoskeleton and therefore contributes to adaptation to mechanical stimuli through mechanosensing [114]. CAV1 regulates actin organisation, actomyosin contraction and focal adhesion stability through Rho signalling [111; 115; 116]. In many cases a linear pattern of CAV1 that co-aligns with actin stress fibres is evident in confocal images. The reasons for this co-alignment are still not completely clear, but some kind of coordination between two tension-controlling systems has been proposed as an explanation [111]. The expression of CAV1 or the presence of CAV1-rich membrane structures caveolae was described predominantly in mechanically stressed cells like endothelial or muscle cells. Accordingly, mechanical stimuli like tension, stretching, shear stress or osmotic swelling was linked with caveolae flattening, which suggest that caveolae and CAV1 act as a buffer system preventing a rupture of plasma membrane [111]. Such fact is possibly employed in aggressive cancer cells, which are exposed to mechanical stress through migration and invasion and such phenomenon was supported by our results. We demonstrated no CAV1 expression in primary prostate cancer cells, which do not induce tumors *in vivo* and pronounced expression in metastasis-derived cells [2]. Inconsistently, zinc-resistance, which was linked with increase in migration and colony-forming capacity was not linked with further CAV1 expression increase. Yet, the role of CAV1 and the caveolae remains enigmatic [111]. According to the EMBO Workshop on Caveolae 2019 [111], several questions need to be addressed either in caveolae physiology as well as in pathology, namely what is the role of non-caveolar CAV1, what are the dynamics of caveolae in different tissues *in vivo* and what is the relationship between exosomes and caveolae[111].

In disease, specifically in the tumor progression, the link between CAV1 and the long-term cellular response to mechanical and metabolic signals still remains unanswered. Specifically, in cancer cells the fact whether CAV1 is a tumor suppressor or oncogene is not straightforward [117-119]. The cellular context is important and changes during cancer progression and between cell types exist [120]. CAV1 expression reflects the actual needs of the cancer cells and therefore this expression can differ during cancer progression [4; 118]. Beyond that, multiple cell types in tumor microenvironment were shown to differ in CAV1 expression. Through this mechanism, a modulation of metabolic symbiosis between populations of cells might be established. As described by Dimmer and colleagues, low-CAV1-expressing cancer-associated fibroblasts were characteristic by lactate production and excretion, thereby supplying nutrients for high-CAV1-expressing cancer cells [4; 26].

Metabolism targeting seems to be an attractive therapeutic target. However, because such mechanisms exist, simplistic strategies, like glycolysis inhibition, fail. To fully understand the role of CAV1 in cancer, more complex models might be needed, and it still remains an exciting area of research.

6 Conclusions

Invasion of cancer cells and metastasis formation is energetically highly demanding process. Increase of mobility and overcoming of mechanical stress during metastasis formation is accompanied by a reinforcement of the cytoskeletal architecture and by changes of cell-cell and ECM-cell interactions. During past decades, key understandings were made to address questions how the cells interact with ECM and how they transduce mechanical signals, however, the aspect of mechanical properties of cancer cells itself is not fully addressed. Accordingly, how the metabolic reprogramming of cancer cells is related to the change of cell mechanical properties remains to be explained. There is a tempting theory that more deformable cells are favoured for metastatic spreading. However, data regarding prostate tumor cells and some other cell types indicate this is not always that straightforward.

Although a panel of approaches exists to describe cell mechanical properties, the results are technique-, model- and experimental-condition dependent. Above that, the metastatic process of cancer cells is complex, and cell biomechanical parameters cannot be reduced to a single value of modulus. Most of the existing mechanophenotyping methods are either low-throughput, low-resolution or invasive, with atomic force microscopy as a typical example. Here we demonstrated potential of quantitative phase imaging for fast label-free and non-contact cell mechanophenotyping. As the acquisition is fast, the generation of large datasets makes it possible to extract complex information from these datasets using machine learning in image analysis. In this habilitation thesis, artificial intelligence was demonstrated to be powerful for image segmentation cellular and as well subcellular structures. Artificial intelligence thus enables, at least to some extent to explain the organelle specificity of a technique primarily showing biophysical and mechanical features of the cells.

7 References

1. GUMULEC, J., M. RAUDENSKA, J. BALVAN, T. VICAR, et al. Label-free quantitative phase imaging: applications for cancer cell mechanobiology studies. In *ASCB EMBO 2019 Meeting.* Washington DC, USA: ASCB, 2019.

2. RAUDENSKA, M., M. KRATOCHVILOVA, T. VICAR, J. GUMULEC, et al. Cisplatin enhances cell stiffness and decreases invasiveness rate in prostate cancer cells by actin accumulation. Scientific Reports, 2019/02/07 2019, 9(1), 1660.

3. SOUSA, B., J. PEREIRA AND J. PAREDES The Crosstalk Between Cell Adhesion and Cancer Metabolism. International Journal of Molecular Sciences, 2019, 20(8), 1933.

4. RAUDENSKA, M., J. GUMULEC, J. BALVAN AND M. MASARIK Caveolin-1 in oncogenic metabolic symbiosis. International Journal of Cancer, 2020, n/a(n/a).

5. BERNSTEIN, B. W. AND J. R. BAMBURG Actin-ATP hydrolysis is a major energy drain for neurons. Journal of Neuroscience, 2003, 23(1), 1-6.

6. PARK, J. S., C. J. BURCKHARDT, R. LAZCANO, L. M. SOLIS, et al. Mechanical regulation of glycolysis via cytoskeleton architecture. Nature, 2020/02/01 2020, 578(7796), 621-626.

7. EIDELMAN, E., J. TWUM-AMPOFO, J. ANSARI AND M. M. SIDDIQUI The Metabolic Phenotype of Prostate Cancer. Frontiers in Oncology, 2017-June-19 2017, 7(131).

8. STEPKA, P., V. VSIANSKY, M. RAUDENSKA, J. GUMULEC, et al. Metabolic and amino acid alterations of the tumor microenvironment. Curr Med Chem, Feb 6 2020.

9. MOEENDARBARY, E. AND A. R. HARRIS Cell mechanics: principles, practices, and prospects. Wiley interdisciplinary reviews. Systems biology and medicine, Sep-Oct 2014, 6(5), 371-388.

10. ALIBERT, C., B. GOUD AND J. B. MANNEVILLE Are cancer cells really softer than normal cells? Biol Cell, 2017, 109(5), 167-189.

11. ROYLANCE, D. *Mechanical Properties of Materials*. Edtion ed. Cambridge: Massachusetts Institute of Technology, 2008.

12. DEVILLE, S. S. AND N. CORDES The Extracellular, Cellular, and Nuclear Stiffness, a Trinity in the Cancer Resistome-A Review. Front Oncol, 2019, 9(1376).

13. COX, T. R. AND J. T. ERLER Remodeling and homeostasis of the extracellular matrix: implications for fibrotic diseases and cancer. Disease Models & Mechanisms, 2011, 4(2), 165-178.

14. YEH, Y.-C., J.-Y. LING, W.-C. CHEN, H.-H. LIN, et al. Mechanotransduction of matrix stiffness in regulation of focal adhesion size and number: reciprocal regulation of caveolin-1 and β1 integrin. Scientific Reports, 2017/11/08 2017, 7(1), 15008.

15. DRIFKA, C. R., A. G. LOEFFLER, K. MATHEWSON, A. KEIKHOSRAVI, et al. Highly aligned stromal collagen is a negative prognostic factor following pancreatic ductal adenocarcinoma resection. Oncotarget, 2016, 7(46).

16. HAMIDI, H. AND J. IVASKA Every step of the way: integrins in cancer progression and metastasis. Nature Reviews Cancer, 2018/09/01 2018, 18(9), 533-548.

17. SURESH, S. Biomechanics and biophysics of cancer cells. Acta biomaterialia, 2007, 3(4), 413-438.

18. WU, P.-H., D. R.-B. AROUSH, A. ASNACIOS, W.-C. CHEN, et al. A comparison of methods to assess cell mechanical properties. Nature Methods, 2018/07/01 2018, 15(7), 491-498.

19.   HOLENSTEIN, C. N., A. HORVATH, B. SCHÄR, A. D. SCHOENENBERGER, et al. The relationship between metastatic potential and in vitro mechanical properties of osteosarcoma cells. Molecular Biology of the Cell, 2019, 30(7), 887-898.

20.   BALVAN, J., J. GUMULEC, M. RAUDENSKA, A. KRIZOVA, et al. Oxidative Stress Resistance in Metastatic Prostate Cancer: Renewal by Self-Eating. Plos One, Dec 15 2015, 10(12).

21.   DAVIES, H. G. AND M. H. WILKINS Interference microscopy and mass determination. Nature, Mar 29 1952, 169(4300), 541.

22.   BARER, R. Refractometry and interferometry of living cells. J Opt Soc Am, Jun 1957, 47(6), 545-56.

23.   LUO, Q., D. KUANG, B. ZHANG AND G. SONG Cell stiffness determined by atomic force microscopy and its correlation with cell motility. Biochim Biophys Acta, 2016, 9(60), 8.

24.   ELDRIDGE, W. J., S. CEBALLOS, T. SHAH, H. S. PARK, et al. Shear Modulus Measurement by Quantitative Phase Imaging and Correlation with Atomic Force Microscopy. Biophysical Journal, 2019/08/20/ 2019, 117(4), 696-705.

25.   VETTORE, L., R. L. WESTBROOK AND D. A. TENNANT New aspects of amino acid metabolism in cancer. British Journal of Cancer, 2020/01/01 2020, 122(2), 150-156.

26.   DIMMER, K. S., B. FRIEDRICH, F. LANG, J. W. DEITMER, et al. The low-affinity monocarboxylate transporter MCT4 is adapted to the export of lactate in highly glycolytic cells. Biochem J, 2000, 1(Pt 1), 219-27.

27.   HUI, S., J. M. GHERGUROVICH, R. J. MORSCHER, C. JANG, et al. Glucose feeds the TCA cycle via circulating lactate. Nature, 2017/11/01 2017, 551(7678), 115-118.

28.   NWOSU, Z. C., M. P. EBERT, S. DOOLEY AND C. MEYER Caveolin-1 in the regulation of cell metabolism: a cancer perspective. Molecular Cancer, 2016/11/16 2016, 15(1), 71.

29.   HA, T.-K. AND S.-G. CHI CAV1/caveolin 1 enhances aerobic glycolysis in colon cancer cells via activation of SLC2A3/GLUT3 transcription. Autophagy, 2012/11/09 2012, 8(11), 1684-1685.

30.   COHEN, A. W., R. HNASKO, W. SCHUBERT AND M. P. LISANTI Role of Caveolae and Caveolins in Health and Disease. Physiological Reviews, 2004, 84(4), 1341-1379.

31.   SINHA, B., D. KÖSTER, R. RUEZ, P. GONNORD, et al. Cells respond to mechanical stress by rapid disassembly of caveolae. Cell, Feb 4 2011, 144(3), 402-13.

32.   NAVARRO, A., B. ANAND-APTE AND M.-O. PARAT A role for caveolae in cell migration. The FASEB Journal, 2004, 18(15), 1801-1811.

33.   CHENG, J. P. X., C. MENDOZA-TOPAZ, G. HOWARD, J. CHADWICK, et al. Caveolae protect endothelial cells from membrane rupture during increased cardiac output. Journal of Cell Biology, 2015, 211(1), 53-61.

34.   LO, H. P., S. J. NIXON, T. E. HALL, B. S. COWLING, et al. The caveolin–cavin system plays a conserved and critical role in mechanoprotection of skeletal muscle. Journal of Cell Biology, 2015, 210(5), 833-849.

35.   PARTON, R. G. AND M. A. DEL POZO Caveolae as plasma membrane sensors, protectors and organizers. Nat Rev Mol Cell Biol, Feb 2013, 14(2), 98-112.

36.   GUMULEC, J., M. MASARIK, S. KRIZKOVA, V. ADAM, et al. Insight to Physiology and Pathology of Zinc(II) Ions and Their Actions in Breast and Prostate Carcinoma. Current Medicinal Chemistry, Nov 2011, 18(33), 5041-5051.

37.   BASTATAS, L., D. MARTINEZ-MARIN, J. MATTHEWS, J. HASHEM, et al. AFM nano-mechanics and calcium dynamics of prostate cancer cells with distinct metastatic potential. Biochim Biophys Acta, 2012, 7(20), 16.

38.   KIM, J. J., B. YIN, C. S. CHRISTUDASS, N. TERADA, et al. Acquisition of paclitaxel resistance is associated with a more aggressive and invasive phenotype in prostate cancer. J Cell Biochem, 2013, 114(6), 1286-93.

39.   GUMULEC, J., J. BALVAN, M. SZTALMACHOVA, M. RAUDENSKA, et al. Cisplatin-resistant prostate cancer model: Differences in antioxidant system, apoptosis and cell cycle. International Journal of Oncology, Mar 2014, 44(3), 923-933.

40.   GUMULEC, J., J. SOCHOR, M. HLAVNA, M. SZTALMACHOVA, et al. Caveolin-1 as a potential high-risk prostate cancer biomarker. Oncology Reports, Mar 2012, 27(3), 831-841.

41.   ABUHATTUM, S., K. KIM, T. M. FRANZMANN, A. EßLINGER, et al. Intracellular Mass Density Increase Is Accompanying but Not Sufficient for Stiffening and Growth Arrest of Yeast Cells. Frontiers in Physics, 2018-November-20 2018, 6(131).

42.   SCARCELLI, G., W. J. POLACHECK, H. T. NIA, K. PATEL, et al. Noncontact three-dimensional mapping of intracellular hydromechanical properties by Brillouin microscopy. Nature Methods, 2015/12/01 2015, 12(12), 1132-1134.

43.   SCHLÜßLER, R., S. MÖLLMERT, S. ABUHATTUM, G. COJOC, et al. Mechanical Mapping of Spinal Cord Growth and Repair in Living Zebrafish Larvae by Brillouin Imaging. Biophysical Journal, 2018/09/04/ 2018, 115(5), 911-923.

44.   VICAR, T., M. RAUDENSKA, J. GUMULEC AND J. BALVAN The Quantitative-Phase Dynamics of Apoptosis and Lytic Cell Death. Scientific Reports, 2020/01/31 2020, 10(1), 1566.

45.   BALVAN, J., A. KRIZOVA, J. GUMULEC, M. RAUDENSKA, et al. Multimodal Holographic Microscopy: Distinction between Apoptosis and Oncosis. Plos One, Mar 24 2015, 10(3).

46.   MIR, M., B. BHADURI, R. WANG, R. ZHU, et al. Chapter 3 - Quantitative Phase Imaging. In E. WOLF ed. *Progress in Optics*. Elsevier, 2012, vol. 57, p. 133-217.

47.   VICAR, T., J. BALVAN, J. JAROS, F. JUG, et al. Cell segmentation methods for label-free contrast microscopy: review and comprehensive comparison. BMC Bioinformatics, June 28 2019, 20(1), 360.

48.   GUO, S.-M., L.-H. YEH, J. FOLKESSON, I. E. IVANOV, et al. Revealing architectural order with quantitative label-free imaging and deep learning. eLife, 2020/07/27 2020, 9, e55502.

49.   KIM, Y. S., S. LEE, J. JUNG, S. SHIN, et al. Combining Three-Dimensional Quantitative Phase Imaging and Fluorescence Microscopy for the Study of Cell Pathophysiology. The Yale journal of biology and medicine, 2018, 91(3), 267-277.

50.   KANG, J. W., N. LUE, C.-R. KONG, I. BARMAN, et al. Combined confocal Raman and quantitative phase microscopy system for biomedical diagnosis. Biomedical optics express, 2011, 2(9), 2484-2492.

51.   KIM, K., R. SCHLÜßLER, T. BECK, S. GIRARDO, et al. *Correlative Brillouin microscopy and optical diffraction tomography for quantitative characterization of mechanical and biophysical properties of biological samples (Conference Presentation)*. Edtion ed.: SPIE, 2020.

52.   JUNG, J., K. KIM, J. YOON AND Y. PARK Hyperspectral optical diffraction tomography. Optics express, 2016, 24(3), 2006-2012.

53.   CHOWDHURY, S., W. J. ELDRIDGE, A. WAX AND J. A. IZATT Structured illumination multimodal 3D-resolved quantitative phase and fluorescence sub-diffraction microscopy. Biomedical optics express, 2017, 8(5), 2496-2518.

54.   FEITH, M., T. VICAR, J. GUMULEC, M. RAUDENSKA, et al. Quantitative Phase Dynamics of Cancer Cell Populations Affected by Blue Light. Applied Sciences-Basel, Apr 2020, 10(7).

55.   LEE, K., K. KIM, J. JUNG, J. HEO, et al. Quantitative phase imaging techniques for the study of cell pathophysiology: from principles to applications. Sensors (Basel, Switzerland), 2013, 13(4), 4170-4191.

56.   LITJENS, G., T. KOOI, B. E. BEJNORDI, A. A. A. SETIO, et al. A survey on deep learning in medical image analysis. Medical Image Analysis, 2017/12/01/ 2017, 42, 60-88.

57.   TING, D. S. W., L. R. PASQUALE, L. PENG, J. P. CAMPBELL, et al. Artificial intelligence and deep learning in ophthalmology. British Journal of Ophthalmology, 2019, 103(2), 167-175.

58.   POPLIN, R., A. V. VARADARAJAN, K. BLUMER, Y. LIU, et al. Prediction of cardiovascular risk factors from retinal fundus photographs via deep learning. Nature Biomedical Engineering, 2018/03/01 2018, 2(3), 158-164.

59.   FALK, T., D. MAI, R. BENSCH, Ö. ÇIÇEK, et al. U-Net: deep learning for cell counting, detection, and morphometry. Nature Methods, 2019/01/01 2019, 16(1), 67-70.

60.   VICAR, T., J. GUMULEC, J. BALVAN AND R. KOLAR. Unpaired image to image translation for microscopic cell images. In *ELMI.* Brno, 2019.

61.   ZARITSKY, A., A. R. JAMIESON, E. S. WELF, A. NEVAREZ, et al. Interpretable deep learning of label-free live cell images uncovers functional hallmarks of highly-metastatic melanoma. bioRxiv, 2020, 2020.05.15.096628.

62.   MAJERCIK, J., M. SPACEK, T. VICAR AND J. GUMULEC. Prostatic Cells Classification using deep learning. In V. NOVÁK. *Proceedings I of the 26th Conference STUDENT EEICT.* Brno: Brno University of Technology, 2020.

63.   ROITSHTAIN, D., L. WOLBROMSKY, E. BAL, H. GREENSPAN, et al. Quantitative phase microscopy spatial signatures of cancer cells. Cytometry Part A, 2017, 91(5), 482-493.

64.   LIU, R., D. K. DEY, D. BOSS, P. MARQUET, et al. Recognition and classification of red blood cells using digital holographic microscopy and data clustering with discriminant analysis. JOSA A, 2011, 28(6), 1204-1210.

65.   PAVILLON, N., A. J. HOBRO, S. AKIRA AND N. I. SMITH Noninvasive detection of macrophage activation with single-cell resolution through machine learning. Proceedings of the National Academy of Sciences, 2018, 115(12), E2676-E2685.

66.   JO, Y., J. JUNG, M.-H. KIM, H. PARK, et al. Label-free identification of individual bacteria using Fourier transform light scattering. Optics express, 2015, 23(12), 15792-15805.

67.   JO, Y., S. PARK, J. JUNG, J. YOON, et al. Holographic deep learning for rapid optical screening of anthrax spores. Science advances, 2017, 3(8), e1700606.

68.   MIRSKY, S. K., I. BARNEA, M. LEVI, H. GREENSPAN, et al. Automated analysis of individual sperm cells using stain-free interferometric phase microscopy and machine learning. Cytometry Part A, 2017, 91(9), 893-900.

69.   GUMULEC, J. AND T. VICAR. Multimodal image segmentation. In *Imaging Modalities for Biological and Preclinical Research: A Compendium, Volume 2.* IOP Publishing, 2021, p. III.4.d-1-III.4.d-12.

70.   VICAR, T., J. CHMELIK, R. JAKUBICEK, L. CHMELIKOVA, et al. Self-Supervised Pretraining for Transferable Quantitative Phase Image Cell Segmentation. bioRxiv, 2021, 2021.05.24.445397.

71.   MAJERCIK, J. AND M. SPACEK. Cell and sub-cellular segmentation in quantitative phase imaging using U-Net. In V. NOVAK. *The 27th Student EEICT 2021.* Brno: Brno University of Technology, Faculty of Electrical Engineering and Communication, 2021, p. 9-12.

72.   VICAR, T., J. GUMULEC, J. BALVAN, M. HRACHO, et al. Label-Free Nuclear Staining Reconstruction in Quantitative Phase Images Using Deep Learning. In *World Congress on Medical Physics and Biomedical Engineering.* Prague: Springer, 2019, p. 239-242.

73.   BERG, S., D. KUTRA, T. KROEGER, C. N. STRAEHLE, et al. ilastik: interactive machine learning for (bio)image analysis. Nature Methods, 2019/12/01 2019, 16(12), 1226-1232.

74.   ARGANDA-CARRERAS, I., V. KAYNIG, C. RUEDEN, K. W. ELICEIRI, et al. Trainable Weka Segmentation: a machine learning tool for microscopy pixel classification. Bioinformatics, 2017, 33(15), 2424-2426.

75.   BOYKOV, Y. AND V. KOLMOGOROV An experimental comparison of min-cut/max-flow algorithms for energy minimization in vision. IEEE Transactions on Pattern Analysis and Machine Intelligence, 2004, 26(9), 1124-1137.

76.   BAHLMANN, C. 2012. Fast radial symmetry detection under affine transformations. In *Proceedings of the Proceedings of the 2012 IEEE Conference on Computer Vision and Pattern Recognition (CVPR)*2012 IEEE Computer Society, 932–939.

77.   PARVATI, K., P. RAO AND M. MARIYA DAS Image segmentation using gray-scale morphology and marker-controlled watershed transformation. Discrete Dynamics in Nature and Society, 2008, 2008.

78.   OUNKOMOL, C., S. SESHAMANI, M. M. MALECKAR, F. COLLMAN, et al. Label-free prediction of three-dimensional fluorescence images from transmitted-light microscopy. Nature Methods, 2018/11/01 2018, 15(11), 917-920.

79.   ZHU, J., T. PARK, P. ISOLA AND A. A. EFROS. Unpaired Image-to-Image Translation Using Cycle-Consistent Adversarial Networks. In *2017 IEEE International Conference on Computer Vision (ICCV)*. 2017, p. 2242-2251.

80.   GULRAJANI, I., F. AHMED, M. ARJOVSKY, V. DUMOULIN, et al. 2017. Improved training of wasserstein GANs. In *Proceedings of the Proceedings of the 31st International Conference on Neural Information Processing Systems*, Long Beach, California, USA2017 Curran Associates Inc., 5769–5779.

81.   RAUDENSKA, M., J. BALVAN, M. FOJTU, J. GUMULEC, et al. Unexpected therapeutic effects of cisplatin. Metallomics, 2019.

82.   WU, P. H., D. R. AROUSH, A. ASNACIOS, W. C. CHEN, et al. A comparison of methods to assess cell mechanical properties. Nat Methods, 2018, 15(7), 491-498.

83.   HANAHAN, D. AND ROBERT A. WEINBERG Hallmarks of Cancer: The Next Generation. Cell, 2011, 144(5), 646-674.

84.   FRITSCH, A., M. HÖCKEL, T. KIESSLING, K. D. NNETU, et al. Are biomechanical changes necessary for tumour progression? Nature Physics, 2010/10/01 2010, 6(10), 730-732.

85.   HOLUBOVA, M., M. AXMANOVA, J. GUMULEC, M. RAUDENSKA, et al. KRAS NF-kappa B is involved in the development of zinc resistance and reduced curability in prostate cancer. Metallomics, 2014 2014, 6(7), 1240-1253.

86.   VICAR, T., J. GUMULEC, J. CHMELIK, J. NAVRATIL, et al. Cancer Cells Viscoelasticity Measurement by Quantitative Phase and Flow Stress Induction. bioRxiv, 2021, 2021.08.05.455201.

87.   VICAR, T., J. GUMULEC, R. KOLAR, J. CHMELIK, et al. Parametric Deconvolution for Cancer Cells Viscoelasticity Measurements from Quantitative Phase Images. bioRxiv, 2021, 2021.04.06.438595.

88.   ELSAYAD, K., G. URSTÖGER, C. CZIBULA, C. TEICHERT, et al. Mechanical Properties of cellulose fibers measured by Brillouin spectroscopy. Cellulose, 2020/03/02 2020.

89.   GUMULEC, J., J. BALVAN, T. VICAR, M. KRATOCHVILOVA, et al. Mass redistribution – not accumulation characteristic for aggressive prostate cancer: simultaneous employment of quantitative phase microscopy techniques. In *COMULIS & BioImaging Austria/CMI Conference.* Vienna, Austria: COMULIS COST, 2019.

90.   GUMULEC, J., J. BALVAN, K. ELSAYAD, T. VICAR, et al. Cell stifness and cancer progession: from AFM to correlative brillouin scattering with digital holographic microscopy. In *3rd BioBrillouin Meeting.* Porto, Portugal: BioBrillouin COST, 2019.

91.   GUMULEC, J., M. MASARIK, V. ADAM, T. ECKSCHLAGER, et al. Serum and Tissue Zinc in Epithelial Malignancies: A Meta-Analysis. Plos One, Jun 18 2014, 9(6).

92.   FRANKLIN, R. B., J. ZOU, Z. YU AND L. C. COSTELLO EAAC1 is expressed in rat and human prostate epithelial cells; functions as a high-affinity L-aspartate transporter; and is regulated by prolactin and testosterone. BMC Biochemistry, 2006, 7(1), 10.

93.   COSTELLO, L. C. AND R. B. FRANKLIN The intermediary metabolism of the prostate: a key to understanding the pathogenesis and progression of prostate malignancy. Oncology, 2000, 59.

94.   CUTRUZZOLA, F., G. GIARDINA, M. MARANI, A. MACONE, et al. Glucose Metabolism in the Progression of Prostate Cancer. Frontiers in Physiology, Feb 2017, 8.

95.   KRATOCHVILOVA, M., M. RAUDENSKA, Z. HEGER, L. RICHTERA, et al. Amino Acid Profiling of Zinc Resistant Prostate Cancer Cell Lines: Associations With Cancer Progression. Prostate, May 2017, 77(6), 604-616.

96.   KHAN, A. P., T. M. RAJENDIRAN, B. ATEEQ, I. A. ASANGANI, et al. The role of sarcosine metabolism in prostate cancer progression. Neoplasia (New York, N.Y.), 2013, 15(5), 491-501.

97.   HEGER, Z., J. GUMULEC, N. CERNEI, H. POLANSKA, et al. Relation of exposure to amino acids involved in sarcosine metabolic pathway on behavior of non-tumor and malignant prostatic cell lines. Prostate, May 2016, 76(7), 679-690.

98.   KÖPF-MAIER, P. AND S. K. MÜHLHAUSEN Changes in the cytoskeleton pattern of tumor cells by cisplatin in vitro. Chemico-Biological Interactions, 1992/05/01/ 1992, 82(3), 295-316.

99.   KUNG, M.-L., C.-W. HSIEH, M.-H. TAI, C.-H. WENG, et al. Nanoscale characterization illustrates the cisplatin-mediated biomechanical changes of B16-F10 melanoma cells. Physical Chemistry Chemical Physics, 2016, 18(10), 7124-7131.

100.   ZEIDAN, Y. H., R. W. JENKINS AND Y. A. HANNUN Remodeling of cellular cytoskeleton by the acid sphingomyelinase/ceramide pathway. J Cell Biol, Apr 21 2008, 181(2), 335-50.

101.   VASSILOPOULOS, A., C. XIAO, C. CHISHOLM, W. CHEN, et al. Synergistic therapeutic effect of cisplatin and phosphatidylinositol 3-kinase (PI3K) inhibitors in cancer growth and metastasis of Brca1 mutant tumors. J Biol Chem, Aug 29 2014, 289(35), 24202-14.

102.   BOEKELHEIDE, K., M. E. ARCILA AND J. EVELETH cis-diamminedichloroplatinum (II) (cisplatin) alters microtubule assembly dynamics. Toxicol Appl Pharmacol, Sep 1992, 116(1), 146-51.

103.   RAUDENSKA, M., J. BALVAN, M. FOJTU, J. GUMULEC, et al. Unexpected therapeutic effects of cisplatin. Metallomics, Jul 2019, 11(7), 1182-1199.

104.   MANDAL, K., A. ASNACIOS, B. GOUD AND J. B. MANNEVILLE Mapping intracellular mechanics on micropatterned substrates. Proc Natl Acad Sci U S A, 2016, 113(46), E7159-E7168.

105.   LI, Y., J. SCHNEKENBURGER AND M. H. DUITS Intracellular particle tracking as a tool for tumor cell characterization. J Biomed Opt, 2009, 14(6), 3257253.

106.   NIJENHUIS, N., X. ZHAO, A. CARISEY, C. BALLESTREM, et al. Combining AFM and acoustic probes to reveal changes in the elastic stiffness tensor of living cells. Biophysical Journal, 2014, 107(7), 1502-1512.

107.   AGUS, D. B., J. F. ALEXANDER, W. ARAP, S. ASHILI, et al. A physical sciences network characterization of non-tumorigenic and metastatic cells. Sci Rep, 2013, 3(1449).

108.   HERZOG, F. A. AND C. R. JACOBS. 5.506 - Effects of Mechanical Stress on Cells. In P. DUCHEYNE ed. *Comprehensive Biomaterials.* Oxford: Elsevier, 2011, p. 73-80.

109.   MATTHEWS, B. D., D. R. OVERBY, R. MANNIX AND D. E. INGBER Cellular adaptation to mechanical stress: role of integrins, Rho, cytoskeletal tension and mechanosensitive ion channels. Journal of Cell Science, 2006, 119(3), 508-518.

110.   JIU, Y. Vimentin intermediate filaments function as a physical barrier during intracellular trafficking of caveolin-1. Biochemical and Biophysical Research Communications, 2018/12/09/ 2018, 507(1), 161-167.

111.	PARTON, R. G., M. A. DEL POZO, S. VASSILOPOULOS, I. R. NABI, et al. Caveolae: The FAQs. Traffic, 2020, 21(1), 181-185.

112.	HALESTRAP, A. P. The monocarboxylate transporter family--Structure and functional characterization. IUBMB Life. , 2012, 64(1521-6551 (Electronic)).

113.	TAHIR, S. A., G. YANG, A. GOLTSOV, K. D. SONG, et al. Caveolin-1-LRP6 signaling module stimulates aerobic glycolysis in prostate cancer. Cancer Res, Mar 15 2013, 73(6), 1900-11.

114.	MORENO-VICENTE, R., D. M. PAVÓN, I. MARTÍN-PADURA, M. CATALÀ-MONTORO, et al. Caveolin-1 Modulates Mechanotransduction Responses to Substrate Stiffness through Actin-Dependent Control of YAP. Cell Reports, 2018/11/06/ 2018, 25(6), 1622-1635.e6.

115.	GOETZ, JACKY G., S. MINGUET, I. NAVARRO-LÉRIDA, JUAN J. LAZCANO, et al. Biomechanical Remodeling of the Microenvironment by Stromal Caveolin-1 Favors Tumor Invasion and Metastasis. Cell, 2011/07/08/ 2011, 146(1), 148-163.

116.	LIN, H.-H., H.-K. LIN, I. H. LIN, Y.-W. CHIOU, et al. Mechanical phenotype of cancer cells: cell softening and loss of stiffness sensing. Oncotarget, 2015, 6(25), 20946-20958.

117.	WANG, Z., N. WANG, W. LI, P. LIU, et al. Caveolin-1 mediates chemoresistance in breast cancer stem cells via β-catenin/ABCG2 signaling pathway. Carcinogenesis, 2014, 35(10), 2346-56.

118.	WANG, Z., N. WANG, P. LIU, F. PENG, et al. Caveolin-1, a stress-related oncotarget, in drug resistance. Oncotarget, 2015, 6(35).

119.	GALBIATI, F., D. VOLONTÉ, J. LIU, F. CAPOZZA, et al. Caveolin-1 expression negatively regulates cell cycle progression by inducing G(0)/G(1) arrest via a p53/p21(WAF1/Cip1)-dependent mechanism. Mol Biol Cell, 2001, 12(8), 2229-44.

120.	QUEST, A. F., J. L. GUTIERREZ-PAJARES AND V. A. TORRES Caveolin-1: an ambiguous partner in cell signalling and cancer. J Cell Mol Med, 2008, 12(4), 1130-50.